

國立臺灣大學農業化學系

博士論文

Department of Agriculture Chemistry

National Taiwan University

Doctoral Thesis



奈米鐵顆粒分散性與有機酸對含鹵素有機污染物反應性影響之研究

The effects of dispersion methods and organic acids on the reactivity
of iron nanoparticles to remove halogenated organic contaminants

左致平

Chih-ping Tso

指導教授：施養信 博士

Advisor: Yang-hsin Shih, Ph.D.

中華民國 105 年 7 月

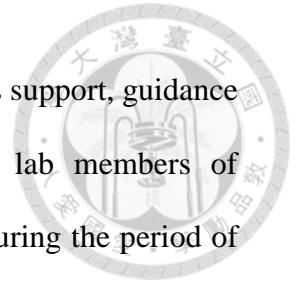
July 2016

Acknowledgment

I express my deep sense of gratitude to Prof. Yang-hsin Shih for his support, guidance and encouragement. I also wish to express my gratitude to the lab members of Environmental Nanotechnology Laboratory who rendered their help during the period of my PhD work. I sincerely thank committee for their guidance in carrying out this thesis work.

I am very much thankful to Instrumentation Center (National Taiwan University) and National Synchrotron Radiation Research Center (NSRRC) for the assistance in experiments and the financial support from the Ministry of Science and Technology (MOST).

I express deep and sincere gratitude to Prof. Ruben Kretzschmar for providing me the opportunity to do my abroad program at ETH Zürich. I am also express my sincere gratitude to Dr. Iso Christl, Kurt Barmettler and the research group of Soil Chemistry who rendered their help during my project work.




摘要

奈米級零價鐵 (Nanoscale zerovalent iron, NZVI) 及雙金屬奈米鐵顆粒因具高比表面積與還原勢能，能有效移除許多含鹵素有機污染物，而廣泛應用於污染場址整治中。然而奈米鐵顆粒 (Fe nanoparticles, Fe NPs) 因受顆粒特性與環境因子影響而易聚集並沉澱，降低移動性和反應性。此外，奈米鐵顆粒受環境因子如離子組成和離子強度等生成鈍化層改變顆粒表面特性，降低奈米鐵顆粒的反應性與長效性。故如何提升並延長奈米鐵顆粒的有效性為當前一重要課題。除了奈米鐵顆粒的作用外，其反應後生成之鐵離子與鐵氧化物在環境中與天然有機物之作用亦不可忽視。因此本研究透過使用穩定分散的奈米鐵顆粒，探討不同反應條件下其之反應性與反應機制，並探討後續於環境整治中的應用性。奈米鐵顆粒分別以物理性分散法與化學穩定劑修飾法分散懸浮奈米顆粒，添加羧酸以移除鐵顆粒表面的鈍化層以增加並延長有效性，更進一步探討腐植酸 (humic acid, HA) 與鐵 (銅) 離子生成的錯合物和共沉澱物的反應性，用以評估奈米鐵顆粒後續處理之可行性。

相較於奈米鐵團粒，分散之奈米鐵顆粒具較多的比表面積，因而增加對污染物如五氯酚之吸附量。常見陰離子 (Cl^- , NO_3^- 和 HCO_3^-) 對穩定分散之奈米鐵顆粒的影響指出，因 NO_3^- 被鐵還原後於鐵表面生成氫氧化鐵沉澱，進而促進對污染物的吸附/絮聚現象，增加移除效率。而 HCO_3^- 因於鐵表面生成碳酸鐵沉澱而明顯抑制反應速率， Cl^- 則沒有明顯促進作用。使用羧甲基纖維素 (Carboxymethyl cellulose, CMC) 作為分散劑包覆於鐵表面可有效分散並懸浮奈米顆粒。鹼性環境下由於 CMC 的解離使顆粒更為分散而增加 CMC-Fe 的反應性；CMC 層促進污染物如十溴二苯醚擴散至鐵表面，但亦會抑制電子傳輸，降低降解效率。相較於未修飾的奈米鐵顆粒，CMC 層可保護鐵表面受到陰離子的侵蝕作用，故其反應性並未受陰離子之影響。由於 CMC 可延長奈米鐵顆粒的有效性，使 CMC 修飾之奈米鐵顆粒具有現地處理之潛力。

有機羧酸如甲酸 (formic acid, FA)、草酸 (oxalic acid, OA)、檸檬酸 (citric acid, CA) 可透過移除鈍化層改變表面特性，促進鐵顆粒的反應性。在相同酸當量濃度下，鐵顆粒對污染物如三氯乙烯的反應速率為 $\text{FA} > \text{OA} > \text{pure water} \cong \text{CA}$ 。FA 對 Fe^{2+}




無明顯錯合能力，透過提供 H^+ 移除鐵表面鈍化層並生成磁鐵礦而提高吸附率；OA 與 CA 對 Fe^{2+} 具高錯合能力，可藉由形成可溶性錯合物移除鈍化層，OA 和 CA 與鐵的錯合物依其氧化還原電位亦可進一步移除污染物或降解副產物。然而高濃度的 OA 生成草酸鐵沉澱於鐵顆粒表面，反而降低反應性。鐵離子 (Fe^{2+}) 與 HA 的錯合反應亦可能改變其形態與反應性。 Fe^{2+} 的反應性受 pH 影響，於 pH 9 環境中反應性較高。HA 與 Fe^{2+} 錯合物 (HA-Fe) 亦有相同趨勢。還原性 HA 與 Fe^{2+} 的錯合物 (RHA-Fe) 較未處理 HA 與 Fe^{2+} 錯合物 (UHA-Fe) 有較高的反應性；但 HA 與 Fe 的錯合反應可能因與污染物競爭電子而降低 Fe^{2+} 的反應性。此外，RHA 抑制 Fe^{2+} 於鹼性環境下生成沉澱物，卻形成更多的 HA- Fe^{3+} 。而高濃度 Fe^{2+} 和 Cu^{2+} 在 HA 存在下可共沉澱生成膠體顆粒。HA-Fe 的膠體顆粒相比較，HA-Cu 有較高的反應性，並且有較明顯的顆粒外型與結構。RHA-Cu 顆粒的穩定性高甚至有小部分 Cu^{2+} 還原為 Cu^0 ，其反應性也較 UHA-Cu 高。

此研究針對穩定分散的奈米鐵顆粒與污染物之間的反應，得其反應機制與不同環境條件下之反應性；由 CMC 修飾奈米鐵顆粒探討現地應用之可行性；透過表面特性的改變，增加鐵顆粒的有效性，並發現腐植酸與鐵 (銅) 離子之間的錯合反應可生成具反應性之錯合物甚至膠體顆粒。對於奈米鐵顆粒應用於現地整治方面，可提供進一步資訊評估其可行性。鐵 (銅) 離子於厭氧環境中可生成具反應性的錯合物與膠體顆粒，可進一步建立與天然腐植物質相關之綠色整治技術。

關鍵字: 奈米鐵顆粒、顆粒穩定性、CMC 修飾奈米鐵顆粒、羧酸、腐植酸、鐵錯合物、金屬膠體顆粒。

Abstract



Nanoscale zerovalent iron (NZVI) and bimetallic Fe nanoparticles (NPs) have significant potential for the remediation of a wide array of priority pollutants. Their properties of a large surface area and high reduction potential generated significant interest in their application for in-situ remediation. However, Fe NPs aggregate immediately that significantly reduce their mobility and reactivity. Furthermore, corrosion processes form precipitates on the Fe surface, whose passive layers resulted in a rapid decrease in activity and longevity. Therefore, methods to enhance/extend the colloidal stability and reactivity of Fe NPs are needed. On the other hand, it is important to understand the reactivity of Fe ions and Fe oxides after the application of Fe NPs. Fe NPs were dispersed successfully via physical (ultrasonication (US)) and chemical (CMC stabilizer) dispersion methods under different environmental conditions. Carboxylic acids including formic acid (FA), oxalic acid (OA) and citric acid (CA), were applied to prolong the Fe particles reactivity by removing passive layers on the Fe surface. Furthermore, the activity of Fe (Cu) complexes/precipitates with humic acid (HA) to mimic natural environments was assessed for subsequent treatments.

Well-dispersed bare Fe NPs enhanced the adsorption of contaminants such as pentachlorophenol onto the Fe surface, as compared to Fe aggregates. In the presence of common anions (Cl^- , NO_3^- and HCO_3^-), NO_3^- was reduced by Fe NPs and generated more Fe (hydro)oxides that responded to increase the adsorption/coagulation of the target compound. The inhibition of Fe reactivity by HCO_3^- may be due to the formation of precipitates on the Fe surface while Cl^- only caused a small increasing in Fe reactivity. The presence of CMC suspended Fe NPs very well and dispersed them into individual particles

instead of nanoparticle aggregates. Due to the properties of CMC, the reactivity of CMC-Fe NPs toward decabromodiphenyl ether was enhanced under alkaline conditions. The reaction rate was considered as a surface chemical reaction because the CMC layers induced diffusion for the target compound to the Fe surface. But CMC layers may also hinder the electron transfer. Anions did not influence the reactivity of CMC-Fe NPs compared with bare Fe NPs, indicating that the CMC layers may inhibit surface corrossions and thus prolong the reactivity of Fe NPs in the environment.

Common carboxylic ligands (FA, OA and CA) induced the reactivity of Fe particles toward trichloroethylene following an order of FA > OA > pure water \cong CA by dissolving Fe oxides from the Fe surface. FA provided protons to promote the dissolution of passive layers and to convert iron oxides to form magnetite which increased the adsorption of the target compound onto the Fe surface. With the strong complexing ability, OA and CA could form dissoluble complexes to remove passive layers. But a high concentration of OA resulted in reprecipitated of Fe oxalate back onto the Fe surface which then inhibited its reactivity. Moreover, these Fe-ligand complexes could further degrade the target compound depending on their redox properties. The activity of Fe²⁺ and HA-Fe complexes depended on the pH which had strong interactions toward the target compound at pH 9. RHA-Fe complexes had higher reactivity than UHA-Fe, but these complex forms potentially reduced the Fe²⁺ reactivity because of electron competition with the target compound. Moreover, RHA prevented Fe²⁺ from precipitating but also caused higher Fe²⁺ oxidation. Furthermore, HA co-precipitated Fe and Cu colloids showed ability to remove the organic contaminants such as Reactive black 5. HA-Cu colloids had higher reactivity than HA-Fe colloids, which could result from the nature of metal, the shape and the

morphology of particles. RHA-Cu colloids stably dispersed in aqueous solutions. Among them, a small amount of Cu^0 was generated by RHA. RHA-Cu colloids also had a stronger reactivity than UHA-Cu colloids for breaking azo bonds in the target compound.

To conclude, this study presents the reaction characteristics and removal mechanisms of bare Fe NPs that were well suspended under different conditions and the potential for CMC-Fe NPs for in-situ treatments. The characteristics and reactivity of metal complexes/colloids with ligands and HA in reducing environments have pointed out the potential of these Fe (Cu) complexes/colloids for sustainable/green remediation.

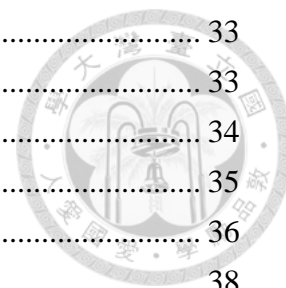
Keyword: Fe nanoparticles (NPs), colloidal stability, CMC-Fe NPs, carboxylic ligands, humic acid (HA), Fe complexes, metallic colloids.

Content



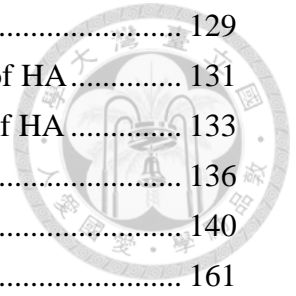
Acknowledgment	I
摘要	I
Abstract	III
Content	VI
Figure content	X
Table content	XVI
Scheme content	XVII
Chapter 1 Introduction	1
Chapter 2 Paper review	8
2.1 Nanoremediation	8
2.1.1 The application of Fe NPs	9
2.1.2 The stability of Fe NPs	12
2.1.2.1 Chemical dispersion methods	13
2.1.2.2 Physical dispersion methods	16
2.1.3 The surface characteristics of Fe NPs	18
2.1.3.1 The removal of passive layers on the metal NPs surface	18
2.1.3.2 Influence of Fe mineral type	20
2.1.4 Life cycle of Fe NPs toward green remediation	21
2.1.4.1 Abiotic formation processes of metal colloids/NPs in the environment	22
2.1.4.2 Green synthesis of metal NPs	25
2.1.4.3 Effect of NOM and its functional groups on the wastewater treatment	27
2.2 Nanoparticle analysis and characterization methodologies	28
2.2.1 Methods for assessing the shape, size and surface structure of NPs	28
2.2.1.1 Scanning electron microscopy (SEM)	28
2.2.1.2 Transmission electron microscopy (TEM)	29
2.2.1.3 Dynamic light scattering (DLS)	29
2.2.1.4 Surface charge (Zeta potential) of nanoparticles	30
2.2.2 Methods for measuring the elemental composition of single nanoparticle	31
2.2.2.1 X-ray diffraction (XRD)	31
2.2.2.2 Synchrotron-based X-ray absorption spectroscopy (XAS)	31
2.2.2.3 Fourier transform infrared spectroscopy (FTIR)	32
2.3 Pollutants of concern	33

2.3.1	Halogenated organic contaminants	33
2.3.1.1	Pentachlorophenol (PCP)	33
2.3.1.2	Brominated flame retardants (BFRs)	34
2.3.1.3	Chlorinated solvents	35
2.3.2	Azo dyes	36
Chapter 3 Materials and methods		38
3.1	Chemicals	38
3.1.1	Analytical standards	38
3.1.2	Solvents	38
3.1.3	Reagents	38
3.2	The preparation and analysis of ZVI, NZVI and bimetallic Fe NPs	39
3.2.1	ZVI pretreatment	39
3.2.2	Synthesis of bare Fe NPs	39
3.2.3	Synthesis of CMC stabilized Fe NPs	40
3.2.4	Characteristics of ZVI and Fe NPs	41
3.2.4.1	The Fe ²⁺ dissolution from the Fe surface	41
3.2.4.2	The surface morphologies of Fe particles	41
3.2.4.3	The atomic and molecular structures of Fe particles	42
3.2.4.4	The Fourier transform infrared spectroscopy (FTIR) technique	43
3.3	Removal kinetics of halogenated organic compounds by well-suspended Fe NPs	44
3.3.1	Physical dispersion methods	44
3.3.2	Chemical dispersion method	45
3.4	Removal kinetics of halogenated organic compound by ZVI and Fe ²⁺ in the presence of ligand	46
3.5	Formation and analysis of HA-Fe complexes and HA-metal colloids	47
3.5.1	Perpetration of HA stock solution	47
3.5.2	Preparation of HA-Fe complexes	48
3.5.3	Preparation of metal colloids in the presence of HA	49
3.6	The reactivity of HA-Fe complexes and HA-metal colloids	51
3.6.1	HA-Fe complexes	51
3.6.2	HA-metal colloids	51
3.7	Analytical methods of halogenated organic compounds	52
3.7.1	Analysis of PCP	52
3.7.2	Analysis of DBDE	52



3.7.3	Analysis of TCE.....	53
3.7.4	Analysis of ions.....	53
3.7.5	Total ROS measurement.....	54
3.8	Modeling	54
3.8.1	Reaction kinetics of halogenated organic compounds with Fe NPs.....	54
3.8.2	Dehalogenation efficiency of halogenated organic compounds	55
3.8.3	Activation energy.....	55
3.8.4	Fe dissolution kinetic of ZVI in the presence of ligands	56
3.8.5	Speciation calculation	56
Chapter 4	Results and discussions	58
4.1	Well-suspended Fe NPs by the physical dispersion method.....	58
4.1.1	The removal of PCP by Fe NPs in different dispersion systems	58
4.1.2	The removal mechanism of PCP by Pd/Fe NPs in US dispersion systems	63
4.1.3	The effect of Pd doping on the removal of PCP by Fe NPs in the US/stirring system	66
4.1.4	The effect of anions on the removal of PCP by Pd/Fe NPs in the US/stirring system	69
4.2	Well-suspended Fe NPs by the chemical dispersion method.....	73
4.2.1	Characteristics of CMC-stabilized Fe NPs	73
4.2.2	The removal of DBDE by CMC-Ni/Fe NPs.....	77
4.2.3	The reaction mechanism of DBDE by CMC-Ni/Fe.....	78
4.2.4	The effect of anion on the reactivity of CMC-Ni/Fe NPs.....	85
4.3	Comparison of physical and chemical dispersion methods	89
4.4	The influence of organic ligands on the surface characteristics of ZVI.....	92
4.4.1	The effect of ligand acids on the removal of TCE by ZVI.....	92
4.4.2	Characteristics of ZVI surface in the presence of ligand acids.....	97
4.4.3	Fe dissolution process in the presence of ligand acids	98
4.4.4	The effect of ligand-Fe complexes on the reactivity of ZVI	103
4.5	The reactivity and transformation of HA-Fe complexes.....	107
4.5.1	Reduction of RB5 in HA control systems.....	107
4.5.2	Reduction of RB5 in Fe ²⁺ systems.....	111
4.5.3	Reduction of RB5 in HA-Fe system	114
4.5.4	The reduction mechanism of HA-Fe.....	116
4.6	The formation and reactivity of metal colloids in the presence of HA	121
4.6.1.	The formation of Cu colloids in the absence and in the presence of HA .	123

4.6.2. The characteristics of Cu colloids in the presence of HA.....	129
4.6.3. The bonding mechanism for Cu colloids in the presence of HA.....	131
4.6.4. The reaction mechanism for Cu colloids in the presence of HA.....	133
Chapter 5 Conclusions	136
Reference	140
Supporting information.....	161



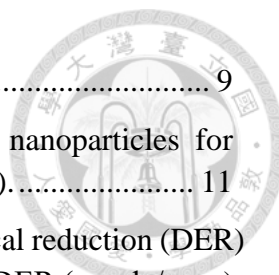


Figure content

Figure 2-1. Nanoremediation map (Nanotechnologies, 2009).....	9
Figure 2-2. Proposed scheme of reactions on the surface of Ni/Fe nanoparticles for reductive or oxidative degradation of contaminants (Bokare et al., 2007).....	11
Figure 2-3. Decrease in solution potential E_h during direct electrochemical reduction (DER) of HA at pH 7 as a function of DER-transferred amount of electrons, Q_{DER} ($\mu\text{mole/g}_{LHA}$) (Aeschbacher et al., 2009).	24
Figure 3-1. The standard curves of (a) RB5, (b) HA, and (c) RB5 with HA. For RB5 with the HA set, a linear relationship was observed between the actual absorbance value and the expected absorbance values.	49
Figure 4-1. TEM images of NZVI and Pd/Fe NPs.	60
Figure 4-2. Removal reactions of PCP with NZVI under shaking and US suspended systems. PCP initial concentration was 6.5 mg/L and NZVI dosage was 1.0 g/L. The error bar in Figure 4-2 represented the standard error of an average over duplicated batch experiments.	60
Figure 4-3. (a) Removal reactions of PCP with Pd/Fe NPs under various suspended systems and (b) the PCP distribution after reacted with Pd/Fe NPs for 60 minutes. PCP initial concentration was 7.2 mg/L, Fe dosage was 4.5 g/L and Pd content was 0.1 wt%. The orbital shaker was operating at 150 rpm, the stirrer was set at 120 rpm, US output intensity was 75 W during US irradiation. The error bar in Figure 4-3 represented the standard error of an average over duplicated batch experiments.	61
Figure 4-4. The average particle size of NZVI and Pd/Fe NPs under US probe irradiation for 60 minutes. Data collected from DLS results as number distribution.	62
Figure 4-5. The sedimentation curves of Pd/Fe NPs under the US and the US/stirring systems. US output intensity was 75 W during US irradiation.....	62
Figure 4-6. The effect of the US irradiation intensity on the removal of PCP and the particle size of Pd/Fe NPs. PCP initial concentration was 7.2 mg/L, Fe dosage was 4.5 g/L and Pd content was 0.1 wt%. US output intensity was 75 W during US irradiation.....	64
Figure 4-7. XRD spectra of Pd/Fe NPs under various conditions. US output intensity was 75 W. Anion concentration was 10 mM in the anion systems. Fe dosage was 4.5 g/L and Pd content was 0.1 wt%.	65
Figure 4-8. (a) The effect of Pd content on the removal kinetics of PCP by Pd/Fe NPs in the US/stirring system and (b) the PCP distribution after reacted with Pd/Fe NPs for 40 minutes. PCP initial concentration was 7.2 mg/L and Fe dosage was 4.5 g/L. The stirrer was set at 120 rpm, US output intensity was 75 W during US irradiation. The error bar in	

Figure 4-8 represent the standard error of an average over duplicated batch experiments.	67
Figure 4-9. The effect of Pd content on (a) the dechlorination reaction rate and (b) the dechlorination efficiency of PCP by Pd/Fe NPs under the US/stirring system. PCP initial concentration was 7.2 mg/L and Fe dosage was 4.5 g/L.	68
Figure 4-10. (a) The effect of anions on the removal of PCP by Pd/Fe NPs in the US/stirring system. (b) The relationship between the reaction rate constants and the anion concentrations. PCP initial concentration was 7.2 mg/L, Fe dosage was 4.5 g/L and Pd content was 0.1 wt%. US output intensity was 75 W during US irradiation. The error bar in Figure 4-10 represent the standard error of an average over duplicated batch experiments.	71
Figure 4-11. The PCP distribution after reacted with Pd/Fe NPs in the presence of anions under US/stirring system after 40 min. The data was collected from Figure 4-10a.	72
Figure 4-12. TEM images and size distribution of CMC stabilized Fe NPs. The size distribution was calculated using ImageJ and OriginLab software (particle number=43).	75
Figure 4-13. The zeta-potential of the CMC-Fe and CMC-Ni/Fe versus pH.	75
Figure 4-14. (a) Fe K-edge and (b) Ni K-edge of XANES spectra of the bare Fe NP and the CMC-stabilized Fe NPs.	76
Figure 4-15. (a) The effect of the Ni loading on the removal of DBDE with the CMC-Ni/Fe and (b) the degradation, adsorption, and residual fractions of DBDE reacted with the CMC-Ni/Fe. The initial concentration of DBDE was 10 mg/L, Fe dosage was 5.0 g/L, and CMC concentration was 4.2 g/L. The error bar in Figure 4-15 represent the standard error of an average over duplicated batch experiments.	81
Figure 4-16. The removal efficiency and the degradation efficiency of DBDE by the CMC-stabilized Fe NPs with different Ni content.	82
Figure 4-17. Fe K-edge of XANES spectra of the CMC-Ni/Fe.	82
Figure 4-18. (a) The effect of temperature on the degradation of DBDE by CMC-Ni/Fe. (b) The plot of $\ln k_{obs}$ versus $1/T$ for the CMC-Ni/Fe. The initial concentration of DBDE was 10 mg/L, Fe dosage was 5.0 g/L, Ni/Fe was 0.5 wt %, and CMC concentration was 4.2 g/L. The error bar in Figure 4-18 represent the standard error of an average over duplicated batch experiments.	83
Figure 4-19. (a) The effect of pH on the removal of DBDE by CMC-Ni/Fe. (b) The relation between k_{obs} and the particle size under different pH conditions. The initial concentration of DBDE was 10 mg/L, Fe dosage was 5.0 g/L, Ni/Fe was 0.5 wt %, and CMC concentration was 4.2 g/L. The error bar in Figure 4-19 represent the standard error of an	

average over duplicated batch experiments. The average particle size (as z-average) was measured using DLS.....	84
Figure 4-20. The removal kinetics of DBDE with the CMC-Ni/Fe in the presence of (a) chloride, (b) nitrate, and (c) bicarbonate. The initial concentration of DBDE was 10 mg/L, Fe dosage was 5.0 g/L, Ni/Fe was 0.5 wt %, and CMC concentration was 4.2 g/L. The error bar in Figure 4-20 represent the standard error of an average over duplicated batch experiments.....	87
Figure 4-21. The reaction rate constants of DBDE by CMC-Ni/Fe in the presence of anions. The values of k_{obs} obtained from fitting of the data in Figure 4-20.....	87
Figure 4-22. Fe K-edge of XANES spectra of the CMC-Ni/Fe in the presence of (a) 1mM and (b) 10 mM of anions.....	88
Figure 4-23. The particle size (as z-average) of Fe NPs and removal rate constant of target compounds in (a) the US/stirring system and (b) the CMC system.	91
Figure 4-24. The removal kinetics of TCE with carboxylic acid.	94
Figure 4-25. (a) The reduction kinetics of TCE by ZVI in the presence of 30 mM of carboxylic molarity of ligands. (b) TCE distribution with ZVI in the presence of ligands. ZVI dosage was 20 g/L and TCE initial concentration was 4.57 μ M. The error bar in Figure 4-25 represent the standard error of an average over triplicated batch experiments.	95
Figure 4-26. Effect of carboxylic acids on the degradation of TCE with ZVI. ZVI dosage was 20 g/L and TCE initial concentration was 4.57 μ M. The error bar in Figure 4-26 represent the standard error of an average over triplicated batch experiments.....	96
Figure 4-27. The relation between the carboxylic concentration and k_{obs} . The values of k_{obs} obtained from fitting of the data in Figure 4-26.	96
Figure 4-28. XRD spectra of (a) fresh ZVI, (b) aged ZVI, ZVI in the presence of (c) FA, (d) OA, and (e) CA. In spextra, (Fe) represents as iron and (M) represents as magnetite.	100
Figure 4-29. SEM images of the surface morphology of ZVI in (a) pure water and in the presence of (b) FA, (c) OA, and (d) CA.	101
Figure 4-30. Fe dissolution in the presence of 30 mM of carboxylic molarity of ligands. ZVI dosage was 20 g/L and TCE initial concentration was 4.57 μ M.....	102
Figure 4-31. Fe dissolution in the presence of different concentrations of (a) FA, (b) OA, and (c) CA. ZVI dosage was 20 g/L and TCE initial concentration was 4.57 μ M.....	102
Figure 4-32. Images of ZVI in the presence of carboxylic ligands.	102
Figure 4-33. The relation between TCE reaction rate constant and Fe dissolution concentration.....	103

Figure 4-34. The removal efficiency of TCE by Fe ²⁺ -ligand complexes after reaction for 16.5 hours. TCE concentration was 4.57 μM, Fe ²⁺ initial concentration was 40 mM, and final pH was about 5.	106
Figure 4-35. The removal kinetics of RB5 in (a) UHA and (b) RHA systems. HA concentration was 31.25 mg/L and RB5 initial concentration was about 6.3 mg/L. Background buffers were 100 mM of acetate, HEPES and Tris buffer at pH 5, 7 and 9, respectively. The error bars in the Figures represent the standard error of an average over triplicated batch experiments.	108
Figure 4-36. The Eh values in Fe ²⁺ , UHA, RHA, UHA-Fe, and RHA-Fe systems. HA concentration was 31.25 mg/L, Fe ²⁺ concentration was 1.6 mmol/g _{HA} (50 μM) and RB5 initial concentration was 6.3 mg/L. Background buffers were 100 mM of acetate, HEPES and Tris buffer at pH 5, 7 and 9, respectively.	109
Figure 4-37. The UV-vis full scan spectra of RB5 after reactions in HA and HA-Fe systems for 6 days. The peak marks were calculated using OriginLab software. Peaks were quantified by fitting the peak center from the selected range of the data plot after subtracting the baseline of HA or HA-Fe.	110
Figure 4-38. Effect of RB5/HA ratio on the removal of RB5 by RHA at pH 7. RB5 removal efficiency was observed after reacting for 6 days. The RB5 removal efficiency increased with a decrease in the RB5/HA ratio. When the RB5/HA ratio decreased to 0.036 (red dot), RB5 removal efficiency also decreased, which might be caused by the interference of high HA concentrations to low concentrations of RB5.	111
Figure 4-39. The degradation kinetics of RB5 in the Fe ²⁺ systems. Fe ²⁺ concentration was 50 μM and RB5 initial concentration was 6.3 mg/L. Background buffers were 100 mM of acetate, HEPES and Tris buffer at pH 5, 7 and 9, respectively. The error bars in this Figure represents the standard error of an average over triplicated batch experiments.	112
Figure 4-40. Fe species distribution in the Fe ²⁺ systems at different pHs. Fe species include Fe ²⁺ , Fe ³⁺ , Fe colloids, and total Fe.	113
Figure 4-41. Fe distribution predicted by Visual MINTEQ 3.0 software. (a) Fe ²⁺ control system. (b) SHM and (c) NICA models for HA-Fe systems. The parameter sets for Fe precipitation and complexation were as follows: Fe ²⁺ and SO ₄ ²⁻ concentration were 50 μM, DOM concentration was 18.6 mg/L (HA).	114
Figure 4-42. The removal kinetics of RB5 in (a) UHA-Fe and (b) RHA-Fe system. HA concentration was 31.25 mg/L, Fe ²⁺ concentration was 1.6 mmol/g _{HA} (50 μM), and RB5 initial concentration was about 6.3 mg/L. Background solutions were 100 mM of acetate, HEPES and Tris buffers at pH 5, 7 and 9, respectively. The error bars in these Figures represent the standard error of an average over triplicated batch experiments.	118

Figure 4-43. Fe species distribution in the two HA-Fe systems under different pH conditions. Fe species include Fe ²⁺ , Fe ³⁺ , Fe colloids, and total Fe.	119
Figure 4-44. The relationship between pH and RB5 removal efficiency. RB5 removal efficiency in the Figure presents an average between day 4 and day 6.	120
Figure 4-45. The relationship between Fe oxidation/precipitation and RB5 removal efficiency. RB5 removal efficiency in the Figure presents an average between day 4 and day 6.	120
Figure 4-46. TEM images of Fe colloids in the presence of UHA and RHA. HA concentration was 20 mg/L and Fe ²⁺ concentration was 10 g/L.	122
Figure 4-47. TEM images of Cu colloids in the presence of UHA and RHA. HA concentration was 20 mg/L and Cu ²⁺ concentration was 10 g/L.	122
Figure 4-48. Removal of RB5 by metal ions in the presence of HA. RB5 initial concentration was 50 mg/L. HA concentrations were 20 and 60 mg/L. Concentration of Fe ²⁺ and Cu ²⁺ was 10 g/L.	122
Figure 4-49. Cu distribution in (a) the Cu ²⁺ system and (b) HA-Cu system predicted by Visual MINTEQ. For speciation prediction, CuSO ₄ concentration was 1.6 g/L and DOM (HA) was 500 mg/L. SHM model was applied for the HA-Cu system in this study.	125
Figure 4-50. The Eh and the pH values in (a) the UHA system and (b) the RHA system. HA concentration was 1.0 g/L and Cu ²⁺ concentration was 1.6 g/L.	126
Figure 4-51. Dissolved Cu in the absence and in the presence of HA after 24 hours of synthesis. Initial Cu ²⁺ concentration was 1.6 g/L and HA concentration was 1.0 mg/L.	126
Figure 4-52. The size distribution of Cu colloids in the presence of UHA and RHA, calculating by ImageJ and OriginLab software. Particle numbers were 159 and 932 in UHA and RHA systems, respectively.	127
Figure 4-53. The hydrodynamic particle size of UHA-Cu and RHA-Cu colloids. The signals were presented by the Number distribution.	128
Figure 4-54. The sedimentation curves of HA-Cu NPs. The reading was performed at an absorbance of 510 nm.	128
Figure 4-55. XANES spectra and LCF results of HA-Cu colloids. HA concentration was 1.0 g/L and Cu ²⁺ concentration was 1.6 g/L. The standards applied for the fitting were Cu foil, Cu ₂ O, CuO and CuSO ₄	130
Figure 4-56. The LCF results of (a) UHA-Cu and (b) RHA-Cu. The fitting range was between -20 and +30 eV of Cu (8979 eV)	130
Figure 4-57. FTIR spectra of HA-Cu. IR technique was associated with synchrotron radiation.	132

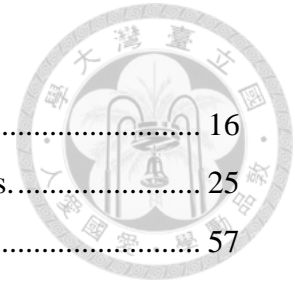
Figure 4-58. The removal of RB5 by HA-Cu colloids. The initial concentration of RB5 was 10 mg/L, HA and Cu²⁺ concentrations were 1 g/L and 1.6 g/L, respectively. The error bar in Figure 4-58 represent the standard error of an average over duplicated batch experiments.

..... 135

Figure 4-59. UV-visible spectra (200-750 nm) of RB5 at different time intervals during the reactions with (a) UHA-Cu and (b) RHA-Cu colloids. 135

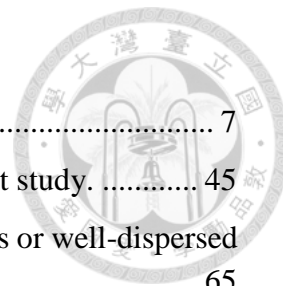
Table content

Table 2-1. The common stabilizers used in the synthesis of Fe NPs.....	16
Table 2-2. The natural metal NPs generated via HSs reducing processes.....	25
Table 3-1. The input data for Visual MINTEQ modeling.	57
Table 4-1. The removal of TCE by MZVI with ligands.	94
Table 4-2. Fe type and distribution in the presence of ligands predicted by Visual MINTEQ.	105
Table 4-3. Peak wavenumber and vibrational mode for HA and HA-Cu systems.	133



Scheme content

Scheme 1-1. Fishbone diagram for the experimental designs.	7
Scheme 3-1. Schematic of the US/stirring setup employed in the present study.	45
Scheme 4-1. The interaction between contaminants and nano-aggregates or well-dispersed NPs.	65
Scheme 4-2. A positively charged Fe (hydro)oxide surface of Fe nanoparticle in water attracts anionic species including PCP^- to the near-surface water.	66
Scheme 4-3. The reaction mechanisms of well-suspended Fe NPs in two dispersion systems.	91
Scheme 4-4. The redox potential of Fe^{2+}/Fe^{3+} in different type of Fe.	105
Scheme 4-5. The diagram of the reaction mechanism of TCE by ZVI in the presence of carboxylic ligands.	106
Scheme 5-1. The concept of this study. (a) The reaction mechanism of well-suspended Fe NP by the physical and the chemical dispersion methods (b) the effect of carboxylic ligands on the surface of Fe particles, (c) the interactions of HA and Fe (Cu) complexes/colloids.	139

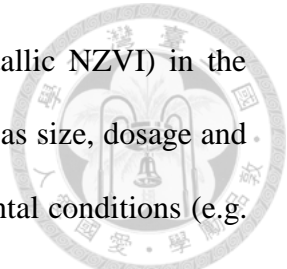


Chapter 1 Introduction



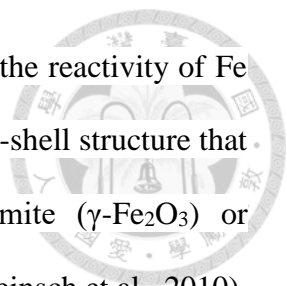
The goal of environmental remediation is to reduce and control the risks for ecological damage and to return blighted land to productive use (Holland, 2011). Many sophisticated remedial technologies have been developed over the years. However, these remedial actions are frequently energy intensive and can also produce their own contaminants with corresponding impacts; moreover, these techniques usually require many years for implementation and long-term monitoring (Mackay and Cherry, 1989; Wolfe et al., 2003). Nanoremediation, the use of nanomaterials for pollutant treatment, is based on the ability of certain nanomaterials to react with the contaminant of concern or create a certain environment for the transformation of pollutants into less toxic or nontoxic forms (Adeleye et al., 2013; Karn et al., 2009). Nanoremediation could reduce the costs, improve effectiveness, and generate fewer hazardous by-products of pollution cleanup.

Nanoscale zero-valent iron (NZVI) and bimetallic NZVI have significant potential for the remediation of a wide array of priority pollutants, including halogenated organic contaminants (Lowry and Johnson, 2004; Shih et al., 2009; Shih et al., 2010; Song and Carraway, 2005; Wang and Zhang, 1997; Zhang, 2003), azo dyes (Shu et al., 2007; Wang et al., 2013; Wang et al., 2015), inorganic anions (Wang et al., 2006; Xiong et al., 2007), and heavy metals (Kanel et al., 2006; Xu and Zhao, 2007). The properties of large surface area and high reduction potential of NZVI generated significant interest in the application for in-situ remediation of groundwater. However, a number of challenges remain before the technology can be widely adopted. Recently, studies have noted limited mobility of NZVI and other reactive nanoparticles (NPs) in both water and saturated porous media (Hsiung et al., 2016; Kim et al., 2009; Peng et al., 2015; Phenrat et al., 2007; Reinsch et al., 2010; Tso



et al., 2010). The aggregation of Fe NPs (including NZVI and bimetallic NZVI) in the environment depends upon their physical and chemical properties, such as size, dosage and surface characteristics, as well as on the presence of various environmental conditions (e.g. salinity, solution composition and pH) (Hu et al., 2010; Mylon et al., 2004; Yang et al., 2007). It is difficult to maintain the stability of reactive NPs in their original size. Once Fe NPs aggregate and precipitate their mobility and reactivity in the environment is significantly reduced (Glavee et al., 1995; He and Zhao, 2007). Therefore, various dispersion methods have been studied in order to prevent the aggregation of Fe NPs.

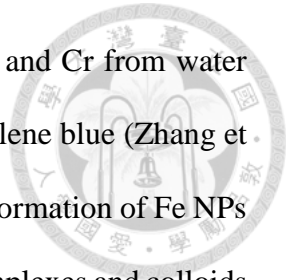
It is now generally considered that the use of solution additives and surface modifiers on Fe NPs could reduce aggregation and settlement so that they remain dispersed in aqueous solutions which extended transport distances (He and Zhao, 2007; Kaifas et al., 2014; Kustov et al., 2011; Parshetti and Doong, 2009; Soukupova et al., 2015; Wang and Zhou, 2010). These stabilizer molecules provide inter-particle electrostatic forces and steric repulsion which are strong enough to overcome the present interfacial forces (Harendra and Vipulanandan, 2008; He and Zhao, 2005; 2007; Sakulchaicharoen et al., 2010). Although these amendments can enhance the colloidal stability, they alter the surface properties of Fe NPs and affect their interaction with contaminants (Kim et al., 2009; Phenrat et al., 2007; Tiraferri et al., 2008). Modifiers can also affect the adsorption and desorption of contaminants; consequently, they limit the reaction rates of the reactions that occur on the iron surface (Phenrat et al., 2009). The reaction mechanisms vary with the used surface modifier. Therefore, in order to assess the application of stabilized Fe NPs, the physical suspension technique should be employed on bare Fe NPs to compare their surface characteristics and reactivity with the one achieved by the chemical dispersion method.



Aside from colloid stability, the other factor that largely influences the reactivity of Fe NPs is the aging process. Fe particles are usually reported to have a core-shell structure that contains oxidized iron such as mostly magnetite (Fe_3O_4), maghemite ($\gamma\text{-Fe}_2\text{O}_3$) or lepidocrocite ($\gamma\text{-FeOOH}$) (Díez-Pérez et al., 2006; Farrell et al., 1999; Reinsch et al., 2010). It is also expected that the interactions between Fe particles and common electrolytes to form Fe (hydro)oxides on the surface further cause a rapid decrease in the activity and longevity of Fe particles (Agrawal et al., 2002; Kober et al., 2002). Thus, a refreshed process for Fe particles could be available for extending the long-term reactivity of Fe particles. The most important dissolutions of metal oxides in soil environments are related to adsorbed-exchanged protons and activated surface metal-ligand complexes, which are the proton-promoted pathway and the ligand-promoted pathway (Furrer and Stumm, 1986). Under milder and weak acidic conditions, the reactivity of Fe particles is enhanced because of the corrosion effect on their surface (Bokare et al., 2008; Epolito et al., 2008; Shih et al., 2011). Protons dissolve the precipitated Fe (hydro)oxides precipitated on the particle surface, exposing more fresh reactive sites (Shih et al., 2011); ligands induce metal dissolution by the formation of soluble surface complexes (Furrer and Sticher, 2014; Hamer et al., 2003). The major sources of protons and ligands in natural soil environments are commonly composed of carboxylic acids and aromatic acids, originating from the microbial degradation of humic substances, plant debris, and root exudation (Biver and Shotyck, 2012). Moreover, some organic ligands, such as catecholate, hydroxamate and organothiol, promote Fe^{2+} reactivity toward nitroaromatic compounds via complexation (Naka et al., 2008; Naka et al., 2006). So far studies have examined the performance of ligand-Fe complexes in groundwater treatments. Information about the influence of organic ligands on the reactivity of Fe particles

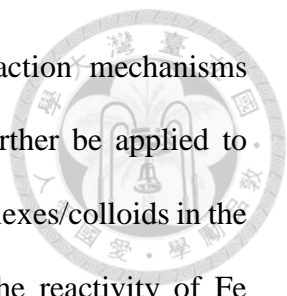
and their reaction mechanisms remain unknown. Organic acids with low molecular weight could act as providers for both the proton and functional groups to affect the surface characteristic of Fe. Once Fe complexes have been formed during the dissolution process of Fe particle, they might further influence the transformation of the target compound.

While the effectiveness of Fe NPs has been proved by many studies in pollution remediation, several studies have investigated the potential impact the use of this technology on both the physical environment and on biological systems (Adeleye et al., 2013; Pawlett et al., 2013; Rónavári et al., 2016). Studies have noted that Fe NPs and their oxides may have toxic effects on a variety of life forms (Auffan et al., 2008; Wang et al., 2011). Many metal ions including Fe and Cu could form complexes and even colloids by humic substances and microorganisms in soils, sediments, and aquatic systems (Weber et al., 2009; Weber et al., 2009). These metal complexes/colloids originated from metal ions via a complexation process with natural organic molecules that exploit ligand properties. Once the metal complexes/colloids are formed in environmental matrices, they may tend to transfer into groundwater depending on the properties of the specific metal colloids. Natural organic matter (NOM), a heterogeneous mixture of organic compounds, is known to play important roles in the interaction with metal ions in the environment. NOM revealed a wide range of standard redox potentials between 0.15 and -0.3 V depending on the composition of its functional groups (Aeschbacher et al., 2009; Aeschbacher et al., 2011). Once NOM-metal complexes are formed, electrons could transfer from NOM such as humic acid (HA) to chelated-metal ions (Chen et al., 2003; Maurer et al., 2012; Pham et al., 2012). Fe solid were generated from Fe^{2+} and dissolved organic matter (DOM) and transformed nitroaromatic pesticides in natural systems (Hakala et al., 2007). In anaerobic conditions, HA-coated Fe_3O_4



not only effectively removed heavy metal ions such as Hg, Pb, Cd, Cu and Cr from water (Jiang et al., 2014; Liu et al., 2008), but also organic dyes such as methylene blue (Zhang et al., 2013). Therefore, NOM may have a high potential to affect the transformation of Fe NPs and their oxides in remediation sites; furthermore, these NOM related complexes and colloids could be considered as a green remediation technique which continuously reacts with pollutants in the environment.

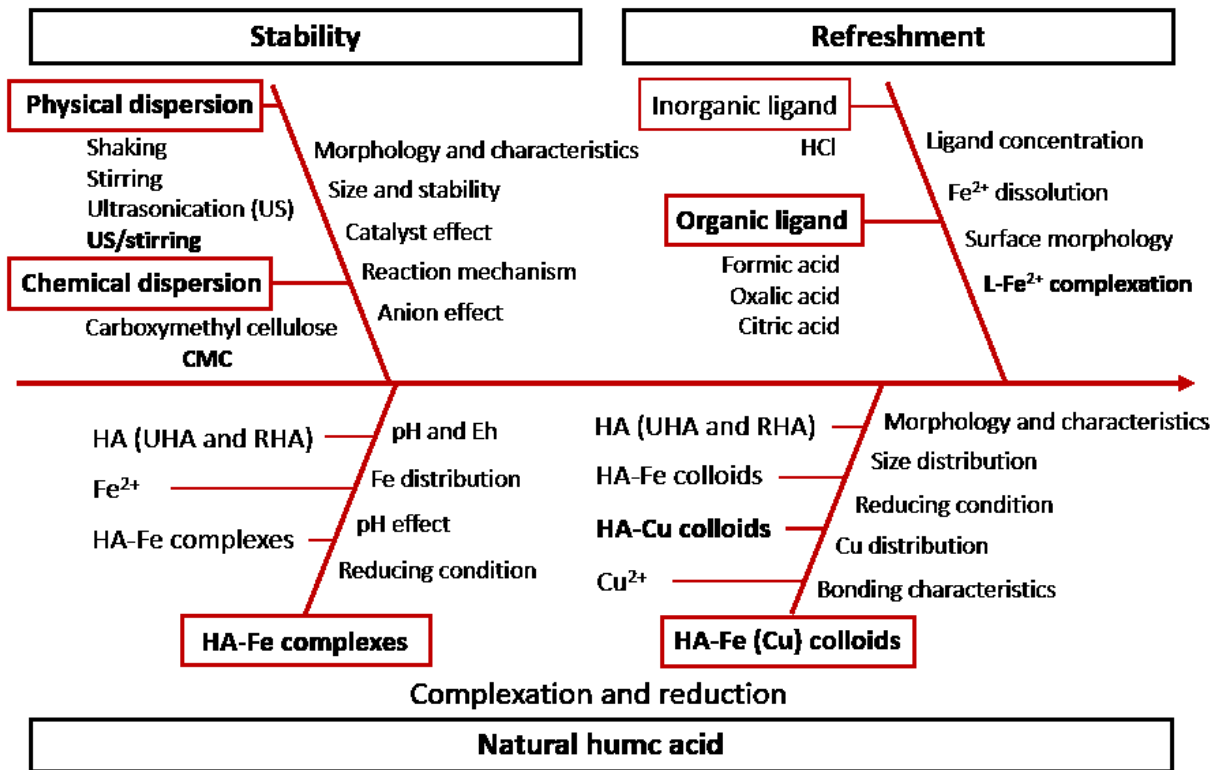
For the organic contaminants of concern, halogenated organic pollutants such as chlorinated solvent, chlorinated pesticides and the emerging halogenated contaminants (i.e. brominated flame retardants) have been an important issue because of their persistence and toxicity in the environment. Therefore, Fe NPs (NZVI and bimetallic Fe NPs) are considered a potential reductant to treat halogenated organic contaminants. The aim of this study is to enhance the reactivity of Fe NPs by increasing the colloidal stability and refreshing the Fe surface. Furthermore, for subsequent assessment the effect of NOM is examined to investigate the reactivity of Fe complexes and colloids as a green remediation method (Scheme 1-1). The physical dispersion was conducted together with the chemical dispersion to compare the reactivity of Fe NPs. For physical dispersion, four mechanical methods (shaking, stirring, ultrasonication (US), and a combination of US and stirring) were developed and applied to disperse Fe NPs. For chemical dispersion, a common stabilizer, carboxymethyl cellulose sodium (CMC), was used to suspend Fe NPs. Further, the reaction mechanisms of bare Fe NPs and stabilized Fe NPs were investigated and the influence of common anions on the stability and reactivity of both Fe NPs evaluated. Carboxylic organic ligands were applied to assess the refreshment process on the Fe surface. The effects of three simple carboxylic ligands (formic acid, oxalic acid and citric acid) on the surface



characteristics of Fe particle were used to assess possible multi-reaction mechanisms between Fe particles and ligand-Fe complexes. These findings can further be applied to forecast and predict the possibility of sequential treatments with Fe complexes/colloids in the presence of organic ligands. Humic acid was chosen to investigate the reactivity of Fe complexes/colloids under reducing conditions like anaerobic sediments. The characteristics and behaviors of these metal complexes/colloids were further analyzed to evaluate the possibility of their degradation of organic contaminants.

The goals of the present study were approached by pursuing the following objectives.

1. To suspend Fe NPs. Here a physical suspension method was applied to study the reactivity and the reaction mechanisms of bare Fe NPs. A chemical dispersion method was used to synthesize Fe NPs with modified surface to assess their potential for wastewater remediation.
2. To refresh the Fe particles by removing the passive layers from the Fe surface. Inorganic (HCl) and organic ligands (formic acid, oxalic acid and citric acid) with the low molecular weight were applied to study the interactions between metal Fe/Fe²⁺ and ligands. The reactivity of ligand-Fe complexes forming during the reactions has also been considered in this study.
3. To understand the sustainability of Fe NPs, a complicated NOM (humic acid in this study) was utilized to investigate its influence on Fe ions and Fe (or Cu) colloids in natural environment. From these results the reactivity of metal complexes and colloids in the presence of NOM under anaerobic conditions could be understood.

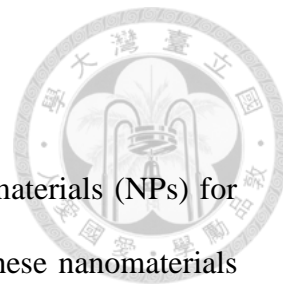


To enhance the reactivity of Fe⁰ nanoparticles in anaerobic environment

1. Catalyst metal: Ni and Pd
2. Stabilizer: CMC
3. Inorganic acid: HCl
4. Organic acid: FA, OA and CA
5. Humic acid: complexes and precipitates

Scheme 1-1. Fishbone diagram for the experimental designs.

Chapter 2 Paper review



2.1 Nanoremediation

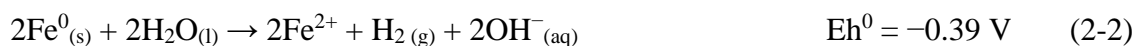
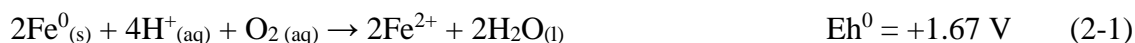
Nanoremediation methods imply the application of reactive nanomaterials (NPs) for transformation and detoxification of pollutants (Karn et al., 2009). These nanomaterials have properties that enable adsorption, reduction and catalysis to alleviate the risk. For many pollutants of concern, for example, chlorinated organic solvents, persistent organic pollutants (POPs) such as pentachlorophenol (PCP) and polybrominated diphenyl ethers (PBDE), nanoremediation may be an efficient and cost effective alternative to traditional in-situ remediation technologies (e.g. pump-and-treat, advanced oxidation processes, and bioremediation) due to their higher reactivity (Karn et al., 2009; Otto et al., 2008; Zhang, 2003). The reactive NPs in the environment are mainly from (i) the application of engineered NPs into the remediation sites, and (ii) geological and environmental processes. Many nanoscale materials have been explored for nanoremediation including nanoscale metal oxides, carbon nanotubes/fibers, noble metals, and titanium dioxide (Karn et al., 2009). Nanoscale zero-valent iron (NZVI) and bimetallic Fe NPs are the most widely used (Lowry and Johnson, 2004; Shih et al., 2009; Shih et al., 2010; Song and Carraway, 2005; Wang and Zhang, 1997; Zhang, 2003). To date, the application of NZVI and bimetallic Fe NPs in contaminated sites is increase, as show in Figure 2-1 (data is available online for doi:10.1289/ehp.0900793.S1 via <http://dx.doi.org/>, Nanotechnologies, 2009).



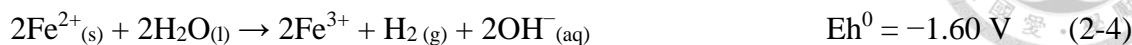
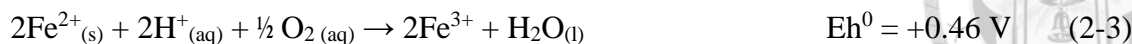
Figure 2-1. Nanoremediation map (Nanotechnologies, 2009).

2.1.1 The application of Fe NPs

NZVI is a strong reductant with a standard electrode potential ($Eh^0_{Fe^{2+}/Fe^0}$) of -0.44 V (Bratsch, 1989). NZVI is well recognised as being highly susceptible to corrosion in aqueous matrix due to its strong reduction potential ($Eh^0_{Fe^{2+}/Fe^0}$ is -0.44 V) (Bratsch, 1989). NZVI reaction is considered as a corrosion that occurred primarily through an electrochemical process with anodic and cathodic components. The anodic reaction involves the dissolution of Fe^0 and forming soluble ionic products or insoluble (hydro)oxide; at the cathode, is coupled with reduction of redox amenable species. The primary elements available for corrosion reactions in natural water are dissolved oxygen and water, as shown in eq. 2-1 and 2-2.



A primary product is ferrous ion from these reactions that can undergo further oxidative transformation (Eqs. (3) and (4)).



The solution pH increases during the above reactions as either protons are consumed or hydroxyl ions are produced. Also, because of the high surface area of NZVI, when added a significant mass of material into an aqueous system, it would achieve a suitable chemically reducing condition very soon through the H₂ production processes (eq. 2-3 and 2-4); inducing local conditions far from equilibrium and favorable for contaminant removal (Crane and Scott, 2012).

Compared with NZVI, the bimetallic Fe NPs have exhibited higher potential for the treatment of many halogenated aromatic compounds (Shih et al., 2011; Shih et al., 2009; Wang et al., 2013; Zhao et al., 2014). The addition of catalysts on NZVI can (i) increase surface area and density of reactive surface sites; (ii) catalyze the lower hydrogen overpotential metal, which is effective in hydrodehalogenation reactions; and (iii) inhibit the corrosion products from accumulating on the surface reactive sites of zero-valent metals (Bokare et al., 2007). Kim and Carraway (2003) reveal the dechlorination rate of trichloroethene (TCE) by bimetallic Fe particles are in the order of: Pd/Fe > Pd/Zn > Ni/Fe > Cu/Fe > Ni/Zn > Cu/Zn > Fe > Zn, suggesting that Fe metal and bimetals exhibit a higher reactivity than zinc metal, and bimetals exhibit faster reaction rates than pure metals. The proposed mechanism of bimetallic Fe NPs is that the catalytic metal enhances the formation of atomic hydrogen or hydride on the surface and alters the electronic properties of the iron. The catalytic reduction and dehalogenation reaction is believed to take place on the surface

site of the nanoscale catalysts. Figure 2-2, for example, depicts the various processes occurring on the Ni/Fe bimetallic nanoparticle surface. Bokare et al. (2007) noted that Ni/Fe nanoparticles preceded reductive reactions via transfer of atomic hydrogen from the nickel surface (reaction 1 in Figure 2-2). In the reaction, Ni played a role of catalyst decreasing activation energy of hydrogenolysis of C-X bonds and the Fe was corroded to produce hydrogen gas. Additionally, they could generate hydroxyl radicals from water (reactions 2 and 3 in Figure 2-2) and created radical centers on the contaminant molecule, leading to different cross coupling products. A majority of the Fe^{2+} species formed by iron corrosion was retained on the particle surface and Fenton's reaction was only a minor contributor for hydroxyl radical generation (reaction 4 in Figure 2-2).

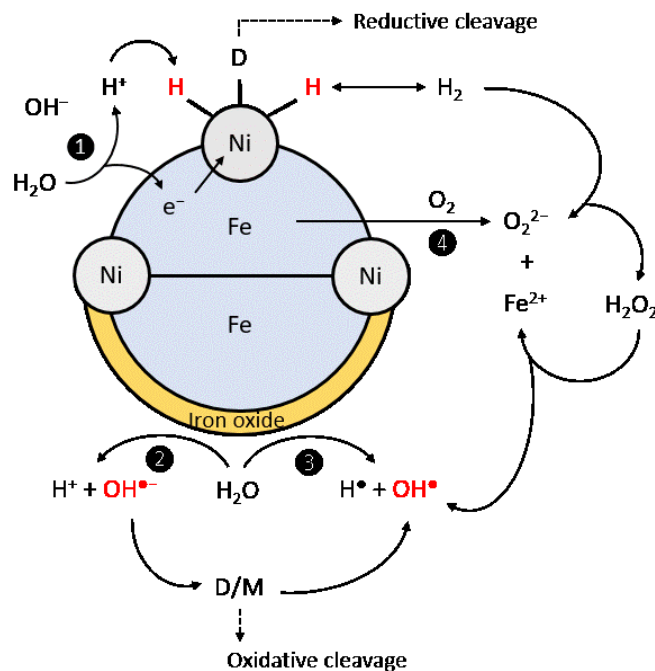


Figure 2-2. Proposed scheme of reactions on the surface of Ni/Fe nanoparticles for reductive or oxidative degradation of contaminants (Bokare et al., 2007).

2.1.2 The stability of Fe NPs

However, it is hard to keep the size of NZVI in their minute size under various environmental. In aquatic environment, aggregation of metal NPs results from the interaction between the particle surface and water components and is strongly influenced by several factors such as salinity, solution composition, surface chemistry, concentration of suspended particles and aqueous pH (Hu et al., 2010; Mylon et al., 2004; Yang et al., 2007). The aggregation of nanoparticles depends on their surface charge and, in the case of Fe NPs, higher attractive magnetic and van der Waals forces between particles and its low surface charge (-1.45 ± 1.11 mV) (Phenrat et al., 2007; Saleh et al., 2008; Schrick et al., 2004). The behavior of Fe NPs and its associations with numerous aqueous and solid species, will depend on the types of Fe-mineral phases present on the particle surface because each species may have a different point of zero charge (pH_{PZC}) value. Magnetite, maghemite, and goethite have pH_{PZC} values of 6.0, 6.6, and 8.4 respectively (Cornell and Schwertmann, 2006; Reinsch et al., 2010), hence the particles may be positive or negatively charged at pH close to 7 according to the species present on the surface.

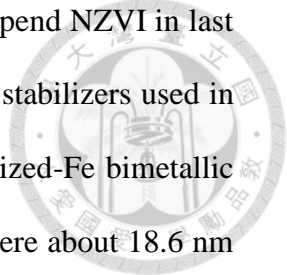
The stability of metal NPs also depends on the ion concentration and ionic composition. With increasing ion concentrations and ionic strength, the repulsive forces between NPs decreased and then caused the compression of double layer of nanoparticles, resulting in aggregation of NPs (Tso et al., 2010). The aggregation of commercial TiO_2 NPs (25 nm) was observed in the presence of various environmentally relevant solution chemistries containing different concentrations of monovalent (Na^+ and K^+) and divalent (Ca^{2+}) electrolytes (Shih et al., 2012). Berka and Rice (2004) reported that with increasing NaCl concentration, kaolinite particle ($< 0.2 \mu\text{m}$) suspension became more unstable. While NaCl

concentration reached the critical coagulation concentration (CCC), a rapid aggregation was occurred. With the increase of ionic strength, the zeta-potential of metal NPs decreased (i.e. became less negative) due to electric double layer compression (Hu et al., 2010). Moreover, the effect of divalent ions was more important than monovalent ones on NP aggregation (Chen and Elimelech, 2006; Shih et al., 2012; Tso et al., 2010).

Aggregation and sedimentation significantly alter the mobility of Fe NPs in aquatic environment and reduce the efficacy for remediation purposes (Glavee et al., 1995; Kim et al., 2009; Sun et al., 2007). Therefore, various dispersion methods have been studied in order to prevent the aggregation of metallic nanoparticles. Two different approaches to separate NPs are usually used: physical methods and chemical methods.

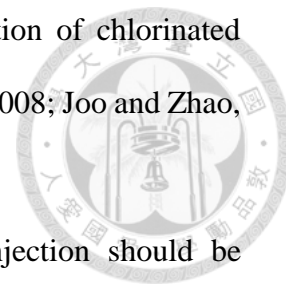
2.1.2.1 Chemical dispersion methods

The polymer amendments include the solution additives and surface modifier. These amendments can serve several functions including (i) reducing aggregation, (ii) modifying surface charge of the aggregates to decrease electrostatic interactions between the aggregates and the soil grains, and (iii) potentially increasing the role that hydrodynamics can play in removing aggregates from soil surfaces. These amendments can be sorbed or covalently bonded to NPs and may also help to target contaminant “source zones” containing nonaqueous-phase liquids (Johnson et al., 2009). The stabilizer molecules are designed to provide inter-particle electrostatic and steric repulsions, which are strong enough to overcome the interfacial force. For example, the stabilizers can regulate the iron nucleation and particle growth during the synthesis process, further prevent agglomeration of the resultant NZVI particles effectively.



According to researches, many polyelectrolytes were applied to suspend NZVI in last decade, including PVP, PAA, and SDS. Table 2-1 shows the common stabilizers used in the synthesis of Fe NPs. He and his group dispersed NZVI and palladized-Fe bimetallic NPs (Pd/Fe) effectively by carboxymethylcellulose (CMC) with size were about 18.6 nm and 18-22 nm, respectively (He and Zhao, 2007; He and Zhao, 2005; 2007; 2008). CMC mostly interacts with the Fe surface through carboxylate groups (i.e. $\text{Fe}^{2+}/\text{-COO}^-$). Since the carboxylate group bring a formal negative charge, CMC-stabilized Fe was more suspended in aqueous phase compared with other polymer-stabilized Fe (Phenrat et al., 2008; Raychoudhury et al., 2010; Sakulchaicharoen et al., 2010; Saleh et al., 2007). It was observed that surfactants enhanced the trichloroethylene desorption from soil with the anionic surfactant being the most effective (Zhang et al., 2011). Surfactant adsorption on the Fe surface was also confirmed by an increase in the electrophoretic mobility of the Fe NPs. The higher MW polyelectrolytes, such as CMC, showed greater adsorbed masses and slower desorption rates. The desorption of surfactants was slow with less than 30 wt% desorbed after 4 months (Kim et al., 2009). Moreover, CMC-stabilized NZVI has been proved to be transported at least 1 meter to the contaminated source zone at significant NZVI concentrations (Kocur et al., 2014). The conceptual scheme of CMC-Fe was pointed out that CMC was coated on the NZVI surface with brush structures which can provide steric stabilization to prevent aggregates (Lin et al., 2010). He and co-workers applied CMC-stabilized Pd/Fe bimetal NPs (CMC-Pd/Fe) for in-situ destruction of chlorinated ethylenes and polychlorinated biphenyls (He et al., 2010). This also demonstrates that over the long run, the existing biological degradation process is boosted with the use of a CMC coating as a carbon source and hydrogen as an electron donor, which is available from the

abiotic/biotic processes, resulting in the sustained enhanced destruction of chlorinated organic contaminants in the subsurface (He et al., 2010; He and Zhao, 2008; Joo and Zhao, 2008).



The significance that amendment used during reactive NPs injection should be environmentally benign. Surface modification can also occur by the adsorption of natural organic matter (NOM) on metal NPs. The presence of natural polymers, NOM, on the metal surface of NPs may prevent the aggregation and maintain the stability of NPs (Badawy et al., 2010; Cumberland and Lead, 2013; Johnson et al., 2009). Recent studies have shown that NOM can stabilize suspensions of NPs such as carbon nanotube, fullerenes, gold, and iron oxide (Baalousha et al., 2008; Diegoli et al., 2008; Saleh et al., 2008; Xie et al., 2008). NOM has an abundance of carboxylic ($-\text{COOH}$ and $-\text{COO}^-$) and phenolic ($-\text{OH}$) functional groups that exist as negative charged and it is believed that NOM coating the metal surface can suppress positive charge of NPs while enhancing the negative charge (Christian et al., 2008; Dickson et al., 2012). NOM has also been shown to enhance the mobility of Fe NPs (Johnson et al., 2009; Kretzschmar and Sticher, 1997). At NOM concentration of 20 mg L^{-1} or greater, the NZVI is stable and highly mobile. The sorption of NOM onto NZVI resulted in a reduced sticking coefficient and enhanced mobility (Johnson et al., 2009).

Although the modifiers can enhance the colloidal stability, they alter the surface property of NPs and affect their interaction with contaminants (Kim et al., 2009; Phenrat et al., 2007; Tiraferri et al., 2008). For instance, the presence of excess free CMC that is unadsorbed onto the Fe surface would presumably serve the depletion stabilization to stabilize CMC-Fe suspension, causing larger particles with size of 40-100 nm. Furthermore, modifiers can affect the sorption and desorption of contaminants, introduce additional mass

transfer limitations of contaminants to active surface sites, and decrease the reaction rate of the reactions that could be taking place at the surface (Phenrat et al., 2009).

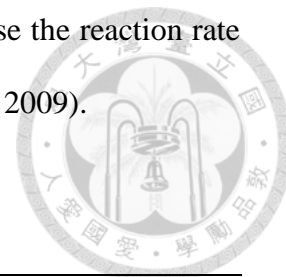


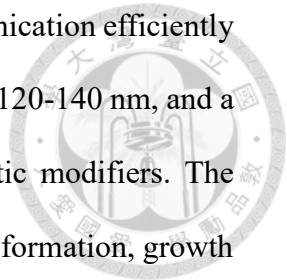
Table 2-1. The common stabilizers used in the synthesis of Fe NPs

Stabilizer	Iron type	Particle size (nm)	Reference
Poly(acrylic acid) (PAA)	NZVI	~20 nm	Schrick et al. (2004)
PAA	Pd/Fe	150-600 nm	Lin et al. (2009)
Polyvinyl-co-vinyl acetate-co-itaconic acid (PV3A)	NZVI	< 10 nm	Sun et al. (2007)
Tween 20	NZVI	2-10 nm	Kanel et al. (2007)
Starch	Pd/Fe	14.1±11.7 nm	He and Zhao (2005)
Cellulose acetate	Ni/Fe	7-11 nm	Wu and Ritchie (2006)
PEG/PVDF	N/Fe	81±12 nm	Parshetti and Doong (2009)
PEG/nylon 66		55±14 nm	
CMC	Pd/Fe	22.8±4.3 nm	He et al. (2007)
		18.1±2.5 nm	He et al. (2009)
Poly(methyl methacrylate) (PMMA)	NZVI	80-100 nm	Wang and Zhou (2010)
Mesoporous silica microsphere	NZVI	450 nm	Qiu et al. (2011)
PVP	Ni/Fe	20-50 nm	Fang et al. (2011)

2.1.2.2 Physical dispersion methods

Physical dispersion methods including ball milling, grinding, high speed shearing, mechanical mixing and ultrasonication (Dickson et al., 2012; Imamura et al., 2005; Lai et al., 2013; Mondragon et al., 2012; Xing, 2004; Xu et al., 2012). Ultrasonication (US) is commonly used to induce a chemical or physical change on the target medium (Jamei et al., 2014). Ultrasound disruption is more energy efficient and can achieve a higher degree of powder fragmentation, at constant specific energy, than other conventional dispersion techniques (Mandzy et al., 2005; Park et al., 1993). Consequently, US has found extensive application in environmental studies, where it is used to break down powders or redisperse stock suspensions to their nanoscale constituents, and allow for the evaluation of the properties and behavior of the dispersed metal NPs in relevant systems.

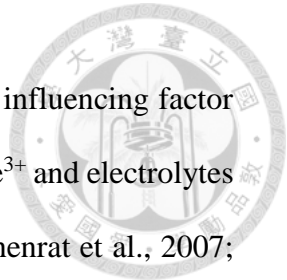
US efficiency can break down the particle-particle interactions of Fe NPs directly



(Rasheed et al., 2011). Dickson et al. (2012) indicated that probe ultrasonication efficiently broke down the particle-particle interactions of NPs with the size about 120-140 nm, and a degree of colloidal stability was achieved without the use of synthetic modifiers. The ultrasonic dispersion mechanism in media involves acoustic cavitation (formation, growth and implosion of bubbles resulting in the rupture of agglomerates) and acoustic streaming - inducing chaotic mixing. Rasheed et al. (2011) presented an effective treatment of petroleum refinery wastewater using NZVI in the presence of US. Liang et al. (2008) reported on the reduction of nitrite by ultrasound dispersed NZVI particles and showed that NZVI can be an efficient reductant. Increased the duration of US of the reaction system, the higher the reduction efficiency of nitrite was achieved. However, it is worth noting that particle adhesion (especially van der Waals forces) increases when the particle size decreases. Metal NPs may regroup back into several hundred nanometer clusters shortly after US if the suspension is not stabilized enough against re-agglomeration (Liang et al., 2008).

The complex physical and chemical phenomena that may occur during US may significantly alter the properties of dispersed NPs. During ultrasound irradiation, the collapse of cavitation bubbles induced localized high temperatures and pressures, which might allow the formation of oxidizing species, such as $\cdot\text{OH}$, superoxide radical and H_2O_2 . Therefore, the combination of ultrasound with heterogeneous oxidation reaction is an also important approach in the degradation of organic compounds (Hou et al., 2012).

2.1.3 The surface characteristics of Fe NPs



Electrolytes that are dissolved in the environment are an important influencing factor on the reactivity of Fe particles because the interactions between $\text{Fe}^{2+}/\text{Fe}^{3+}$ and electrolytes forming Fe (hydro)oxides on the Fe surface (Giasuddin et al., 2007; Phenrat et al., 2007; Shih et al., 2010; Wang and Zhang, 1997). Fe particles are usually reported to have a core-shell structure that contains oxidized iron such as mostly magnetite, maghemite ($\gamma\text{-Fe}_2\text{O}_3$) or lepidocrocite ($\gamma\text{-FeOOH}$) (Díez-Pérez et al., 2006; Farrell et al., 1999; Reinsch et al., 2010). As surface precipitated Fe (hydro)oxides are initially porous, the material can develop the core-shell structure during the early stages of reaction with both sorption (at the (hydro)oxide) and chemical reduction (at the interface of Fe (hydro)oxides) able to occur simultaneously. However, as the reaction progresses, an increase in the quantity of corrosion products and a decrease in the particles porosity significantly limit the interactions between $\text{Fe}^0\text{-H}_2\text{O}/\text{O}_2$ and $\text{Fe}^0\text{-pollutant}$ (Agrawal et al., 2002; Kober et al., 2002; Noubactep, 2008). The process causes a kinetics of the initial stages of Fe^0 oxidation (rapid, the corrosion will proceed even in extremely controlled conditions). Consequently, Fe^0 will already have a film of surface oxide acquired directly after synthesis. Therefore, each Fe particle exists in natural conditions is covered a thin but encapsulating layer of surface oxide (Crane et al., 2011; Scott et al., 2010)

2.1.3.1 The removal of passive layers on the metal NPs surface

The dissolution of metal oxides is related to adsorbed protons and f surface metal-ligand complexes, such as proton-promoted and ligand-promoted pathways (Furrer and Stumm, 1986). The pH value is one of the important influencing factors during dissolution

processes of metal. Under weak acidic conditions, the reactivities of MZVI and NZVI are enhanced due to the corrosion effect on the Fe surface (Bokare et al., 2008; Epolito et al., 2008; Shih et al., 2011). Protons could dissolve away iron (hydro)oxides precipitated on the surface of Fe at lower pH solutions, thus exposing more fresh reactive sites (Shih et al., 2011).

Low molecular weight organic acids (LMWOAs) in soil are usually involved in the enhancement of mineral dissolution processes, which play an important role in the soil formation process, as well as the mobility and bioavailability of metals (Johnson et al., 2004; Liang et al., 2000). These organic ligands mainly originate from the microbial degradation of humic substances (HSs), plant debris, and root exudation (Biver and Shoty, 2012). LMWOAs are commonly composed of carboxylic acids and aromatic acids. Hou et al. (2009) had pointed out that the reduction rate of PCP by MZVI was enhanced in the presence of carboxylic acids (acetic acid, oxalic acid, tartaric acid, and citric acid). With the strong complexing and pH buffering properties, carboxylic acids benefits to the dechlorination of PCP by MZVI. The results also showed that the oxalate-iron complexes have more reductive activities and then lead to the highest dechlorination efficiency of PCP by ZVI. Also, the degradation of tetrachloride (CT) by MZVI with organic ligand (ethylenediaminetetraacetic acid (EDTA), citric acid, tartaric acid, malic acid, and oxalic acid) under various pH values was investigated by Zhang et al. (2011). The results demonstrated that addition of organic ligands significantly enhanced the rates and the extents of CT removal, as indicated by the rate constant increases of 39, 31, 32, 28, and 18 times in the presence of EDTA, citric acid, tartaric acid, malic acid and oxalic acid, respectively. The enhanced reductions in the presence of organic ligands are primarily

attributed to the elimination of surface passivation layers on MZVI through chelating of organic ligands with iron (hydro)oxides, thus maintaining the exposure of active sites on the Fe surface (Zhang et al., 2011). Su and Puls (2004) applied MZVI to reduce nitrate in the presence of inorganic acids and organic acids, the reduction rates of nitrate increased in the order of $\text{H}_3\text{PO}_4 < \text{citric acid} < \text{H}_3\text{BO}_3 < \text{oxalic acid} < \text{H}_2\text{SO}_4 < \text{formic acid} < \text{HCl}$. This sequence of reactivity also corresponded to surface adsorption and complexation of the three organic ligands to iron oxides.

2.1.3.2 Influence of Fe mineral type

During aqueous corrosion processes Fe particles are forming precipitates such as $\text{Fe}(\text{OH})_2$, $\text{Fe}(\text{OH})_3$, Fe_3O_4 , Fe_2O_3 , FeOOH , and green rusts, which are responsible for the reductive transformation and/or physical removal (sorption or enmeshment) of exposed chemical species (Crane and Scott, 2012). For examples, Fe_3O_4 NPs have a strong reductive degradation ability for 2,4-D in solution (Si et al., 2010). The structure of Fe_3O_4 contains both Fe^{2+} and Fe^{3+} , and Fe^{2+} might play an important role as an electron donor to remain available for reaction with the chlorinated organic compounds. Fe_3O_4 is the sole oxidation product of Fe^0 and Fe^{2+} , which facilitated the oxidation process by Fe^0 . With adsorbed Fe^{2+} on the iron surface, the Fe^{3+} -oxides of high electrical resistance (10^{-1} - $10^4 \Omega \cdot \text{cm}$) covering the iron surface could act as semiconductor Fe_3O_4 of lower electrical resistance ($10^{-3} \Omega \cdot \text{cm}$) (Schlicker et al., 2000). Thus, adding Fe_3O_4 to the reaction solution containing Fe^0 and Fe^{2+} may favor the electron transfer on the iron surface and accelerate the reduction rates (Xu et al., 2012). Additionally, combining Fe_3O_4 NPs with indigenous

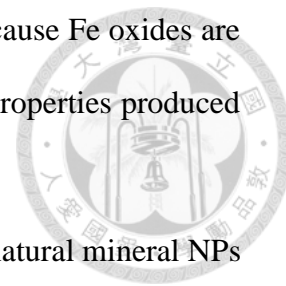
soil microbes offer great benefits for the application of nanotechnology in remediation of herbicide contaminated soil (Fang et al., 2012).

In addition, mackinawite (FeS), has been shown to mediate reductive dechlorination under anoxic conditions (Butler and Hayes, 1999; 2000; He et al., 2010; Jeong and Hayes, 2003; Liu et al., 2003). Trace metal such as Co^{2+} , Ni^{2+} , and Hg^{2+} in soil and groundwater significantly increased reductive dechlorination of hexachloroethane (HCA), tetrachloroethene (PCE), and TCE by FeS through forming reductive metal sulfates (Jeong and Hayes, 2003; 2007). These copresent metals impact also both the reaction rates and pathways in reductive dechlorination of PCE and TCE by FeS (Jeong and Hayes, 2007). The high reactivity of CoS suggests that it may be useful in reactive permeable barrier applications because of its stability in anoxic waters. The dechlorination rates of PCE and TCE significantly varied with Fe^{2+} amendment concentrations, indicating the presence of different types of solid-bound Fe phases with Fe^{2+} (Jeong and Hayes, 2007).

2.1.4 Life cycle of Fe NPs toward green remediation

Once Fe NPs released into the environment, they aggregate to some degree and behave like natural nanomaterials. That is, Fe NPs needs to form stable dispersions in water so it can be delivered to water-saturated porous material in the contaminated area. The mobility of natural or synthetic colloids/NPs in the environment strongly depend on the composition of soil/groundwater (Weber et al., 2009; Weber et al., 2009). Certain nanoscale colloids have an ability to travel a long distance in the environment (Shankar et al., 2003). Fe oxide NPs (a potential final product from the redox reactions of Fe NPs), in some case, may be internalized by cells and cause cell death (Auffan et al., 2008; Wang et al., 2011). But

generally, there would be little concern with the toxicity of Fe NPs because Fe oxides are essential component in rust and because there were no radically new properties produced from Fe NPs (Karn et al., 2009; Watlington, 2005).

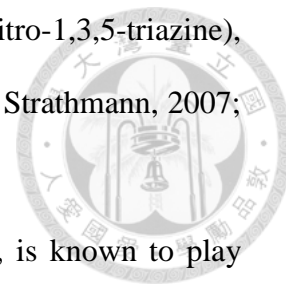


Also, nanoscale Fe (oxy)hydroxides are among the most common natural mineral NPs formed by precipitation from solution after oxidation of aqueous ferrous Fe (van der Zee et al., 2003). Several natural inorganic and biologically mediated processes produce these mineral nanoparticles, such as metal sulfides and metal oxides (Kirk, 2004; Martínez-Villegas and Martínez, 2012; Weber et al., 2009). Once the metal colloids formed in environmental matrixes, they may tend to transfer through groundwater or interact with inorganic/organic pollutants depend on the properties of metal types. Weber et al. (2009) pointed out that on flooding, bacteria dispersed in the pore water mobilize copper by inducing biomineralization of metallic Cu⁰ NPs with particle size of ~50-150 nm. However, the knowledge regarding the fate and transport of metal colloids/NPs is very limited. The complex structures of natural metal NPs, morphologies, and their colloidal behaviors are affected by environmental factors. These natural metal NPs are attracting attention in decade due to their unique role as agents of elemental transport and their reactivity in geologic systems.

2.1.4.1 Abiotic formation processes of metal colloids/NPs in the environment

Some organic ligands in environments, such as catecholate, hydroxamate, and organothiols, could enhance the reduction potential of Fe²⁺/Fe³⁺ and promote Fe²⁺ reactions with nitroaromatic compounds (Naka et al., 2008; Naka et al., 2006). Complexation of Fe²⁺ by ligands leads to the formation of aqueous species that are capable of reducing substituted

nitroaromatic compounds (NACs), oxmayl, RDX (hexahydro-1,3,5-trinitro-1,3,5-triazine), and polyhalogenated alkanes (Bussan and Strathmann, 2007; Kim and Strathmann, 2007; Naka et al., 2006; Strathmann and Stone, 2002).



Natural organic matter (NOM), a mixture of organic compounds, is known to play important roles in the interaction and transport of elements throughout the environment. The oxide metal particles are embedded in a matrix of organic carbon (OC), equivalent to about 1.4 mg OC m⁻² oxide for many soils of the collection, forming NOM-mineral colloids/NPs (Hiemstra et al., 2010). Moreover, the functional groups in NOM could serve as reducing agents for metal ions, such as phenolic-OH, quinones, hydroxyls, methoxyls, aldehydes, ketones, enolic-OH, and thiols (Stevenson, 1994; Urban et al., 1999). It reveals standard redox potentials of NOM between 0.15 and -0.3 V (Figure 2-3) (Aeschbacher et al., 2009; Aeschbacher et al., 2011). This is supposed that quinones are the predominant redoxactive moieties in NOM. Ratasuk and Nanny (2007) also pointed out that the reversible electron-carrying capacity (ECC) of non-quinone structure sites ranged from 21-56% of the total ECC of the humic acid (HA) and fulvic acid (FA). Thus, fractionation of total NOM offered advantages by separating one group of organic compounds (or a subcomponent) from the others on the basis of their physical and chemical properties.

Likewise, electron can transfer from reduced NOM and HA to metal ions (Chen et al., 2003; Maurer et al., 2012; Pham et al., 2012). Table 2-2 shows that metal colloids formed via NOM complexation and reduction. Recently, Fulda et al. (2013) reported the potential for formation of Cu colloids by interaction between HA and Cu ions under anoxic conditions. Under anoxic conditions, HA was complexed with Cu²⁺ and Cu⁺, thus formed as HA-Cu⁺ and Cu⁰ NPs due to the competitive processes of electron transfer and copper

binding (Fulda et al., 2013). For reduced HA, free Ag^+ was reduced and formed Ag NP with particle size about 5-15 nm (Maurer et al., 2012). NOM formed Ag NPs of a spherical small size to be observed (Litvin et al., 2012).

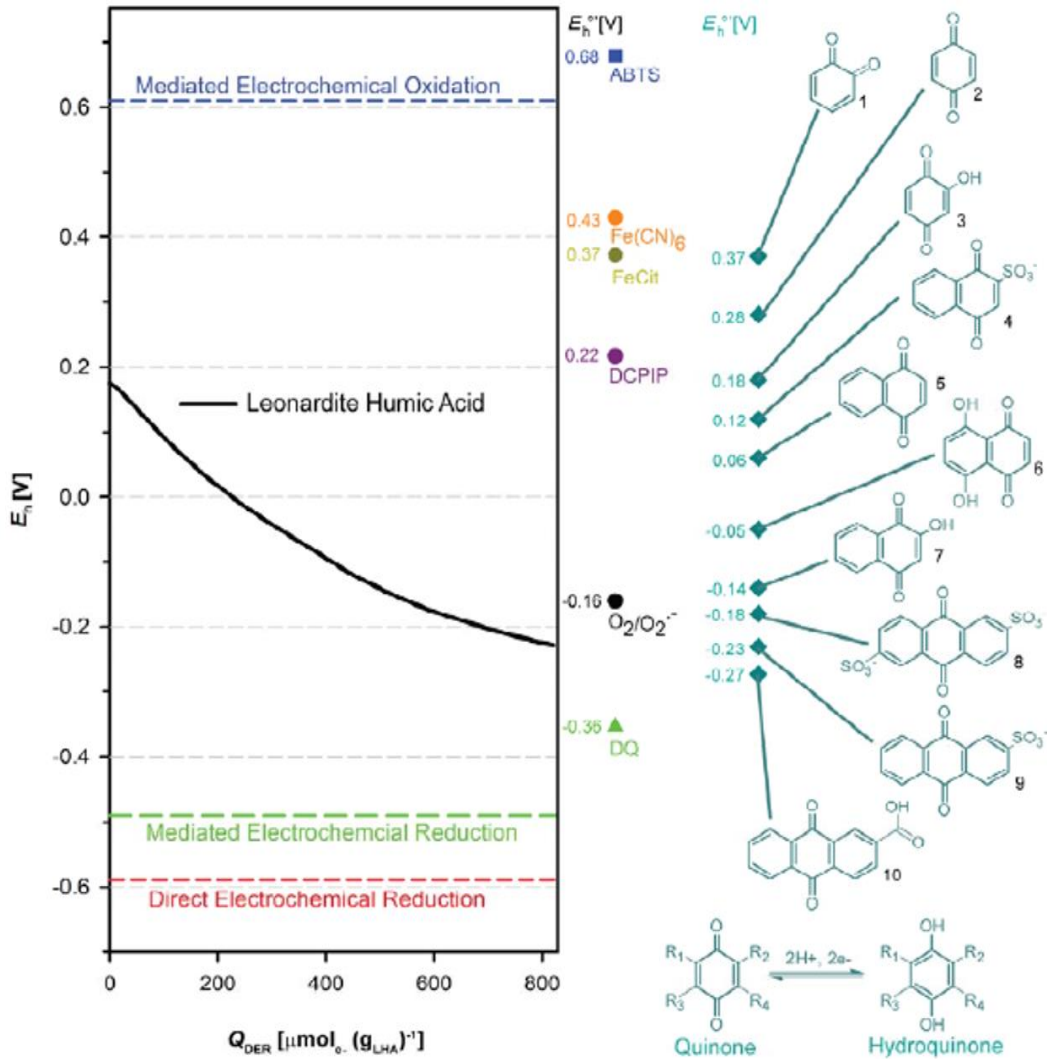
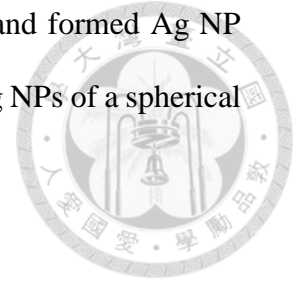


Figure 2-3. Decrease in solution potential E_h during direct electrochemical reduction (DER) of HA at pH 7 as a function of DER-transferred amount of electrons, Q_{DER} ($\mu\text{mole/g}_{\text{LHA}}$) (Aeschbacher et al., 2009).

Table 2-2. The natural metal NPs generated via HSs reducing processes.

Humic substances	Metals	Particle size (nm)	Reference
HA, soil samples	Ag	74.5-158.5 nm	Akaighe et al. (2011)
HA	Ag	5-10 nm	Akaighe et al. (2012, 2013)
NOM	Ag	5-50 nm	Akaighe et al. (2012, 2013)
FA	Ag	9.5±0.3 nm	Litvin et al. (2012)
HA		26.5±1.1 nm	Litvin and Minaev (2013)
HS	Au		Baigorri et al. (2008)
HSs	Au	8-20 nm	Litvin and Minaev (2014)
NOM	α -Al ₂ O ₃	52 nm	da Costa Cunha et al. (2014)
HS	Ferrihydrite	5-20 nm	Angelico et al. (2014)
		100-1000 nm	
HA	b-FeOOH	30±15 nm	Pédrot et al. (2011)
HAs and FAs	ZnS	<10 nm	Deonarine et al. (2011)
Soil samples	Pd	20 nm	Coccia et al. (2012)
HA and FA	HgS	5 nm	Deonarine and Hsu-Kim (2009)

2.1.4.2 Green synthesis of metal NPs

Green nanoparticle synthesis is vouched based on the natural of the solvent, reducing and capping agent, coupled with minimal wastage in terms of energy and raw materials, reduced impact on environment and safety in nanomaterial synthesis (Luque et al., 2012). Shankar et al. (2003) reported on the use of Geranium (*Pelargonium graveolens*) leaf extract in the extracellular synthesis of Ag NPs. On treating aqueous Ag ions with geranium leaf extract, rapid reduction of the Ag ions is observed leading to the formation of highly stable, crystalline Ag NPs with size of 16-40 nm. The antioxidant compounds in plants such as polyphenol could reduce Fe³⁺ producing NZVI with the average size were 10-20 nm (Machado et al., 2013). It was also noticed that both green tea and black tea are among the leaves with the highest phenolic content, and that the leaves from forest trees, oak and eucalyptus, can be used to produce NZVIs. Green tea extract can use for NZVI and Pd/Fe NPs synthesis, instead of the well-known sodium borohydride (Luque et al., 2012; Machado et al., 2013; Smuleac et al., 2011). Tannic acid (TA), an environmentally friendly

and water-soluble polyphenol, is proven to act as a reducing and stabilizing agent to reduce and generate Ag NPs in solution (Sivaraman et al., 2010; Zhang et al., 2012). Green tea extract contains a number of polyphenols that can act as both chelating/reducing and capping agents for metal NPs. Therefore, the particles are protected from oxidation and aggregation, which increases their stability and longevity. Pd and Fe NPs were synthesized using coffee extract (Nadagouda et al., 2010; Nadagouda and Varma, 2008).

Smuleac et al. (2011) applied the green synthesized Fe NPs for the degradation of a common and highly important pollutant, TCE. The rate of TCE degradation was found to increase linearly with the amount of Fe with rate constant k_{SA} being 0.005 L/m² h. Although the initial reaction rates for engineered NZVI were one order of magnitude higher than the green-synthesized Fe NPs, the rapid oxidation reduced their reactivity to less than 20% within 4 cycles. For the green synthesized Fe NPs, the initial reactivity was preserved even after 3 months of repeated use.

In natural environments, the formation of colloids/NPs is highly dependent on various parameters, such as functional groups in NOM (Chen et al., 2003; Nilsson et al., 2008; Schmidt et al., 2013; Straub et al., 2001), pH (Chen et al., 2003), metal/NOM molar ratio (Fulda et al., 2013), reducing degree (Maurer et al., 2013) and temperature (Hofacker et al., 2013). The application of green nanotechnology exhibit attracting for the environmental treatment, however, the related information is still insufficient. A systematic comparison of particle size, colloid stability, morphology, surface characteristics of green metal colloids/NPs is needed to understand the transformation of metallic elements in geologic systems. Moreover, the reactivity and lifetime of metal colloids/NPs toward organic contaminants are expected influenced by environmental factors.



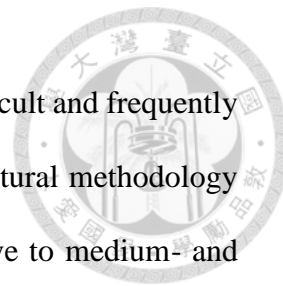
2.1.4.3 Effect of NOM and its functional groups on the wastewater treatment

In the anaerobic condition, NOM can also influence the adsorption of heavy metals on the amorphous and crystalline of Fe and Mn hydroxides (Jiang et al., 2014; Liang et al., 2013; Liu et al., 2008). HA-coated Fe_3O_4 (HA- Fe_3O_4) as magnetic adsorbents were prepared with coprecipitation of HAs and Fe_3O_4 NPs. The average diameter of the spherical HA- Fe_3O_4 core is about 10-15 nm; however, it is aggregated in aqueous suspensions to form aggregates with an average hydrodynamic size of approximately 140 nm (Liu et al., 2008). HA- Fe_3O_4 NPs can not only effectively remove the heavy metals such as Hg, Pb, Cd, Cu and Cr from water (Jiang et al., 2014; Liu et al., 2008), and even the organic pollutants such as methylene blue (MB) (Zhang et al., 2013). The adsorption isotherm of the HA- Fe_3O_4 NPs agreed well with Langmuir adsorption equation, and the maximum adsorbed amount of MB was 0.291 mmol/g with $t_{1/2}$ was 7 min (Zhang et al., 2013). However, the information about the reaction of natural metal NPs toward organic contaminants is still insufficient.

NOM appears to act as both a reducing and a capping agent at environmentally relevant conditions, further endows colloidal stability to the synthesized metallic NPs by preventing agglomeration. The stable NPs formed through the reduction under various environmental conditions may be transported over significant distances and might also influence the overall bioavailability and ecotoxicity of nanoparticles. Additionally, the use of NOM in the synthesis of nanomaterials is a procedure that was efficient, ecofriendly and economically viable (Cunha et al., 2012; Cunha et al., 2010).

2.2 Nanoparticle analysis and characterization methodologies

Structure analysis for numerous metal nanoparticles/colloids is difficult and frequently incomplete because of their minus size and/or poor crystallinity. Structural methodology can be divided into two groups: the diffraction techniques are sensitive to medium- and long-range order, and the spectroscopic techniques are sensitive to electronic or local structure.



2.2.1 Methods for assessing the shape, size and surface structure of NPs

The most common methods for nanoparticle visualization are based on electron and scanning probe microscopy: scanning electron microscopy (SEM) and transmission electron microscopy (TEM). These analytical tools not only provide visual characterization of NPs at a nano-range, but also offer information about size, shape and dispersion of NPs (Mavrocordatos et al., 2004).

2.2.1.1 Scanning electron microscopy (SEM)

Scanning electron microscopy (SEM), a versatile technique, allows analyzing the microstructure morphology and chemical composition of NPs. A high energy focused beam of electrons scan the sample via its surface measuring secondary electrons and producing large amounts of signals, which are converted to a visual signal displayed on a cathode ray tube (Zhou et al., 2007). SEM has a broad operational sizing range from 1 nm to 1 μm . As coupled with complementary techniques such as energy dispersive X-ray spectroscopy (EDS), it is possible to analysis the element component of the target particle (Silva et al., 2011). However, dry samples are required for SEM analysis under vacuum

conditions, it was possible to alter the sample and dehydrate artifacts (Mavrocordatos et al., 2007).



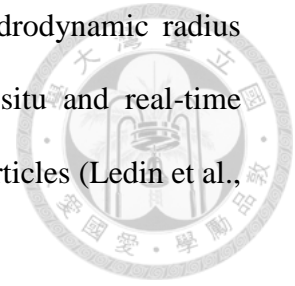
2.2.1.2 Transmission electron microscopy (TEM)

Transmission electron microscopy (TEM) performed with a very thin sample using an electron beam. Interaction between electrons and the sample atoms occurs by elastic and inelastic scattering, which makes a requirement to have very thin samples (5-100 nm). Once the electrons are transmitted through the sample, the electrons that were not absorbed are then focused onto an imaging detector (fluorescence screen or charged coupled device camera) (Reimer, 2013). The electrons (contrast image) that absorbed in the sample material depends on the elemental composition and density of the sample. Therefore, sample preparation plays an important role especially for the preparation techniques such as cryofixation, embedding and electropolishing. TEM provides a number of advantages over other techniques for the characterization of nanoparticles: capability of determining crystallographic structure, size and shape of particles, in addition to an extreme high visual resolution (Lens et al., 2013).

2.2.1.3 Dynamic light scattering (DLS)

Dynamic light scattering (DLS), also referred as photon correlation spectroscopy (PCS), is a well-known technique for measuring hydrodynamic size and size distribution of particles in the range of 3 to 1000 nm. The colloidal dispersions utilizes the illumination of a suspension of particles or molecules undergoing Brownian motion by a laser beam (Winter, 1983). The time-dependent intensity yields the velocity of the Brownian motion;

thus the Stokes-Einstein relationship is applied to determine the hydrodynamic radius distribution (Pecora, 2013). DLS is particularly useful for fast in situ and real-time nanoparticle sizing and physical characterization of aggregated nanoparticles (Ledin et al., 1994).



However, it should be noted that DLS only speculates the particle size of a dispersion based on the measurement of scattering intensity weighted diffusion coefficients, instead of direct determination of the particle size (Hassellöv et al., 2008). Also, DLS cannot be used to characterize suspensions at low concentrations and/or polydispersion conditions (Hoque et al., 2012).

2.2.1.4 Surface charge (Zeta potential) of nanoparticles

The zeta potential, used to characterize the nanoparticle's surface charge, is known as the electric potential at the boundary of the double layer of particles. The zeta potential could offer the information about the potential impact of commercial NPs on the environment (Zhang et al., 2008). The surface charge of suspensions can be assessed by electrophoretic light scattering (ELS), which can be performed via the determination of the Doppler shifts in the scattered light. Electrophoresis occurs when charged particles in dispersion move toward the electrode of opposite polarity once an electric field is applied to them. Therefore, as the laser light is scattered by the moving particles, a shift in the frequency can be observed when a laser beam passes through the sample undergoing electrophoresis (Xu, 2001).

2.2.2 Methods for measuring the elemental composition of single nanoparticle

2.2.2.1 X-ray diffraction (XRD)

X-ray diffraction (XRD) determines the crystalline structure and the chemical composition of the material, basing on the principle that each crystalline solid has a unique characteristic X-ray pattern (Naumov, 2012). The X-ray beam is scattered by the sequence of atoms when passing through the sample, this technique depends on the particular crystalline structure. This non-destructive technique is the main method for crystal structure characterization for bulk, thin film and nano-materials. However, the information about the elemental composition is needed to confirm by other elemental analysis methods such as IPC-MS/-OES (Lens et al., 2013).

2.2.2.2 Synchrotron-based X-ray absorption spectroscopy (XAS)

XAS is an element specific method to investigate the electronic and geometric structure of materials. Specifically applied to the study of nanoparticles, XAS provides information about the oxidation state, the elemental composition and the structure of the particles (Lens et al., 2013; Tiede et al., 2008). The technique is based on the concept that each element has unique electron binding energy that makes the X-ray absorption edge occurred at a unique energy. The X-ray beam produced by synchrotron radiation interacts with the sample through electrons bound in an atom, leading a scattering of the X-ray photons or an absorption by the material in the sample (Attwood, 2007). XAS spectrum can roughly divide into two parts: X-ray near edge structure (XANES) below the edge and up to 30-50 eV, and extended X-ray absorption fine structure (EXAFS) above 30-50 eV. XANES region offers the information about the valence state (Bazin and Rehr, 2003); EXAFS range,

in contrast, reveals the average local atomic structures and nearest neighboring atoms to the atom of interest (Koningsberger and Prins, 1988).

XAS is a well-known analytical method permitting direct and in-situ determination of speciation of trace elements that present in the complex solid samples at low concentration (Chaurand et al., 2007). Whereas XRD yields information on long-range structural aspects, XAS provides complementary details on the electronic environments of the metals and on the short-range structure. The application of these analysis technologies can identify the structure characteristics of mineral colloids/NPs.


2.2.2.3 Fourier transform infrared spectroscopy (FTIR)

Infrared spectroscopy (IR) spectroscopy is based on the principle that atoms vibrate at a unique frequency when they are exposed to an incident infrared light, absorbing IR vibration in a specific wavelength. The unabsorbed light passes through the sample to a detector, which yields the IR spectrum (absorbed energy versus frequency). The Fourier transform infrared spectroscopy (FTIR) consists of irradiating the sample with a wider range of frequencies. The obtained results are then mathematically converted to a typical spectrum through the use of Fourier transform (Larkin, 2011). FTIR spectrum demonstrates the information about the specific molecular components and bonding structures, and it allows quantitative analysis since the strength of the absorption is proportional to the concentration (Reig et al., 2002). FTIR is considered one of the most powerful techniques for chemical analysis as well as for characterization of nanoparticles due to its simplicity, sensitivity and speed of analysis (Lemine, 2009).

2.3 Pollutants of concern

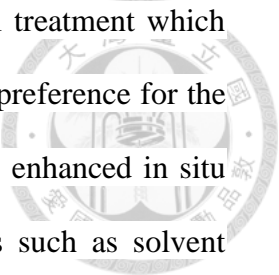
2.3.1 Halogenated organic contaminants

2.3.1.1 Pentachlorophenol (PCP)



Pentachlorophenol (PCP) has been widely used throughout the world as disinfectants, biocides, wood preservative, and pesticides. PCP can be found in the air, surface water, soil, and groundwater aquifers due to its broad use, sorption properties, and environmental stability (Goerlitz et al., 1985; Mannisto et al., 2001; Valo et al., 1984). PCP are versatile biocides in widespread use. Worldwide production is about 150,000 tons per year in 1977. About 80% of the PCP in the United States were used as the wood- preserving after PCP is proven to have a strong antibacterial or fungicidal activity for yeasts, fungi, mosses, algae and other microorganisms (Jorens and Schepens, 1993). Chlorinated phenol congeners comprise of 19 chlorinated phenol compounds, including 3 monochlorophenols (MCP), 6 dichlorophenols (DCP), 6 trichlorophenols (TCP), 3 tetrachlorophenols (TeCP), and one pentachlorophenol (PCP). In general, the increase in toxicity correlates with the number of chlorine substituents introduced into the molecule. Consequently, pentachlorophenol is the most toxic chlorinated phenol. An-shun site was a serious PCP contaminated site, which also contaminated with dioxin and mercury by China petrochemical development corporation. Until now, the residual PCP in soil is around the site ranged from 0.312 mg/kg to 110 mg/kg (Thuan and Chang, 2012).

The remediation methods for PCP contaminated soil have been found to be inefficient mainly due to: (i) sorption of hydrophobic organic pollutant to natural organic matter with a very slow desorption rate and (ii) the high reactivity of hydroxyl radicals with soil constituents (Lindsey and Tarr, 2000). In order to enhance the migration of pollutants from



soil to water phase, various approaches had been applied : (i) thermal treatment which relied on an increase in soil temperature, where PCP tended to show a preference for the aqueous phase rather than the soil matrix (Tse and Lo, 2002), and (ii) enhanced in situ flushing technology, which was based on the use of flushing agents such as solvent mixtures (Chu and Kwan, 2003) and surfactant foam (Wang and Mulligan, 2004) that acted to increase the HOCs' apparent aqueous solubility. However, some of the intermediate products during the decomposition of PCP might be more toxic than the original PCP, such as polychlorinated dibenzo-*p*-dioxins (PCDDs) and polychlorinated dibenzofurans (PCDFs) in the environment (Harnly et al., 2000). And with ZVI treatment, the transformation of chlorinated organic compounds was slow; some chlorinated byproducts might be produced and accumulated (Wei et al., 2006), or the PCP degradation might not

2.3.1.2 Brominated flame retardants (BFRs)

Brominated flame retardants (BFRs) are widely used as additives in many household and commercial products to reduce their flammability. Concerns have increased due to their occurrence in the environment and humans during the past years (Soderstrom et al., 2004). Reactive BFRs, such as tetrabromobisphenol A (TBBPA), are chemically bonded into the plastics. Additive BFRs, which include polybrominated diphenyl ethers (PBDEs) and hexabromocyclododecane (HBCD), are simply blended with polymers through physical bonds instead of chemical bonds, allowing PBDEs to leach out of the products into the surrounding environment (Hutzinger and Thoma, 1987). Due to their hydrophobic characteristic, high chemical stability, and widespread use, BFRs have been detected at a highly contaminated level in the environment (Eljarrat et al., 2004; Morris et al., 2004;

Ruan et al., 2009; Sellstrom et al., 1998). The levels of BFRs detected in biota and environmental matrices have been found to be increasing in recent years (Fernie et al., 2009; Law et al., 2006; Morris et al., 2004). BFRs has been detected in human, especially in human breast milk (Eljarrat et al., 2009). BFRs is being considered to be listed as one of persistent organic pollutants (POPs) since 2013, and is under review now.

Decabrominated diphenyl ethers (DBDE) comprises approximately 80% of the world market demand for PBDEs, which in 2001 was reported at 56,100 metric tons (Stapleton et al., 2004). It is expected to adsorb onto soil or sediment particles owing to its hydrophobicity, causing increasing concern over its occurrence in wildlife and humans during recent years (Gorgy et al., 2010; Soderstrom et al., 2004). Although PBDEs have shown low acute toxicities, they have been linked to hepatocellular carcinomas, thyroid adenomas, and reproductive toxicity (Kunisue et al., 2007; Talsness et al., 2005). PBDEs may also have endocrine disrupting effects because they can interact as antagonists or agonists at androgen, progesterone, and estrogen receptors (Hamers et al., 2006). However, information regarding the effective remediation of BFRs in the environment is still limited. Previous studies have also reported the microbial debromination of BFRs (He et al., 2006; Robrock et al., 2008); however, the biotic reductive debromination method was found to be inefficient, and further disposal treatment strategies were needed.

2.3.1.3 Chlorinated solvents

DNAPLs such as Trichloroethylene (TCE) are common source of groundwater contamination in many industrialized sites. Until now, there are a variety of technologies have been explored to remediate sites where contaminated with chlorinated hydrocarbons.

Though it remains highly challenging to remove or destroy these DNAPLs in a timely and cost-effective manner owing to the magnitude and complexity of the problem.

TCE is one of the common chlorinated organic compounds in the areas adjacent to dry cleaners, automobile manufacturers or shops, asphalt processing plants, and military bases. The major use for trichloroethylene is as a solvent. Various technologies have been explored for dechlorination of chlorinated hydrocarbons, including bioremediation, thermal treatment, and permeable reactive barriers. Among many technologies tested so far, abiotic dechlorination using ZVI appears to be one of the most promising technologies (Cheng and Wu, 2000; Schlicker et al., 2000). However, due to the limited reactivity of ZVI, TCE reduction rate has been found very slow (Agrawal et al., 2002; Johnson et al., 1996; Kober et al., 2002). Recently, NZVI and bimetallic Fe NPs such as Pd/Fe and Ni/Fe have been used for in-situ TCE dechlorination. The degradation rate constant of TCE with Fe⁰ was 1.0×10^{-3} L/hr·m² after 20 days and remained constant for 160 days (Liu and Lowry, 2006). Kim et al. (2010) pointed out that over 99% of TCE was removed by 50 g/L of Pd/Fe with rate constant of 1.6 L/h g. However, as results, toxic intermediate byproducts may form during reduction process (Arnold and Roberts, 2000; Johnson et al., 1996).

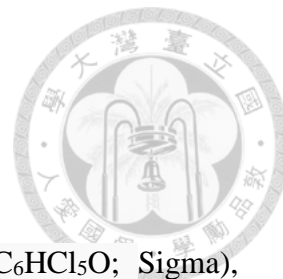
2.3.2 Azo dyes

Wastewater from the textile industry constitutes a significant source of water pollution because dyes are highly colored and are recalcitrant to degradation in the environment. Worldwide, approximately 80% of synthetic dyes were produced for modern textile industry, and over 700,000 tons of dyes were applied to 40 million tons of fabric every year (Bilgi and Demir, 2005; Molinari et al., 2004). Recent estimates indicate that each year

about 1-20% of the total world production of dyes is lost in effluent during manufacturing and processing operations (Houas et al., 2001; Ràfols and Barceló, 1997). Aromatic azo dyes, which contain the azo group (-N=N-), constitute about half of the dyes traded in markets worldwide (Maynard, 1983; Weber and Adams, 1995), are widely used in textile, plastic, leather, cosmetic and pharmaceutical industries (Kulkarni et al., 1985; Zollinger, 2003). Azo dyes have been recognized as potential carcinogens in recent years (Chung and Cerniglia, 1992; Kusic et al., 2006; Oliveira et al., 2006).

Azo dye effluents are highly resistant to microbial biodegradation, and thus conventional biological treatment processes are generally ineffective. Dye wastewaters, especially in a high effluent concentration, are also resistant to destruction by physical-chemical treatment methods such as activated carbon method, UV light-degradation and chemical oxidation-reduction treatments (Perey et al., 2002). In order to remove complex compounds of dye from the wastewater, the degradation of azo dyes by Fe particles has attracted much attention over the past decade (Cao et al., 1999; Hou et al., 2007; Perey et al., 2002)

Chapter 3 Materials and methods



3.1 Chemicals

3.1.1 Analytical standards

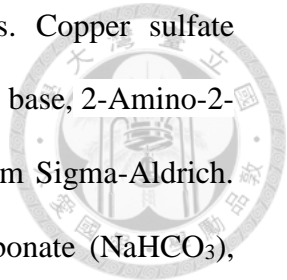
The analytical standards used were pentachlorophenol (PCP, C_6HCl_5O ; Sigma), chlorophenol standards including 19 chlorophenols (Supelco), deca-brominated diphenyl ether (DBDE, $C_{12}Br_{10}O$; Fluka), trichloroethylene (TCE, C_2HCl_3 ; Acros), reactive black 5 (RB5, $C_{26}H_{21}N_5Na_4O_{19}S_6$; Sigma-Aldrich), and Leonardite HA (LHA, 1S104H; International Humic Substances Society (IHSS)). The chemical properties of LHA was listed at Table S1 in the supporting information.

3.1.2 Solvents

The following solvents were used: ethyl acetate, methanol, and *n*-hexane (J.T. Baker), acetonitrile (Acros), deionized water (Milli-Q system, $18.2\text{ M}\Omega\text{ cm}^{-1}$; Millipore). The deionized water was deoxygenated by boiling for 30 min and then purging with nitrogen gas.

3.1.3 Reagents

All chemicals were of reagent grade. Formic acid (FA, $C\ H_2O_2$) was purchased from Sigma. HEPES (4-(2-Hydroxyethyl)piperazine-1-ethanesulfonic acid, $C_8H_{18}N_2O_4S$) were purchased from Fluka. Potassium hexachloropalladate (K_2PdCl_6), microscale ZVI (MZVI, 325 mesh, BET surface area of $0.17\text{ m}^2/\text{g}$), citric acid (CA, $C_6H_8O_7$), oxalic acid (OA, $C_2H_2O_4$), and Ferrozine™ iron reagent ((3-(2-Pyridyl)-5,6-diphenyl-1,2,4-triazine-*p,p'*-disulfonic acid monosodium salt hydrate, $C_{20}H_{13}N_4NaO_6S_2 \cdot xH_2O$), and 2',7'-



dichlorofluoresceinacetate (DCFH-DA) were purchased from Acros. Copper sulfate pentahydrate ($\text{CuSO}_4 \cdot 5\text{H}_2\text{O}$), palladium (Pd) powder, and Tris (Trizma[®] base, 2-Amino-2-(hydroxymethyl)-1,3-propanediol, $\text{NH}_2\text{C}(\text{CH}_2\text{OH})_3$) were obtained from Sigma-Aldrich. Sodium sulfate (Na_2SO_4), sodium carbonate (Na_2CO_3), sodium bicarbonate (NaHCO_3), carboxymethyl cellulose sodium (CMC, $\text{C}_{28}\text{H}_{30}\text{Na}_8\text{O}_{27}$, M.W. =982 g/mol), sodium phosphate monobasic (NaH_2PO_4), and potassium hydroxide (KOH) were purchased from Riedel-deHaën. Ferrous sulfate heptahydrate ($\text{FeSO}_4 \cdot 7\text{H}_2\text{O}$), sodium chloride (NaCl), sodium nitrate (NaNO_3), sodium hydroxide (NaOH), ammonium acetate ($\text{C}_2\text{H}_3\text{O}_2\text{NH}_4$), and hydrochloric acid (HCl) were obtained from J.T. Baker. Sodium borohydride (NaBH_4) was purchased from Shiyaku Kogyo Co. Ltd., Japan. Nickel sulfate hexahydrate ($\text{NiSO}_4 \cdot 6\text{H}_2\text{O}$) was obtained from Hayasi Pure Chemical Industries Ltd. All solutions were made in deionized water.

3.2 The preparation and analysis of ZVI, NZVI and bimetallic Fe NPs

3.2.1 ZVI pretreatment

1 g of ZVI particles were pretreated with a HCl washing process to remove the passive film followed by soaking with 0.1 M HCl (10 mL), then washed with deoxygenated DI water and dried at 70 °C overnight in the anoxic glovebox (Coy Lab Products, Inc.) under a H_2/N_2 atmosphere (95% N_2 and 5% H_2).

3.2.2 Synthesis of bare Fe NPs

NZVI particles and bimetallic Pd-doped Fe (Pd/Fe) NPs were chemically synthesized in the anoxic glovebox. A 180 mM ferrous sulfate solution was reduced using sodium

borohydride at a molar ratio for $\text{BH}_4^-/\text{Fe}^{2+}$ of 2.0. The obtained black nanoparticle suspension was filtered through a 0.45 μm membrane (mixed cellulose ester) and then washed with pH 4 sulfuric acid and deionized water several times to remove the residual reagents and salts. The final dosage of NZVI was theoretically 10 g/L. Bimetallic Pd/Fe NPs were synthesized by injecting potassium hexachloropalladate (IV) solution into fresh NZVI suspension. For instance, the concentration of free Pd ions in NZVI suspension to form 0.1% wt Pd^0 decreased from 16.4 mg/L to 0.06 mg/L after synthesis, that is, over 99% of Pd ions were deposited and reduced on the NZVI surface. Pd/Fe NPs were then rinsed with deionized and deoxygenated ultrapure water to remove salts. The resultant Fe NP suspension was used for reactions performed immediately.

3.2.3 Synthesis of CMC stabilized Fe NPs

CMC coated Fe NPs were prepared according to the method modified from He and co-workers (He et al., 2007). The stabilizer CMC stock solution was prepared by dissolving 33.3 g CMC powder in 1000 mL DI water. A 50 g/L ferrous sulfate solution (8.5 mL) was mixed with 6.25 mL CMC stock solution at room temperature to obtain the desired amount of CMC- Fe^{2+} complex. After stirring for 20 min, a 400 mM sodium borohydride solution was added dropwise into the CMC- Fe^{2+} complex to obtain a stabilized atomic Fe NP suspension (25 mL). The $\text{BH}_4^-/\text{Fe}^{2+}$ molar ratio was higher than 2.0 to ensure the efficient reduction of Fe^{2+} by BH_4^- . Next, CMC-stabilized Ni bimetallic Fe (CMC-Ni/Fe) NPs were prepared by injecting the nickel sulfate solution into the CMC- Fe^0 solution and stirring until the hydrogen gas evolution ceased. The CMC sorption should not prevent the accessibility of the CMC-stabilized core Fe particles for the electron acceptors because of

the chain-like structure and macromolecular nature of CMC (Doong and Lai, 2005). Thus, Fe NPs reduced Ni^{2+} to Ni^0 , resulting in the formation of Ni/Fe bimetallic NPs (Xu et al., 2009). The resultant CMC-stabilized Fe NPs were used for reactions performed within 24 hours. The final CMC/Fe molar ratio was 0.0005, which was theoretically calculated from a Fe^0 dosage of 180 mM and CMC concentration of 0.093 mM. The dosage of Ni was 0.5-5.0 wt% of Fe.

3.2.4 Characteristics of ZVI and Fe NPs

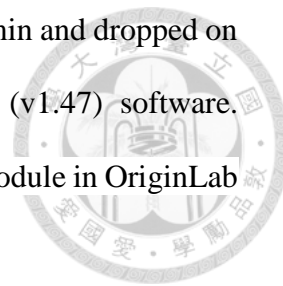
3.2.4.1 The Fe^{2+} dissolution from the Fe surface

Fe^{2+} and Fe complex concentrations were measured colorimetrically using the ferrozine method (Viollier et al., 2000). A ferrozine agent (10 mM) was prepared in an ammonium acetate solution of 100 mM. 1 mL of 0.22 μm -filtered sample (non-pyrogenic, Minisart) or standard was mixed to 100 μL of ferrozine agent. The absorbance was measured at the maximal absorption of Fe^{2+} -ferrozine complex of 562 nm. The concentrations of total Fe and noble metal were quantified using an inductively coupled plasma optical emission spectrometry (ICP-OES) (The Perkin Elmer® Optima™ 8000). Each sample was digested using concentrated nitric acid and then diluted to nitric acid of 2% before ICP analysis.

3.2.4.2 The surface morphologies of Fe particles

The surface morphologies of Fe were analyzed using a scanning electron microscope (SEM, JOEL JSM-7600F). A diluted ZVI sample was dropped on an acid-washed silicon wafer and heated at 120-150 $^{\circ}\text{C}$ for 15 min under an anaerobic condition. The morphology of the NPs and colloids was determined using a transmission electron microscope (TEM)

(JEOL Corp. JEM2010), the diluted Fe samples were sonicated for 15 min and dropped on a Cu grid to dry. The particle size was calculated using ImageJ (v1.47) software. The fitting of size distribution is based on the non-linear curve fitting module in OriginLab (v8.1). The peaks were fitted as the accumulation of Gaussian function.



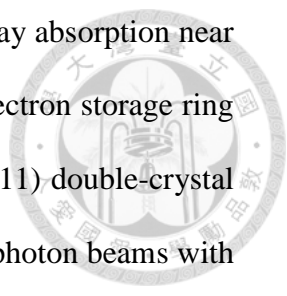
The hydrodynamic particle size (z-average) of the suspended Fe NPs was analyzed by dynamic light scattering (DLS) (Nano-ZS, Malvern). Diluted samples were used in order to avoid multiple scattering which can make data interpretation difficult. The CONTIN algorithm was used to convert intensity autocorrelation functions to intensity-weighted particle hydrodynamic diameter distributions, assuming the Stokes-Einstein relationship for spherical particles.

The zeta-potential of Fe NP suspension was monitored using a Zetasizer (Nano-ZS, Malvern). Measured values were converted to apparent zeta-potentials using the Helmholtz-Smoluchowski relationship.

The colloid stability of metal particles was evaluated using a sedimentation curve: the reading was performed with time in a UV-vis (CT 2200, ChromTech) at an absorbance of 510 nm.

3.2.4.3 The atomic and molecular structures of Fe particles

The atomic and molecular structures of the crystals of ZVI and Fe NPs were determined using X-ray diffraction (XRD) (13A1 beamline of National Synchrotron Radiation Research Center (NSRRC), Taiwan). The Fe samples were prepared inside the glove box and sealed with plastic bags with original solutions. XRD scan range of $10\text{-}60^\circ 2\theta$ were acquired for iron and iron oxides with a scan speed of 2°min^{-1} .



The Fe components of Fe NP suspensions were analyzed using X-ray absorption near edge structure (XANES) (16A1 beamline of NSRRC, Taiwan). The electron storage ring was operated with energy of 1.5 GeV and current of 300 mA. A Si (111) double-crystal monochromator (DCM) was used to provide highly monochromatized photon beams with energies of 2-8 keV and an energy resolution of 1.5×10^{-4} - 2.1×10^{-4} . The data were collected using the transmission mode and the fluorescent mode with a Lytle detector in the region of the Fe K-edge (7115 eV) and Ni K-edge (8333 eV) at room temperature. The K-edge XANES scans for Fe (7092-7192 eV) and Ni (8132-8629 eV) were recorded with incremental steps of 0.2 eV and 4.0 eV, respectively. The XANES data were then analyzed by Athena version (0.8.058). For XRD and XANES analysis, the samples were prepared inside the glove box and sealed with plastic bags with their original solutions.

3.2.4.4 The Fourier transform infrared spectroscopy (FTIR) technique

Synchrotron radiation based infrared microspectroscopy (SR-IMS) beamline provide considerable brightness advantages over conventional IR sources (14A1 beamline of NSRRC, Taiwan). The combination of IMS with high brightness synchrotron radiation has greatly improved the spatial resolution of this technique by allowing high quality spectra to be collected from samples whole size is approaching the diffraction limit for this wavelength of infrared. The samples for FTIR analysis were treated through an air-drying process under the anaerobic condition. For this, samples were prepared with 99.9 wt% (250 mg) of KBr and approximately 0.1 wt% (0.3 mg) of the analyzed HA-Cu powder using the KBr pellet mode.

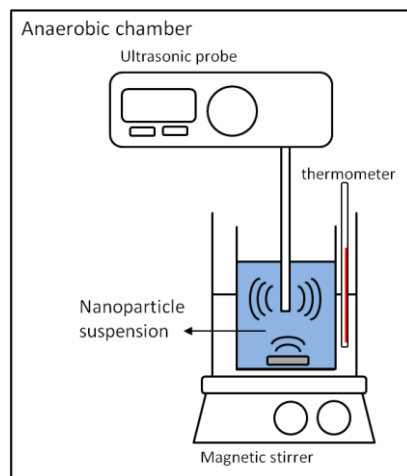
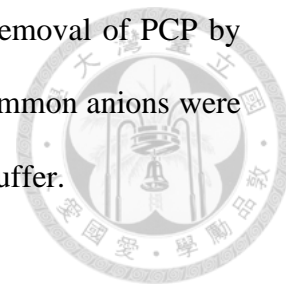
3.3 Removal kinetics of halogenated organic compounds by well-suspended Fe NPs

3.3.1 Physical dispersion methods

The PCP stock solution (15 mg/L) was prepared by dissolving PCP in methanol/water (1:200, v/v) as a stock solution and this was stored at 4 °C. In order to compare the different dispersion techniques, a shaker (LM-530R, YIH DER), a magnetic stirrer (PC-420D, Corning), an US probe (Ultrasonic 250, HOYU), as well as a combination of a magnetic stirrer and an US probe (US/stirring) were used to disperse Fe NPs.

For shaking, the batch reactions were conducted in 5 mL amber vials, sealed with Teflon-lined septa. Each vial contained 2 mL of PCP stock solution, 2.5 mL of Fe NPs suspension, and around 0.5 mL deoxygenated ultrapure water to eliminate headspace, which was prepared in the anaerobic chamber. An orbital shaker operating at 150 rpm was used and the stirrer was set at 120 rpm. For the US (23 kHz and a rated output power of 250 W) and US/stirring systems, all of the time-dependent experiments were performed in the anaerobic glovebox. 10 mL of PCP stock solution and 12.5 mL Fe NPs suspension were mixed in a 100 mL beaker placed in a water bath and maintained at a constant temperature of 25°C during sonication. The initial concentration of the PCP in all reactors was 7.2 mg/L. The Fe dosage for all the experiments quantified using ICP-OES was 4.5 g/L. The initial pH of medium was approximately 6.7. The setting for the US/stirring system is shown in Scheme 3-1. The magnetic stirring rate was 120 rpm. Control experiments were run under different physical dispersion methods without addition of Fe NPs. The solution pH and the reduction potential were monitored during these reactions.

The effect of Fe dosage, noble metal loading and anions on the removal of PCP by well-suspended Fe NPs was determined. Individual solutes of three common anions were used in sodium form (i.e. chloride, nitrate and bicarbonate) without a buffer.



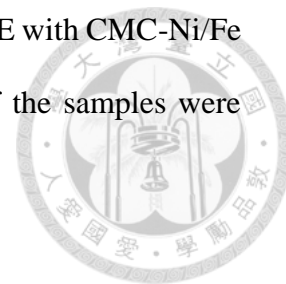
Scheme 3-1. Schematic of the US/stirring setup employed in the present study.

3.3.2 Chemical dispersion method

A DBDE-simulated solution was prepared by spiking a known volume of the stock solution with a fixed proportion of EA:methanol:water to combine the stock solution with an aqueous system. 27 mg of DBDE was dissolved in 80 mL EA and then diluted with methanol up to 200 mL.

Batch experiments were conducted in amber vials capped with Teflon-coated septa. Next, 2 mL of freshly prepared CMC-Ni/Fe NPs were added to an amber vial that contained 2 mL of the 2 mg/L DBDE stock solution. The final DBDE concentration was approximately 10 mg/L, and the CMC-Ni/Fe NPs dosage was 5 g/L. Blank experiments were conducted in the absence of CMC-Ni/Fe NPs. Each batch reactor was operated at room temperature (25 °C) with continuous shaking (100 rpm) throughout the experiments. To study the effects of environmental factors, such as temperature, pH value, and anions

(chloride, nitrate, and bicarbonate), on the removal kinetics of the DBDE with CMC-Ni/Fe NPs, all experiments were performed in duplicate. The pH values of the samples were adjusted using 1 M HCl and NaOH.



3.4 Removal kinetics of halogenated organic compound by ZVI and Fe^{2+} in the presence of ligand

TCE saturated stock solution was prepared by dissolving excess TCE in deoxygenated DI water. Three organic ligands, FA ($pK_a = 3.75$), OA ($pK_{a1} = 1.25$ and $pK_{a2} = 4.27$) and CA ($pK_{a1} = 3.13$, $pK_{a2} = 4.76$ and $pK_{a3} = 6.40$), were selected to investigate the enhancement on the reactivity of ZVI. HCl was applied as an inorganic ligand conducted to this study was performed to compare with organic ligands.

Batch experiments were performed in 110 mL anaerobic septum-sealed vials in triplicates. Each vial contains 50 mL of reactants and reagents including TCE (2 μL), a ligand of interest (30 mM), and acid-pretreated ZVI (1 g). The final Fe dosage was 20 g/L and TCE initial concentration was 4.57 μM . Blank experiments were run in the presence of ligand without addition of ZVI. The effect of Fe^{2+} -Ligand complexes on the removal kinetic of TCE was also investigated in this study. Fe^{2+} was applied with a concentration of 40 mM, which was higher than it released from ZVI in the inorganic ligand system after the reaction. Fe^{2+} was mixed with carboxylic ligands and TCE stock solution under a same condition mentioned above. All sample preparations were performed in the glovebox. Reactors were mixed on an orbital shaker with 100 rpm at room temperature. All experiments were performed in triplicate.

3.5 Formation and analysis of HA-Fe complexes and HA-metal colloids

3.5.1 Perpetration of HA stock solution

A LHA stock solution was prepared by dissolving HA powder (3.98 g/L) in pH 9 solution (adjusted with 5 M KOH) and then filtered through a 0.45 μm filter (Nylon 66, BGB). The total organic carbon content was 1.86 g/L – measured with total organic carbon (TOC) analyzer (DIMATOC[®] 2000, TIMATEC Inc.).

Untreated HA (UHA) solution was prepared by diluting LHA stock solution with deoxygenated buffer inside a glovebox (MBraun, $\text{O}_2 < 0.1$ ppm). In this study there were two methods applied to reduce HA according to the purpose of the system. For the first method, Reduced HA (RHA) was prepared using the H_2 gas method as described by Kappler et al. (2004) and Peretyazhko and Sposito (2006). Diluted HA stock suspensions (398 mg/L) in 100 mL serum bottles were prepared in pH 7 deoxygenated DI water in the presence of 15 mg of Pd catalysts. The serum bottles were then sealed and the suspensions were incubated on a shaker at laboratory temperature (25 °C) for 48 hours under N_2/H_2 atmospheric condition (95% N_2 and 5% H_2). Stock suspensions of H_2 -reduced HA were flushed with N_2 gas to remove excess H_2 gas and then transferred to the glovebox for subsampling and chemical analyses. This RHA stock solution was applied to form RHA-Fe complexes, as described in section 3.5.2.

The second method used was the NaBH_4 reducing method, as described by Tinnacher and Honeyman (2007) and Sharpless (2012). The HA concentration was diluted to approximately 1.1 g/L and then reduced by adding an excess of NaBH_4 (approximately 15 mmol/L). After mixing for 4 to 6 hours, the standard Eh of RHA reached -0.2 V. The pH value of RHA was adjusted to pH 7 to halt the activity of the reducing agent (Kojima et al.,

2002; Schlesinger et al., 1953). This RHA solution was applied to form metal colloids as described in section 3.5.3.



3.5.2 Preparation of HA-Fe complexes

A HA-Fe complex solution was formed by adding Fe^{2+} solution into UHA or RHA gently mixed for 48 hours inside the glovebox. For the reduction of RB5, it need 8 mmol/L e^- were needed to destroy the molecular structure of 1 mmol/L RB5. The electron accepting capacity (EAC) of LHA was 8.6 mmol/mol_c -1711 $\mu\text{mol/g}_{\text{HS}}$ (Aeschbacher et al., 2009; Peretyazhko and Sposito, 2006), i.e. approximately 28-30 mg/L HA (about 50 $\mu\text{mol/L e}^-$) or 50 $\mu\text{mol/L Fe}^{2+}$ was applied in this study to decompose 6 mg/L RB5. Therefore the Fe^{2+}/HA ratio was 2 mmol/g ($[\text{Fe}^{2+}] = 50\text{-}60 \mu\text{M}$) in this study to observe the reactivity of HA-Fe complexes toward RB5. The pH/Eh values and Fe concentration were monitored during the mixing process.

Fe^{2+} concentration was measured colorimetrically using the ferrozine method (Viollier et al., 2000). The ferrozine agent (10 mM) was prepared in an ammonium acetate solution of 100 mM. 1 mL of unfiltered or 0.02 μm -filtered sample (Whatman) and the standard was mixed to 100 μL of ferrozine agent. The absorbance was measured at the maximal absorption of the Fe^{2+} -ferrozine complex of 562 nm without interference from LHA. The ferrozine assay could be used to determine free Fe^{2+} and HA-Fe species without the interference of HA, as shown in Figure 3-1. Total Fe (Fe^{tot}) concentration was measured by inductively coupled plasma optical emission spectrometry (ICP-OES, Agilent 5100). 1.0 mL of filtered/unfiltered samples and standards were digested by concentrated HCl, then diluted with DI water until the HCl background concentration was 2.6%.

The different between total Fe and Fe^{2+} filtered samples could represent as the sum of Fe^{3+} and oxidized HA-Fe.

$$Fe^{3+}/HA-Fe^{3+} = \text{filtered } Fe^{tot} - \text{filtered } Fe^{2+} \quad (3-1)$$

The precipitated Fe could be derived from the difference between unfiltered total Fe and filtered total Fe, as shown in eq. 3-2

$$Fe \text{ colloids} = \text{unfiltered } Fe^{tot} - \text{filtered } Fe^{tot} \quad (3-2)$$

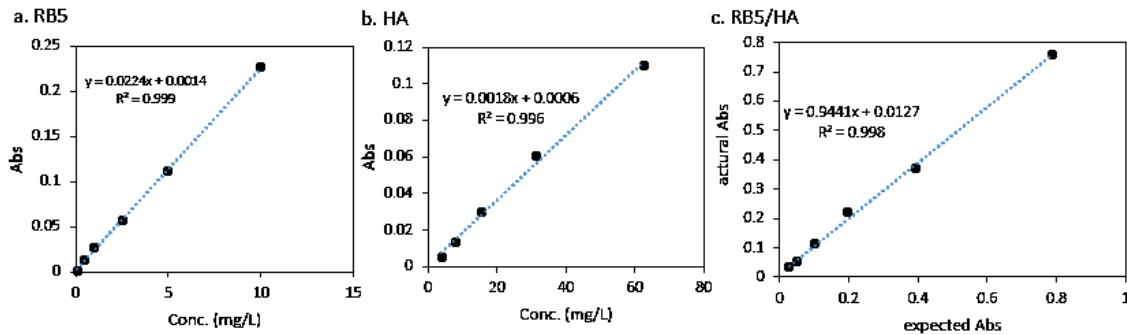


Figure 3-1. The standard curves of (a) RB5, (b) HA, and (c) RB5 with HA. For RB5 with the HA set, a linear relationship was observed between the actual absorbance value and the expected absorbance values.

3.5.3 Preparation of metal colloids in the presence of HA

For a pretest experiment, HA-metal colloids were formed by mixing high concentration (10 g/L) of Fe^{2+} or Cu^{2+} solution with HA (20 and 60 mg/L) at the gentle mixture for 48 hours in the glove box. This test offered a rough result about the morphology and the reactivity of Fe and Cu colloids in the presence of UHA. After evaluating their properties, Cu^{2+} was chosen as a precursor.

To investigate the formation of Cu colloids, an overdose of Cu²⁺ was applied in this study. 1.6 g/L CuSO₄ stock solution was mixed with 1 g/L of UHA or RHA for 24 hours. The color of HA solution turned to black-brown and formed suspension. Samples washed with deoxygenated ultrapure water and then resuspended in deoxygenated ultrapure water with a final Cu²⁺/HA ratio of 6.4 mmol/g. The final pH of the HA-Cu suspension was adjusted to a range of pH 7.5 to 8.0 with 1 M HCl and 1 M KOH. All suspensions were kept at 25 °C in the dark under anaerobic conditions for the batch degradation experiments.

Cu concentration was analysed using atomic absorption spectrometry (AAs) and ICP-OES, as mentioned above. Metal concentrations in both the solid ($c_{colloid}$) and dissolved in solution ($c_{dissolution}$) were calculated from the concentrations measured in the unfiltered (c_{unf}) and the 0.1- μ m filtered (c_{fill}) solutions according to equations modified from Maurer et al. (2012):

$$c_{colloid} = c_{unf} - c_{fill} \quad (3-3)$$

$$c_{dissolution} = c_{fill} \quad (3-4)$$

The K-edge XANES (16A1 and 17C1 beamlines of NSRRC, Taiwan) was applied to determine the oxidation state and local structure of the Cu colloids. 5 mL of the HA-Cu suspension was filtered through a 0.1 μ m filter (mixed cellulose ester, Advantec) and then sealed in a plastic bag. The data of Cu were collected transmission mode with a Lytle detector in the region of the Cu K edge (8979 eV) at room temperature. The K-edge XANES scans for Cu were in the range of 8778-9275 eV and were recorded with increments of 5.0 eV. All edge-normalized spectra and the contributions of Cu species to the total Cu were calculated by the linear combination fitting (LCF) tool in Athena.

3.6 The reactivity of HA-Fe complexes and HA-metal colloids

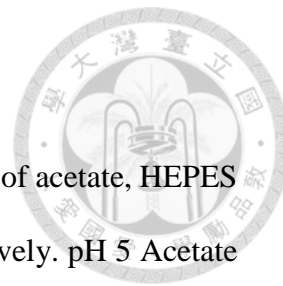
3.6.1 HA-Fe complexes

There were three buffer solutions applied in this study, i.e. 100 mM of acetate, HEPES and Tris buffer to mimic the pH 5, pH 7, and pH 9 conditions, respectively. pH 5 Acetate buffer was prepared by mixing sodium acetate (64.3 mM) and acetic acid (35.7 mM), then solution was adjusted to a pH of 5 with acetic acid.

Batch experiments were carried out in 50 mL vials containing 6.3 mg/L RB5 mixed with Fe²⁺, HA or HA-Fe complexes at 25 °C a shaker speed of 160 min⁻¹ in the dark. The concentration of RB5 was measured using a Cary 50 BIO UV-visible spectrometer (Varian) with a full scan from 250-900 nm and a specific absorption at 596 nm. All batch experiments were performed in triplicates. Fe concentrations were measured over time. Samples were unfiltered or collected by using a 0.22 µm-filter (Nylon 66, BGB) and then analysed for the concentration of Fe²⁺ and total Fe.

3.6.2 HA-metal colloids

In the batch experiments, 100 mL vials contained HA-Cu suspension and RB5 stock solution with a final Cu²⁺/HA ratio of 6.4 mmol/g. the experiments were carried out at 25 °C a shaker speed of 100 min⁻¹ in the dark. HA control system was proceeding at the same condition as control experiments. In order to eliminate the concern about the effect of NaBH₄ that remained in solution, the same procedure for the HA reducing process was performed at the same condition without adding HA and Cu²⁺. All batch experiments were performed in duplicates. The sample was filtered through a 0.22 µm filter and then analyzed using UV-vis (CT 2200, ChromTech).





3.7 Analytical methods of halogenated organic compounds

3.7.1 Analysis of PCP

The concentration of PCP was quantified using HPLC (Agilent 1200) with a UV-vis detector and gas chromatography (GC) (Agilent 6890) with a micro-electron capture detector (μ -ECD) and mass spectrometer (MS) equipped with an ESI source (Agilent 5975B). The mobile phase was a mixture of methanol and 1% H_3PO_4 (80:20 v/v) at a flow rate of 1.0 mL/min and the wavelength was set at 254 nm for PCP analysis. The GC was equipped with a HP-5 column (30 m \times 0.25 mm, 0.25 μm film). The carrier gas was ultrahigh-purity N_2 of 99.999% and the flow rate was 60 cm/sec. The injector temperature was 250 $^\circ\text{C}$, the oven temperature was maintained at 80 $^\circ\text{C}$ for 2 min and then increased at 7 $^\circ\text{C}/\text{min}$ to 280 $^\circ\text{C}$, at which temperature was maintained for 5 min. The detector temperature was 320 $^\circ\text{C}$. For byproduct analysis, chlorophenols were separated using a GC program with an initial temperature of 60 $^\circ\text{C}$ for 2 min, ramping at 20 $^\circ\text{C}/\text{min}$ to 140 $^\circ\text{C}$ with 0.5 min holding, 1 $^\circ\text{C}/\text{min}$ to 150 $^\circ\text{C}$ with 0.5 min holding, and 15 $^\circ\text{C}/\text{min}$ to 300 $^\circ\text{C}$ with 3 min final holding time. The flow rate was 30 cm/sec. To determine the adsorbed PCP on the Fe NPs, the Fe particles were dried and extracted with hexane and concentrated HCl, until there was no PCP residue in the extract.

3.7.2 Analysis of DBDE

The DBDE concentration was quantified using GC- μ ECD. The carrier gas was N_2 having an ultrahigh-purity of 99.999%. Next, a DB-5HT column with the dimensions of 15 m \times 0.25 mm and a 0.1- μm film (J&W Scientific, Agilent Technologies Inc.) was used

at a flow rate of 7.0 mL/min. The temperatures of the injector and the detector were set at 310 and 340 °C, respectively. An initial oven temperature of 150 °C was maintained for 0.5 min; it was then increased to 320 °C at 25 °C/min and was maintained for 5 min.

In addition, the samples were analyzed to determine the concentration of the DBDE that was adsorbed on the Fe surface and that which remained as a residue in the solutions. After 60 min, each vial was centrifuged at 6000 rpm for 10 min (Hermle, Z323) to separate the solid and liquid phases, and samples were extracted three times with EA until no DBDE was detected.

3.7.3 Analysis of TCE

TCE was quantified using gas chromatography with GC- μ ECD equipped with a HP-5 column (30 m \times 0.32 mm, 0.25 μ m film). The injector and detector temperatures were 200 °C and 280 °C, respectively. The flow rate was 1.0 mL/min. The oven temperature of 110 °C was held for 4.5 min. As the adsorption of TCE on the Fe surface occurred during reactions, Fe particles were separated from liquid phases using a magnet after reactions. Fe particles were dried and extracted with hexane until there was no TCE residue in the extract.

3.7.4 Analysis of ions

The anion concentrations (chloride, nitrate, and ligands) in the solutions were monitored using ion chromatography (IC) (Metrohm, Switzerland) after filtering through a 0.22 μ m filter (Minisart, non-pyrogenic). For chloride, nitrate, and formic acid, the eluent was the mixture of 1.0 mM NaHCO₃ and 3.2 mM Na₂CO₃ with the flow rate of 0.7 mL/min.

3.7.5 Total ROS measurement

The reactive oxygen species (ROS) was measured by the 2',7'-dichlorofluorescein diacetate (DCFH-DA) assay (LeBel et al., 1992). DCFH-DA can be de-esterified by NaOH to form nonfluorescent DCFH. First, 0.5 mL of 1.0 mM DCFH-DA was mixing with 2.0 mL of 0.01 N NaOH. This de-esterification proceeded at room temperature for 30 min, and then the mixture was neutralized with 10 mL of 25 mM NaH₂PO₄. The DCFH solution was kept on ice in the dark until use. The presence of ROS could rapidly oxidised DCFH to highly fluorescent 2', 7'-dichlorofluorescein (DCF). Reactions were conducted in a 200 µL tube that contained 195 µL of sample and 5 µL of DCFH solution. Fluorescence reading was obtained 5 min, which was monitored on an infinite M200PRO (TECAN, Switzerland), with excitation wavelength at 488 nm and emission wavelength 525 nm.

3.8 Modeling

3.8.1 Reaction kinetics of halogenated organic compounds with Fe NPs

The removal rate constant is described by a pseudo-first order reaction, as described in eq.3-5.

$$C_t = C_0 e^{-kt} \quad (3-5)$$

where C_0 and C_t are the initial concentration (mg/L) of target compound and its concentration at reaction time t (min), and k is the measured rate constant (min⁻¹). In addition, the ratio of the removal target compound to its initial concentration is defined as the *removal efficiency* (eq. 3-6). The ratio of the measured adsorbed target compound to the initial concentration is defined as the *adsorption efficiency*. The difference between

removal efficiency and adsorption efficiency is defined as the degradation efficiency (eq. 3-7).

$$\text{Removal efficiency (\%)} = (C_0 - C_{\text{final}}) / C_0 \times 100 \quad (3-6)$$

$$\text{Degradation efficiency (\%)} = \text{removal efficiency} - \text{adsorption efficiency} \quad (3-7)$$

where C_{final} is the final target compound concentration (mg/L) in the aqueous phase.

3.8.2 Dehalogenation efficiency of halogenated organic compounds

The amounts of chloride or bromide released from target compounds into solutions were calculated as follow,

$$\text{Dehalogenated efficiency (\%)} = M_{\text{halo},f} / M_{\text{halo},0} \times 100 \quad (3-8)$$

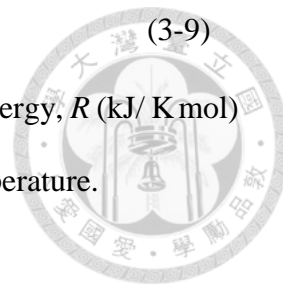
where $M_{\text{halo},0}$ and $M_{\text{halo},f}$ are the total halide ions (mM) from the substrate and the produced halide ions (mM) in the degradation solution, respectively. The degradation efficiency described above was compared with the dehalogenation efficiency in many results. For the system contained HCl as mentioned in chapter 3.4, as it was difficult to determine the chloride concentration released from TCE, the *degradation efficiency* was calculated as the *dechlorination efficiency*. Also, for the system contained CMC as mentioned in section 3.3.2, the degradation efficiency applied due to the interference of CMC on the analysis. However, the dehalogenation represented the efficiency of halide ions released from the parent compound; the degradation means that the transformation of the parent compound.

3.8.3 Activation energy

The Arrhenius equation was used to describe the relationship between rate constants and temperature:

$$k = Ae^{(-E_a/RT)}, \quad (3-9)$$

where A (L/min m²) is a frequency factor, E_a (kJ/mol) is the activation energy, R (kJ/ K mol) is the ideal gas constant (8.314 J/K mol), and T (K) is the absolute temperature.



3.8.4 Fe dissolution kinetic of ZVI in the presence of ligands

Fe dissolution processes were calculated via the measurement of Fe²⁺/Fe complex concentrations released from ZVI with time. The Fe dissolution kinetics could be described as a pseudo-first order kinetic model, as shown in eq. 3-6,

$$M_{Fe,t} = M_{Fe,0} - M_{Fe,0} e^{-k_{Fe}t} \quad (3-10)$$

where $M_{Fe,t}$ and $M_{Fe,0}$ are the dissolved Fe²⁺/Fe complex concentration (mM) at time t and the total Fe concentration, respectively. k_{Fe} was the reaction rate constant of Fe dissolution kinetic.

3.8.5 Speciation calculation

Aqueous and solid species of Fe and Cu were calculated using Visual MINTEQ 3.0 to estimate precipitation or complexation between Fe and ligand or HA under the conditions tested. The predominant species of Fe²⁺ complexes mentioned in chapter 4.4 were calculated using the Fe²⁺ concentration that measured after reactions, with the condition of the ligand (formic, oxalic, and citric acid) concentration and final pH value, as shown in Table 3-1.

For chapter 4.5, HA modeling was performed using both the Stockholm humic model (SHM) and the non-ideal competitive adsorption (NICA) model for prediction. The additions of acid (HCl) and base (KOH) that were used to adjust the pH of the HA stock

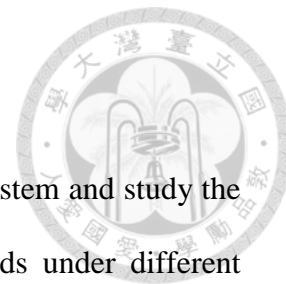
solution were excluded in the models. The concentrations of FeSO₄ and dissolved organic matter (DOM) were 50 μM and 18.6 mg/L (HA), respectively. The modeling was used to identify the main Fe species for further investigation.

For chapter 4.6, HA modeling was performed using the SHM model for the prediction. The concentrations of CuSO₄ and dissolved organic matter (DOM) were 1600 mg/L and 500 mg/L (HA), respectively. The modeling was used to identify the dissolved Cu and precipitated Cu for further investigation.

Table 3-1. The input data for Visual MINTEQ modeling.

System	pH	ligand concentration (mM)	Fe ²⁺ (mM)
30 mM HCl	6.84	30	12.6
15 mM FA	6.74	15	6.0
30 mM FA	5.84	30	24.4
10 mM CA	6.53	10	6.5
30 mM CA	5.36	30	10.8

Chapter 4 Results and discussions



4.1 Well-suspended Fe NPs by the physical dispersion method

The application of physical dispersion methods can simplify the system and study the catalytic behavior of Fe NPs toward halogenated organic compounds under different conditions as close to nanoscale without the additives on the Fe surface.

The range of the particle sizes for the synthesized NZVI and Pd/Fe NPs was 50-100 nm, as shown in the TEM images (Figure 4-1). However, the hydrodynamic particle sizes of two nanoparticles in aqueous solutions were more than 10 μm (about 34 μm -58 μm) measured by DLS. Fe NPs tend to form micro-sized aggregates in solution because of the magnetic attractive force and the van der Waals forces between nanoparticles (Giasuddin et al., 2007; Shih et al., 2010; Wang and Zhang, 1997). In order to determine the effect of well-suspended Fe NPs on the removal of PCP, comparative experiments were performed for the four different physical dispersion methods: the shaking, the stirring, the US and the US/stirring system.

4.1.1 The removal of PCP by Fe NPs in different dispersion systems

Approximately 52% of PCP was removed using NZVI under US irradiation while no obvious removal was noted in the shaking system. However, there was no chloride ion produced in the US system, showing that dechlorination did not occur with NZVI, as will be discussed later (Figure 4-2). As compared to NZVI, PCP was removed by Pd/Fe NPs under four different dispersion conditions, as shown in Figure 4-3. The PCP removal efficiencies by Pd/Fe NPs were increased to approximately 81% and 93% for the US and the US/stirring systems after 1 hr while 43% and 74% for the shaking and the stirring

system, respectively. k_{obs} of PCP for the shaking, the stirring, the US and the US/stirring systems were 0.01, 0.05, 0.06 and 0.13 min^{-1} , respectively.

The PCP adsorption fractions for the stirring, the US, and the US/stirring systems were about 63%, 65%, and 73%, respectively, which were much higher than that for the shaking system (12%) (Figure 4-3b). Under these four physical dispersion methods, the size of Pd/Fe NPs remained on the micro-scale with an exception of the ultrasonic method, which decreased the average particle size from the micro-scale (34 μm) to the nano-scale (123 nm) after US irradiation for 60 min (Figure 4-4). The same trend was also observed for NZVI. Also, Pd/Fe NPs were suspended continuously in solutions for 60 min in both the US and the US/stirring systems (Figure 4-5). The hydrodynamic particle size was 295 ± 176 nm during US irradiation. PCP was not removed in the US control system, indicating that the US power used in this study was not strong enough to eliminate the molecular structure of PCP. As large NP aggregates become smaller and were dispersed uniformly, the more surface area would expose to the substance. Pd/Fe NPs was dispersed at a nano-scale level using the US probe, and then cause more active sites on the Fe surface than that for nano-aggregates. Therefore, US irradiation did increase the PCP removal via enhancing its adsorption on the surface of Pd/Fe NP.

Several dechlorination byproducts such as 2,3,4,5-tetrachlorophenol (TeCP), 2,3,4,6-TeCP, 2,3,4-trichlorophenol (TCP), and 3,4,5-TCP were identified in the US/stirring system. Three byproducts (2,3,4,5-TeCP, 2,4,5-TCP, and 3,4,5-TCP) were detected in the stirring system; however, only one byproduct (2,3,4,5-TeCP) was found in the shaking system (Figure S1). The result indicated that further dechlorination occurred on the surface of Pd/Fe NPs in the other systems but not in the shaking system though it had the highest

degradation of parent compound.

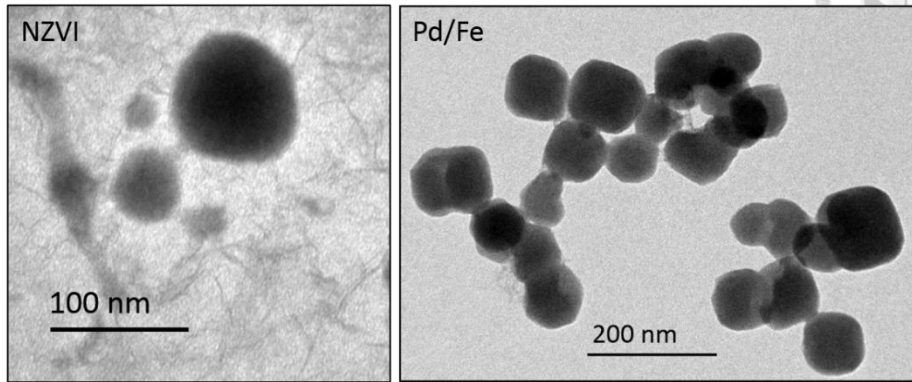


Figure 4-1. TEM images of NZVI and Pd/Fe NPs.

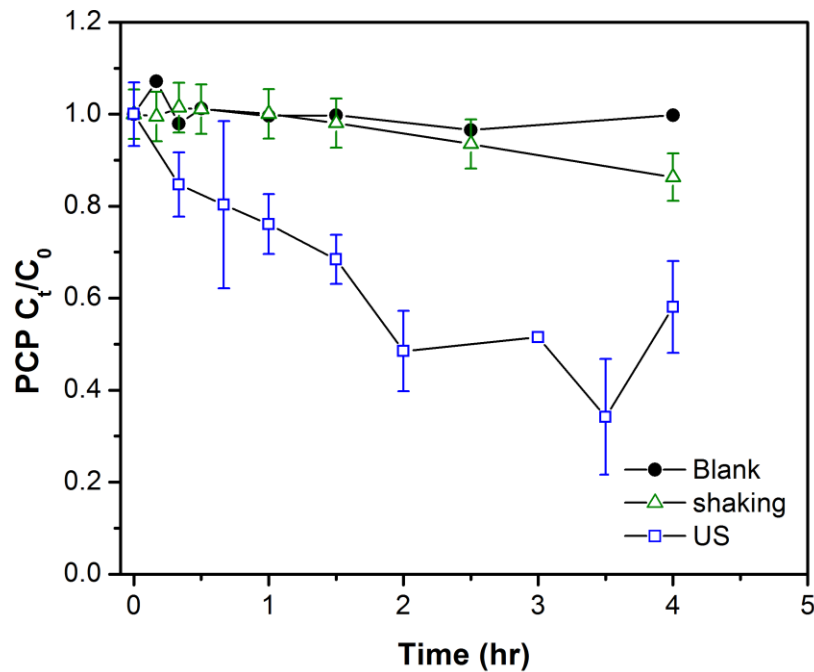


Figure 4-2. Removal reactions of PCP with NZVI under shaking and US suspended systems. PCP initial concentration was 6.5 mg/L and NZVI dosage was 1.0 g/L. The error bar in Figure 4-2 represented the standard error of an average over duplicated batch experiments.

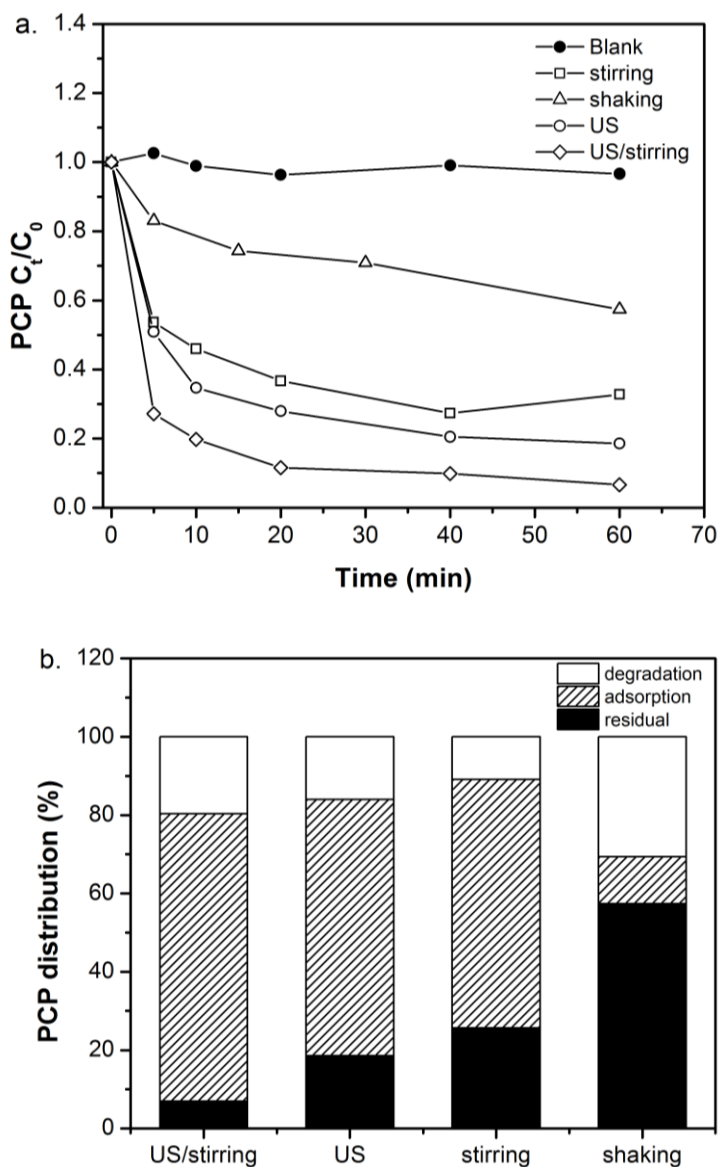


Figure 4-3. (a) Removal reactions of PCP with Pd/Fe NPs under various suspended systems and (b) the PCP distribution after reacted with Pd/Fe NPs for 60 minutes. PCP initial concentration was 7.2 mg/L, Fe dosage was 4.5 g/L and Pd content was 0.1 wt%. The orbital shaker was operating at 150 rpm, the stirrer was set at 120 rpm, US output intensity was 75 W during US irradiation. The error bar in Figure 4-3 represented the standard error of an average over duplicated batch experiments.

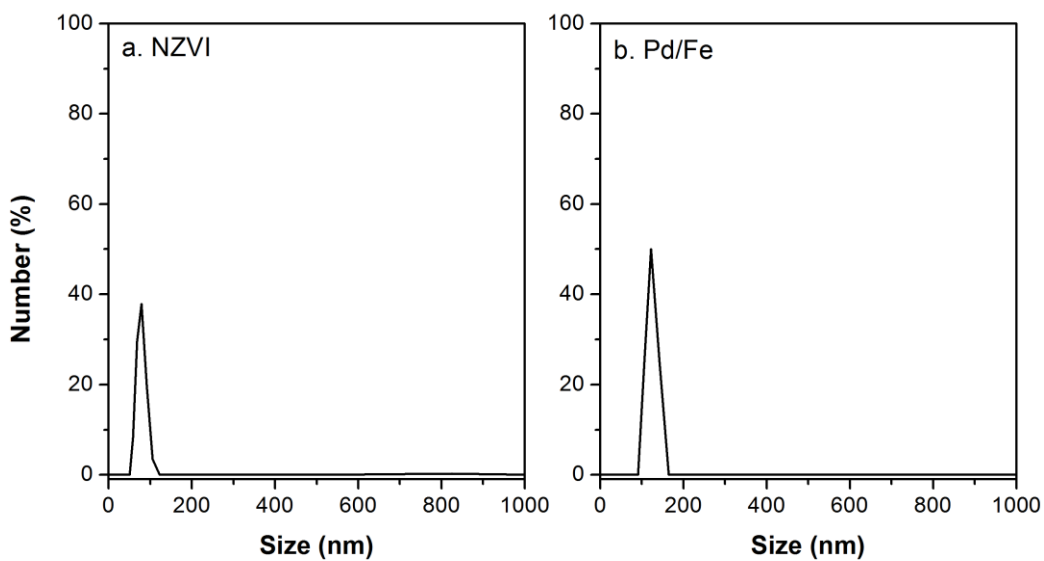


Figure 4-4. The average particle size of NZVI and Pd/Fe NPs under US probe irradiation for 60 minutes. Data collected from DLS results as number distribution.

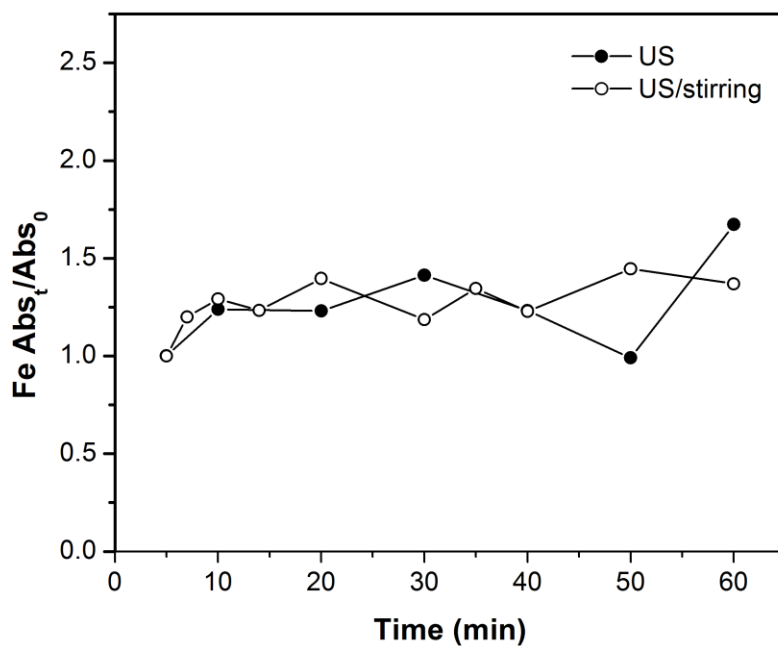


Figure 4-5. The sedimentation curves of Pd/Fe NPs under the US and the US/stirring systems. US output intensity was 75 W during US irradiation.

4.1.2 The removal mechanism of PCP by Pd/Fe NPs in US dispersion systems

The removal rates of PCP increased with an increase in the output intensity of US from 0 to 75 W, accompanied with a decrease in the hydrodynamic particle size of Pd/Fe NPs (Figure 4-6). However, the US irradiation did not enhance the PCP removal efficiency but increased the particle size of Pd/Fe NPs when the US output intensity increased from 75 W to 250 W. It was worth noting that particle adhesion (especially van der Waals forces) increased when the particle size decreased. NPs may regroup back into several hundred nanometer clusters shortly after irradiating US if the suspension was not stabilized enough against re-agglomeration (Thi Thuy et al., 2011). Therefore, the output intensity of the US probe about 75 W (i.e. 30% of 250 W) was chosen in this study to proceed with following experiments.

The surface characteristic of Pd/Fe NPs under US irradiation was analysed using XRD (Figure 4-7). Pd/Fe NPs at 2 theta of 44 ° have a weak peak which was expected as zerovalent iron (Fe^0), although most of Fe^0 oxidized to hematite ($\alpha\text{-Fe}_2\text{O}_3$) by the reduction process of Pd ions on the NZVI surface, or oxidized during the specimen preparation for XRD analysis. No obviously oxidation was observed in a comparison of Pd/Fe NPs before and after US irradiation. US had a little effect on the promotion of total ROS generation (Figure S2), this demonstrated that the ROS that were generated by cavitation under US irradiation did not affect the surface character of Pd/Fe NPs. In general, an increase in the power and duration of the US irradiation results in the generation of more ROS because of cavitation (Hou et al., 2012). However, under the operating conditions in this study, cavitation did not destroy the molecular structure of PCP and seemed not to modify the surface of Pd/Fe NPs.

The removal rates for PCP by Pd/Fe NPs were accelerated via adsorption because of dispersion of NPs in both the US and the US/stirring systems (Scheme 4-1). Fe particles in natural water are almost charged because there are Fe (hydro)oxides on the Fe surface that can be ionized. This surface charge is opposite in sign to that of the existing ionized PCP ($pK_a=4.75$) in common neutral pH, so there is an electrostatic attraction between the PCP anions in solution and the generally positive Fe (hydro)oxides on the surface of Pd/Fe NPs (Scheme 4-2). The same interactive force attracts PCP anions and chlorides that are released from PCP near a positively charged Fe surface in water. The PCP adsorption on the Pd/Fe NPs surface also increases when the particle size decreases for systems using US irradiation. Kim et al. (2000) also noted that PCP loss occurred during ZVI and bimetallic ZVI treatments because of strong sorption on the ZVI, rather than by dechlorination.

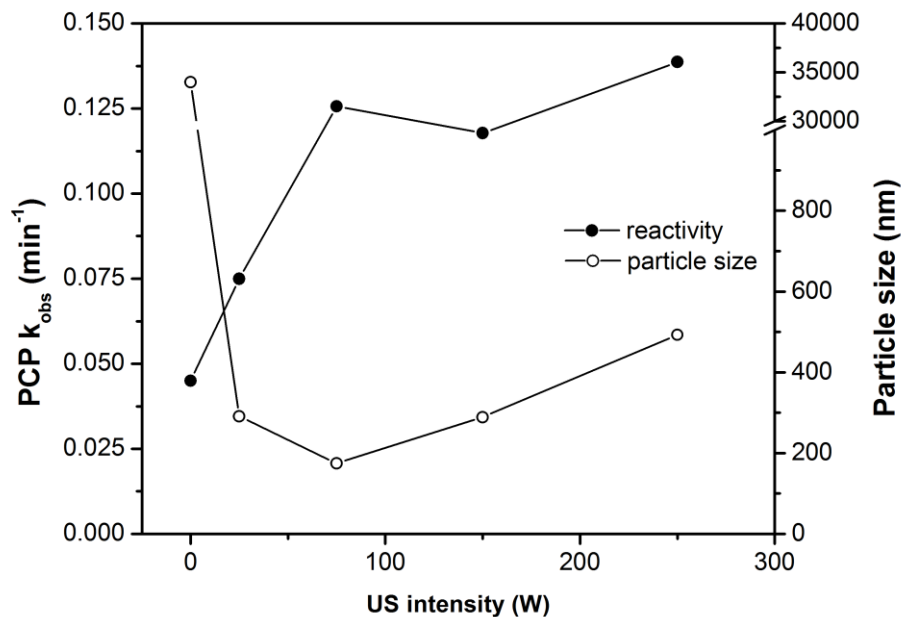


Figure 4-6. The effect of the US irradiation intensity on the removal of PCP and the particle size of Pd/Fe NPs. PCP initial concentration was 7.2 mg/L, Fe dosage was 4.5 g/L and Pd content was 0.1 wt%. US output intensity was 75 W during US irradiation.

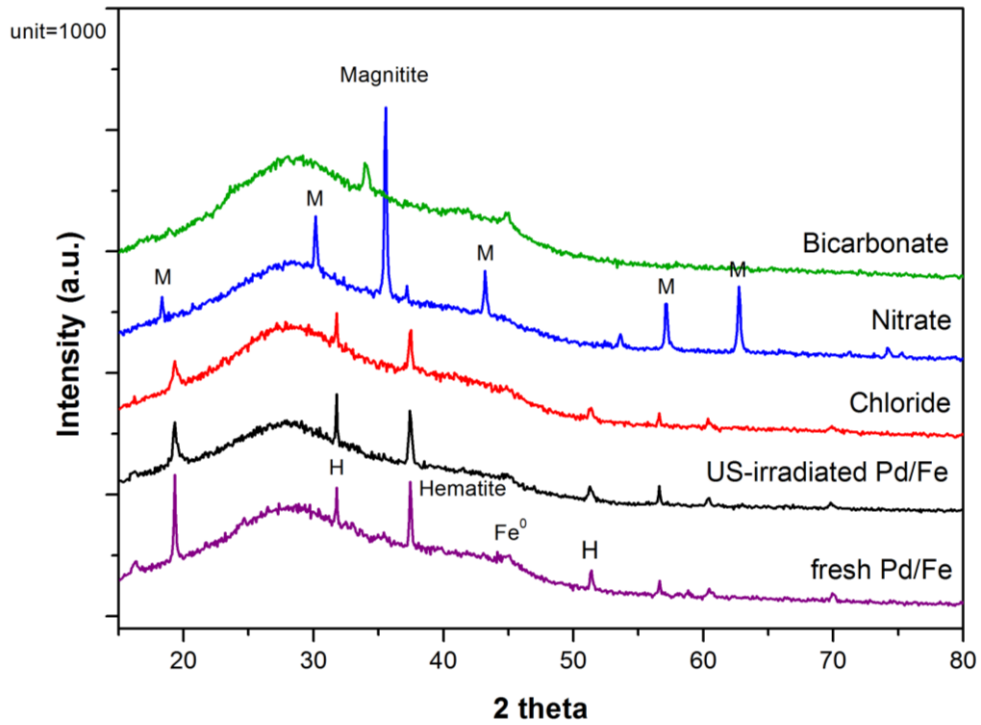
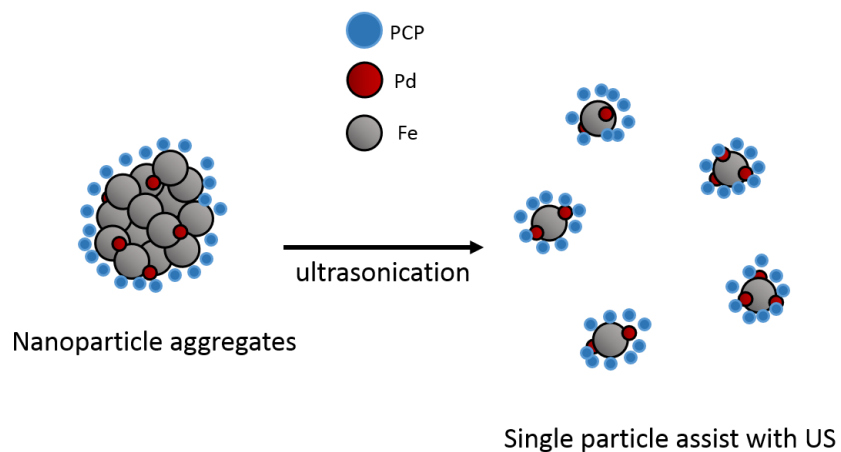
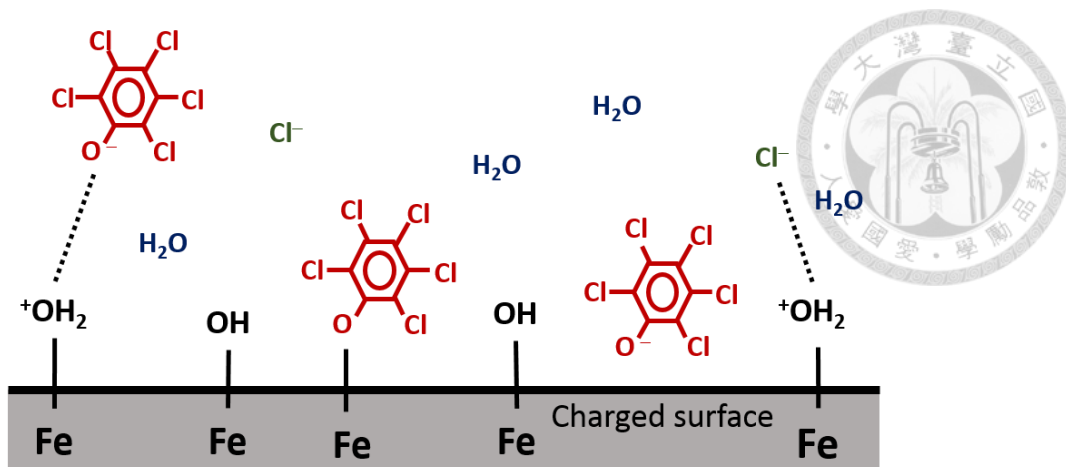


Figure 4-7. XRD spectra of Pd/Fe NPs under various conditions. US output intensity was 75 W. Anion concentration was 10 mM in the anion systems. Fe dosage was 4.5 g/L and Pd content was 0.1 wt%.



Scheme 4-1. The interaction between contaminants and nano-aggregates or well-dispersed NPs.



Scheme 4-2. A positively charged Fe (hydro)oxide surface of Fe nanoparticle in water attracts anionic species including PCP^- to the near-surface water.

4.1.3 The effect of Pd doping on the removal of PCP by Fe NPs in the US/stirring system

The addition of Pd onto Fe NPs increased both the removal rate and the degradation efficiency of PCP as compared to NZVI (Figure 4-8a). For the US/stirring system, when the Pd loading increased from 0 to 0.20 wt% of Fe NPs, k_{obs} for PCP gradually increased from 0.038 to 0.140 min^{-1} . More than 90% PCP was removed by Pd/Fe NPs with different amounts of Pd doping after 40 minutes in the US/stirring system. Most of the PCP was adsorbed on the Pd/Fe surface and only 12% of PCP was further degraded in the presence of 0.05 wt% Pd (Figure 4-8b). When the Pd doping increased to 0.20 wt% of Fe, the degradation efficiency of PCP increased to around 30% but the adsorption efficiency decreased to 60%.

The dechlorination rate constants and the dechlorination efficiencies for PCP for Pd/Fe NPs with different Pd contents were shown in Figure 4-9. The dechlorination rate constants, which were calculated from the release of chloride and the pseudo-first order kinetics,

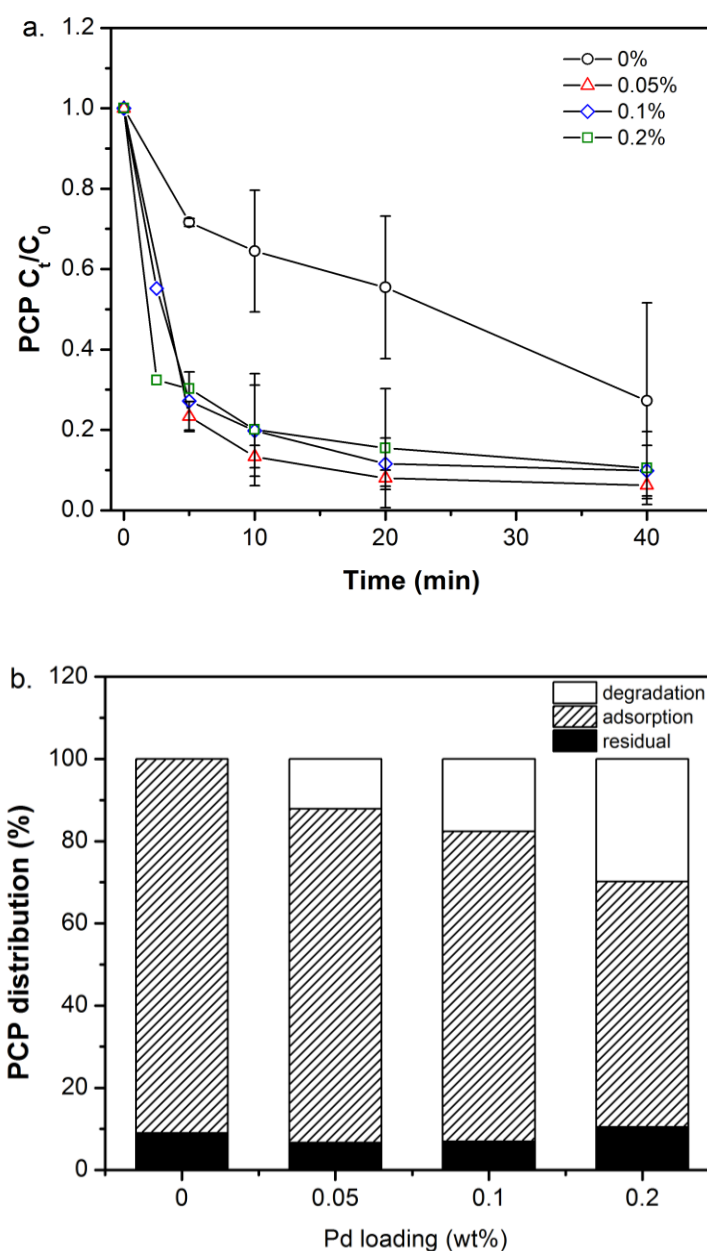


Figure 4-8. (a) The effect of Pd content on the removal kinetics of PCP by Pd/Fe NPs in the US/stirring system and (b) the PCP distribution after reacted with Pd/Fe NPs for 40 minutes. PCP initial concentration was 7.2 mg/L and Fe dosage was 4.5 g/L. The stirrer was set at 120 rpm, US output intensity was 75 W during US irradiation. The error bar in Figure 4-8 represent the standard error of an average over duplicated batch experiments.

increased from 0.002 to 0.006 min^{-1} when increased the Pd content from 0.05 wt% to 0.20 wt% of Fe (Figure 4-9a). As no significant dechlorination of PCP was observed for NZVI without the Pd content, the well-dispersed Fe NPs removed PCP by adsorption onto the surface of Fe NPs. There was also a strong linear relationship between the Pd doping and the dechlorination efficiency ($R^2=0.968$) of well-dispersed Fe NPs (Figure 4-9b). The dechlorination of PCP increased from 12% to 30% when increased the Pd content from 0.05 wt% to 0.20 wt%. As the Pd content increased, more hydrogen adsorbed onto the Pd during Fe corrosion and increases the reactivity (Cheng et al., 1997). Fe oxidation was in greatly speeding the oxidation of Fe by the galvanic contact between Pd and Fe (Cheng et al., 1997; Cwiertny et al., 2006; Yan et al., 2010).

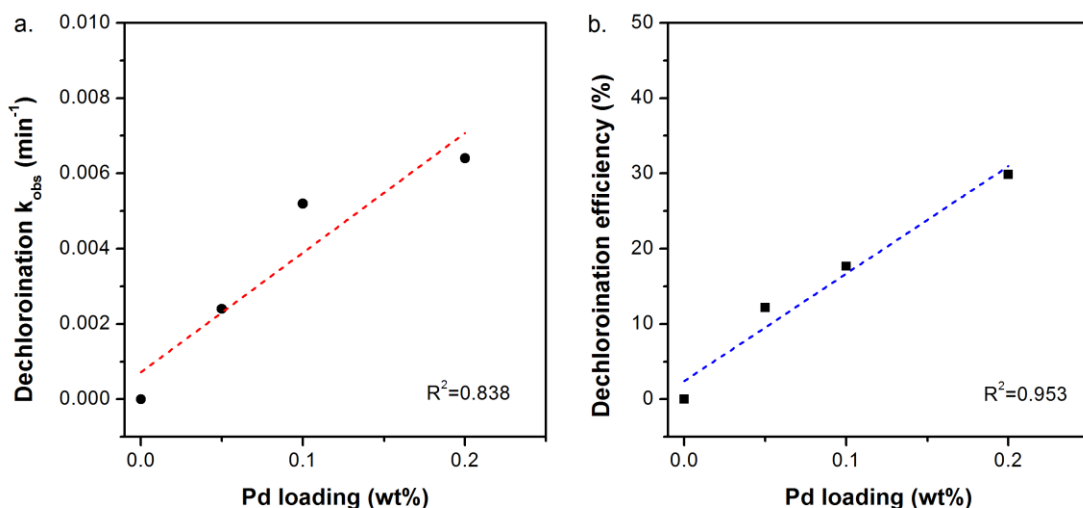


Figure 4-9. The effect of Pd content on (a) the dechlorination reaction rate and (b) the dechlorination efficiency of PCP by Pd/Fe NPs under the US/stirring system. PCP initial concentration was 7.2 mg/L and Fe dosage was 4.5 g/L.

4.1.4 The effect of anions on the removal of PCP by Pd/Fe NPs in the US/stirring system

Three common electrolytes, NaCl, NaNO₃ and NaHCO₃, were applied to investigate the effect of anion on the removal of PCP by using well-dispersed Pd/Fe in the US/stirring system (Figure 4-10a). In the presence of chloride, k_{obs} for PCP increased slightly from 0.120 min⁻¹ to 0.160 min⁻¹ when the chloride concentration increased from 5 mM to 10 mM. As compared to the control (pure water) system, the reaction rate and the dechlorination efficiency enhanced slightly in the presence of chloride (Figure 4-10b and Figure 4-11). In general, Cl⁻ promotes Fe corrosion and increases the reactivity of granular Fe toward chlorinated compounds (Devlin and Allin, 2005; Gotpagar et al., 1999; Johnson et al., 1998). However, Cl⁻ does not affect the reactivity of Pd/Fe NPs in a well dispersion system.

In the presence of NO₃⁻, most of PCP was removed in 40 minutes (Figure 4-10a). When nitrate concentrations were 5 mM and 10 mM, k_{obs} were found to be respectively 2.6- and 5.5-times magnetite higher than the control system. NO₃⁻ generally inhibits the reduction power of Fe NPs because it competes electrons with chemicals that have a high oxidation state, such as halogenated compounds. Once NO₃⁻ obtains electrons from the Fe surface, it reduces to NO₂⁻ and NH₄⁺. NO₃⁻ was almost transformed by Pd/Fe NPs and further reduced to NH₄⁺, in which approximately 72% and 63% of NO₃⁻ transformation were measured in the presence of 5 mM and 10 mM NO₃⁻, respectively. The NO₃⁻ transformation by Fe was also a corrosive process that caused more Fe (hydro)oxides to form a passive layer on the Fe surface. According to the XRD spectra, the specific peaks for zerovalent metals were almost completely disappeared and more peaks for Fe oxides were found as magnetite on the Pd/Fe surface in the presence of NO₃⁻ (Figure 4-7). The

adsorption fraction (about 89%) of PCP was the highest among these anions while only approximately 10% of PCP was degraded in both concentrations. Since the electrochemical reduction of PCP is mediated in the range, -1.6 to -2.3V (Lin and Tseng, 1999; Ross et al., 1997), which is higher than the reduction potential of nitrate (0.88 V), the Pd/Fe surface reacts with the nitrate first and generates Fe (hydro)oxides. Therefore, the fast removal kinetics of PCP was mainly due to the adsorption or coagulation of PCP on these Fe oxides. This result suggested that nitrate did accelerate the removal rate of PCP by Fe NPs via adsorption.

For HCO_3^- , both the removal rate and the removal efficiency for PCP were significantly decreased in the same dispersion system (Figure 4-10). The degradation and the adsorption fractions were less than those for other anionic media and the control system (Figure 4-11). The presence of high concentration of Fe^{2+} in carbonate-bearing water formed ferrous carbonates, according to eq. 4-1.



In natural groundwater, ferrous carbonate (the solubility limit at room temperature and ionic strength I was 0 is reported to be in the range from 3.72×10^{-11} to $9.33 \times 10^{-12} \text{ mol}^2/\text{L}^2$ (Sun et al., 2009)) controls the concentration of Fe^{2+} at pH values below 10.5 in solution. Instead of FeHCO_3^+ and other carbonate complexes (Singer and Stumm, 1970). Therefore, Fe carbonate precipitates may block the reactive and attachment sites for PCP on the Pd/Fe surface. There was no significant peak for metal oxides on the Pd/Fe surface (Figure 4-7), suggesting the formation of sediments of amorphous Fe carbonate. These inner-sphere complexes form passivation layers that inhibit the

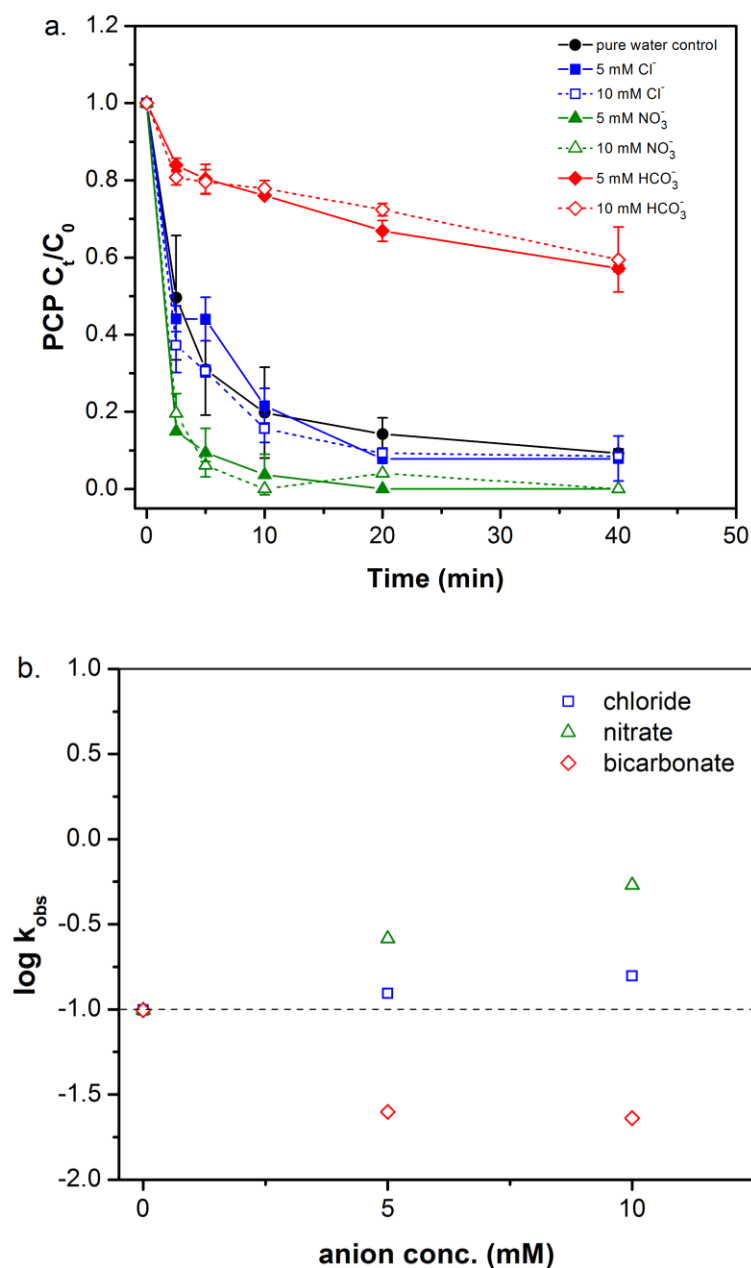


Figure 4-10. (a) The effect of anions on the removal of PCP by Pd/Fe NPs in the US/stirring system. (b) The relationship between the reaction rate constants and the anion concentrations. PCP initial concentration was 7.2 mg/L, Fe dosage was 4.5 g/L and Pd content was 0.1 wt%. US output intensity was 75 W during US irradiation. The error bar in Figure 4-10 represent the standard error of an average over duplicated batch experiments.

adsorption and degradation of PCP by Pd/Fe NPs (Agrawal et al., 2002; Phenrat et al., 2007). The solution pH was also found to increase from 5.4 to 8.9 in the presence of 10 mM HCO_3^- . As the chemical reduction of polychlorinated aromatic compounds by NZVI favors acidic conditions (Shih et al., 2009), this high solution pH that buffered by hydrogen carbonate would also decrease the removal rate of PCP by Pd/Fe NPs.

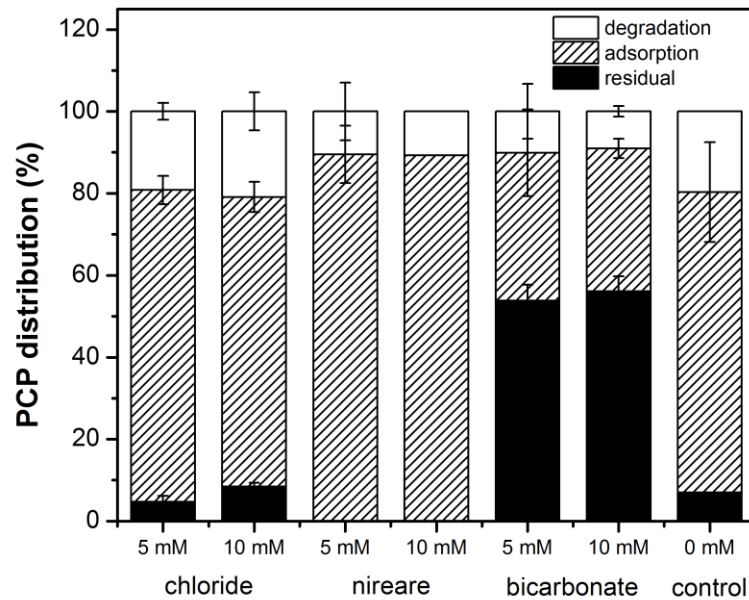


Figure 4-11. The PCP distribution after reacted with Pd/Fe NPs in the presence of anions under US/stirring system after 40 min. The data was collected from Figure 4-10a.

4.2 Well-suspended Fe NPs by the chemical dispersion method

Unlike the physical dispersion methods mentioned previously, chemical additives, such as polyelectrolytes, can alter the surface properties of Fe NPs to prevent self-aggregation. The compositions of functional groups in polyelectrolytes have been proved that they can stabilize the Fe NPs in suspensions and silica columns under different conditions. For this reason, the investigation about the catalytic behavior of these polyelectrolyte stabilized Fe NPs is needed. In previous studies, CMC-stabilized Fe NPs has shown its ability to treat halogenated organic compounds effectively (He et al., 2010; He and Zhao, 2008; Joo and Zhao, 2008), therefore the reaction mechanism of CMC-Fe is going to be explored in this section, then to examine the influence of anions and ion strengths on the reactivity of CMC-Fe.

4.2.1 Characteristics of CMC-stabilized Fe NPs

The morphology of the CMC-stabilized Fe was determined by TEM (Figure 4-12), in which the individual particles of the CMC-stabilized Fe NPs appear spherical. The particle size of CMC-Fe NPs was determined from TEM images using ImageJ. Based on the analysis of 43 particles, the mean size of CMC stabilized Fe NPs was found to be 96.8 ± 23.4 nm. There were many small unshaped NPs packed together on the Fe surface with a size of approximately 5-10 nm (see the small TEM image in Figure 4-12a). A similar phenomenon was also observed by Lin et al. (2010). The packing was likely the self-assembling of amorphous primary Fe into spherical secondary Fe as a result of the excess CMC and Ostwald ripening (Lin et al., 2010; Zhong et al., 2006). The metal surfaces also reflected a CMC-coating artifact instead of amorphous Fe (see both TEM images in Figure

1b and c) (Lin et al., 2010). The Fe surface was negatively charged (-16.3 to -30.1 mV) when the pH ranged between 3.4 and 10 (Figure 4-13), explaining the stability of the CMC-stabilized Fe NPs. The attached CMC stabilizer molecule provides a strong inter-particle electrostatic force and/or steric repulsion force to overcome the attractive van der Waals and magnetic forces between the particles (He and Zhao, 2005; 2008; He et al., 2007). Therefore, the CMC molecules reduce nanoparticle aggregation and maintain a great specific surface area of the finer NPs, which results in greater nanoparticle reactivity than for the nanoaggregates.

The normalized Fe K-edge XANES results were analyzed for fresh bare Fe NPs and the CMC-stabilized Fe (Figure 4-14a). An obvious absorbance feature representing Fe^0 (7112-7115 eV) existed in both the fresh CMC- Fe^0 and the CMC-Ni/Fe, and another broad feature between 7128 eV and 7134 eV for the CMC-stabilized Fe indicates the existence of Fe^{2+} and Fe^{3+} . In general, the higher oxidation state of an element shifts to higher energy in the position of the XANES absorption edge. The Ni K-edge XANES spectra of the bare Ni/Fe and CMC-Ni/Fe were shown in Figure 4-14b. Pre-edge spectra at 8320-8350 eV for the nickel and a weak feature at 8333 eV (Ni^0) of the bare Ni/Fe and CMC-Ni/Fe indicate that the reduction states of the Ni on the bare Ni/Fe and the CMC-Ni/Fe were not all zerovalent. Therefore, the spectra of the samples located between the reference spectra of Ni^0 and Ni^{2+} indicated a partial reduction; some of Ni remained in the Ni^{2+} state. The XANES results summarize that the lab-synthesized CMC-Ni/Fe NPs contain partially metallic Fe^0 and an amount of iron oxides when compared with bare Fe NPs. The oxidation state also showed Ni^{2+} reduced to Ni^0 in the CMC-Ni/Fe, which was similar to the bare Ni/Fe.

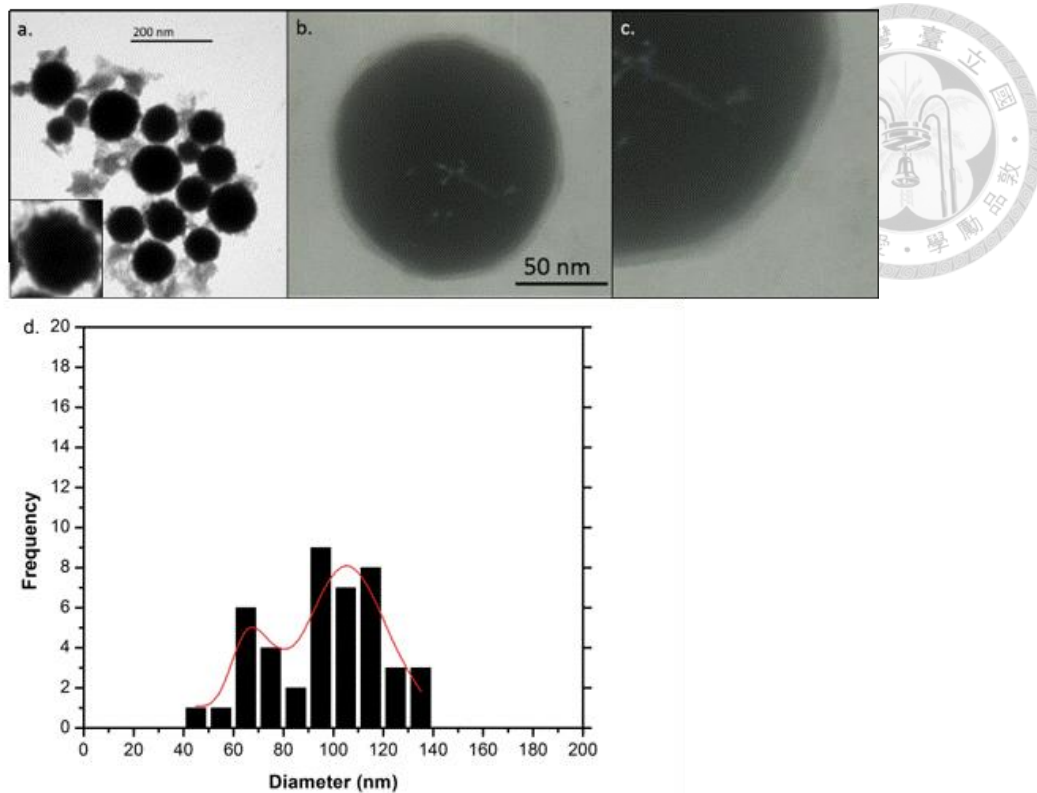


Figure 4-12. TEM images and size distribution of CMC stabilized Fe NPs. The size distribution was calculated using ImageJ and OriginLab software (particle number=43).

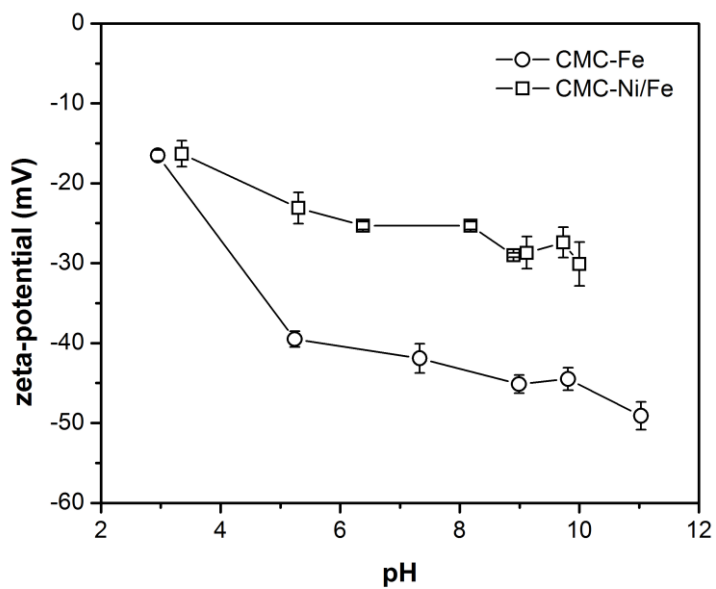


Figure 4-13. The zeta-potential of the CMC-Fe and CMC-Ni/Fe versus pH.

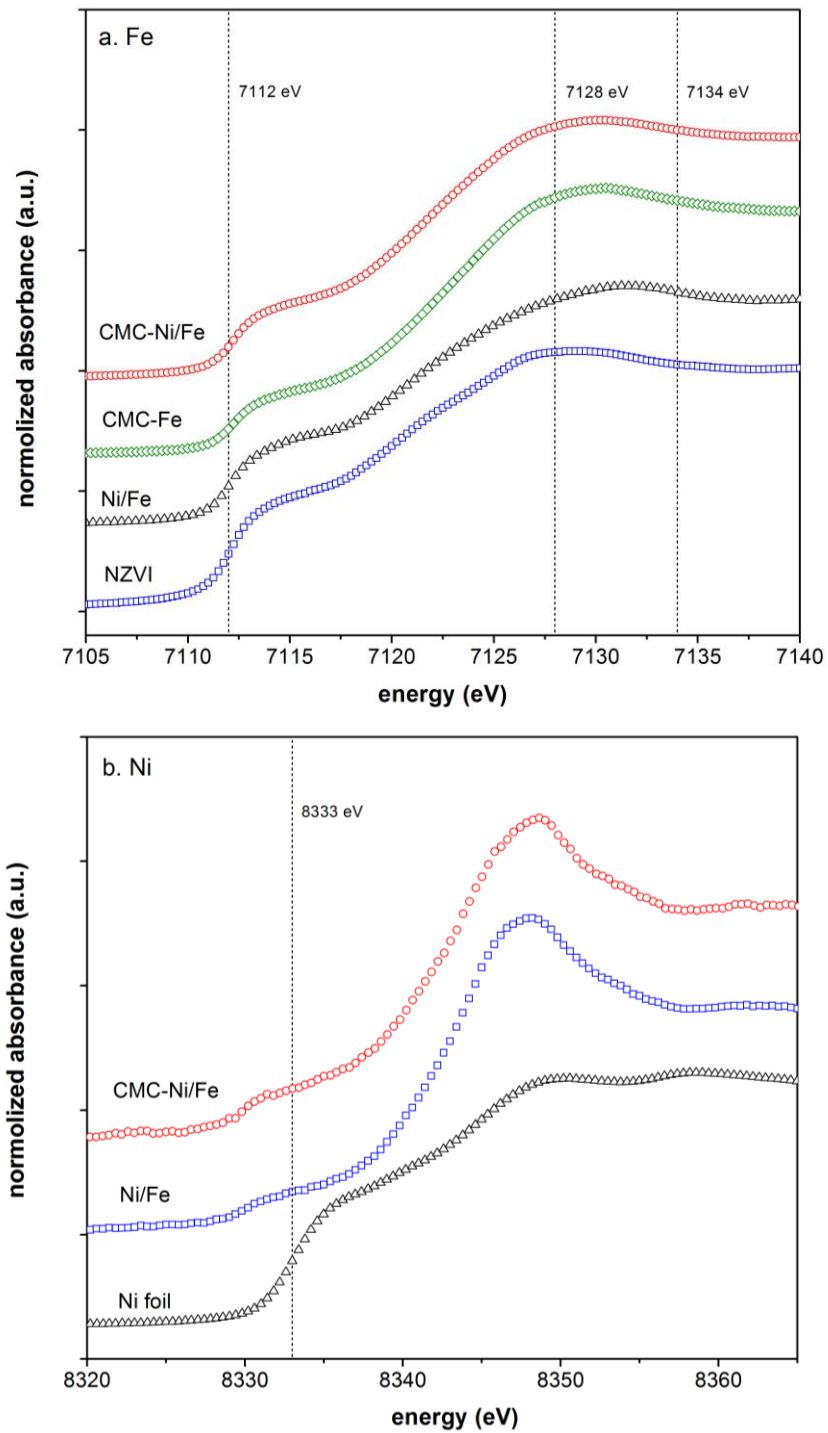


Figure 4-14. (a) Fe K-edge and (b) Ni K-edge of XANES spectra of the bare Fe NP and the CMC-stabilized Fe NPs.

4.2.2 The removal of DBDE by CMC-Ni/Fe NPs

In our previous study (Lin, 2012), PCP cannot be removed by both CMC-Fe and CMC-Ni/Fe due to the repulsing force between deprotonated PCP and CMC under the neutral pH condition (Figure S3). To examine the catalytic behavior of CMC-Fe toward halogenated organic compounds, DBDE was chosen as the target compound in this chapter.

The removal of DBDE by both the CMC-Fe and the CMC-Ni/Fe NPs was observed in the beginning for approximately 60 minutes (Figure 4-15a). Without Ni doping, no degradation was found in the CMC-Fe. The DBDE removal efficiency was only 20%, which is primarily attributed to an adsorption process on the CMC-Fe surface (Figure 4-15b). k_{obs} of the DBDE was 0.042 min^{-1} by CMC-Fe⁰. Compared with our previous result, the CMC-Fe particles enhanced the reaction rate by approximately 7 times that of the bare NZVI (Shih and Tai, 2010). The properties of the CMC coating on the Fe surface could enhance the colloidal stability and also influence the attachment between the DBDE molecules and the Fe reactive sites.

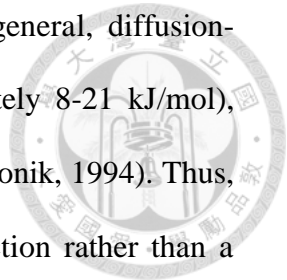
In contrast, the k_{obs} value increased from 0.140 to 0.220 min^{-1} with an increase in the Ni loading from 0.5 to 5.0 wt% (Figure 4-16). The bromide cannot be measured by ion chromatography (IC) in the CMC systems because the high CMC concentration in this study would block the IC column and underestimate the debromination efficiency, so that the degradation efficiency was calculated from the difference between the removal and adsorption efficiencies. The DBDE degradation increased from 0.9% to 11% with an increase in the Ni loading from 0.5 to 5 wt% of in the CMC-Ni/Fe NPs (Figure 4-16). The degradation using Fe NPs proceeded through hydride transfer from Ni; whereas, the formation of a galvanic cell (Fe²⁺-Ni⁰) in the stored NPs generated hydroxyl radicals from

water in a non-Fenton reaction (Bokare et al., 2007). When the Ni catalyst was present on the CMC-Fe NPs, an approximating linear model of the k_{obs} value with the Ni loading content from 0.1% to 1% was estimated; however, with the Ni loading in CMC-Fe NPs increased to 5.0%, the k_{obs} value increased to a stable value (Figure 4-16). According to the Fe K-edge XANES spectra, the oxidation state of the aged CMC-Ni/Fe was higher than for the fresh one, indicating that the corrosion reaction occurred on the Fe surface even in the presence of the CMC coatings on the Fe surface (Figure 4-17). This result also confirmed that the electrons transferred from the Fe to the DBDE molecules, further decomposed the DBDE and formed less-brominated byproducts.

4.2.3 The reaction mechanism of DBDE by CMC-Ni/Fe


To understand the reaction mechanisms of the CMC-stabilized Fe NPs, the reaction was carried out under different temperatures and initial pH values. Figure 4-18a shows the effects of temperature on the removal kinetics of DBDE. The reaction temperature had a positive effect on the removal kinetics of DBDE. The calculated k_{obs} values at 5, 25, and 45 °C were 0.046, 0.200 and 0.350 min⁻¹, respectively. The results showed that the removal rate of DBDE increased with an increase in the temperature. This was caused by the high number of effective collisions of the DBDE molecules at the CMC-Ni/Fe NP surface at high temperatures.

The activation energy (E_a) is determined by the Arrhenius equation (eq. 3-9) to describe the relationship between the rate constants and temperatures (Figure 4-18b), thus with the slope of -4533, the E_a was calculated as 37.7 kJ/mol. The effect of temperature on the reaction rate can be used to identify the rate-limiting step, which may involve a chemical



reaction on the surface or the physical diffusion of a reactant. In general, diffusion-mediated reactions in solution require relatively low E_a (approximately 8-21 kJ/mol), whereas surface-mediated reactions require high E_a (>29 kJ/mol) (Brezonik, 1994). Thus, the E_a obtained in this study suggesting that a surface chemical reaction rather than a diffusion-mediated reaction was the rate-limiting step in the removal of DBDE. A similar result was also observed by Singh et al. (2012); the E_a for the removal of hexachlorocyclohexane by CMC-Pd/Fe was approximately 33.7 kJ/mol. Surfactants, such as CMC, not only enhance the colloidal stability but also alter the surface properties of the metal NPs and affect their interactions with contaminants by influencing the sorption and desorption processes (Kim et al., 2009; Phenrat et al., 2007; Tiraferri et al., 2008). The use of surfactants could enhance the water solubility of hydrophobic nonionic organic compounds by the successive micellization of the heterogeneous monomer species (Kile and Chiou, 1989). The diffusion process whereby the DBDE from a solution phase to the Fe surface may be induced by a CMC layer on the Fe surface. However, the CMC layer could also reduce the electron transfer from the surface to the target compound molecules (Phenrat et al., 2009).

On the other hand, it is generally believed that the pH value could affect the behavior of CMC-stabilized Fe NPs. The removal efficiency and removal rate increased with an increase in the pH value (Figure 4-19a). The k values were 0.068, 0.098, and 0.160 min^{-1} when the initial pH values of the reaction solutions were at 5, 8.5, and 10, respectively. Meanwhile, the average particle size (as z-average) of the CMC-Ni/Fe NPs that measured by DLS decreased from 175 nm to 85 nm with an increase in pH from 5 to 10 (Figure 4-19b). Liu and Lowry (2006) noted that a decrease in the solution pH would increase the



H₂ evolution and further produce Fe⁰ in the particles via a corrosion process. Our previous research shows a negative regression in the *k* values with the bare NZVI, accompanied by a small coefficient (Shih and Tai, 2010). It was a weak pH dependence in the DBDE removal by bare NZVI due to the rapid reaction kinetics on the bare Fe surface. In contrast, there was a complete positive correlation between the rate constants and the pH values, revealing that the influence of the pH value on the surfactant stabilized Fe NPs in the presence of CMC coatings on the Fe surface was oppositely correlated. The p*H*_{zpc} of CMC is approximately 2.0 (Yan et al., 2011) and the *pK_a* of CMC is in a range of 4.0 to 5.1 (Girard et al., 2002; Guzenko et al., 2011). Changes in the pH can result in the dissociation of these carboxyl groups of CMC, thus the negative surface charge of the CMC-Ni/Fe increased when the pH increased (Figure 4-13). The conceptual scheme of the CMC-Fe NPs indicated that CMC was coated on the Fe surface with brush structures which can provide steric stabilization to prevent aggregates (Lin et al., 2010). The carboxyl groups of the CMC are protonated under acidic conditions, and reduce the colloidal stability. At a high pH value, the carboxyl groups are fully deprotonated, resulting in a smaller particle size. The same results were reported by Wang and Wang (2010). In addition, CMC was a stabilizing and efficient reducing agent in alkaline media (Abdel-Halim et al., 2010). The strong pH dependence of CMC was the most influential factor in the tendency of DBDE removal at various pH values, demonstrating the usefulness of CMC-Ni/Fe NPs in general neutral to alkaline conditions.

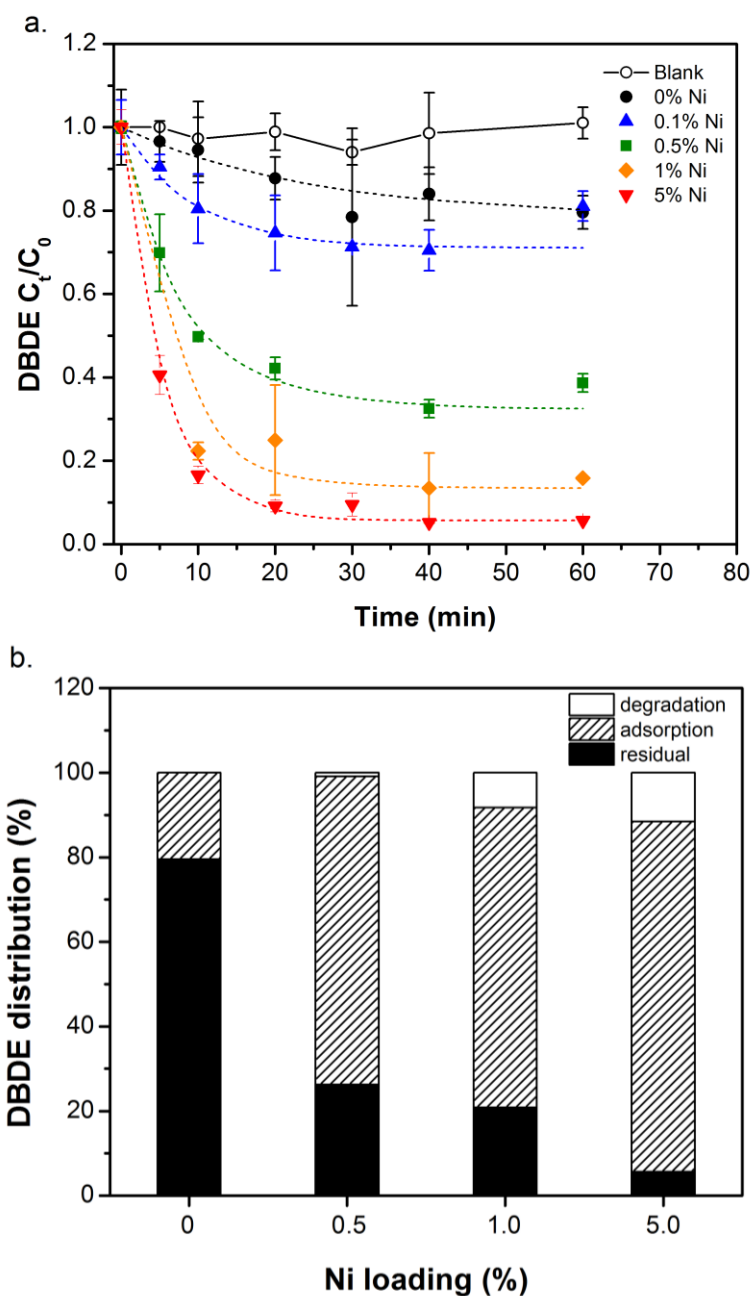


Figure 4-15. (a) The effect of the Ni loading on the removal of DBDE with the CMC-Ni/Fe and (b) the degradation, adsorption, and residual fractions of DBDE reacted with the CMC-Ni/Fe. The initial concentration of DBDE was 10 mg/L, Fe dosage was 5.0 g/L, and CMC concentration was 4.2 g/L. The error bar in Figure 4-15 represent the standard error of an average over duplicated batch experiments.

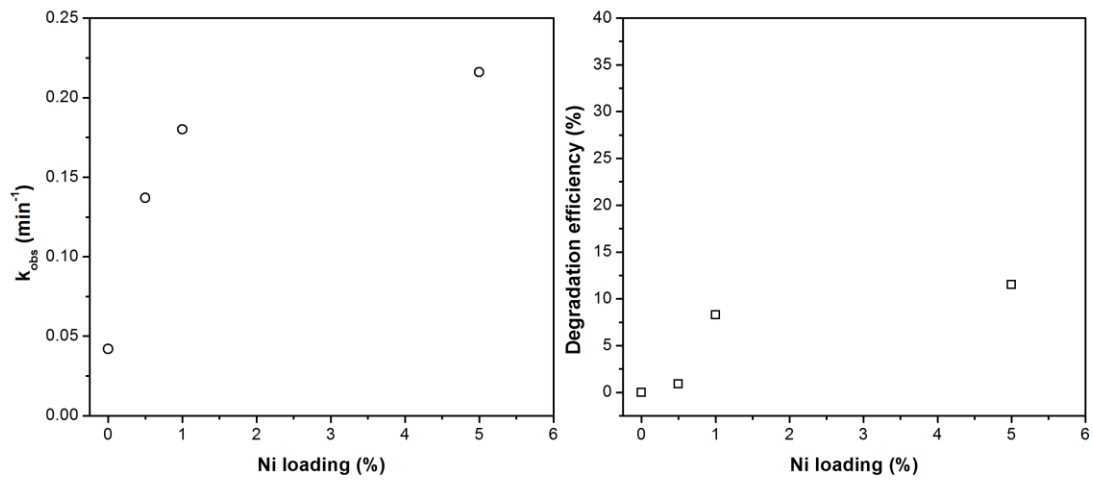


Figure 4-16. The removal efficiency and the degradation efficiency of DBDE by the CMC-stabilized Fe NPs with different Ni content.

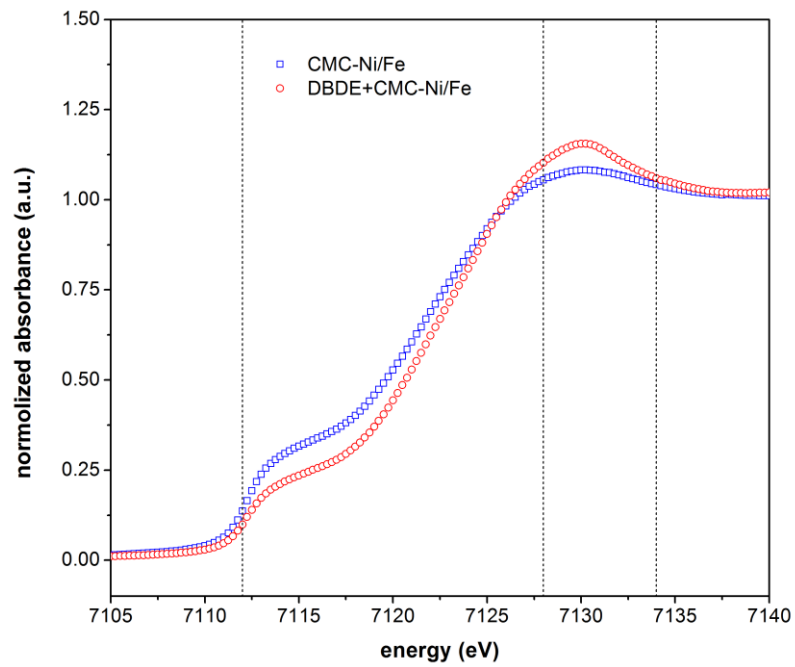


Figure 4-17. Fe K-edge of XANES spectra of the CMC-Ni/Fe.

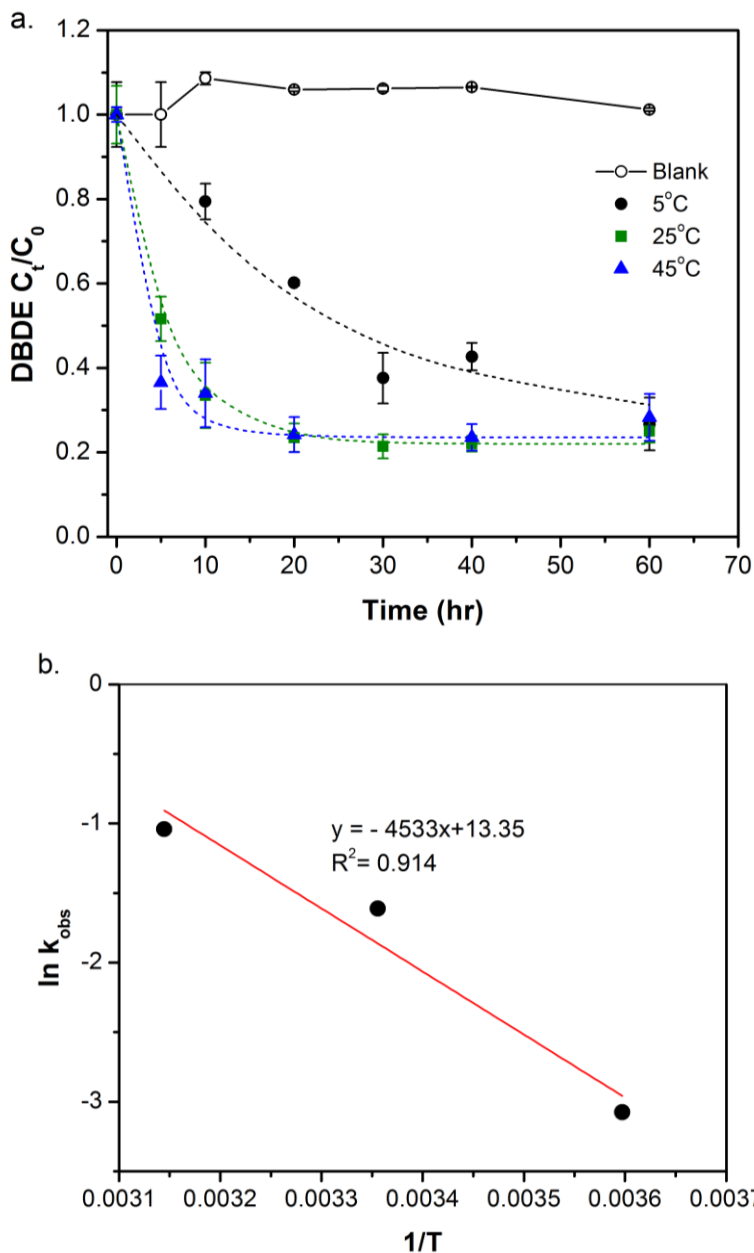


Figure 4-18. (a) The effect of temperature on the degradation of DBDE by CMC-Ni/Fe. (b) The plot of $\ln k_{obs}$ versus $1/T$ for the CMC-Ni/Fe. The initial concentration of DBDE was 10 mg/L, Fe dosage was 5.0 g/L, Ni/Fe was 0.5 wt %, and CMC concentration was 4.2 g/L. The error bar in Figure 4-18 represent the standard error of an average over duplicated batch experiments.

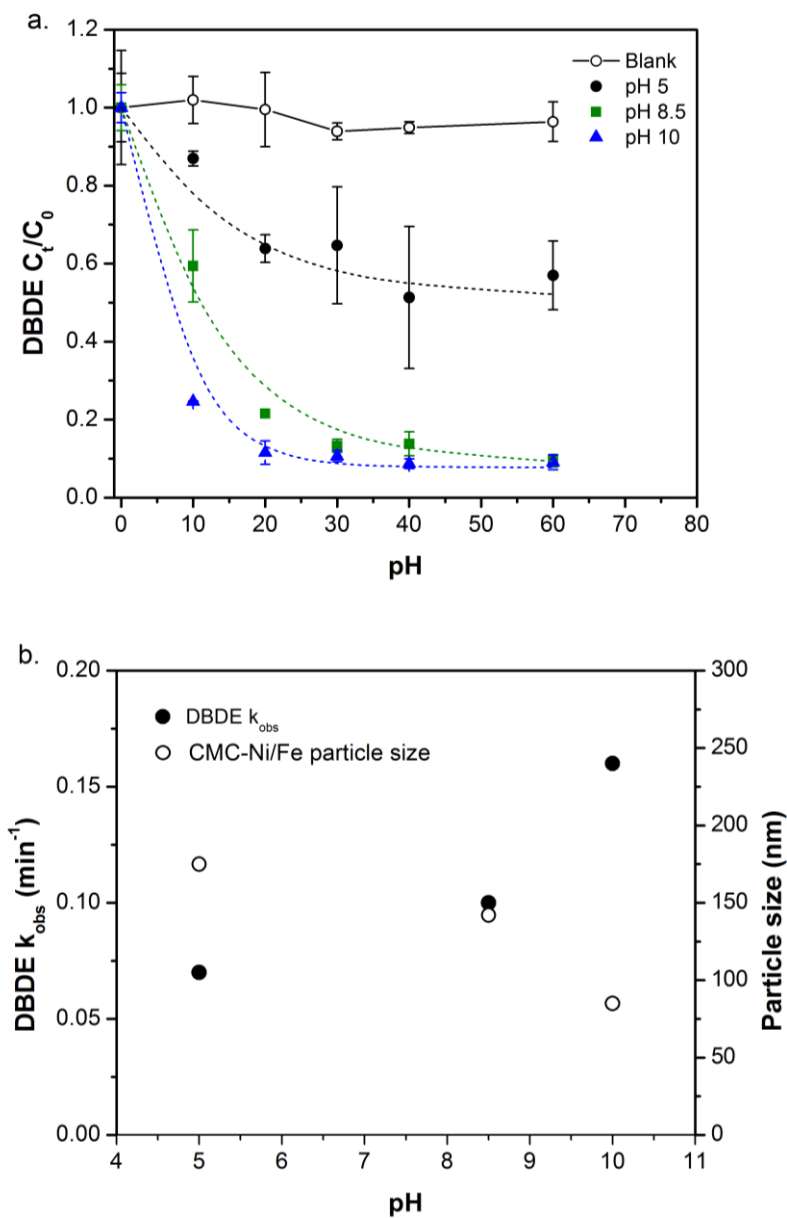
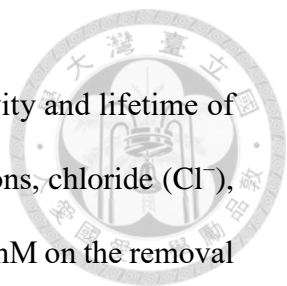


Figure 4-19. (a) The effect of pH on the removal of DBDE by CMC-Ni/Fe. (b) The relation between k_{obs} and the particle size under different pH conditions. The initial concentration of DBDE was 10 mg/L, Fe dosage was 5.0 g/L, Ni/Fe was 0.5 wt %, and CMC concentration was 4.2 g/L. The error bar in Figure 4-19 represent the standard error of an average over duplicated batch experiments. The average particle size (as z-average) was measured using DLS.

4.2.4 The effect of anion on the reactivity of CMC-Ni/Fe NPs



Electrolytes commonly found in groundwater may affect the reactivity and lifetime of bare Fe NPs. For CMC-Ni/Fe NPs, the influence of three common anions, chloride (Cl^-), nitrate (NO_3^-), and bicarbonate (HCO_3^-), with concentration of 1 to 10 mM on the removal of DBDE was shown in Figure 4-20. The DBDE removal efficiency ranged from approximately 81% to 92% when the Cl^- concentration increased from 1 to 10 mM. The k_{obs} values were approximately 0.200, 0.210, 0.250, and 0.260 min^{-1} when the Cl^- concentrations were 0, 1, 5, and 10 mM, respectively, indicating that the removal rate and removal efficiency slightly increased in the presence of a high concentration of Cl^- (5-10 mM) (Figure 4-21). Compared with the pure water system (DBDE removal rate constant = 0.20 min^{-1}), 1 mM NO_3^- hindered the DBDE reaction rate by approximately 1.8-fold. k_{obs} increased from 0.110 to 0.320 min^{-1} with an increase in the NO_3^- concentration from 1 to 10 mM. The inhibition of the debromination of DBDE in the presence of NO_3^- can occur as a result of the competition between NO_3^- and DBDE. Once NO_3^- is reduced by the CMC-Ni/Fe NPs, the generated Fe (hydro)oxides on the surface coagulate with the organic molecules (Tso and Shih, 2015), which contributes the removal of DBDE.

The k values of DBDE were in the range of 0.180 to 0.200 min^{-1} in the presence of 1-10 mM HCO_3^- , revealing that HCO_3^- seemed to have no effect on the reactivity of the CMC-Ni/Fe NPs toward DBDE. The influence of anions was possibly caused by the passive layers, which can block the active sites on the Fe surface where the electron transfer takes place (Agrawal et al., 2002; Bi et al., 2009; Larese-Casanova and Scherer, 2008). However, with the coating of CMC on the Fe surface, the CMC-Ni/Fe NPs seemed unaffected by anions with concentrations of 1-10 mM, with the exception of NO_3^- . Cl^- and

HCO_3^- did not appear to affect the DBDE removal by CMC-Ni/Fe significantly; whereas, a high NO_3^- concentration slightly enhanced the reactivity of CMC-Ni/Fe in this research. XANES is also applied to explain the oxidation states of CMC-Ni/Fe in the presence of anions (Figure 4-22). The Fe K-edge XANES spectra show a shift with the presence of 10 mM NO_3^- as compare to the oxidation state of Fe in the 1 mM NO_3^- system. The smallest value of Fe^0 was shown on the CNC-Ni/Fe surface after reacting with NO_3^- and produced an insubstantial peak for Fe oxides. No obvious shift was observed in the presence of Cl^- and HCO_3^- even at a high concentration of 10 mM. In addition, for Cl^- and HCO_3^- , there was no specific peak on the CMC-Ni/Fe surface in the XRD analysis (data not shown), indicating that the CMC coating not only provides colloidal stability but also prevent the passivation of Fe in the presence of anions. Nevertheless, the Fe K-edge of the CMC-Ni/Fe reacted with 10 mM anions reflected that most of the Fe^0 was turned into Fe (hydro)oxides on the CMC-Ni/Fe after reacted with NO_3^- .

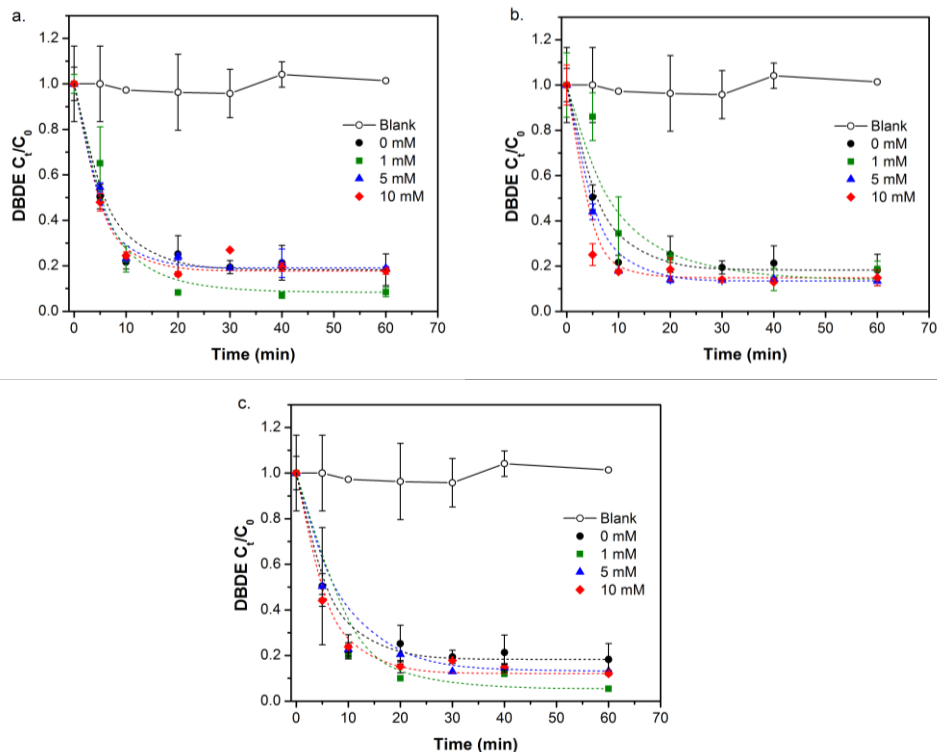


Figure 4-20. The removal kinetics of DBDE with the CMC-Ni/Fe in the presence of (a) chloride, (b) nitrate, and (c) bicarbonate. The initial concentration of DBDE was 10 mg/L, Fe dosage was 5.0 g/L, Ni/Fe was 0.5 wt %, and CMC concentration was 4.2 g/L. The error bar in Figure 4-20 represent the standard error of an average over duplicated batch experiments.

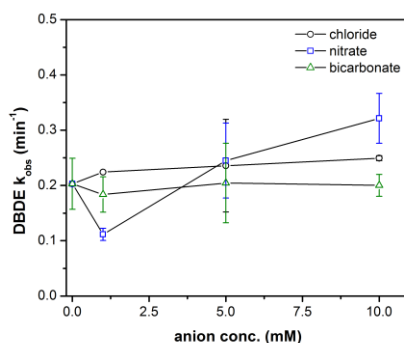


Figure 4-21. The reaction rate constants of DBDE by CMC-Ni/Fe in the presence of anions.

The values of k_{obs} obtained from fitting of the data in Figure 4-20.

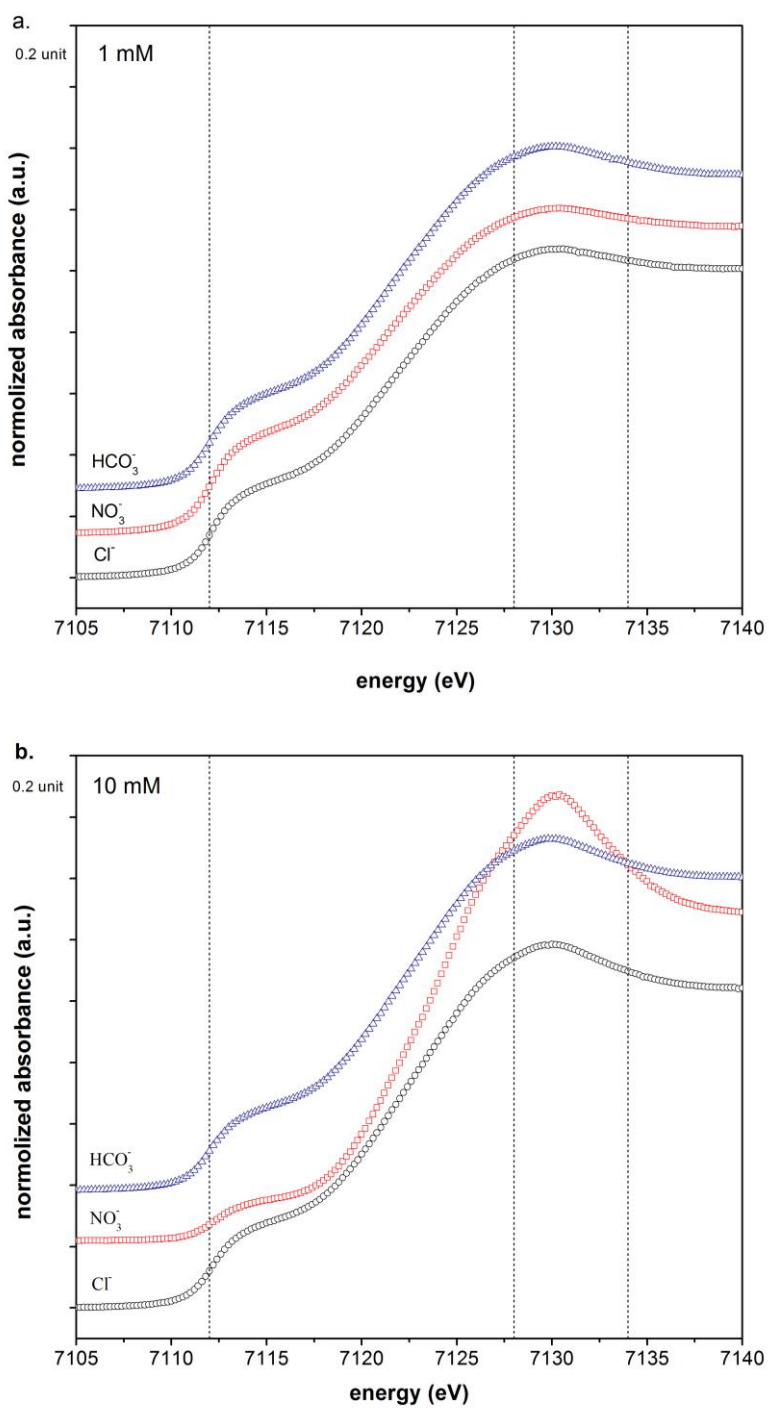


Figure 4-22. Fe K-edge of XANES spectra of the CMC–Ni/Fe in the presence of (a) 1mM and (b) 10 mM of anions.

4.3 Comparison of physical and chemical dispersion methods

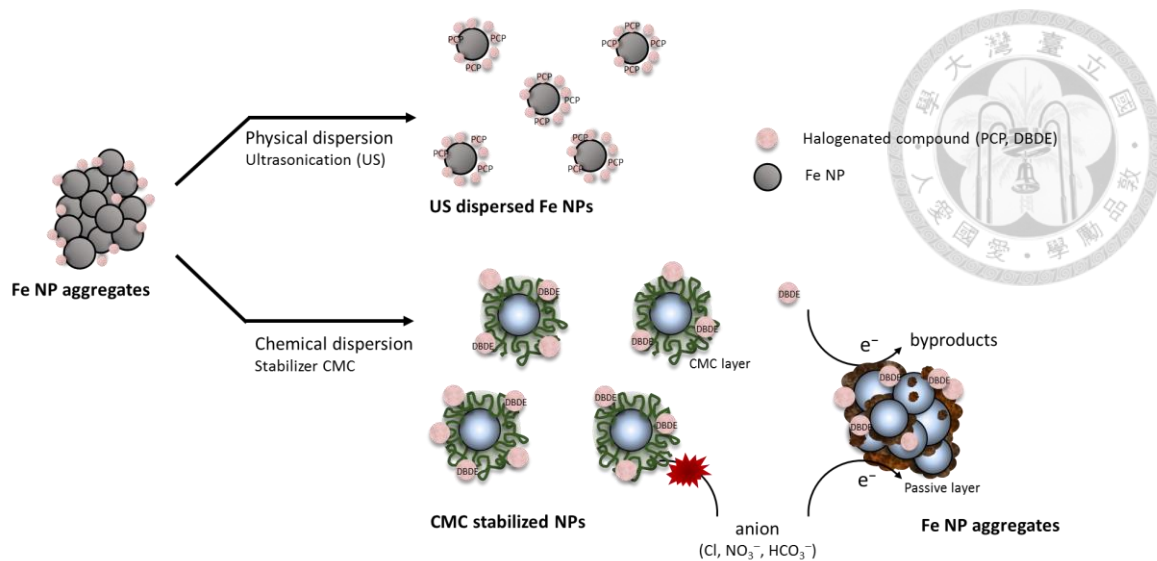
The application of the physical dispersion methods that mentioned in chapter 4-1, can study the catalytic behavior of Fe NPs in nanoscale toward halogenated organic compounds under various conditions. The chemical additive, CMC, supported Fe NPs, however, could be appropriate for the in-situ soil remediation (as described in chapter 4-2).

For bare Fe NPs, as large Fe NP aggregates became smaller, there was more surface area of the finer Fe NPs exposed for the reaction. Most of PCP was removed by well-suspended Pd/Fe NPs via the adsorption process (Scheme 4-3.). The CMC layer suspended Fe NPs very well and dispersed particles into individual particle instead of nanoparticle aggregates. Approximately 20% of DBDE was removed by CMC-Fe in this study while no significant removal was observed using NZVI by Fang et al. (2011). Therefore, well-suspended Fe NPs accelerate the adsorption rate on the Fe surface (Scheme 4-3.). With the coating of CMC on the Fe surface, the property of CMC layer could also enhance the solubility of organic contaminants on the stabilized Fe NPs but reduce the electron transfer from the surface on the other hand.

The study also offers an opposite view to that indicated by the effect of pH value on the reactivity of CMC stabilized Fe NPs. For bare Fe NPs, lower pH generally accelerates Fe corrosion and prevents the Fe oxide or hydroxide from forming on the Fe surface. However, when the pH reaches a certain level, the extensive corrosion of bare Fe NPs will lead to an excess of H₂ covering on the surface of Ni (Powell et al., 1995), and hindering the contact of DBDE with Ni/Fe NPs (Xie et al., 2014). A weak acid pH is more likely to promote the corrosion of Fe; at higher pH values, Fe NPs are apt to sediment and generate passive layers on the Fe surface, thus hindering the electronic transfer and the removal rate

would further decrease. For CMC-Ni/Fe NPs, the removal rate of DBDE increased with an increase in the initial pH values from pH 5 to 10, which resulted from that the pH-dependent property of carboxyl groups in the CMC molecules.

Electrolytes that are dissolved in the environment are an important influencing factor on the reactivity of Fe particles by (i) forming passive layers on the Fe surface (Agrawal et al., 2002; Kober et al., 2002) and (ii) decreasing the colloidal stability (Domingos et al., 2009). Fe NPs were suspended successfully by both the ultrasonication and the CMC coating. For the well-dispersed bare Fe NPs, the effect anions seem influence the stability and reactivity of bare Fe NPs when increased anion concentration to 10 mM (Figure 4-23). Cl^- only caused a small increasing in the removal kinetics; but NO_3^- ions were reduced by Pd/Fe NPs and generated more Fe (hydro)oxides, which further enhanced the adsorption of PCP from water. HCO_3^- significantly inhibited the removal of PCP because precipitates formed on the Fe surface and then blocked the adsorption and reaction sites. However, the removal rate of DBDE by CMC-Ni/Fe NPs did not change in the presence of anions with concentrations of 1-10 mM. CMC has been reported as a corrosion inhibitor (Khairou and El-Sayed, 2003; Umoren et al., 2010). Surfactants with their functional groups, formed complexes with metal ions and on the metal surface. These complexes occupy a large surface area, thereby coating the surface and protecting the metal from corrosive agents present in the solution. The CMC layers may hinder the attachment between anions and the Fe surface, thus in turn influencing the adsorption characteristics of the Fe surface, and also prolonging the reactivity of Fe NPs in the environment. This study verifies that the feasibility of using CMC-Ni/Fe NPs for the in-situ remediation.



Scheme 4-3. The reaction mechanisms of well-suspended Fe NPs in two dispersion systems.

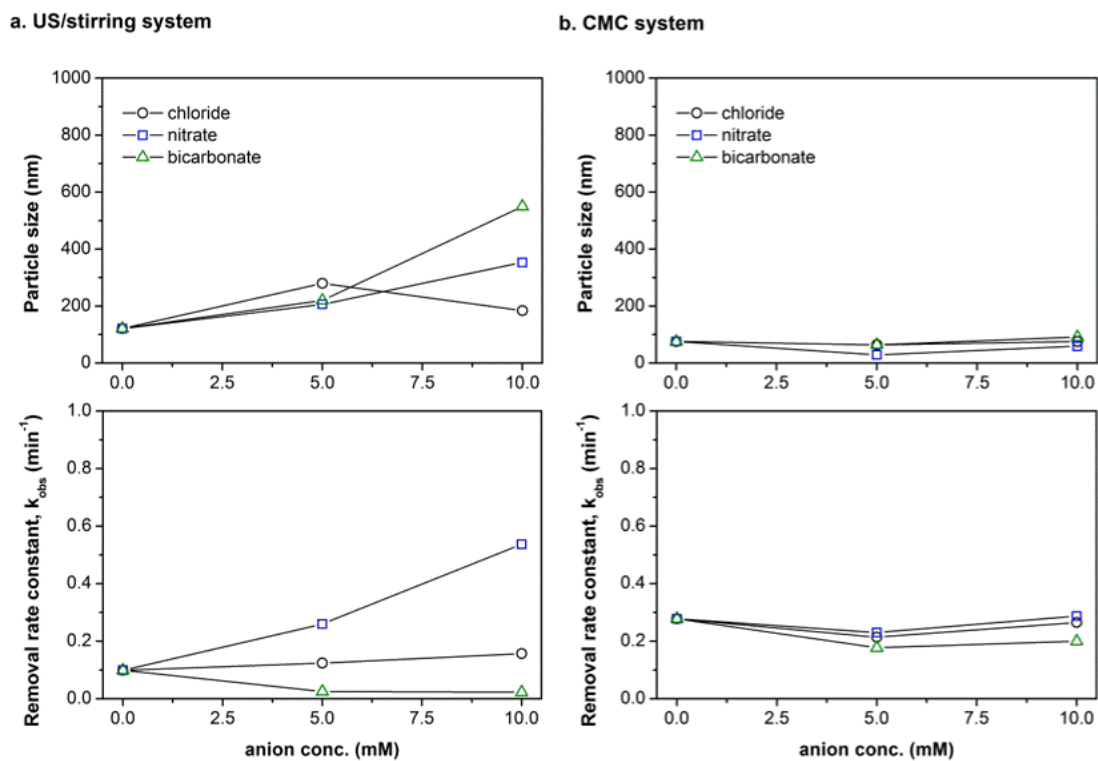


Figure 4-23. The particle size (as z-average) of Fe NPs and removal rate constant of target compounds in (a) the US/stirring system and (b) the CMC system.

4.4 The influence of organic ligands on the surface characteristics of ZVI

It has been noted that the simple carboxylic acids can enhance the reaction rates of ZVI via the dissolution of passive layer on the Fe surface. However, the influence of the carboxylic acid on the reactivity of Fe particles remains unknown. Here, we propose a hypothesis that the carboxylic acid not only refresh the Fe surface, but also the formation of Fe-complexes adsorbed on the Fe surface via a dissolution can further interact with pollutants. Thus, the effect of carboxylic acids with one to three carboxylic groups on the dechlorination of PCP by NZVI is investigated. The findings can be applied further to forecast and predict the results of sequential treatment with iron oxides in the presence of ligands.

Our previous study (Ou, 2012) pointed out that the reduction of PCP by NZVI did not occur in the absence of organic ligands (Figure S4). The removal rate of PCP by NZVI enhanced in the following order: oxalic acid (1.50 h^{-1}) > citric acid (0.49 h^{-1}) > \cong pure water. However, the reaction mechanism for ligands on the removal of PCP by NZVI is more complicated due to the characteristics of PCP varying with solution pH, and particle size may play an important role to affect the behavior of Fe NPs. Furthermore, due to the low reactivity of micro-scale ZVI or NZVI for PCP, TCE was chosen as the target contaminant in this study. In the following, micro-scale ZVI was applied to investigate the effect of carboxylic ligands on the removal of TCE.

4.4.1 The effect of ligand acids on the removal of TCE by ZVI

An equal molarity of 30 mM carboxylic groups (-COOH) for each carboxylic ligand, i.e. 30 mM FA, 15 mM OA and 10 mM CA, was applied for assessing the effect of

carboxylic ligand on the removal of TCE by ZVI. The effect of 30 mM HCl also resulted from an effort to mimic the proton-dissolution process. The reactions were proceeding with pH higher than the pK_a values of carboxylic ligands so that ligands were deprotonated completely (Table 4-1). TCE concentration did not change by carboxylic ligands in blank systems, indicating these organic ligands have no ability to remove TCE in this study (Figure 4-24). Approximately 44% of TCE was removed by acid-washing ZVI in 48 hr with k_{obs} of 0.083 hr^{-1} in the control system (Figure 4-25 and Table 4-1). The TCE removal efficiencies in this study was higher than what was reported in reference at pH 6-7 conditions (Chen et al., 2001). A higher k_{obs} (0.106 hr^{-1}) was observed in the 30 mM HCl system with 69.0% of the TCE removal efficiency. In addition, 30 mM HCl induced a significant decrease in the TCE adsorption from 14.8% to 5.1% on the ZVI surface, which in turn increased the TCE degradation efficiency. Therefore, the acid-wash process and 30 mM HCl enhanced the reactivity of ZVI toward TCE.

In the presence of 30 mM carboxylic groups, the removal rates of TCE by ZVI increased in the order of 10 mM CA (enhancement factor: 0.93) \cong control (1.00) < 30 mM HCl (1.28) < 15 mM OA (1.42) \cong 30 mM FA (1.48) (Table 4-1 and Figure 4-26). FA and OA increase the dechlorination efficiency from 29.1% to 46.9% and 61.6% respectively, as compared with the control system. While only 20.2% of TCE was dechlorinated by ZVI in the presence of CA. The reactivity of ZVI increased with a decrease in carboxylic groups in ligand molecules. Similar results were also noted by Su and Puls (2004).

The reactivity of ZVI was also influenced by the carboxylic concentration. In Figure 4-27, the TCE removal rate increased with an increase in the concentration of FA and CA. k_{obs} increased approximately 1.6-times when the carboxylic (-COOH) concentration in FA

molecules increased 2-times. A same result was observed in the CA system, k_{obs} values increased approximately 2.8-times when the concentration in CA molecules increasing 2.2-times. Although the final pH in the 30 mM CA system was pH 5.36 that was smaller than its pK_{a3} value. Under this condition the CA molecular contains only first and second $-COOH$ virtually complete protonolyses. However, an opposite tendency was found in the OA system. The k_{obs} decreased roughly 4.3-times when OA increased from 15 mM to 30 mM, i.e. OA could induce a dramatically decrease on the reactivity of ZVI in the presence of high concentration of OA.

Table 4-1. The removal of TCE by MZVI with ligands.

#	System	COOH/H ⁺ (mM)	Finial pH	k _{obs} (hr ⁻¹)
1	Control (pure water)	0	6.70	0.083
2	30 mM HCl	30.00	6.84	0.106
3	30 mM FA	29.79	5.84	0.122
4	15 mM FA	14.86	6.74	0.076
5	30 mM OA	59.89	6.47	0.026
6	15 mM OA	29.94	6.46	0.118
7	30 mMCA	56.35	5.36	0.215
8	10 mM CA	25.58	6.53	0.077

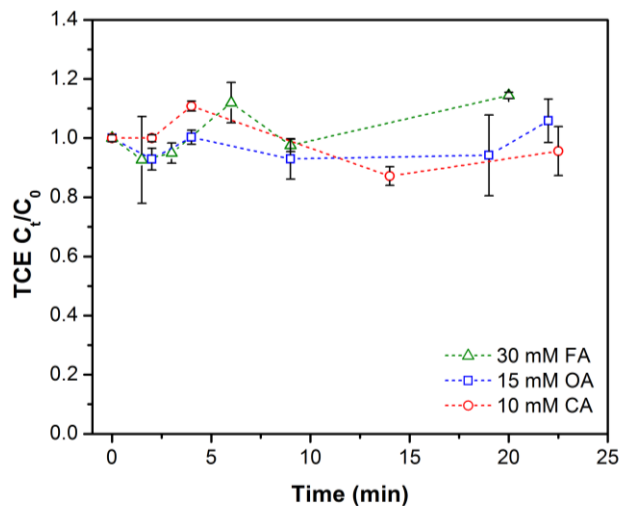


Figure 4-24. The removal kinetics of TCE with carboxylic acid.

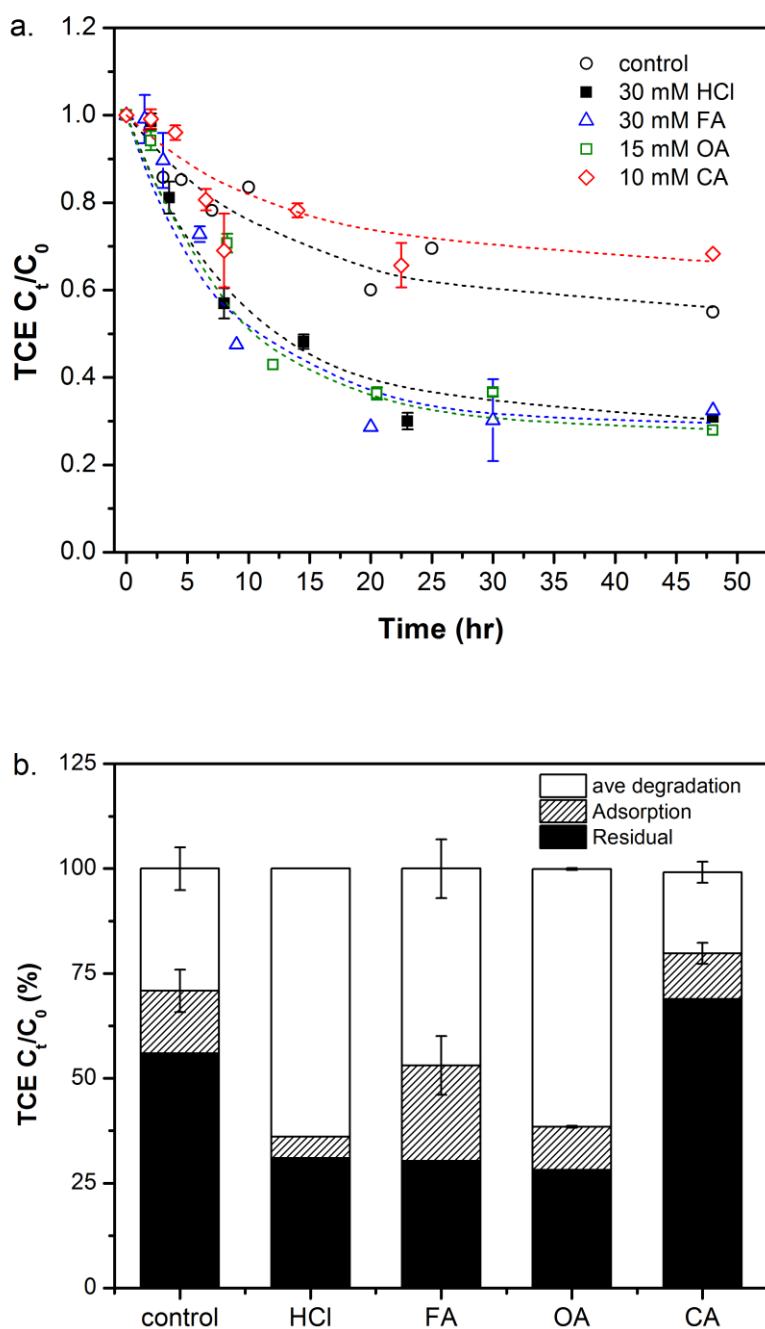


Figure 4-25. (a) The reduction kinetics of TCE by ZVI in the presence of 30 mM of carboxylic molarity of ligands. (b) TCE distribution with ZVI in the presence of ligands. ZVI dosage was 20 g/L and TCE initial concentration was 4.57 μ M. The error bar in Figure 4-25 represent the standard error of an average over triplicated batch experiments.

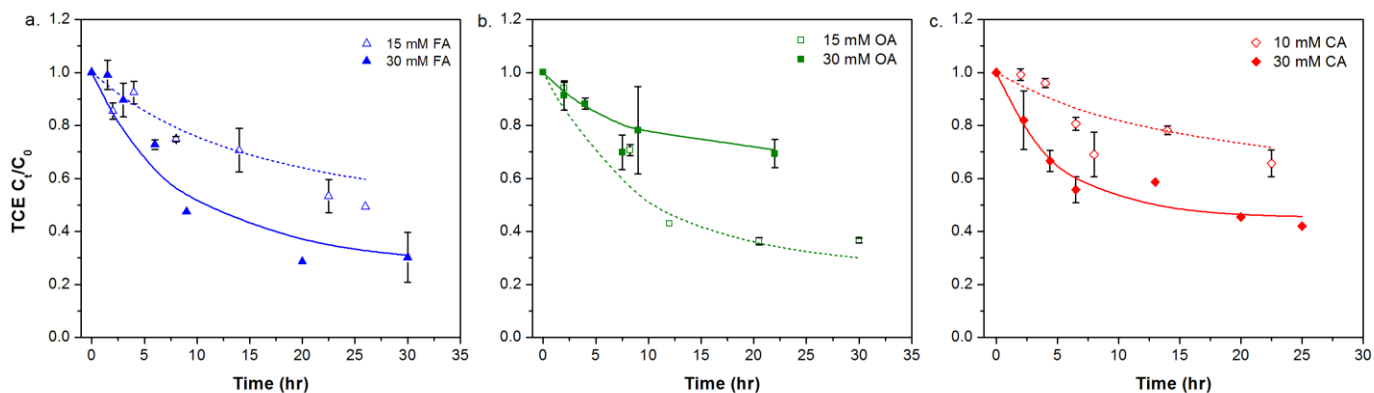


Figure 4-26. Effect of carboxylic acids on the degradation of TCE with ZVI. ZVI dosage was 20 g/L and TCE initial concentration was 4.57 μM . The error bar in Figure 4-26 represent the standard error of an average over triplicated batch experiments.

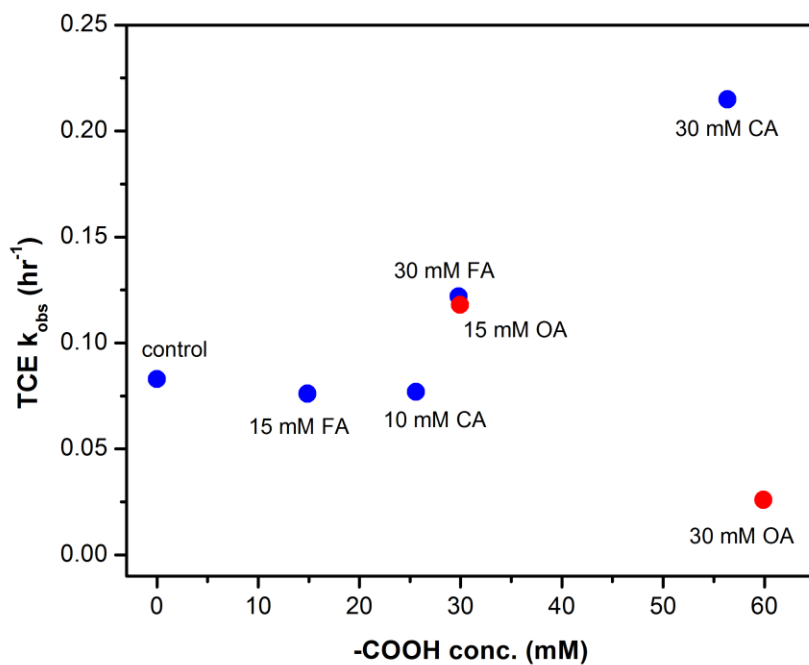


Figure 4-27. The relation between the carboxylic concentration and k_{obs} . The values of k_{obs} obtained from fitting of the data in Figure 4-26.

4.4.2 Characteristics of ZVI surface in the presence of ligand acids

The TCE adsorption efficiencies on the ZVI surface were respectively 10.2% and 10.9% in the presence of OA and CA, which were lower than that in the control system (14.8%) (Figure 4-25b). In the contrary, FA induced an increase in the TCE adsorption to 22.8%. The fresh ZVI surface was identified as a nearly pure Fe sample via XRD analysis (Figure 4-28). Magnetite ($\text{Fe}^+\text{Fe}^{2+}_3\text{O}_4$) was the main Fe oxide generated on the surface of aged ZVI in both the absence and the presence of ligands. Special peaks of Fe^0 reduced in the presence of FA, indicating a strong corrosion occurred on the ZVI surface. Both Fe^0 and Fe oxides were measured on the ZVI surface in the presence of OA. A different phenomenon occurred in the CA system, where the most intense peaks were Fe^0 with insignificant signal of Fe oxides that were found on the ZVI surface.

From SEM analysis (Figure 4-29), fresh ZVI particles have a smooth surface as compared with that in the presence of carboxylic ligands. In the presence of FA, ZVI surface was composed of a layer substructure. On these layer-like particle surfaces also observed the substructure of smaller particles, i.e. ZVI particles were made up of many, much smaller particles with size of about 200 nm, which could precipitated by Fe oxides (Ristić et al., 2006; Štajdohar et al., 2013). These small particles as Fe oxides were confirmed by XRD spectra, which covered on the ZVI surface and further contribute a higher TCE adsorption.

In the presence of OA, lots pit corroded sites were observed on the ZVI surface, revealing the formation of Fe oxides built of porous iron shell. For the CA system, it can be seen that a flake of the flower-like structure has been found on the ZVI surface and form a porous iron shell. The flower-like structure was also observed on the surface of Fe

(hydro)oxides, including α -FeOOH and α -Fe₂O₃ (Cao et al., 2012; Han et al., 2011; Li et al., 2011), which might compose of hundreds of small petals, making the surface of the overall structure uniform than that in other treatments. Therefore, the passive layers that formed on the ZVI surface in the presence of FA may further coagulate with TCE (Shih and Tai, 2010; Tso and Shih, 2015), then enhanced the adsorption efficiency. Both OA and CA, by contrast, induced a decrease in the TCE adsorption. Inorganic ligand (i.e. HCl in this study) changed the conformation of Fe oxides on the ZVI surface from magnetite and maghemite to the fresher Fe, explaining the decrease in TCE adsorption on the ZVI surface.

4.4.3 Fe dissolution process in the presence of ligand acids

The Fe dissolution kinetic followed a nonlinear process, the increase of Fe²⁺/Fe complexes diminishes over time and eventually levels out to a plateau concentration (Figure 4-30 and Figure 4-31). ZVI dissolution was approximately 3.71 mmol/m² in 23 hours in the presence of 30 mM HCl. Both an acid-wash process and 30 mM HCl induce the reactivity of ZVI by removing Fe oxides from the ZVI surface, then leaving a fresh amorphous Fe hydroxide film that is more reactive (Johnson et al., 1996), which was in agreement with the result on XRD analysis.

The Fe dissolution with 30 mM FA reached an equivalent level in 4 hours was 7.17 mmol/m², then gradually slows down the dissolution process (Figure 4-30). The final Fe²⁺ concentration was 8.06 mmol/m² after 22.5 hours. The dissolved Fe²⁺/Fe complexes was 2.04 mmol/m² in the presence of 10 mM CA. However, with 15 mM OA, only 0.21 mmol/m² of dissolved Fe²⁺/Fe complexes released from the ZVI surface in 2 hours, and the value decreased with time until only 0.03 mmol/m² had been detected after 20.5 hours

(Figure 4-31). The dissolution rate was decreased in the order of 30 mM FA > 30 mM HCl > 10 mM CA > 15 mM OA (Figure 4-30). Carboxylic ligands, such as oxalate and citrate, can be consumed by forming inner-sphere surface complexes between Fe²⁺/Fe³⁺ and the adsorbed ligands at the Fe surface. The stability constants, $\log K_{\text{Fe}^{2+}\text{-L}}$ and $\log K_{\text{Fe}^{3+}\text{-L}}$, express the strengths of the main soluble ligand-complexes increases as the number carboxylic groups in each ligand molecule increases (Martell and Smith, 1974), while no stability constant value for the Fe²⁺-FA complex was reported.

The Fe dissolution rate increased with ligand concentration excepted the OA sets (Figure 4-31). Although oxalate has strong complex ability to Fe²⁺/Fe³⁺ and forming chelates, ferrous/ferric oxalate themselves are only slightly soluble in water (Koene et al., 2006). As a result of this very low solubility the dissolution of Fe was followed by precipitation as yellow-white ferrous/ferric oxalate with poor crystal structure on the ZVI surface (Figure 4-32). Also, the ligand-metal complexes from a strongly absorbing ligand that are released to solution may quickly re-adsorb or precipitate back onto the metal surface, forming a species different from the precursor complex for dissolution or insoluble Fe oxides (Hamer et al., 2003; Wang and Stone, 2008). These precipitates of Fe oxalates on the ZVI surface further inhibited the active sites for TCE reduction with high concentration of OA.

There was a linear relation (R^2 was 0.777) between the k_{obs} of TCE and the Fe dissolution, indicating that the reactivity of ZVI was related to their dissolved Fe oxides from the ZVI surface via proton- and ligand-promoted processes (Figure 4-33). However, in the OA system (15 mM) and the CA system (30 mM), there was an exception that both systems show a high TCE removal rate but with lower Fe dissolution as compared with

other systems. For 30 mM CA, the final pH of the system was lower than other systems that may influence the reactivity of ZVI. In the presence of 15 Mm OA, those oxalate not only remove the passive layers on the ZVI surface via the complex process, but the formation of Fe-oxalate complexes probably have abilities to degrade TCE themselves; then in the end most of dissolved Fe^{2+}/Fe complexes precipitated onto the ZVI surface.

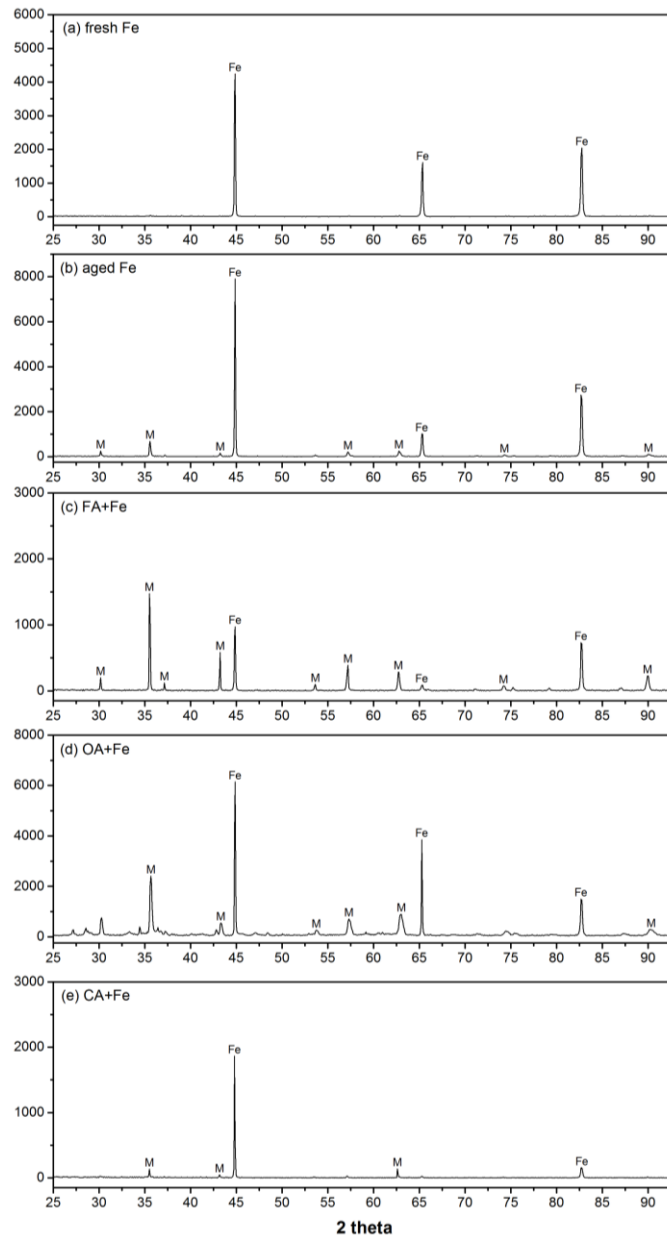


Figure 4-28. XRD spectra of (a) fresh ZVI, (b) aged ZVI, ZVI in the presence of (c) FA, (d) OA, and (e) CA. In spectra, (Fe) represents as iron and (M) represents as magnetite.

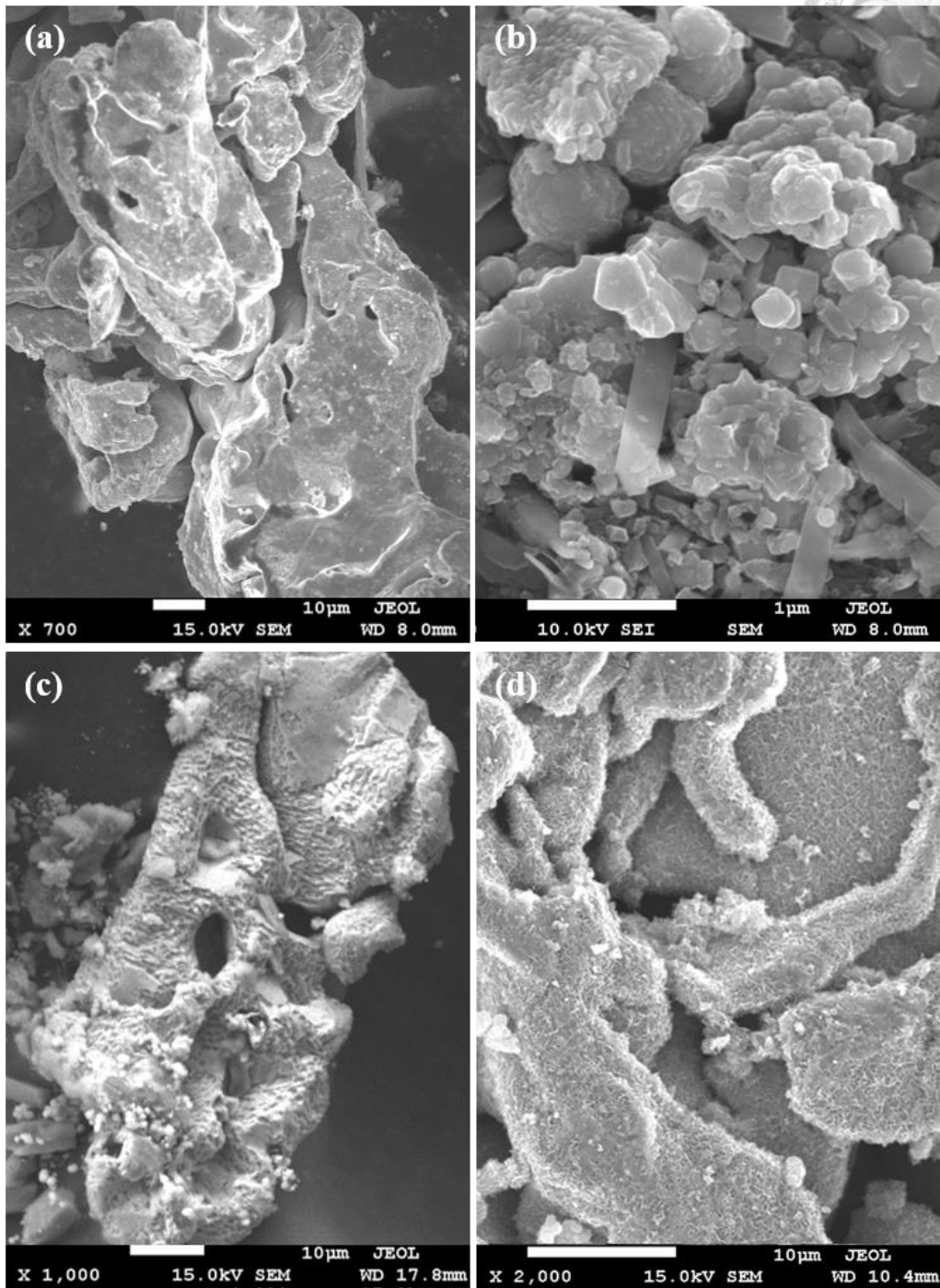
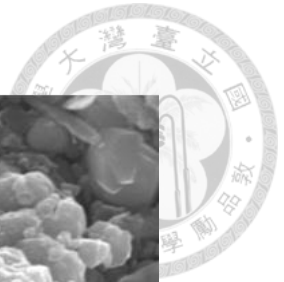


Figure 4-29. SEM images of the surface morphology of ZVI in (a) pure water and in the presence of (b) FA, (c) OA, and (d) CA.

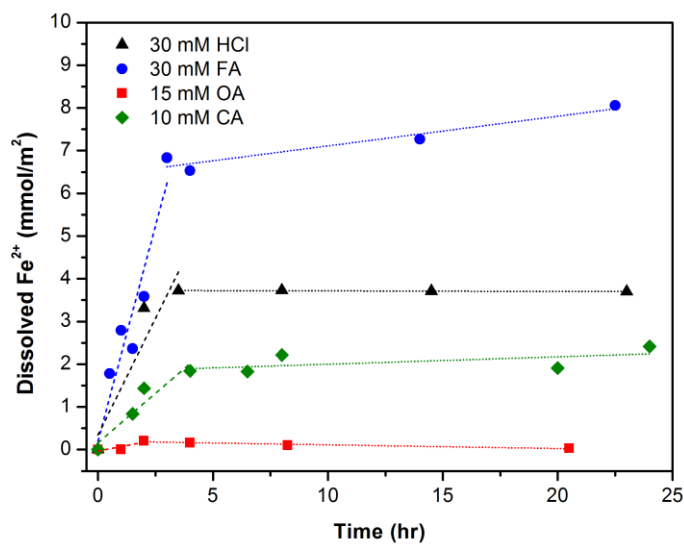


Figure 4-30. Fe dissolution in the presence of 30 mM of carboxylic molarity of ligands.

ZVI dosage was 20 g/L and TCE initial concentration was 4.57 μM .

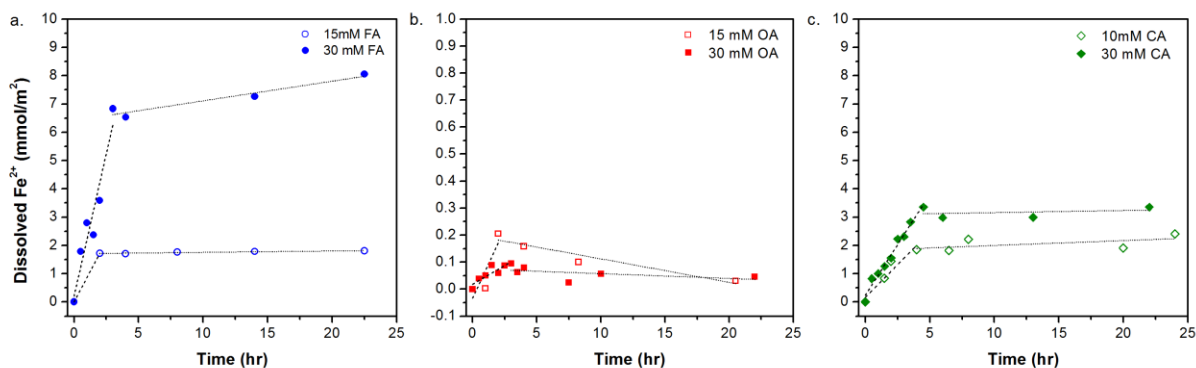


Figure 4-31. Fe dissolution in the presence of different concentrations of (a) FA, (b) OA, and (c) CA. ZVI dosage was 20 g/L and TCE initial concentration was 4.57 μM .



Figure 4-32. Images of ZVI in the presence of carboxylic ligands.

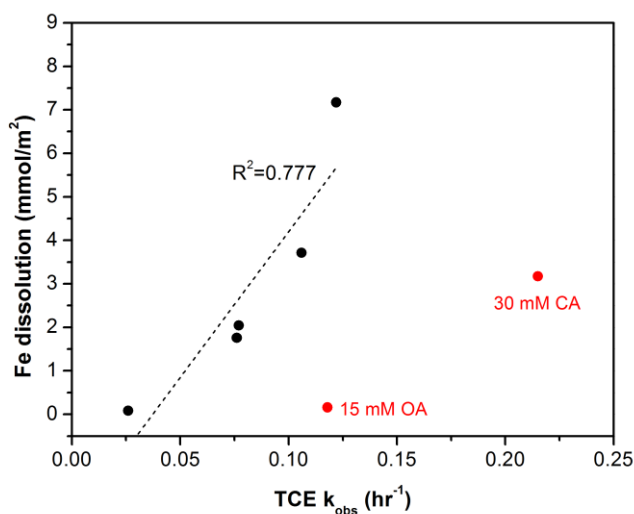


Figure 4-33. The relation between TCE reaction rate constant and Fe dissolution concentration.

4.4.4 The effect of ligand-Fe complexes on the reactivity of ZVI

Fe type and distribution were estimated using Visual MINTEQ (Table 4-2). With FA, the main species of dissolved Fe was Fe^{2+} (over 99%) because of the almost no complex ability with Fe^{2+} . In the presence of OA, the dissolution process occurred at the beginning and then the dissolved Fe reduced to only 0.03-0.05 $mmol/m^2$ after 2 hours with the concentration of OA in a range of 15-30 mM (Figure 4-31b). This phenomenon would be due to the precipitation of Fe complexes, which may re-adsorb back on the ZVI surface. The predicted complexes of Fe^{2+} -ligand were Fe-oxalate followed a minor species Fe-oxalate $_2^{2-}$ according to its stability constant and reaction conditions. With CA, the dissolved Fe species was mainly in a form of Fe-citrate $^-$ then followed FeH-citrate. The standard reduction potentials (E_h^0) of Fe^{2+} -oxalate, Fe^{2+} -oxalate $_2^{2-}$, and Fe^{2+} -citrate $^{1-}$ are respectively 0.47, 0.21, and 0.37 V (Thamdrup, 2000), which were greater than the E_h^0 values for TCE

(0.55-0.53 V) (Dolfing et al., 2006). Fe^{2+} -oxalate $_2^{2-}$ even have the ability to reduce dichloroethylene (DCE) and vinyl chloride (VC) theoretically (Scheme 4-4).

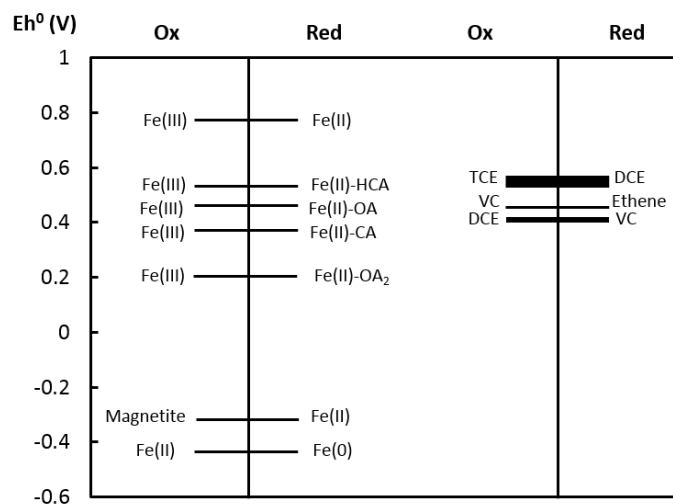
To study the reactivity of those Fe complexes, the removal efficiency of TCE by Fe^{2+} in the presence of carboxylic ligands with the same carboxyl molar concentration was shown in Figure 4-34. TCE was removed for approximately 25% of by 40 mM Fe^{2+} in the presence of 15 mM OA after 16.5 hours while no obviously change in the FA and the CA systems. This result suggested that the formation of Fe-oxalate complexes such as Fe^{2+} -oxalate (31.9%) and Fe^{2+} -oxalate $_2^{2-}$ (1.9%) have an ability to degrade TCE and byproducts. Therefore, TCE could be degraded effectively by ZVI in the presence of OA than CA and FA that can be partially considered as the interaction of ligands with the implication of dissolved Fe^{2+} -complexes in-situ.

The ZVI corrosion released Fe^{2+} that subsequently precipitated as mixed-valent phases such as magnetite, siderite, or green rust under anaerobic conditions. Carboxylic ligands, such as oxalate and citrate, adsorbed to the Fe oxides on the ZVI surface through a ligand exchange reaction and slowly formed Fe-ligand complexes, and then detached from the ZVI surface into solution (Furrer and Stumm, 1986; Reichard et al., 2007). Those Fe oxides such as magnetite and maghemite may induce an increase on TCE adsorption, further reduce it to DCE and VC via the electron transfer although both magnetite/ Fe^{2+} and $\text{Fe}^{2+}/\text{Fe}^0$ are theoretically capable to reducing TCE to ethylene (Scheme 4-4). HCl offers proton to disrupt the adherent magnetite film on the ZVI surface through a proton-promoted dissolution process (Sun et al., 2011), which exposed more reactive sites on the fresh ZVI surface, and then enhanced the reduction of TCE through a directly electron transfer from fresh reactive sites. Carboxylic ligands that without complex ability with Fe^{2+} like FA,

would offer proton to promote the dissolution of passive layers on ZVI surface. For carboxylic ligands with strong stability constants, such as OA and CA, would remove passive layers on the ZVI surface via the formation of Fe-ligand complexes. For one thing, the ligand-promoted dissolution increased the fresh reactive sites on the ZVI surface and enhanced the reactivity of ZVI. Besides, these Fe-ligand complexes have ability to further degrade TCE depend on their complex forms and the reaction conditions. Those dissolved Fe may also precipitate back onto the ZVI surface as amorphous Fe oxides that may gradually inhibit the reactivity of ZVI (Scheme 4-5).

Table 4-2. Fe type and distribution in the presence of ligands predicted by Visual MINTEQ.

Batch	Species	Distribution (%)	Concentration (mM)
30 mM HCl	Fe ²⁺	99.9	12.61
15 mM FA	Fe ²⁺	99.8	5.99
30 mM FA	Fe ²⁺	99.9	24.4
10 mM CA	Fe ²⁺	0.24	0.02
	Fe-citrate ⁻	99.2	6.45
	FeH-citrate	0.48	0.03
30 mM CA	Fe ²⁺	0.37	0.04
	Fe-citrate ⁻	93.3	10.1
	FeH-citrate	6.31	0.68



Scheme 4-4. The redox potential of Fe²⁺/Fe³⁺ in different type of Fe.

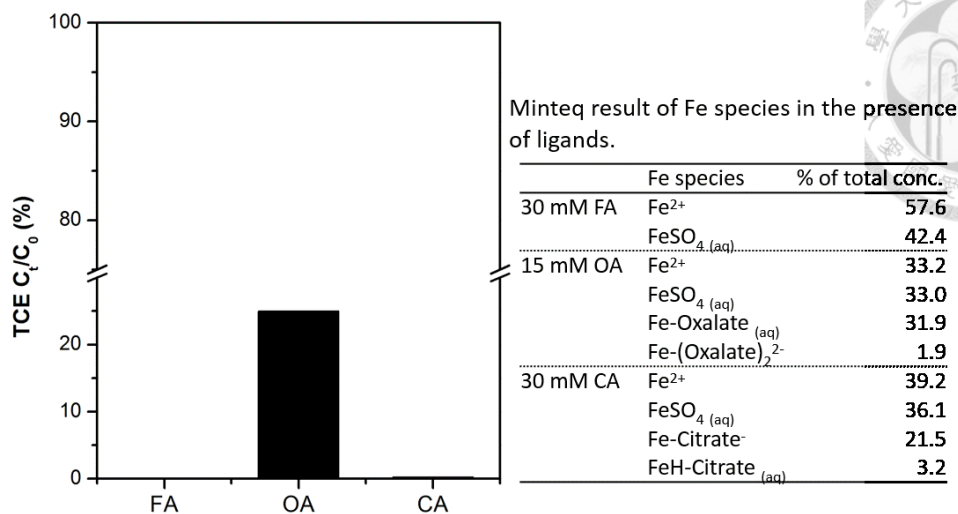
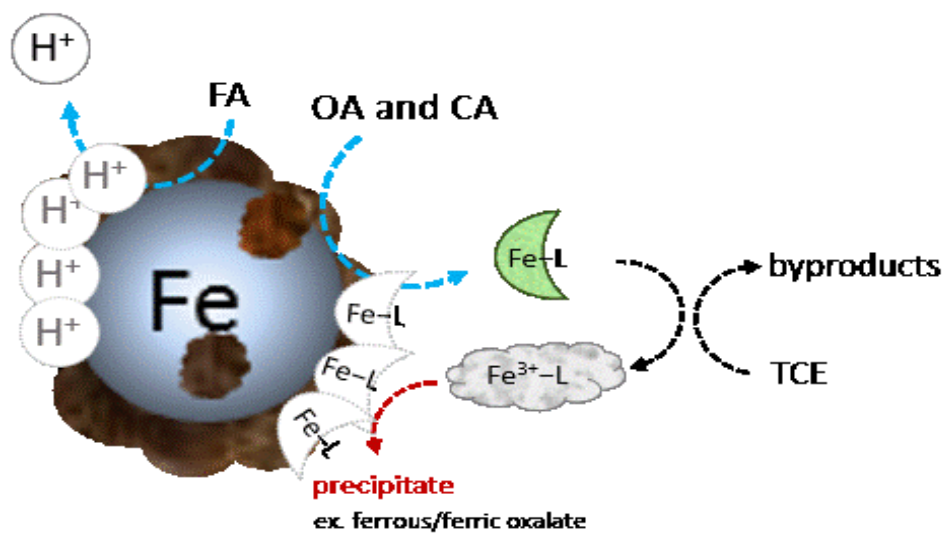



Figure 4-34. The removal efficiency of TCE by Fe²⁺-ligand complexes after reaction for 16.5 hours. TCE concentration was 4.57 μM, Fe²⁺ initial concentration was 40 mM, and final pH was about pH 5.



Scheme 4-5. The diagram of the reaction mechanism of TCE by ZVI in the presence of carboxylic ligands.

4.5 The reactivity and transformation of HA-Fe complexes

4.5.1 Reduction of RB5 in HA control systems



In the UHA system, no reduction of RB5 occurred under any of the three pH conditions (Figure 4-35). By contrast, RHA reduced approximately 40% of RB5 within 6 days under the three pH conditions displaying similar removal kinetics. Azo-dyes show an irreversible reduction peak in a range of -0.13 to -0.48 V vs. NHE which was associated with irreversible redox reactions leading to cleavage of the azo bonds (Zille et al., 2004). There were more redox couples shown in the voltammograms with increasing numbers of azo bonds, which can be attributed to the sequential reduction of the azo groups (Mezohegyi et al., 2009; Zille et al., 2004). According to Mezohegyi et al. (2009), the first azo bond in RB5 requires mild anaerobic conditions for reduction. For hydrolysed RB5 with a monoazo bond, a reduced product, the reduction potential of the second azo bond would be -257 mV (Mezohegyi et al., 2009). At all three pH conditions, the Eh value increased to 276-310 mV immediately after mixing with RB5, whereas the initial Eh values of RHA might be strong enough to break the first azo bond (Figure 4-36). Although Leonardite HA contained a significant amount of reduced moieties with significant reducing capacity, UHA showed no ability to reduce RB5 in this study. The reducing capacities of RHA on the contrary was higher than that of UHA (Kappler and Haderlein, 2003).

The RB5 parent compound shows two main characteristic absorption bands, one in the UV region (310 nm) and the other in the visible region (596 nm). The UV band is characteristic of two adjacent rings, whereas the visible band represents the long conjugated π system linked by two azo groups (Lucas and Peres, 2006). When RB5 was mixed with HA, only the visible band was clearly observed without any interference by

HA (Figure 4-37). From the UV-vis full scans of RB5, the peak shows a blue-shift when pH was increased from 5 to 9, suggesting a structural change in the RB5 molecules in neutral and alkaline conditions. No peak shift was measured in the UHA system compared with the RHA system under all three pH conditions. As RB5/HA ratios varied by a factor of 0.036-0.200 among reaction sets, it was expected that RHA could supply sufficient electrons to reduce the molecular structure of RB5. However, RB5 reduction efficiency did not change consistently with HA concentration (Figure 4-38). It was possible that there was absorbance overlap of the main RB5 compound and RB5 (hydro)byproducts which caused an underestimation of the reduction efficiency.

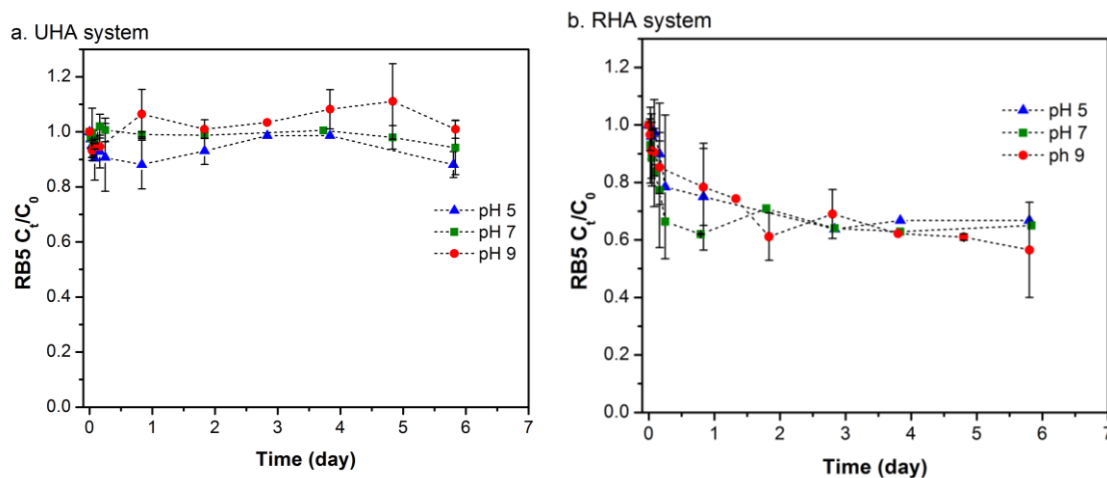


Figure 4-35. The removal kinetics of RB5 in (a) UHA and (b) RHA systems. HA concentration was 31.25 mg/L and RB5 initial concentration was about 6.3 mg/L. Background buffers were 100 mM of acetate, HEPES and Tris buffer at pH 5, 7 and 9, respectively. The error bars in the Figures represent the standard error of an average over triplicated batch experiments.

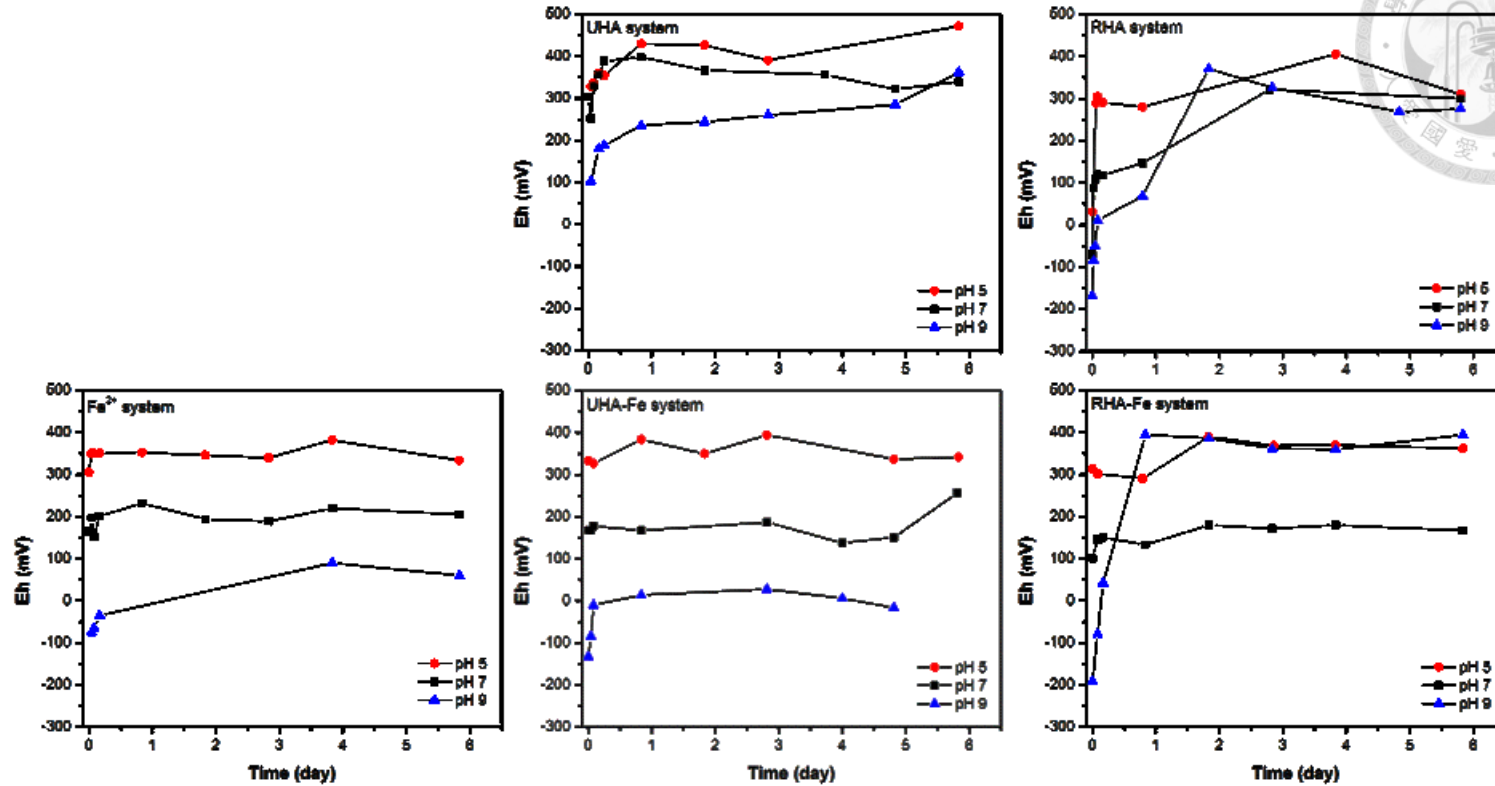
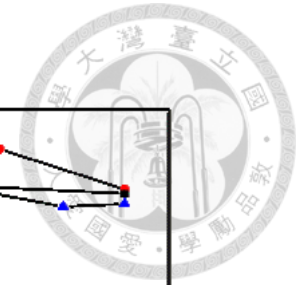


Figure 4-36. The Eh values in Fe²⁺, UHA, RHA, UHA-Fe, and RHA-Fe systems. HA concentration was 31.25 mg/L, Fe²⁺ concentration was 1.6 mmol/g_{HA} (50 μM) and RB5 initial concentration was 6.3 mg/L. Background buffers were 100 mM of acetate, HEPES and Tris buffer at pH 5, 7 and 9, respectively.

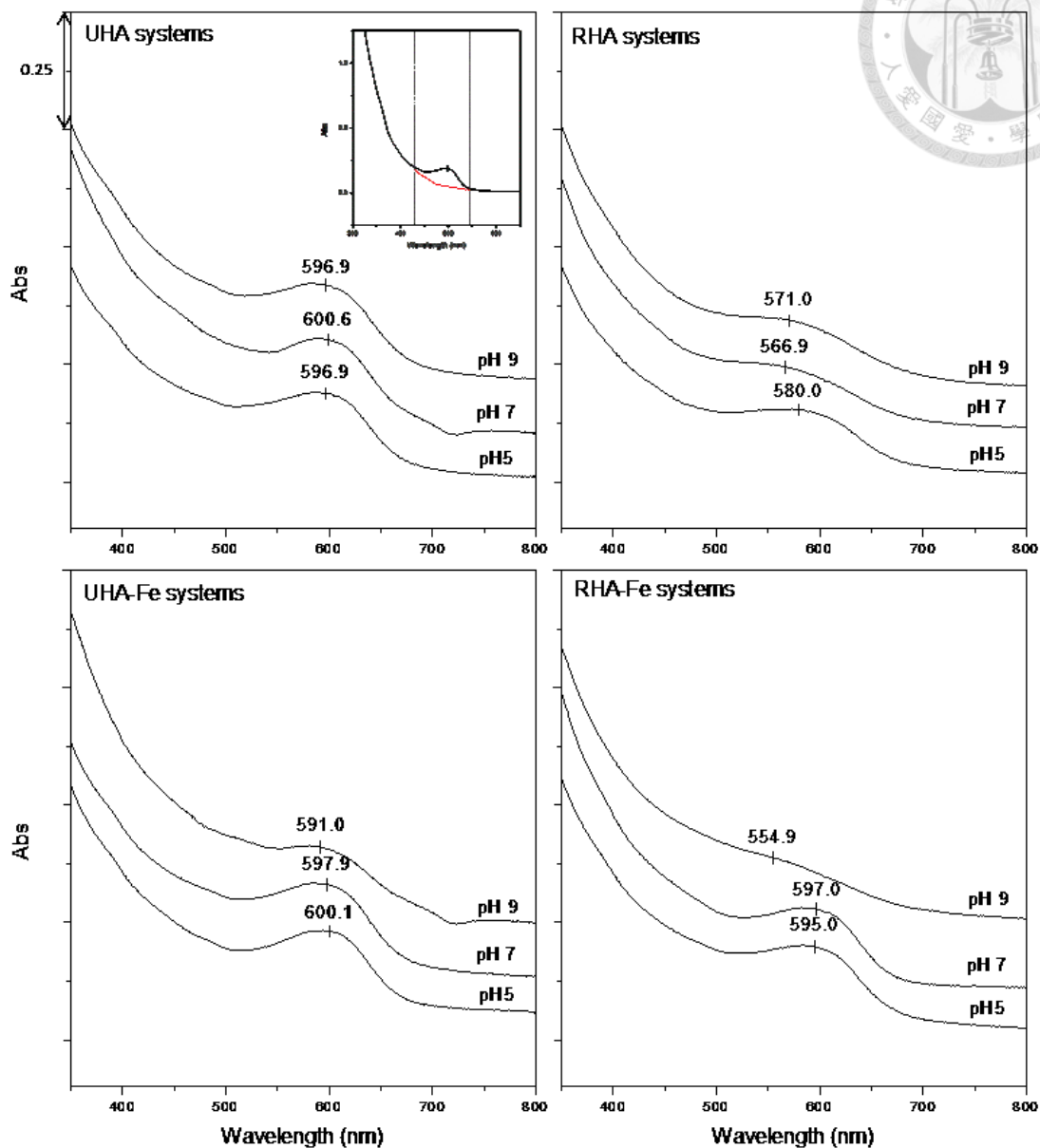


Figure 4-37. The UV-vis full scan spectra of RB5 after reactions in HA and HA-Fe systems for 6 days. The peak marks were calculated using OriginLab software. Peaks were quantified by fitting the peak center from the selected range of the data plot after subtracting the baseline of HA or HA-Fe.

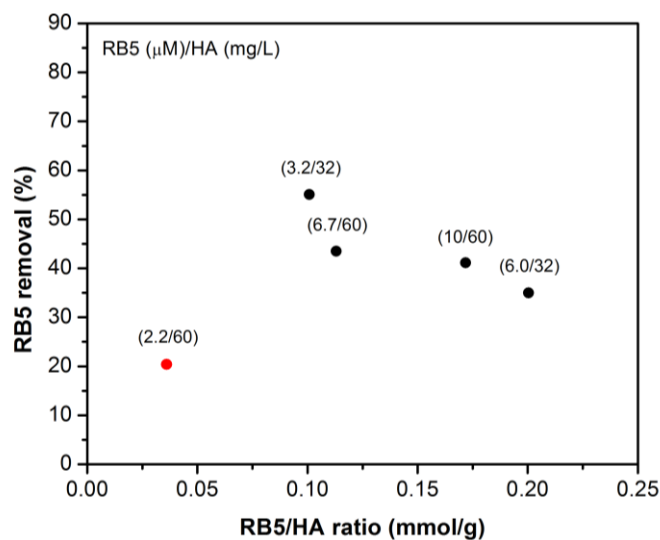


Figure 4-38. Effect of RB5/HA ratio on the removal of RB5 by RHA at pH 7. RB5 removal efficiency was observed after reacting for 6 days. The RB5 removal efficiency increased with a decrease in the RB5/HA ratio. When the RB5/HA ratio decreased to 0.036 (red dot), RB5 removal efficiency also decreased, which might be caused by the interference of high HA concentrations to low concentrations of RB5.

4.5.2 Reduction of RB5 in Fe^{2+} systems

A rapid reduction of RB5 was observed at the pH 9 condition in the Fe^{2+} system with a degradation efficiency of approximately 80% while no obvious removal of RB5 was found at pH 5 and 7 (Figure 4-39). Fe distributions showed that the amount of Fe^{3+} and Fe colloids were increased with an increase in pH (Figure 4-40). After 2.7 days, 94.7% of the dissolved Fe^{2+} oxidized/precipitated at pH 9, but no Fe^{2+} oxidation was observed under the other conditions. The oxidation of Fe^{2+} suggests that electrons were transferred to RB5 molecules and then caused the degradation.

Here the concentration of dissolved Fe^{2+} was independent of the redox potential of the system, but dependent on pH. For 50 μM of Fe^{2+} in equilibrium, $\text{Fe}(\text{OH})_2$ precipitates as

the system pH increased to pH 8.6 (Figure 4-41). Therefore, 30.9 $\mu\text{mol/L}$ of Fe^{2+} precipitated as $\text{Fe}(\text{OH})_2$ at pH 9 (Figure 4-40). $\text{Fe}(\text{OH})_2$ is thermodynamically unstable and will decomposed to magnetite, which possibly caused the observed reactivity (Jeong et al., 2011).

However, the precise mechanism of reduction in the Fe^{2+} system cannot be determined from the collected data. It was assumed that RB5 accepts electrons from the $\text{Fe}^{2+}/\text{Fe}^{3+}$ redox pair to decompose azo-bonds, when Fe^{2+} oxidized to Fe^{3+} , it would release both electron and hydrogen, overall the reduction reaction was pH-dependent. As we were limited by our data set in providing a more detailed mechanistic interpretation of these reactions, we performed the Fe^{2+} system as control experiments for comparison with HA-Fe systems.

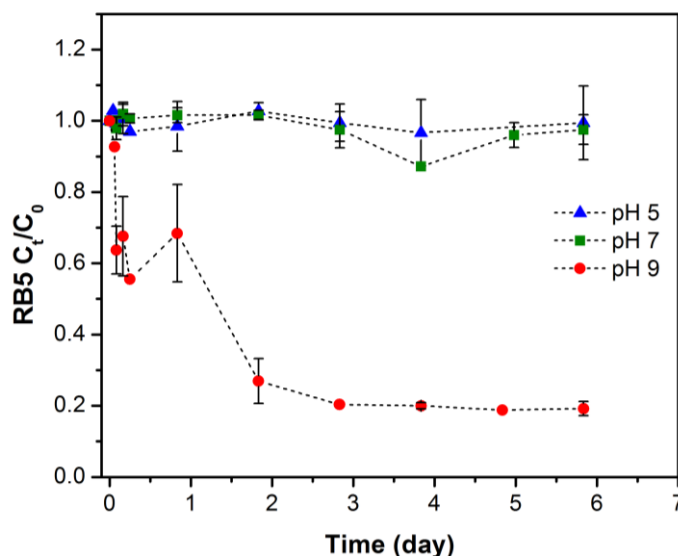


Figure 4-39. The degradation kinetics of RB5 in the Fe^{2+} systems. Fe^{2+} concentration was 50 μM and RB5 initial concentration was 6.3 mg/L. Background buffers were 100 mM of acetate, HEPES and Tris buffer at pH 5, 7 and 9, respectively. The error bars in this Figure represents the standard error of an average over triplicated batch experiments.

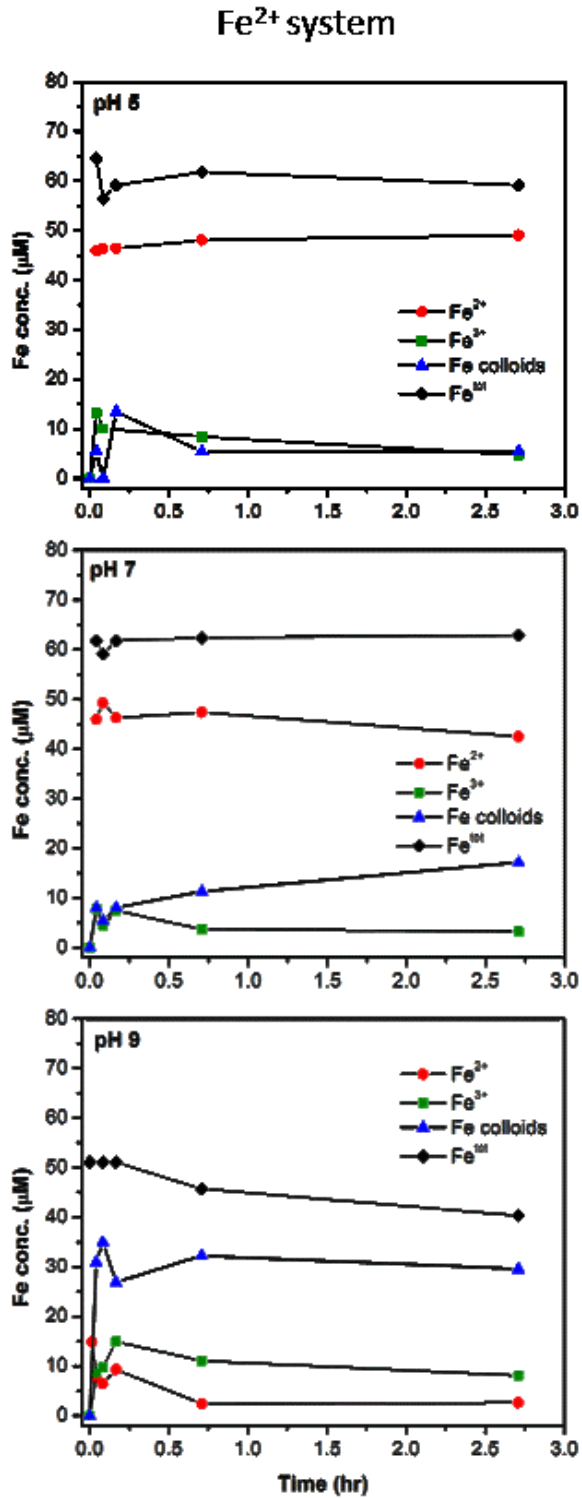


Figure 4-40. Fe species distribution in the Fe²⁺ systems at different pHs. Fe species include Fe²⁺, Fe³⁺, Fe colloids, and total Fe.

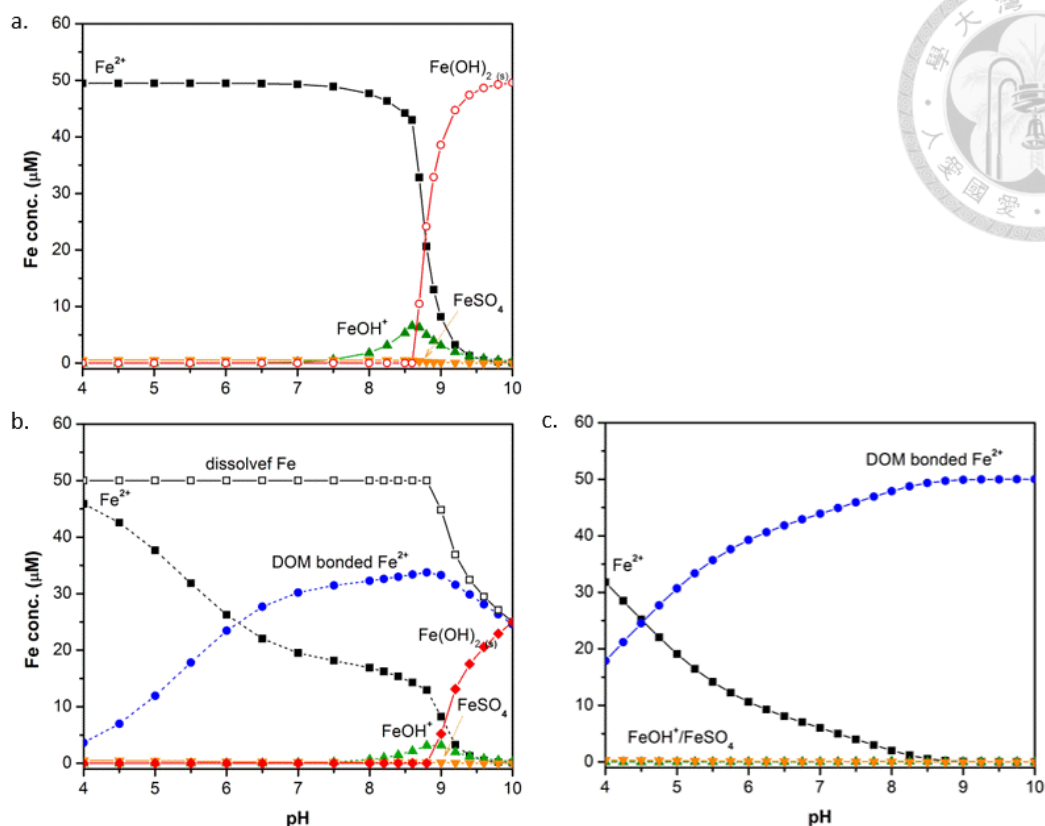


Figure 4-41. Fe distribution predicted by Visual MINTEQ 3.0 software. (a) Fe²⁺ control system. (b) SHM and (c) NICA models for HA-Fe systems. The parameter sets for Fe precipitation and complexation were as follows: Fe²⁺ and SO₄²⁻ concentration were 50 μM, DOM concentration was 18.6 mg/L (HA).

4.5.3 Reduction of RB5 in HA-Fe system

RB5 reduction in UHA-Fe reactions was slower as compared to RHA-Fe and Fe²⁺ control systems (Figure 4-42). Comparison between the both HA-Fe reactions can only be made within the same reaction set as reduction potential and colloid formation within the solutions may vary between reaction sets. For RHA-Fe systems, approximately 48% of RB5 was reduced under the pH 9 condition after 6 days, which required approximately

24.3 $\mu\text{mol/L}$ electrons supplied from the $\text{Fe}^{2+}/\text{Fe}^{3+}$ pair and RHA-Fe. The Fe distribution indicated that Fe^{3+} in the medium increased to 23.0 $\mu\text{mol/L}$ (about 38.2% of total Fe), which is in very good agreement with the data on RB5 reduction (Figure 4-43). Complexation certainly changes the redox potential of the element which means that a strong complex can stabilize the bound ion against redox transformation. For HA, Fe^{3+} complexation is much stronger than Fe^{2+} complexation. As compared with the Fe^{2+} system, the Eh was lower at the beginning in the RHA-Fe system, suggesting that RHA was reduced to a higher electron availability that the Fe^{2+} corresponds to (Figure 4-36).

Both UHA-Fe and RHA-Fe reduced RB5 under the pH 9 conditions (Figure 4-42). There was a positive relationship between pH and RB5 reduction efficiency (Figure 4-44). As compared with HA system and Fe^{2+} control system, HA-Fe sets show a pH dependence similar to the Fe^{2+} control system, while no obvious tendency could be found in the HA systems. On the other hand, the reduction potential indicated that the Eh values increased from -200 mV to 400 mV in 1 day at the pH 9 condition in the RHA-Fe system, a similar result could be found in the pH 9 condition of the UHA-Fe system (Figure 4-36). Therefore, HA-Fe complexes and Fe colloids were likely the main reason for RB5 degradation. However, Fe^{2+} might compete with RB5 for the electrons supplied by RHA in the RHA-Fe systems as compared to the RHA and the Fe^{2+} systems. In the other hand, a slower reduction rate for RB5 in the RHA-Fe reaction may result from inhibition of Fe colloid formation by RHA, limited availability of reactive ligands in HA molecules, re-reduction of Fe^{3+} to Fe^{2+} , or a combination of these effects. Fe distribution also indicated that in the presence of Fe^{2+} , HA decreased the Fe precipitation but increased the Fe^{2+} oxidation in both RHA and UHA systems (Figure 4-45). Both SHM and NICA models show that most

of Fe^{2+} forms complexes with HA and Fe^{2+} precipitates as $\text{Fe}(\text{OH})_2$ at pH 8.9-9.0 as suggested by SHM model calculations. The binding ability between HA and Fe is likely dependent on the structural features of HA. According to the hard and soft acid-base (HSAB) theory, Fe^{2+} is classified as a borderline acid, which would have an affinity for both hard bases (e.g., carboxylic acids, phenolic hydroxyl groups and aliphatic amines) and soft bases (e.g., thiol and carbonyl groups, *p*-electrons from aromatic rings and olefins). Yamamoto et al. (2010) noted that the bonding constant, K_b , of HA with Fe^{2+} was approximately 5.8, larger than that of fulvic acid (FA), which may be attributed to the presence of strong binding sites, such as nitrogen- and sulfur- containing ligands in HA. Hakala et al. (2007) suspected that complexation of Fe^{3+} with HA interfered with the formation of Fe oxide colloids. Pullin and Cabaniss (2003) also reported that the kinetics of Fe colloid formation in solutions containing Fe^{2+} and FA was slower than in solutions without FA. In addition, ligands in HA such as quinone/hydroquinone redox couples have reduction potentials that are capable of reducing Fe^{3+} .

4.5.4 The reduction mechanism of HA-Fe

In the RHA-Fe system, the absorbance peak shows an obvious blue shift to approximately 555 nm after 6 days in the pH 9 condition, the same result was also observed in the Fe^{2+} control system (Figure 4-37). A shift in visible absorbance is an indication of a structural change in the RB5 molecules which leads to a change in its color. Azo dyes can be reduced by two or four electrons to produce usually colorless hydro-azocompounds or amines, respectively. In the case of diazo dyes the reduction of the azo bonds occur consecutively (Zille et al., 2004). As expected, the height of the absorbance peak at 596

nm decreased accompanied by a blue shift, suggesting a cleavage of one azo-bond in RB5 molecules in RHA-Fe system at the pH 9 condition.

The reduction in RHA-Fe systems may be regulated by both solution phase and solid phase pathways in which HA-Fe complexes/Fe colloids are the primary reductants, whereby the reductive capacity of Fe^{2+} is decreased by complexation with functional groups present within the HA molecules. The reduction byproducts were identified as 2,2'-disulfonyl azobenzene or 1,2,7-triamino-8-hydroxynaphthalene (TAHNDS) and 2-(4-aminobenzenesulphonyl)ethanol (p-base) via biological treatments under an anaerobic conditions (Bonakdarpour et al., 2011; Libra et al., 2004; Sugano et al., 2009; Wang et al., 2008). However, due to the no identification of byproduct analysis, here we were unable to identify the precise reaction pathway. We can only propose that a different mechanism is responsible for the rate-limiting step in RHA-Fe reactions.

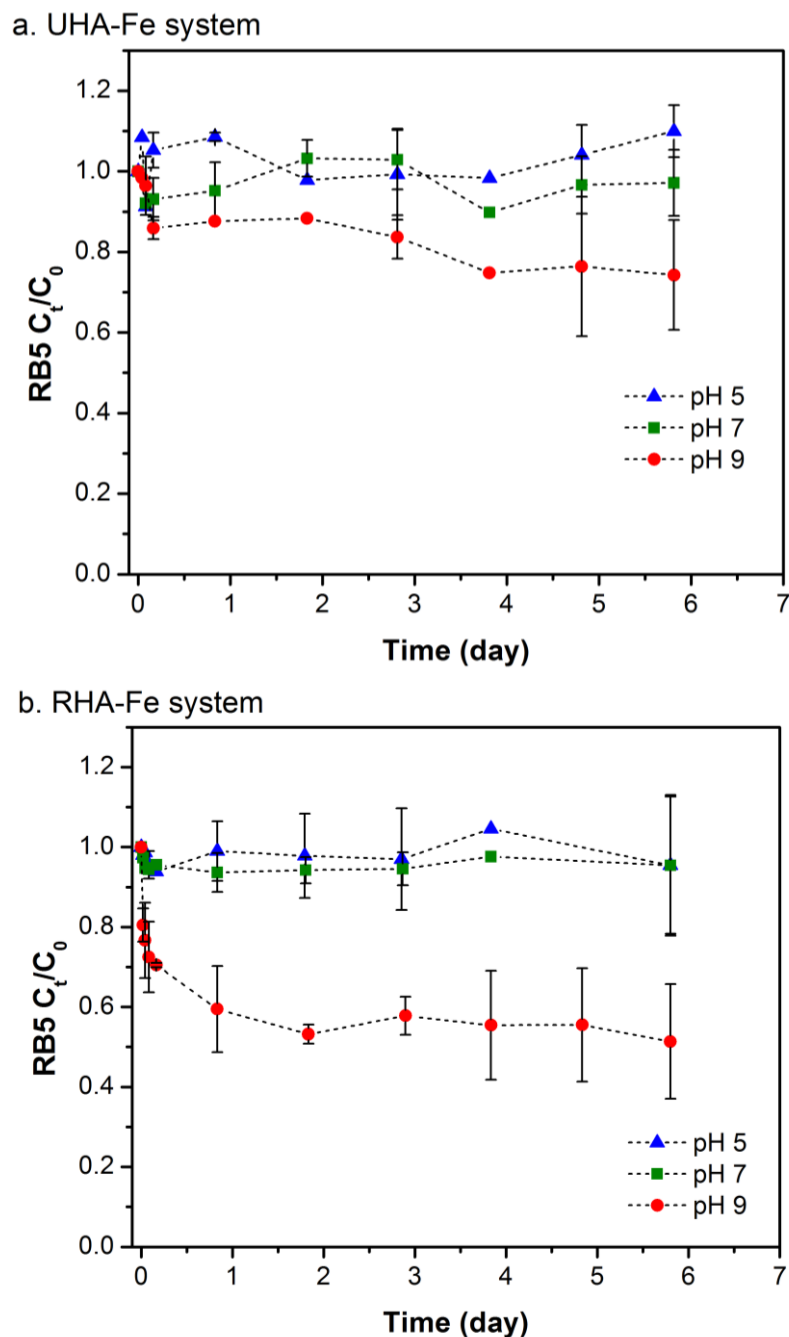


Figure 4-42. The removal kinetics of RB5 in (a) UHA-Fe and (b) RHA-Fe system. HA concentration was 31.25 mg/L, Fe^{2+} concentration was 1.6 mmol/g_{HA} (50 μM), and RB5 initial concentration was about 6.3 mg/L. Background solutions were 100 mM of acetate, HEPES and Tris buffers at pH 5, 7 and 9, respectively. The error bars in these Figures represent the standard error of an average over triplicated batch experiments.

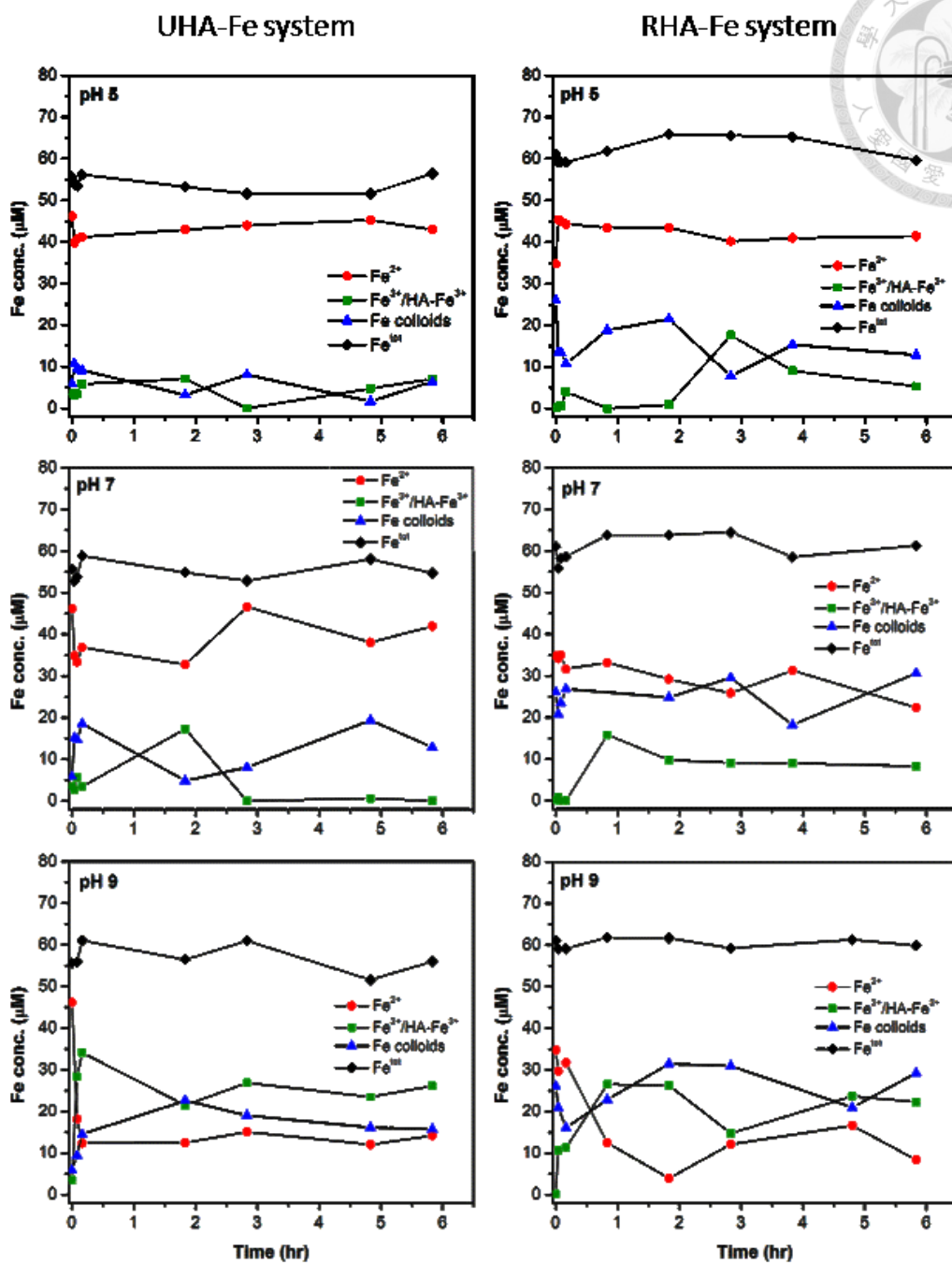
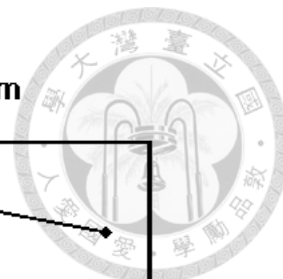


Figure 4-43. Fe species distribution in the two HA-Fe systems under different pH conditions. Fe species include Fe^{2+} , Fe^{3+} , Fe colloids, and total Fe.

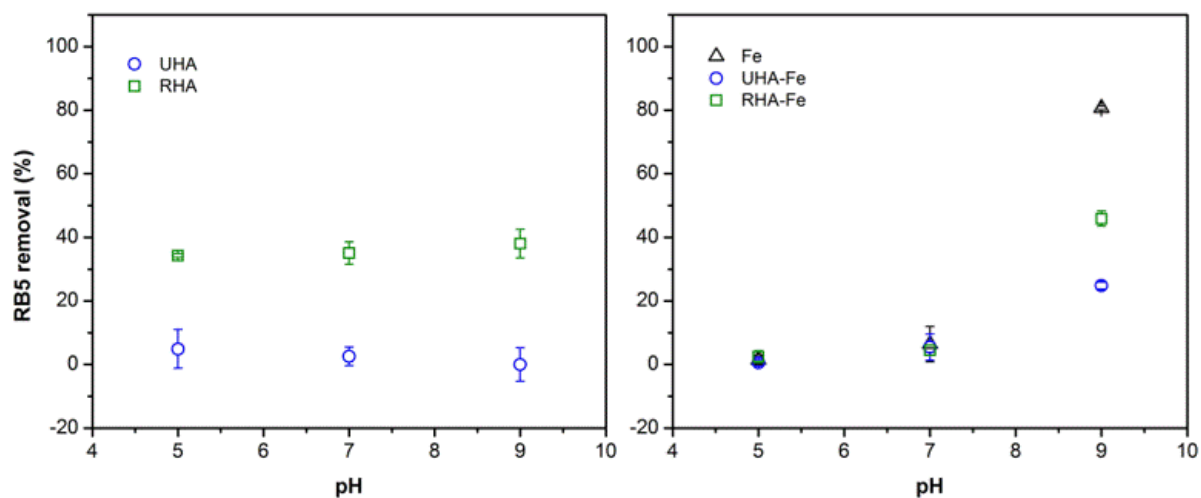


Figure 4-44. The relationship between pH and RB5 removal efficiency. RB5 removal efficiency in the Figure presents an average between day 4 and day 6.

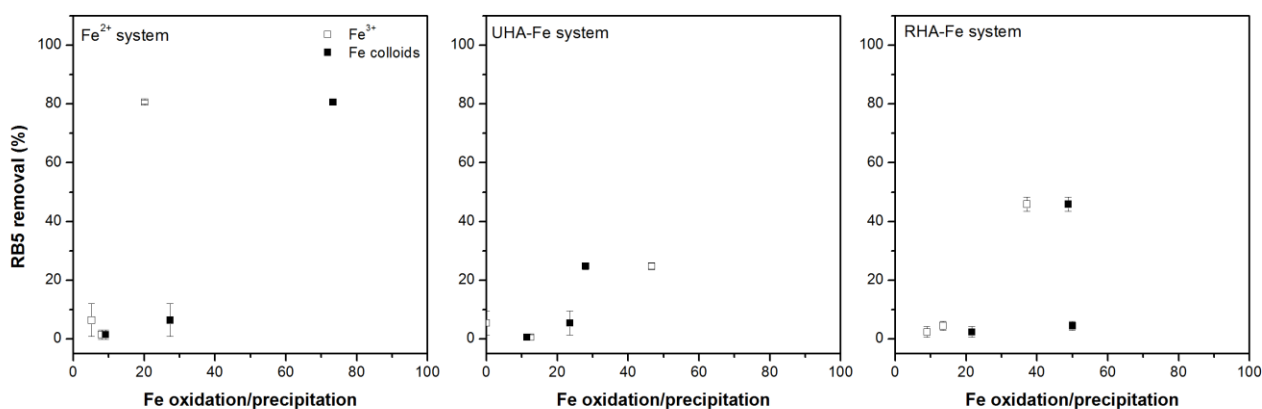


Figure 4-45. The relationship between Fe oxidation/precipitation and RB5 removal efficiency. RB5 removal efficiency in the Figure presents an average between day 4 and day 6.

4.6 The formation and reactivity of metal colloids in the presence of HA

HA was expected to influence the Fe distribution via complexation under different pH and redox conditions. According to the previous section, HA would have an ability to alter the reactivity of Fe^{2+} toward an organic azo dye, RB5. In this section, the study focused on the transformation and reactivity of HA co-precipitated metals, Fe^{2+} and Cu^{2+} .

In the pretest, Fe colloids formed in 24 hours in the presence of either UHA or RHA were not spherical nor shaped, these colloids aggregated into chain-like or larger agglomerates (Figure 4-46). The presence of Cu colloids exhibited a monodispersed with size of 45.5 ± 7.9 nm with RHA; while in the presence of UHA, Cu colloids had been seen of polydispersion colloids in a range of 10 nm to 50 nm (Figure 4-47). RB5 was used as a target compound to examine the reactivity of these HA co-precipitated metals, as shown in Figure 4-48. RB5 was removed within 44 days by both Cu and Fe colloids in the presence of UHA; however, no removal was found for HA only. The removal efficiency was approximately 80% by Cu colloids within 22 hours while 50% of RB5 removal was observed by Fe colloids with similar metal/HA ratio of 6.8×10^2 mol/kg (i.e. the concentrations of HA and metal ions were 20 mg/L and 10 g/L, respectively). As increased the HA concentration to 60 mg/L, RB5 removal rate was slightly increased but with a similar removal efficiency (approximately 80%). To understand the formation process and the reaction mechanism of these small and well-distributed metal colloids, the following experiments were designed to use Cu^{2+} as a precursor to analyse the property of HA co-precipitated Cu colloids.

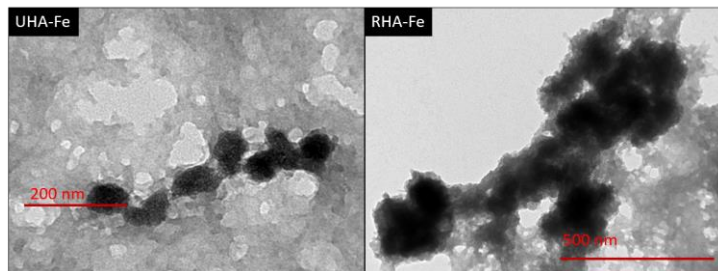


Figure 4-46. TEM images of Fe colloids in the presence of UHA and RHA. HA concentration was 20 mg/L and Fe^{2+} concentration was 10 g/L.

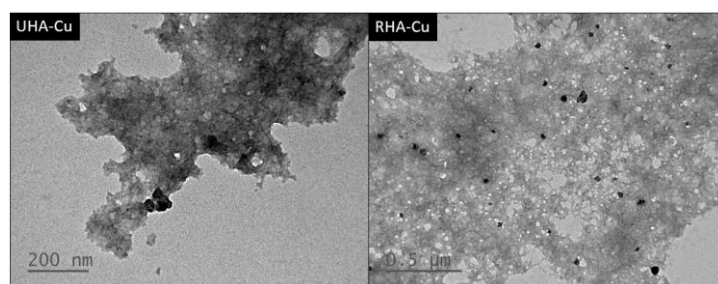


Figure 4-47. TEM images of Cu colloids in the presence of UHA and RHA. HA concentration was 20 mg/L and Cu^{2+} concentration was 10 g/L.

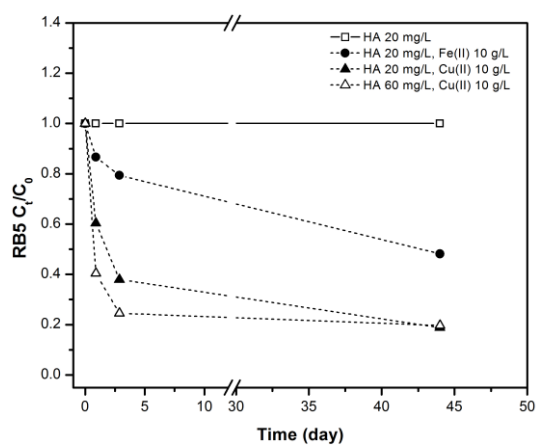


Figure 4-48. Removal of RB5 by metal ions in the presence of HA. RB5 initial concentration was 50 mg/L. HA concentrations were 20 and 60 mg/L. Concentration of Fe^{2+} and Cu^{2+} was 10 g/L.

4.6.1. The formation of Cu colloids in the absence and in the presence of HA

All the experiments were performed in the glovebox to mimic an anoxic condition, in which the oxygen content of these systems should be lower than 0.1 ppm. The species of Cu vary with different factors such as pH, oxygen content and redox level. The Cu speciation was predicted by Visual MINTEQ under different conditions, as shown in Figure 4-49. In the absence of HA, almost 100% of Cu^{2+} precipitated as pH higher than 6.5, and the Cu species was transformed from brochantite ($\text{Cu}_4\text{SO}_4(\text{OH})_6$) into tenorite (CuO , $k_{\text{sp}}=2 \times 10^{-19}$) at pH 6.7 according to the MINTEQ database.

At a ratio of $6.4 \text{ mmol}_{\text{Cu}^{2+}}/\text{g}_{\text{HA}}$, HA enhanced the Cu dissolution from DOM bonded Cu complexes. The presence of HA enhanced the Cu dissolution from DOM bonded Cu complexes and also induced a slight change in conversion point of Cu minerals from pH 6.7 shift to 6.6 (Figure 4-49). As adding the precursor Cu^{2+} into UHA, the pH decreased from pH 9.8 to pH 8.9 with an increase of Eh from 150 mV to 247 mV (Figure 4-50a). The presence of UHA altered the pH and the Eh with time, influencing the type of Cu precipitates. There was 26% of dissolved Cu, including inorganic Cu^{2+} and DOM bonded Cu, that released into the solution after mixing 1.0 g/L UHA with 1.6 g/L Cu^{2+} , i.e. approximately 74% of Cu^{2+} formed colloids in the presence of UHA (Figure 4-51). The stability constant between HA and Cu^{2+} is very strong ($\log K_{\text{Cu}^{2+}\text{-HA}} = 8.65\text{-}10.95$) (Prado et al., 2006; Takamatsu and Yoshida, 1978) because the carboxylic groups in HA molecules cause a high affinity to the metal ions (Gondar et al., 2006; Prado et al., 2006). Cu^{2+} was partially trapped within UHA and then co-precipitated into colloids, as called UHA-Cu, as shown in TEM images (Figure 4-52). These Cu colloids embedded within an

organic matrix that were spherical in shape with an average particle size of 8.25 nm although they have a hydrodynamic size of over 5 μm (Figure 4-53).

RHA may exhibit a different interaction with Cu^{2+} on the formation of Cu co-precipitates. In the beginning, the E_h of HA decreased to -522 mV as adding reductant (NaBH_4) and then increased until -117 mV after reducing for 8 hours (Figure 4-50b). The standard redox potentials of NOM were revealed to be between 150 and -300 mV depend on their functional groups (Aeschbacher et al., 2009; Aeschbacher et al., 2011). LHA has been reported with a redox potential close to -120 mV at the pH of 7 to 9 (under a condition: 2 g/L of LHA; $n_e=0.54$ mmol $_e^-$ /g $_{\text{LHA}}$) (Aeschbacher et al., 2011). After adjusting the pH to 7, the precursor, Cu^{2+} was added to the RHA solution causing a sharp change in E_h (453 mV) and pH (approximately pH 5). These redox conditions change with time after adding the reductant to react with the oxidant of Cu^{2+} . The final E_h of RHA-Cu was approximately 281 mV after 32 hours of mixing. As compared to UHA, most of the free Cu^{2+} was immobilized by RHA due to the presence of Cu co-precipitated with RHA (Figure 4-51). Highly uniform colloids were dispersed in the RHA solution with an average size of 3.6 nm based on the TEM images (Figure 4-52). A z-average size of 433 nm was found by DLS (Figure 4-53).

The particle stability of HA-Cu colloids evaluated using a sedimentation curve was shown in Figure 4-54. The results clearly suggested that RHA-Cu colloids had higher stability as compared to UHA-Cu colloids. RHA-Cu colloids were suspended within the HA medium for 100 minutes while UHA-Cu started sedimentation to the bottom, gradually losing their stability. Aggregation and sedimentation can significantly reduce the mobility and remediation efficiency of engineered NPs in an aquatic environment for water

treatment purposes. With the addition of NOM (1 mg/L), the negative surface charge of the metal NPs increased significantly, and their propensity to aggregate was reduced (Zhang et al., 2009). This behavior was due to the adsorption of NOM molecules onto the surface of metal particles, which sterically stabilizes the particle suspension (Delay et al., 2011). Johnson et al. (2009) noted that Fe NPs were stable and highly mobile at NOM concentrations of 20 mg/L or greater. Bian et al. (2011) noted that ZnO nanoparticle suspensions became more stable in the presence of HA in a range of 7.3 to 14.3 mg/L, but NPs lose their stability at longer durations because the bridging between the NPs via multiple functional groups of HA molecules. HA has different effects on the aggregation and stabilization of metal NPs, and these effects are influenced by the water quality factors such as pH and IS values (Zhu et al., 2014). In this study, NOM was expected to promote not only NP stabilization but also their disaggregation. HA exhibits a strong negative charge from -69.0 ± 2.4 mV at pH 11 to -30.2 ± 0.8 mV at pH 3, mainly due to the presence of carboxylic acid and phenolic functional groups (Piccolo, 2002).

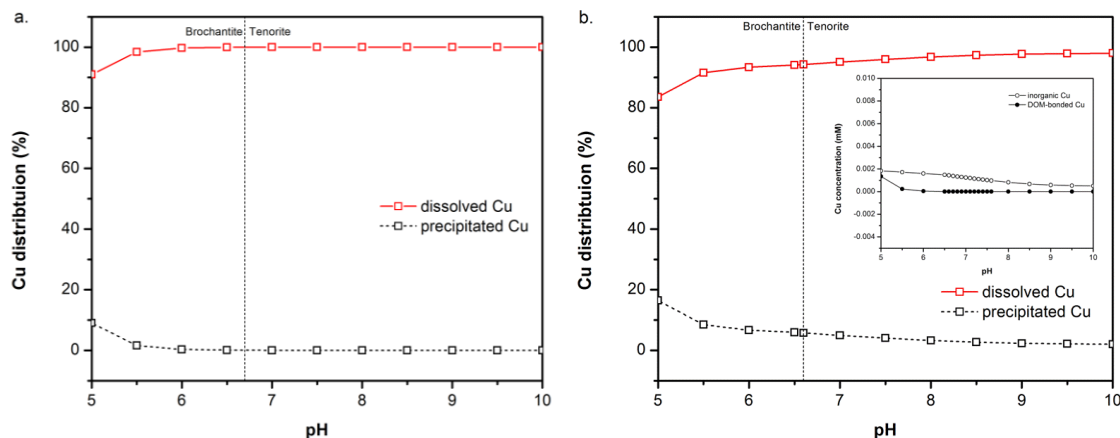


Figure 4-49. Cu distribution in (a) the Cu^{2+} system and (b) HA-Cu system predicted by Visual MINTEQ. For speciation prediction, CuSO_4 concentration was 1.6 g/L and DOM (HA) was 500 mg/L. SHM model was applied for the HA-Cu system in this study.

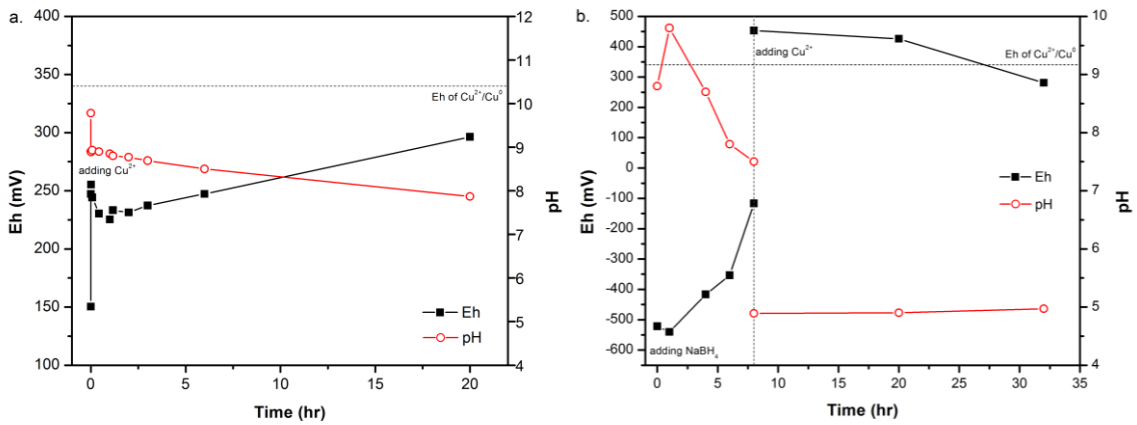


Figure 4-50. The Eh and the pH values in (a) the UHA system and (b) the RHA system.

HA concentration was 1.0 g/L and Cu^{2+} concentration was 1.6 g/L.

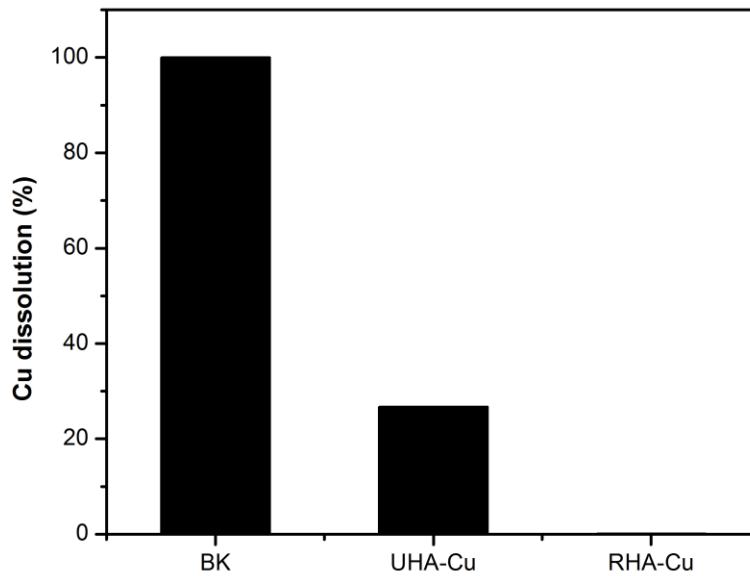


Figure 4-51. Dissolved Cu in the absence and in the presence of HA after 24 hours of synthesis. Initial Cu^{2+} concentration was 1.6 g/L and HA concentration was 1.0 mg/L.

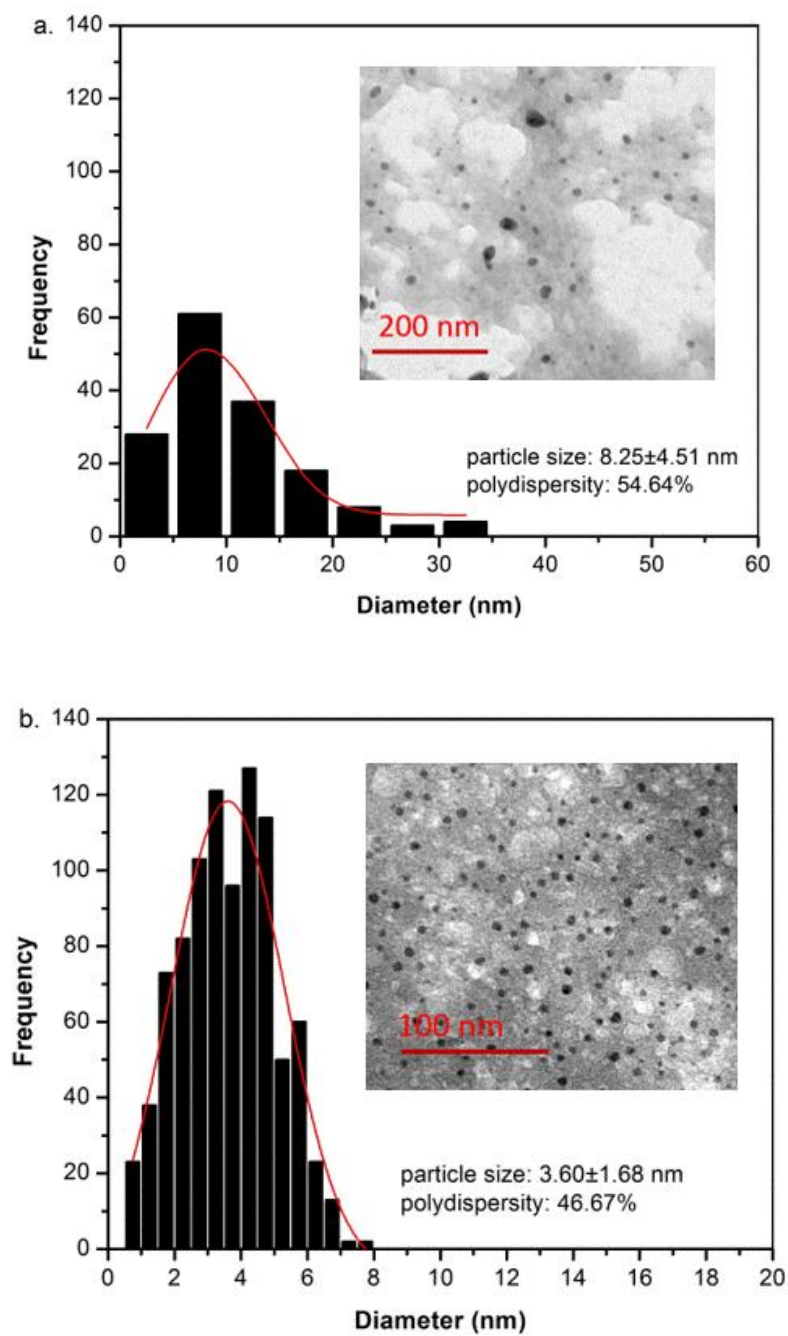


Figure 4-52. The size distribution of Cu colloids in the presence of UHA and RHA, calculating by ImageJ and OriginLab software. Particle numbers were 159 and 932 in UHA and RHA systems, respectively.

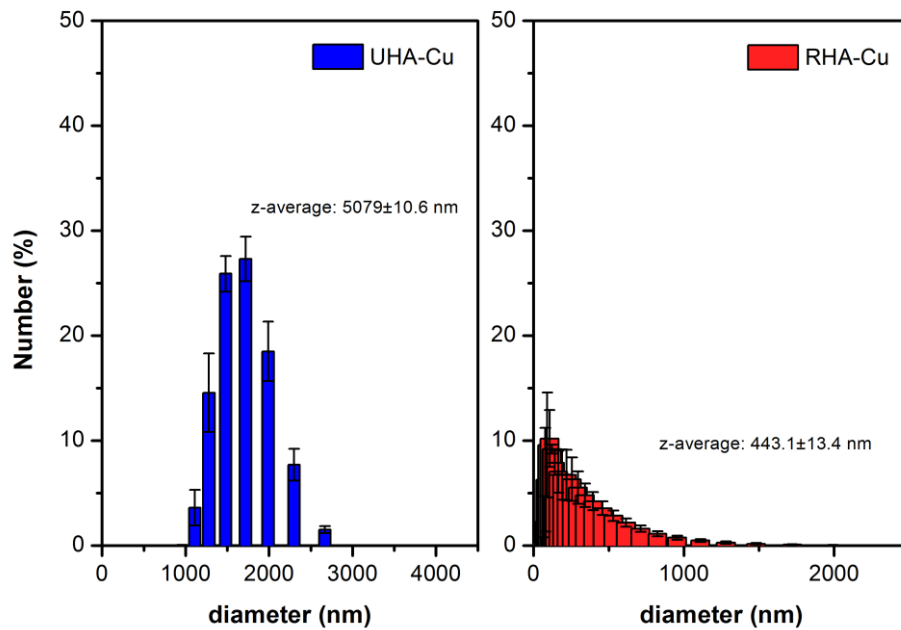


Figure 4-53. The hydrodynamic particle size of UHA-Cu and RHA-Cu colloids. The signals were presented by the Number distribution.

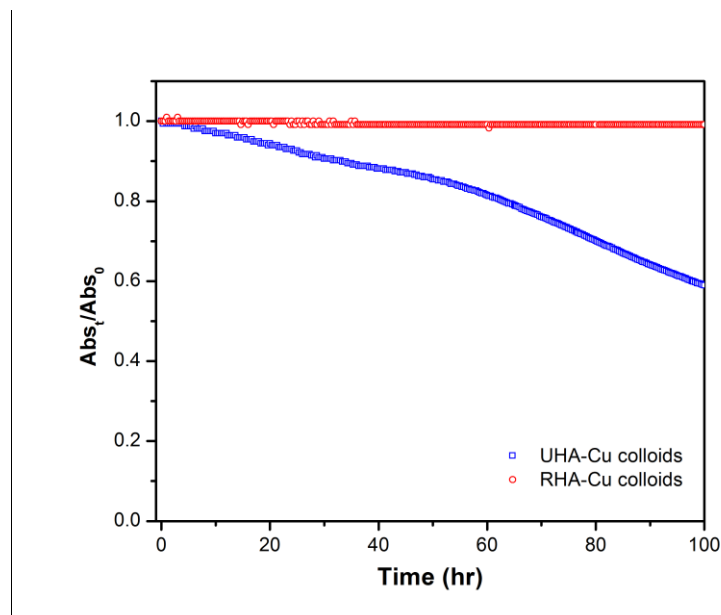


Figure 4-54. The sedimentation curves of HA-Cu NPs. The reading was performed at an absorbance of 510 nm.

4.6.2. The characteristics of Cu colloids in the presence of HA

Cu K-edge XANES spectra of HA-Cu samples were illustrated in Figure 4-55 along with the corresponding linear combination fits (LCF). Both samples showed one resonance-peak range from 8980 to 9000 eV represented “reduced Cu species”. The appearance of a peak below 8984 eV indicates the presence of Cu^+ in the sample. The spectra also appear that the peak at 8979 eV can be taken as a characteristic fingerprint of Cu^0 .

To quantitatively estimate the amounts of Cu, Cu_2O and CuO present, the LCF procedure applies four reference standards, namely Cu^0 , Cu_2O , CuO and CuSO_4 . For Cu, the LCF results shown in Figure 4-55 were compiled from Figure 4-56. The energy and shape of peaks can provide insight into the type of Cu present, and the height of the peak allows quantification of the amount of cuprous ion present. 80% of total Cu was the dominant CuSO_4 form in the UHA-Cu sample, followed CuO comprised for 20%. In contrast, the major Cu species of RHA-Cu colloids comprised CuSO_4 and CuO , but also small amount of Cu^{2+} reduced to Cu_2O as well as Cu^0 . As Cu ions complex with HA, electrons may transfer directly to HA-Cu complexes and further form Cu^0 particles (Fulda et al., 2013). In this study, RHA had a significantly higher reducing ability than UHA.

Maurer et al. (2013) pointed out that the Cu^+ binding to HA was found to be stronger compared to that of other chalcophilic cations such as Ag^+ or Cd^{2+} . According to the differences in Cu^+ and Cu^{2+} binding, the presence of HA was found to extend the stability field of Cu^{2+} to moderately reducing conditions and to reduce the stability field of Cu^0 due to the formation of Cu^+ complexes (Maurer et al., 2013).

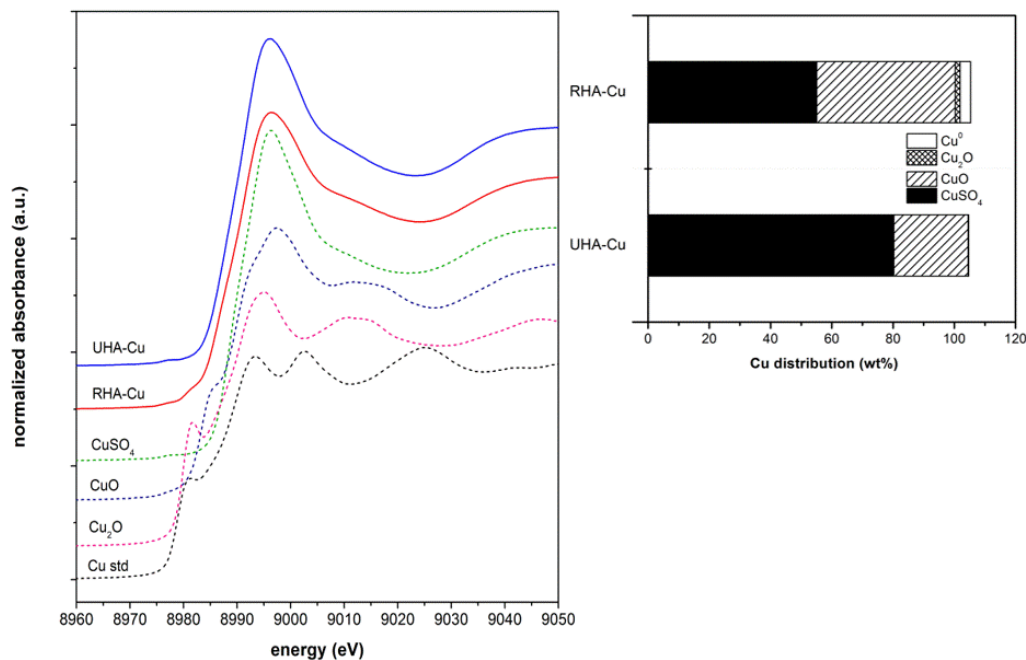


Figure 4-55. XANES spectra and LCF results of HA-Cu colloids. HA concentration was 1.0 g/L and Cu^{2+} concentration was 1.6 g/L. The standards applied for the fitting were Cu foil, Cu_2O , CuO and CuSO_4 .

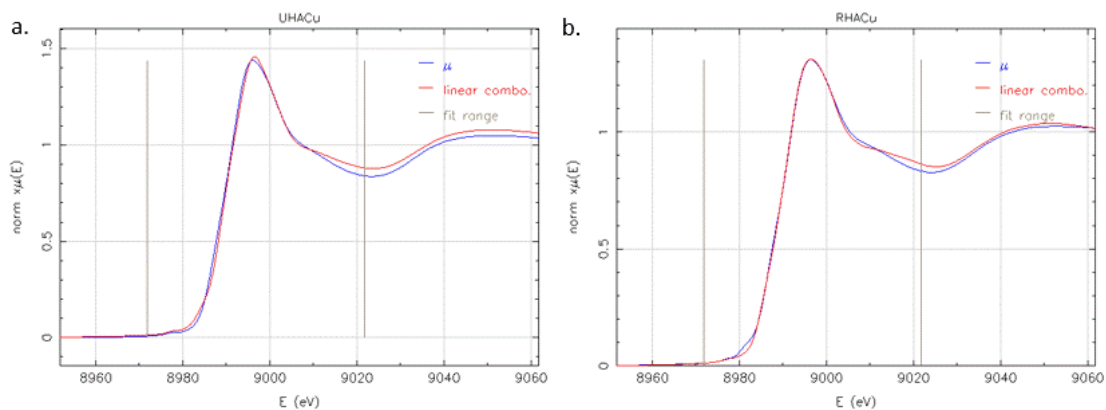


Figure 4-56. The LCF results of (a) UHA-Cu and (b) RHA-Cu. The fitting range was between -20 and $+30$ eV of Cu (8979 eV)

4.6.3. The bonding mechanism for Cu colloids in the presence of HA

From FTIR spectra (Figure 4-57), HA presented a notable peak at approximately 1712 cm^{-1} , representing free carboxylate groups (Figure 4-57). Ricca et al. (1993) noted that for LHA, the carboxyl and phenolic groups represent 30.7 and 69.3% of the total acidity, respectively. Peaks in the 2970-2860 cm^{-1} region was characterized as the CH stretching bands of methyl and methylene groups, accompanying a shoulder at 1425 cm^{-1} that assigned as the deformation of CH_2 groups. A broad band at about 2600-2500 cm^{-1} was due to the OH stretching vibrations of the H-bonded COOH. A sharp and strong band at 1715 cm^{-1} was identified as the C=O stretching vibration of COOH groups in aliphatic acids; a large band at 1630-1610 cm^{-1} could result by overlaying of the asymmetric vibration of carboxylate anion and of the C=O stretching band of COOH groups, and probably of the -CO stretching of amide. The broad band centered at 1230 cm^{-1} confirmed the presence of COOH groups, this band could be due to the OH deformation mode coupled with the C-O stretching mode in carboxylic groups (Cuba-Chiem et al., 2008; Lin et al., 2009; Max and Chapados, 2004; Ricca et al., 1993). For RHA, the IR spectrum was similar with UHA (Maurer et al., 2010).

There were peaks in both UHA-Cu and RHA-Cu at approximately 1380 and 1550-1618 cm^{-1} owing to the symmetric and asymmetric carboxylate vibrations, indicating that the HA complexes with Cu^{2+} via chemical bonding. The carboxylic acid groups of HA (R-COOH) were converted to carboxylates (R-COO^-) by forming coordinate bonds with Cu^{2+} . The separation $\Delta\nu$ between the asymmetric and symmetric stretching vibrations of R-COO^- was obtained from the FTIR spectra of the HA-Cu complexes. The bonding mechanisms are summarized as monodentate chelating ($\Delta\nu$ from 200 to 320 cm^{-1}),

bidentate chelating ($\Delta\nu$ is less than 110 cm^{-1}) and bidentate bridging ($\Delta\nu$ from 140 to 190 cm^{-1}) (Kirwan et al., 2003; Wu et al., 2004). The $\Delta\nu$ value (228 cm^{-1}) for the RHA-Cu was significantly larger than the reference value of $\Delta\nu$ for uncomplexed -COO^- , demonstrating that R-COO^- of RHA formed an unidentate complex with Cu^{2+} . The peaks at 1381 and 1550 cm^{-1} in UHA-Cu were insignificant, and the formation of bonding between UHA and Cu^{2+} was unclear, although a $\Delta\nu$ value of 169 cm^{-1} was observed.

In contrast, Lu and Allen (2002) noted that the phenolic groups in humic substances interact with metal ions. Phenolic, rather than the more acidic carboxyl sites, account for the majority of the DOM-Cu complexation under natural water conditions, and the complexation is principally through the replacement of H^+ by Cu^{2+} at the phenolic binding sites. However, FTIR spectra reveal that carboxylic acid groups were the major sites accounted for the HA-Cu complexation rather than phenolic groups in this study.

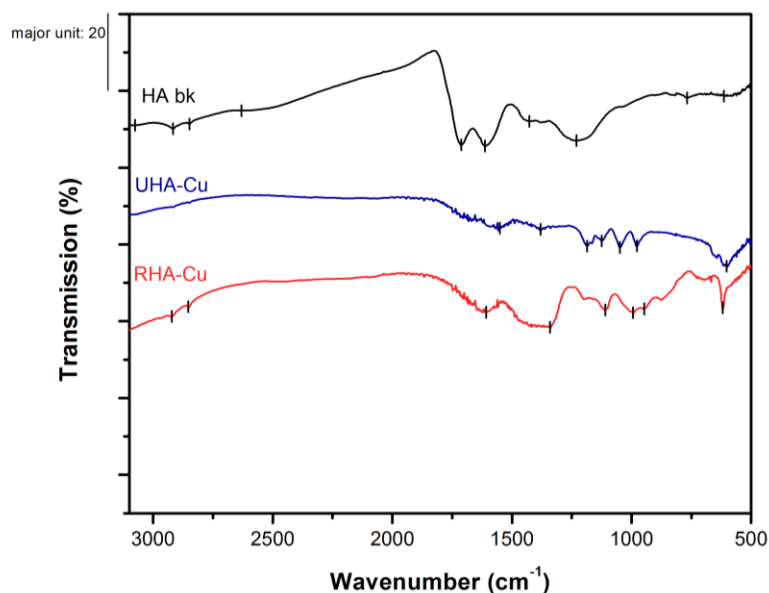


Figure 4-57. FTIR spectra of HA-Cu. IR technique was associated with synchrotron radiation.

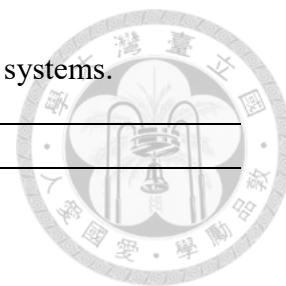


Table 4-3. Peak wavenumber and vibrational mode for HA and HA-Cu systems.

Wavenumber (cm ⁻¹)			Vibrational mode
HA	UHA-Cu	RHA-Cu	
613	601	619	C≡C-H
-	977	947	C-H stretch
-	1124	1109	C-OH stretch
1230	1186	1200	C-O stretch (carboxylic acid)
-	1381	1380	-COO ⁻ symmetric stretch
1427	-	-	-CH ₂ asymmetric deformation
-	1550	1618	-COO ⁻ asymmetric stretch
1612	-	-	C-C stretch (aromatic ring)
1712	-	-	C=O stretch (carboxylate or aldehyde)
2630	-	-	O-H stretch (carboxylic acid)
2848	-	2852	C-H stretch
2916	-	2921	C-H stretch

Ref: (Cuba-Chiem et al., 2008; Lin et al., 2009; Max and Chapados, 2004; Ricca et al., 1993)

4.6.4. The reaction mechanism for Cu colloids in the presence of HA

The removal of RB5 within 24 hours by HA-Cu colloids could be described in terms of its first-order-reaction constant (Figure 4-58). The results revealed that HA did not seem to affect the RB5 removal. The presence of RHA-Cu colloids promoted a removal rate ($k_{\text{obs}}=0.34 \text{ h}^{-1}$) as compared with the UHA-Cu samples ($k_{\text{obs}}=0.11 \text{ h}^{-1}$). RB5 in the NaBH₄ control system did not vary with time in 24 hours, indicating that the reductant of NaBH₄ applied here would merely an effect on the RB5 transformation.

The transformation of RB5 structure causes a color-changed phenomenon that further interrupted the measurement of RB5 concentration, thus notable error bars was observed in HA-Cu systems (Figure 4-58). Therefore, to completely elucidate the decolorization mechanisms of RB5 by UHA-Cu colloids, the UV-vis absorption spectra of RB5 were examined with time, as shown in Figure 4-59. For RB5, the UV-vis spectrum consisted of

two main characteristic absorption bands (Figure 4-59a), one in the UV region (310 nm) and the other in the visible region (596 nm). The UV band is characteristic of two adjacent rings, whereas the visible band represents the long conjugated π system linked by two azo groups (Lucas and Peres, 2006). When RB5 was removed by UHA-Cu colloids, it can clearly be observed that the intensity of the absorption peak in the visible region (596 nm) disappeared in several hours. The UV band at 310 nm was also observed to vanish but at a faster rate than the visible band. During the degradation, the absorbance values diminish across the spectral window and no specific peak remains after the reaction.

A comparison for the RHA-Cu samples exhibited a diminution of the absorption peak at both the visible and the ultraviolet λ_{\max} ; in the meantime, an appearance of new absorption peaks was found at wavelengths of approximately 350 nm and 530 nm (Figure 4-59b). Both the blueshift in the visible λ_{\max} of 596 nm to 530 nm and the redshift in the UV λ_{\max} of 310 nm to 350 nm indicated of structural changes in RB5 molecules that led to the change in their color. Sugano et al. (2009) attributed this phenomenon to the formation of red molecules resulting from the cleavage of one of the two azo bonds in the RB5 molecule, which then mixed with the unreduced RB5 molecules. The absorbance at 596 nm decreased and the absorbance at 500-530 nm increased as the color of the reaction solution became red-brown, which has been identified as 2,2'-disulfonyl azobenzene (Sugano et al., 2009). A change in the structure of RB5 under anaerobic conditions had been previously reported in activated sludge (Bonakdarpour et al., 2011). One of the two azo bonds in the RB5 molecule was stabilized in the ketohydrazone form, whereas the other existed in the azo form. The reduced metal particles with higher chemical reactivity have a preference for the cleavage of the two azo bonds; however, our RHA-Cu colloids could

not have such a good reactivity. RHA-Cu could reduce RB5 by break one azo bond and may form 2,2'-disulfonyl azobenzene.

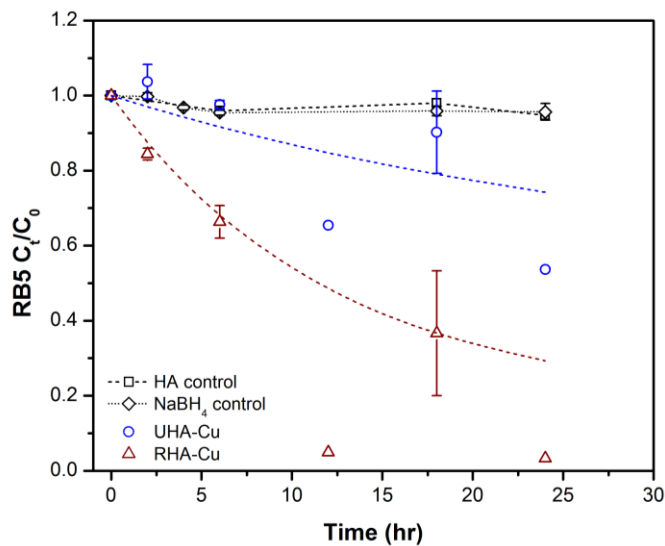


Figure 4-58. The removal of RB5 by HA-Cu colloids. The initial concentration of RB5 was 10 mg/L, HA and Cu²⁺ concentrations were 1 g/L and 1.6 g/L, respectively. The error bar in Figure 4-58 represent the standard error of an average over duplicated batch experiments.

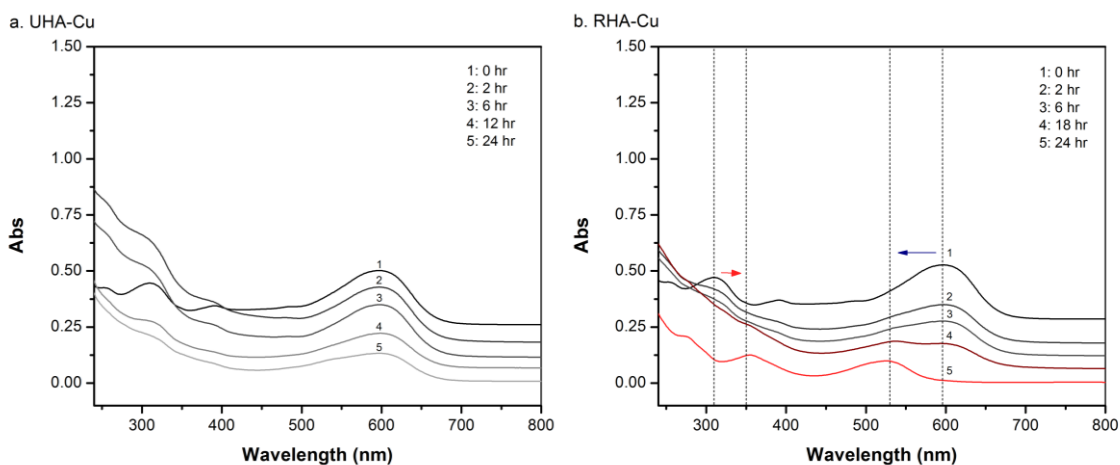


Figure 4-59. UV-visible spectra (200-750 nm) of RB5 at different time intervals during the reactions with (a) UHA-Cu and (b) RHA-Cu colloids.

Chapter 5 Conclusions



The findings of this study can be summarized by pointing out the interactions and detail mechanisms of well-suspended Fe NPs under environmentally relevant conditions and subsequently their potential for remediation in natural environments.

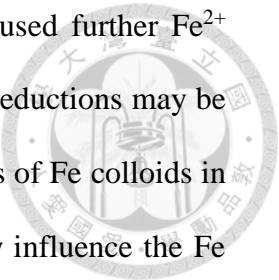
First, the US/stirring system dispersed bare Fe NPs most effectively in all the used physical dispersion methods (shaking, stirring, US and US/stirring) to the original nano-scale size. Dispersing the aggregates of Fe NPs resulted in an increase in adsorption of PCP onto the Fe surface. Under the operating conditions, US did not affect the surface characteristics of Fe NPs. In the presence of common anions (Cl^- , NO_3^- and HCO_3^-), NO_3^- was reduced by Fe NPs and generated more Fe (hydro)oxides that responded to adsorption or coagulation of the target compound; HCO_3^- significantly inhibited the Fe reactivity because the Fe carbonate precipitates blocked the adsorption and reaction sites on the Fe surface while Cl^- only caused a small increase in the Fe reactivity (Scheme 5-1a). These results offer the information to better understand the activity and removal mechanism of bare Fe NPs as well as the common ion effects.

In the CMC dispersion method, the CMC layer could suspend Fe NPs very well and disperse NPs into individual particles instead of nanoparticle aggregates. Due to the properties of CMC, the reactivity of CMC-Fe NPs to DBDE increased under alkaline conditions. The CMC layer may induce diffusion of the target compound to the Fe surface. Therefore, the activation energy of CMC-Fe NPs ($37.69 \text{ kJ mol}^{-1}$) toward DBDE revealed that a surface chemical reaction rather than a diffusion-mediated reaction was the rate-limiting step in the reaction. However, these layers could also inhibit the electron transfer from the surface to the molecules of the target compound. Anions did not influence the

reactivity of CMC-Fe NPs when compared to bare Fe NPs. CMC layers may hinder the attachment between anions and the Fe surface, also prolong the reactivity of Fe NPs in the environment (Scheme 5-1a). These results suggest some potential for CMC-Fe NPs for in-situ treatment which may prove profitable for future studies in the field of nanoremediation.

Second, common carboxylic ligands (FA, OA and CA) were chosen to investigate their effect on the reactivity toward TCE and surface characteristics of Fe particles. The reactivity of Fe particles in the presence of 30 mM carboxylic groups followed an order of $FA > OA > \text{pure water} \cong CA$. These carboxylic ligands did induce the reactivity of Fe particles by dissolving Fe oxides from the Fe surface via proton- and ligand-promoted processes. FA provides protons to promote the dissolution of passive layers. Moreover, magnetite formed on the Fe surface in the presence of FA may further be responsible for a high adsorption of the target compound. With the strong complexing ability of OA and CA, passive layers could form dissoluble complexes via a ligand-promoted dissolution process. For formate and citrate, increasing the ligand concentration enhanced the reaction rates; but high concentration of OA resulted Fe oxalate being reprecipitated back onto the Fe surface which then inhibited its reactivity. Furthermore, the formation of Fe-ligand complexes may have the ability to transform the target compound and its byproducts depending on their redox properties (Scheme 5-1b).

Third, the activities of Fe (Cu) complexes/colloids with HA pointed out the potential of Fe NPs for subsequent treatments. The activity of Fe^{2+} and HA-Fe complexes toward RB5 is a pH-dependent reaction that has strong interactions toward the target compound at pH 9. Fe complexes with RHA have higher reactivity than those with UHA; but the complex form potentially reduced Fe^{2+} reactivity because of electron competition with the

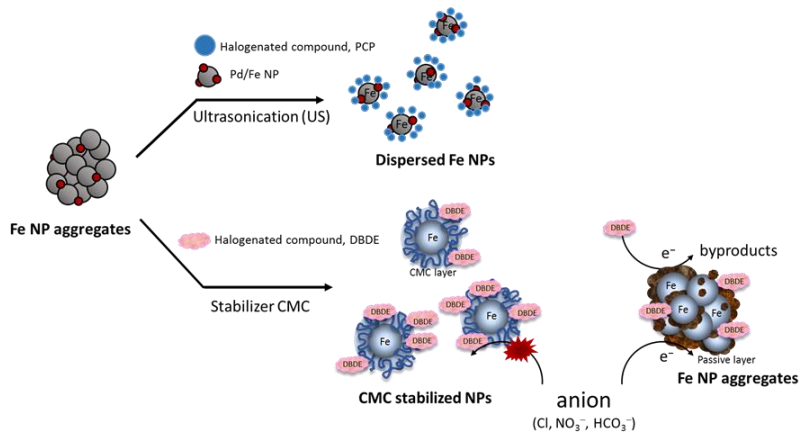


target compound. RHA prevented Fe^{2+} from precipitating but also caused further Fe^{2+} oxidation. Therefore, under anaerobic conditions, Fe colloid-mediated reductions may be the dominant pathway in natural systems containing high concentrations of Fe colloids in solution. In the presence of HA, RHA-Fe complexes may significantly influence the Fe distribution and decrease the reactivity of Fe^{2+} (Scheme 5-1c). Furthermore, HA coprecipitated Fe and Cu colloids showed abilities to remove the target compound. HA-Cu colloids even had a higher capacity than HA-Fe colloids and revealed clearly the shape and morphology. RHA-Cu colloids were stably dispersed in solutions with a size of 3.60 nm. Among them, a small amount of Cu ions was reduced to zero-valent by RHA, whereas UHA resulted in the formation of polydispersed Cu colloids with a size of 8.23 nm. RHA-Cu colloids also had a stronger reactivity than UHA-Cu colloids to break azo bonds in the molecules of the target compound. These results provide us to understand the characteristics and reactivity of metal complexes/colloids with HA in reducing environments and pointed out the potential of these complexes/colloids for the green remediation.

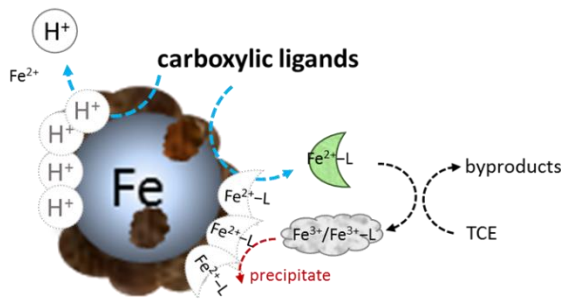
This study presents a clear concept about the reaction characteristics of Fe NPs that were well suspended under different conditions and in the presence of organic ligands. Moreover, for sustainable/green remediation, HA associated Fe (Cu) complexes and colloids in the reducing environment have the ability to transform organic contaminants.



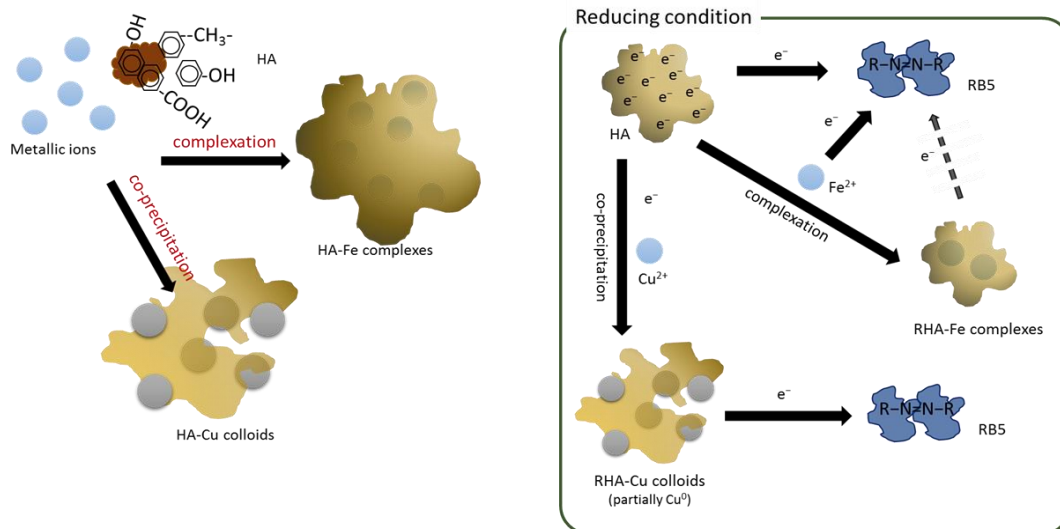
a. Stabilized Fe NPs



b. Refreshed Fe particles



c. Complexation and co-precipitation with HA



Scheme 5-1. The concept of this study. (a) The reaction mechanism of well-suspended Fe NP by the physical and the chemical dispersion methods (b) the effect of carboxylic ligands on the surface of Fe particles, (c) the interactions of HA and Fe (Cu) complexes/colloids.

Reference

- Abdel-Halim, E.S.; Hebeish, A.A.; El-Rafie, M.H.; Abdel-Mohdy, F.A.; Emam, H.E. Carboxymethyl cellulose for green synthesis and stabilization of silver nanoparticles. *Carbohydr Polym* **2010**, *82*, 933-941.
- Adeleye, A.S.; Keller, A.A.; Miller, R.J.; Lenihan, H.S. Persistence of commercial nanoscaled zero-valent iron (nZVI) and by-products. *J. Nanopart. Res.* **2013**, *15*, 1-18.
- Aeschbacher, M.; Sander, M.; Schwarzenbach, R.P. Novel electrochemical approach to assess the redox properties of humic substances. *Environ. Sci. Technol.* **2009**, *44*, 87-93.
- Aeschbacher, M.; Vergari, D.; Schwarzenbach, R.P.; Sander, M. Electrochemical analysis of proton and electron transfer equilibria of the reducible moieties in humic acids. *Environ. Sci. Technol.* **2011**, *45*, 8385-8394.
- Agrawal, A.; Ferguson, W.J.; Gardner, B.O.; Christ, J.A.; Bandstra, J.Z.; Tratnyek, P.G. Effects of carbonate species on the kinetics of dechlorination of 1,1,1-trichloroethane by zero-valent iron. *Environ. Sci. Technol.* **2002**, *36*, 4326-4333.
- Akaighe, N.; Depner, S.W.; Banerjee, S.; Sharma, V.K.; Sohn, M. The effects of monovalent and divalent cations on the stability of silver nanoparticles formed from direct reduction of silver ions by Suwannee River humic acid/natural organic matter. *Sci. Total Environ.* **2012**, *441*, 277-289.
- Akaighe, N.; Depner, S.W.; Banerjee, S.; Sohn, M. Transport and deposition of Suwannee river humic acid/natural organic matter formed silver nanoparticles on silica matrices: The influence of solution pH and ionic strength. *Chemosphere* **2013**, *92*, 406-412.
- Akaighe, N.; MacCusprie, R.I.; Navarro, D.A.; Aga, D.S.; Banerjee, S.; Sohn, M.; Sharma, V.K. Humic acid-induced silver nanoparticle formation under environmentally relevant conditions. *Environ. Sci. Technol.* **2011**, *45*, 3895-3901.
- Angelico, R.; Ceglie, A.; He, J.-Z.; Liu, Y.-R.; Palumbo, G.; Colombo, C. Particle size, charge and colloidal stability of humic acids coprecipitated with ferrihydrite. *Chemosphere* **2014**, *99*, 239-247.
- Arnold, W.A.; Roberts, A.L. Pathways and kinetics of chlorinated ethylene and chlorinated acetylene reaction with Fe(0) particles. *Environ. Sci. Technol.* **2000**, *34*, 1794-1805.
- Attwood, D. **2007**. Soft x-rays and extreme ultraviolet radiation: principles and applications. Cambridge university press.
- Auffan, M.; Achouak, W.; Rose, J.; Roncato, M.-A.; Chanéac, C.; Waite, D.T. et al. Relation between the redox state of iron-based nanoparticles and their cytotoxicity toward Escherichia coli. *Environ. Sci. Technol.* **2008**, *42*, 6730-6735.
- Baalousha, M.; Manciulea, A.; Cumberland, S.; Kendall, K.; Lead, J.R. Aggregation and surface properties of iron oxide nanoparticles: influence of pH and natural organic matter. *Environ. Toxicol. Chem.* **2008**, *27*, 1875-1882.
- Badawy, A.M.E.; Luxton, T.P.; Silva, R.G.; Scheckel, K.G.; Suidan, M.T.; Tolaymat, T.M. Impact of environmental conditions (pH, ionic strength, and electrolyte type) on the surface charge and aggregation of silver nanoparticles suspensions. *Environ. Sci. Technol.* **2010**, *44*, 1260-1266.

- Baigorri, R.; García-Mina, J.M.; Aroca, R.F.; Alvarez-Puebla, R.A. Optical enhancing properties of anisotropic gold nanoplates prepared with different fractions of a natural humic substance. *Chem Mater* **2008**, *20*, 1516-1521.
- Bazin, D.; Rehr, J.J. Limits and advantages of X-ray absorption near edge structure for nanometer scale metallic clusters. *The Journal of Physical Chemistry B* **2003**, *107*, 12398-12402.
- Berka, M.; Rice, J.A. Absolute aggregation rate constants in aggregation of kaolinite measured by simultaneous static and dynamic light scattering. *Langmuir* **2004**, *20*, 6152-6157.
- Bi, E.P.; Bowen, I.; Devlin, J.F. Effect of mixed anions (HCO_3^- - SO_4^{2-} - ClO_4^-) on granular iron (Fe^0) reactivity. *Environ. Sci. Technol.* **2009**, *43*, 5975-5981.
- Bian, S.-W.; Mudunkotuwa, I.A.; Rupasinghe, T.; Grassian, V.H. Aggregation and dissolution of 4 nm ZnO nanoparticles in aqueous environments: influence of pH, ionic strength, size, and adsorption of humic acid. *Langmuir* **2011**, *27*, 6059-6068.
- Bilgi, S.; Demir, C. Identification of photooxidation degradation products of C. I. Reactive Orange 16 dye by gas chromatography–mass spectrometry. *Dyes Pigments* **2005**, *66*, 69-76.
- Biver, M.; Shoty, W. Experimental study of the kinetics of ligand-promoted dissolution of stibnite (Sb_2S_3). *Chemical Geology* **2012**, *294–295*, 165-172.
- Bokare, A.D.; Chikate, R.C.; Rode, C.V.; Paknikar, K.M. Effect of surface chemistry of Fe–Ni nanoparticles on mechanistic pathways of azo dye degradation. *Environ. Sci. Technol.* **2007**, *41*, 7437-7443.
- Bokare, A.D.; Chikate, R.C.; Rode, C.V.; Paknikar, K.M. Iron-nickel bimetallic nanoparticles for reductive degradation of azo dye Orange G in aqueous solution. *Appl Catal B-Environ* **2008**, *79*, 270-278.
- Bonakdarpour, B.; Vyrides, I.; Stuckey, D.C. Comparison of the performance of one stage and two stage sequential anaerobic–aerobic biological processes for the treatment of reactive-azo-dye-containing synthetic wastewaters. *Int. Biodeterior. Biodegrad.* **2011**, *65*, 591-599.
- Bratsch, S.G. Standard electrode potentials and temperature coefficients in water at 298.15 K. *J. Phys. Chem. Ref. Data* **1989**, *18*, 1-21.
- Brezonik, P.L. **1994**. Chemical kinetics and process dynamics in aquatic systems. Lewis Publishers.
- Bussan, A.L.; Strathmann, T.J. Influence of organic ligands on the reduction of polyhalogenated alkanes by iron(II). *Environ. Sci. Technol.* **2007**, *41*, 6740-6747.
- Butler, E.C.; Hayes, K.F. Kinetics of the transformation of trichloroethylene and tetrachloroethylene by iron sulfide. *Environ. Sci. Technol.* **1999**, *33*, 2021-2027.
- Butler, E.C.; Hayes, K.F. Kinetics of the transformation of halogenated aliphatic compounds by iron sulfide. *Environ. Sci. Technol.* **2000**, *34*, 422-429.
- Cao, C.; Qu, J.; Yan, W.; Zhu, J.; Wu, Z.; Song, W. Low-cost synthesis of flowerlike α - Fe_2O_3 nanostructures for heavy metal ion removal: Adsorption property and mechanism. *Langmuir* **2012**, *28*, 4573-4579.
- Cao, J.; Wei, L.; Huang, Q.; Wang, L.; Han, S. Reducing degradation of azo dye by zero-valent iron in aqueous solution. *Chemosphere* **1999**, *38*, 565-571
- Chaurand, P.; Rose, J.; Briois, V.; Olivi, L.; Hazemann, J.-L.; Proux, O.; Domas, J.; Bottero, J.-Y. Environmental impacts of steel slag reused in road construction: A

- crystallographic and molecular (XANES) approach. *J Hazard Mater* **2007**, *139*, 537-542.
- Chen, J.-L.; Al-Abed, S.R.; Ryan, J.A.; Li, Z. Effects of pH on dechlorination of trichloroethylene by zero-valent iron. *J Hazard Mater* **2001**, *83*, 243-254.
- Chen, J.; Gu, B.; Royer, R.A.; Burgos, W.D. The roles of natural organic matter in chemical and microbial reduction of ferric iron. *Sci. Total Environ.* **2003**, *307*, 167-178.
- Chen, K.L.; Elimelech, M. Aggregation and deposition kinetics of fullerene (C60) nanoparticles. *Langmuir* **2006**, *22*, 10994-11001.
- Cheng, I.F.; Fernando, Q.; Korte, N. Electrochemical dechlorination of 4-Chlorophenol to phenol. *Environ. Sci. Technol.* **1997**, *31*, 1074-1078.
- Cheng, S.F.; Wu, S.C. The enhancement methods for the degradation of TCE by zero-valent metals. *Chemosphere* **2000**, *41*, 1263-1270.
- Christian, P.; Von Der Kammer, F.; Baalousha, M.; Hofmann, T. Nanoparticles: Structure, properties, preparation and behaviour in environmental media. *Ecotoxicology* **2008**, *17*, 326-343.
- Chu, W.; Kwan, C.Y. Remediation of contaminated soil by a solvent/surfactant system. *Chemosphere* **2003**, *53*, 9-15.
- Chung, K.T.; Cerniglia, C.E. Mutagenicity of azo dyes: Structure-activity relationships. *Mutat Res* **1992**, *277*, 201-220.
- Coccia, F.; Tonucci, L.; Bosco, D.; Bressan, M.; d'Alessandro, N. One-pot synthesis of lignin-stabilised platinum and palladium nanoparticles and their catalytic behaviour in oxidation and reduction reactions. *Green Chemistry* **2012**, *14*, 1073-1078.
- Cornell, R.M.; Schwertmann, U. **2006**. The iron oxides: structure, properties, reactions, occurrences and uses. John Wiley & Sons.
- Crane, R.A.; Dickinson, M.; Popescu, I.C.; Scott, T.B. Magnetite and zero-valent iron nanoparticles for the remediation of uranium contaminated environmental water. *Water Res.* **2011**, *45*, 2931-2942.
- Crane, R.A.; Scott, T.B. Nanoscale zero-valent iron: future prospects for an emerging water treatment technology. *J Hazard Mater* **2012**, *211-212*, 112-125.
- Cuba-Chiem, L.T.; Huynh, L.; Ralston, J.; Beattie, D.A. In situ particle film ATR FTIR spectroscopy of carboxymethyl cellulose adsorption on talc: binding mechanism, pH effects, and adsorption kinetics. *Langmuir* **2008**, *24*, 8036-8044.
- Cumberland, S.A.; Lead, J.R. Synthesis of NOM-capped silver nanoparticles: size, morphology, stability, and NOM binding characteristics. *ACS Sustainable Chem. Eng.* **2013**, *1*, 817-825.
- Cunha, G.C.; Romão, L.P.C.; Santos, M.C.; Costa, A.S.; Alexandre, M.R. A green strategy for desorption of trihalomethanes adsorbed by humin and reuse of the fixed bed column. *J Hazard Mater* **2012**, *209-210*, 9-17.
- Cunha, G.d.C.; Romão, L.P.C.; Santos, M.C.; Araújo, B.R.; Navickiene, S.; de Pádua, V.L. Adsorption of trihalomethanes by humin: batch and fixed bed column studies. *Bioresource Technol* **2010**, *101*, 3345-3354.
- Cwiertny, D.M.; Bransfield, S.J.; Livi, K.J.T.; Fairbrother, D.H.; Roberts, A.L. Exploring the influence of granular iron additives on 1,1,1-trichloroethane reduction. *Environ. Sci. Technol.* **2006**, *40*, 6837-6843.

- da Costa Cunha, G.; Romão, L.P.C.; Macedo, Z.S. Production of alpha-alumina nanoparticles using aquatic humic substances. *Powder Technol.* **2014**, *254*, 344-351.
- Delay, M.; Dolt, T.; Woellhaf, A.; Sembritzki, R.; Frimmel, F.H. Interactions and stability of silver nanoparticles in the aqueous phase: influence of natural organic matter (NOM) and ionic strength. *J. Chromatogr. A* **2011**, *1218*, 4206-4212.
- Deonaraine, A.; Hsu-Kim, H. Precipitation of mercuric sulfide nanoparticles in NOM-containing water: implications for the natural environment. *Environ. Sci. Technol.* **2009**, *43*, 2368-2373.
- Deonaraine, A.; Lau, B.L.T.; Aiken, G.R.; Ryan, J.N.; Hsu-Kim, H. Effects of humic substances on precipitation and aggregation of zinc sulfide nanoparticles. *Environ. Sci. Technol.* **2011**, *45*, 3217-3223.
- Devlin, J.F.; Allin, K.O. Major anion effects on the kinetics and reactivity of granular iron in glass-encased magnet batch reactor experiments. *Environ. Sci. Technol.* **2005**, *39*, 1868-1874.
- Dickson, D.; Liu, G.L.; Li, C.Z.; Tachiev, G.; Cai, Y. Dispersion and stability of bare hematite nanoparticles: effect of dispersion tools, nanoparticle concentration, humic acid and ionic strength. *Sci. Total Environ.* **2012**, *419*, 170-177.
- Diegoli, S.; Manciuola, A.L.; Begum, S.; Jones, I.P.; Lead, J.R.; Preece, J.A. Interaction between manufactured gold nanoparticles and naturally occurring organic macromolecules. *Sci. Total Environ.* **2008**, *402*, 51-61.
- Díez-Pérez, I.; Sanz, F.; Gorostiza, P. In situ studies of metal passive films. *Curr. Opin. Solid State Mater. Sci.* **2006**, *10*, 144-152.
- Dolfing, J.; VanEckert, D.; Mueller, J. Thermodynamics of low Eh reactions. *Proceedings Battelle's Fifth International Conference on Remediation of Chlorinated and Recalcitrant Compounds* **2006**,
- Domingos, R.F.; Baalousha, M.A.; Ju-Nam, Y.; Reid, M.M.; Tufenkji, N.; Lead, J.R.; Leppard, G.G.; Wilkinson, K.J. Characterizing manufactured nanoparticles in the environment: multimethod determination of particle sizes. *Environ. Sci. Technol.* **2009**, *43*, 7277-7284.
- Doong, R.A.; Lai, Y.J. Dechlorination of tetrachloroethylene by palladized iron in the presence of humic acid. *Water Res.* **2005**, *39*, 2309-2318.
- Eljarrat, E.; De La Cal, A.; Raldua, D.; Duran, C.; Barcelo, D. Occurrence and bioavailability of polybrominated diphenyl ethers and hexabromocyclododecane in sediment and fish from the Cinca River, a tributary of the Ebro River (Spain). *Environ. Sci. Technol.* **2004**, *38*, 2603-2608.
- Eljarrat, E.; Guerra, P.; Martinez, E.; Farre, M.; Alvarez, J.G.; Lopez-Teijon, M.; Barcelo, D. Hexabromocyclododecane in human breast milk: levels and enantiomeric patterns. *Environ. Sci. Technol.* **2009**, *43*, 1940-1946.
- Epolito, W.J.; Yang, H.; Bottomley, L.A.; Pavlostathis, S.G. Kinetics of zero-valent iron reductive transformation of the anthraquinone dye Reactive Blue 4. *J Hazard Mater* **2008**, *160*, 594-600.
- Fang, G.D.; Si, Y.B.; Tian, C.; Zhang, G.Y.; Zhou, D.M. Degradation of 2,4-D in soils by Fe₃O₄ nanoparticles combined with stimulating indigenous microbes. *Environ Sci Pollut R* **2012**, *19*, 784-793.

- Fang, Z.; Qiu, X.; Chen, J.; Qiu, X. Debromination of polybrominated diphenyl ethers by Ni/Fe bimetallic nanoparticles: influencing factors, kinetics, and mechanism. *J Hazard Mater* **2011**, *185*, 958-969.
- Farrell, J.; Kason, M.; Melitas, N.; Li, T. Investigation of the long-term performance of zero-valent iron for reductive dechlorination of trichloroethylene. *Environ. Sci. Technol.* **1999**, *34*, 514-521.
- Fernie, K.J.; Shutt, J.L.; Letcher, R.J.; Ritchie, I.J.; Bird, D.M. Environmentally relevant concentrations of DE-71 and HBCD alter eggshell thickness and reproductive success of American kestrels. *Environ. Sci. Technol.* **2009**, *43*, 2124-2130.
- Fulda, B.; Voegelin, A.; Maurer, F.; Christl, I.; Kretzschmar, R. Copper redox transformation and complexation by reduced and oxidized soil humic acid. 1. X-ray absorption spectroscopy study. *Environ. Sci. Technol.* **2013**, *47*, 10903-10911.
- Furrer, G.; Sticher, H. **2014**. Chemische verwitterungsprozesse. Handbuch der Bodenkunde. Wiley-VCH Verlag GmbH & Co. KGaA.
- Furrer, G.; Stumm, W. The coordination chemistry of weathering: I. Dissolution kinetics of δ -Al₂O₃ and BeO. *Geochim. Cosmochim. Acta* **1986**, *50*, 1847-1860.
- Giasuddin, A.B.M.; Kanel, S.R.; Choi, H. Adsorption of humic acid onto nanoscale zerovalent iron and its effect on arsenic removal. *Environ. Sci. Technol.* **2007**, *41*, 2022-2027.
- Girard, M.; Turgeon, S.L.; Paquin, P. Emulsifying properties of whey protein-carboxymethylcellulose complexes. *J. Food Sci.* **2002**, *67*, 113-119.
- Glavee, G.N.; Klabunde, K.J.; Sorensen, C.M.; Hadjipanayis, G.C. Chemistry of borohydride reduction of iron(II) and iron(III) ions in aqueous and nonaqueous media. Formation of nanoscale Fe, FeB, and Fe₂B powders. *Inorg. Chem.* **1995**, *34*, 28-35.
- Goerlitz, D.F.; Troutman, D.E.; Godsy, E.M.; Franks, B.J. Migration of wood-preserving chemicals in contaminated groundwater in a sand aquifer at Pensacola, Florida. *Environ. Sci. Technol.* **1985**, *19*, 955-961.
- Gondar, D.; Iglesias, A.; López, R.; Fiol, S.; Antelo, J.M.; Arce, F. Copper binding by peat fulvic and humic acids extracted from two horizons of an ombrotrophic peat bog. *Chemosphere* **2006**, *63*, 82-88.
- Gorgy, T.; Li, L.; Grace, J.; Ikonou, M. Polybrominated diphenyl ether leachability from biosolids and their partitioning characteristics in the leachate. *Water Air Soil Pollut* **2010**, *209*, 109-121.
- Gotpagar, J.; Lyuksyutov, S.; Cohn, R.; Grulke, E.; Bhattacharyya, D. Reductive dehalogenation of trichloroethylene with zero-valent iron: surface profiling microscopy and rate enhancement studies. *Langmuir* **1999**, *15*, 8412-8420.
- Guzenko, N.; Gabchak, O.; Pakhlov, E. **2011**. Multilayer films and capsules of sodium carboxymethylcellulose and polyhexamethylguanidine hydrochloride. In: P. J. Reithmaier, P. Paunovic, W. Kulisch, C. Popov and P. Petkov, editors, Nanotechnological Basis for Advanced Sensors. Springer Netherlands, Dordrecht. p. 59-64.
- Hakala, J.A.; Chin, Y.-P.; Weber, E.J. Influence of dissolved organic matter and Fe(II) on the abiotic reduction of pentachloronitrobenzene. *Environ. Sci. Technol.* **2007**, *41*, 7337-7342.

- Hamer, M.; Graham, R.C.; Amrhein, C.; Bozhilov, K.N. Dissolution of ripidolite (Mg, Fe-chlorite) in organic and inorganic acid solutions. *Soil Sci Soc Am J* **2003**, *67*, 654-661.
- Hamers, T.; Kamstra, J.H.; Sonneveld, E.; Murk, A.J.; Kester, M.H.A.; Andersson, P.L.; Legler, J.; Brouwer, A. In vitro profiling of the endocrine-disrupting potency of brominated flame retardants. *Toxicol Sci* **2006**, *92*, 157-173.
- Han, Y.; Wang, Y.; Li, L.; Wang, Y.; Jiao, L.; Yuan, H.; Liu, S. Preparation and electrochemical performance of flower-like hematite for lithium-ion batteries. *Electrochim. Acta* **2011**, *56*, 3175-3181.
- Hao, Z.P.; Tian, H.; Li, J.J.; Mu, Z.; Li, L.D. Effect of pH on DDT degradation in aqueous solution using bimetallic Ni/Fe nanoparticles. *Separation and Purification Technology* **2009**, *66*, 84-89.
- Harendra, S.; Vipulanandan, C. Degradation of high concentrations of PCE solubilized in SDS and biosurfactant with Fe/Ni bi-metallic particles. *Colloid Surface A* **2008**, *322*, 6-13.
- Harnly, M.E.; Petreas, M.X.; Flattery, J.; Goldman, L.R. Polychlorinated dibenzo-p-dioxin and polychlorinated dibenzofuran contamination in soil and home-produced chicken eggs near pentachlorophenol sources. *Environ. Sci. Technol.* **2000**, *34*, 1143-1149.
- Hassellöv, M.; Readman, J.W.; Ranville, J.F.; Tiede, K. Nanoparticle analysis and characterization methodologies in environmental risk assessment of engineered nanoparticles. *Ecotoxicology* **2008**, *17*, 344-361.
- He, F.; Zhang, M.; Qian, T.W.; Zhao, D.Y. Transport of carboxymethyl cellulose stabilized iron nanoparticles in porous media: Column experiments and modeling. *J Colloid Interf Sci* **2009**, *334*, 96-102.
- He, F.; Zhao, D. Manipulating the size and dispersibility of zerovalent iron nanoparticles by use of carboxymethyl cellulose stabilizers. *Environ. Sci. Technol.* **2007**, *41*, 6216-6221.
- He, F.; Zhao, D.; Paul, C. Field assessment of carboxymethyl cellulose stabilized iron nanoparticles for in situ destruction of chlorinated solvents in source zones. *Water Res.* **2010**, *44*, 2360-2370.
- He, F.; Zhao, D.Y. Preparation and characterization of a new class of starch-stabilized bimetallic nanoparticles for degradation of chlorinated hydrocarbons in water. *Environ. Sci. Technol.* **2005**, *39*, 3314-3320.
- He, F.; Zhao, D.Y. Manipulating the size and dispersibility of zerovalent iron nanoparticles by use of carboxymethyl cellulose stabilizers. *Environ. Sci. Technol.* **2007**, *41*, 6216-6221.
- He, F.; Zhao, D.Y. Hydrodechlorination of trichloroethene using stabilized Fe-Pd nanoparticles: Reaction mechanism and effects of stabilizers, catalysts and reaction conditions. *Appl Catal B-Environ* **2008**, *84*, 533-540.
- He, F.; Zhao, D.Y.; Liu, J.C.; Roberts, C.B. Stabilization of Fe-Pd nanoparticles with sodium carboxymethyl cellulose for enhanced transport and dechlorination of trichloroethylene in soil and groundwater. *Ind Eng Chem Res* **2007**, *46*, 29-34.
- He, J.; Robrock, K.R.; Alvarez-Cohen, L. Microbial reductive debromination of polybrominated diphenyl ethers (PBDEs). *Environ. Sci. Technol.* **2006**, *40*, 4429-4434.

- He, Y.T.; Wilson, J.T.; Wilkin, R.T. Impact of iron sulfide transformation on trichloroethylene degradation. *Geochim. Cosmochim. Acta* **2010**, *74*, 2025-2039.
- Hiemstra, T.; Antelo, J.; Rahnemaie, R.; Riemsdijk, W.H.v. Nanoparticles in natural systems I: the effective reactive surface area of the natural oxide fraction in field samples. *Geochim. Cosmochim. Acta* **2010**, *74*, 41-58.
- Hofacker, A.F.; Voegelin, A.; Kaegi, R.; Weber, F.-A.; Kretzschmar, R. Temperature-dependent formation of metallic copper and metal sulfide nanoparticles during flooding of a contaminated soil. *Geochim. Cosmochim. Acta* **2013**, *103*, 316-332.
- Holland, K.S. A framework for sustainable remediation. *Environ. Sci. Technol.* **2011**, *45*, 7116-7117.
- Hoque, M.E.; Khosravi, K.; Newman, K.; Metcalfe, C.D. Detection and characterization of silver nanoparticles in aqueous matrices using asymmetric-flow field flow fractionation with inductively coupled plasma mass spectrometry. *J. Chromatogr. A* **2012**, *1233*, 109-115.
- Hou, L.W.; Zhang, H.; Xue, X.F. Ultrasound enhanced heterogeneous activation of peroxydisulfate by magnetite catalyst for the degradation of tetracycline in water. *Sep. Purif. Technol.* **2012**, *84*, 147-152.
- Hou, M.; Li, F.; Liu, X.; Wang, X.; Wan, H. The effect of substituent groups on the reductive degradation of azo dyes by zerovalent iron. *J Hazard Mater* **2007**, *145*, 305-314.
- Houas, A.; Lachheb, H.; Ksibi, M.; Elaloui, E.; Guillard, C.; Herrmann, J.M. Photocatalytic degradation pathway of methylene blue in water. *Appl Catal B-Environ* **2001**, *31*, 145-157.
- Hsiung, C.; Lien, H.; Galliano, A.E.; Yeh, C.; Shih, Y. Effects of water chemistry on the destabilization and sedimentation of commercial TiO₂ nanoparticles: Role of double-layer compression and charge neutralization. *Chemosphere* **2016**, *151*, 145-151.
- Hu, J.-D.; Zevi, Y.; Kou, X.-M.; Xiao, J.; Wang, X.-J.; Jin, Y. Effect of dissolved organic matter on the stability of magnetite nanoparticles under different pH and ionic strength conditions. *Sci. Total Environ.* **2010**, *408*, 3477-3489.
- Hu, J.D.; Zevi, Y.; Kou, X.M.; Xiao, J.; Wang, X.J.; Jin, Y. Effect of dissolved organic matter on the stability of magnetite nanoparticles under different pH and ionic strength conditions. *Sci. Total Environ.* **2010**, *408*, 3477-3489.
- Hutzinger, O.; Thoma, H. Polybrominated dibenzo-p-dioxins and dibenzofurans: the flame retardant issue. *Chemosphere* **1987**, *16*, 1877-1880.
- Imamura, H.; Masanari, K.; Kusuhara, M.; Katsumoto, H.; Sumi, T.; Sakata, Y. High hydrogen storage capacity of nanosized magnesium synthesized by high energy ball-milling. *J. Alloys Compd.* **2005**, *386*, 211-216.
- Jamei, M.R.; Khosravi, M.R.; Anvaripour, B. A novel ultrasound assisted method in synthesis of NZVI particles. *Ultrason Sonochem* **2014**, *21*, 226-233.
- Jeong, H.Y.; Anantharaman, K.; Han, Y.-S.; Hayes, K.F. Abiotic reductive dechlorination of cis-dichloroethylene by Fe species formed during iron- or sulfate-reduction. *Environ. Sci. Technol.* **2011**, *45*, 5186-5194.
- Jeong, H.Y.; Hayes, K.F. Impact of transition metals on reductive dechlorination rate of hexachloroethane by mackinawite. *Environ. Sci. Technol.* **2003**, *37*, 4650-4655.

- Jeong, H.Y.; Hayes, K.F. Reductive dechlorination of tetrachloroethylene and trichloroethylene by mackinawite (FeS) in the presence of metals: reaction rates. *Environ. Sci. Technol.* **2007**, *41*, 6390-6396.
- Jiang, W.; Cai, Q.; Xu, W.; Yang, M.; Cai, Y.; Dionysiou, D.D.; O'Shea, K.E. Cr(VI) adsorption and reduction by humic acid coated on magnetite. *Environ. Sci. Technol.* **2014**, *48*, 8078-8085.
- Johnson, R.L.; Johnson, G.O.B.; Nurmi, J.T.; Tratnyek, P.G. Natural organic matter enhanced mobility of nano zerovalent iron. *Environ. Sci. Technol.* **2009**, *43*, 5455-5460.
- Johnson, S.B.; Yoon, T.H.; Slowey, A.J.; Brown, G.E. Adsorption of organic matter at mineral/water interfaces: 3. implications of surface dissolution for adsorption of oxalate. *Langmuir* **2004**, *20*, 11480-11492.
- Johnson, T.L.; Fish, W.; Gorby, Y.A.; Tratnyek, P.G. Degradation of carbon tetrachloride by iron metal: complexation effects on the oxide surface. *J. Contam. Hydrol.* **1998**, *29*, 379-398.
- Johnson, T.L.; Scherer, M.M.; Tratnyek, P.G. Kinetics of halogenated organic compound degradation by iron metal. *Environ. Sci. Technol.* **1996**, *30*, 2634-2640.
- Joo, S.H.; Zhao, D. Destruction of lindane and atrazine using stabilized iron nanoparticles under aerobic and anaerobic conditions: effects of catalyst and stabilizer. *Chemosphere* **2008**, *70*, 418-425.
- Jorens, P.G.; Schepens, P.J.C. Human pentachlorophenol poisoning. *Hum Exp Toxicol* **1993**, *12*, 479-495.
- Kaifas, D.; Malleret, L.; Kumar, N.; Fétimi, W.; Claeys-Bruno, M.; Sergent, M.; Doumenq, P. Assessment of potential positive effects of nZVI surface modification and concentration levels on TCE dechlorination in the presence of competing strong oxidants, using an experimental design. *Sci. Total Environ.* **2014**, *481*, 335-342.
- Kanel, S.R.; Grenèche, J.-M.; Choi, H. Arsenic(V) removal from groundwater using nano scale zero-valent iron as a colloidal reactive barrier material. *Environ. Sci. Technol.* **2006**, *40*, 2045-2050.
- Kanel, S.R.; Nepal, D.; Manning, B.; Choi, H. Transport of surface-modified iron nanoparticle in porous media and application to arsenic(III) remediation. *J. Nanopart. Res.* **2007**, *9*, 725-735.
- Kappler, A.; Benz, M.; Schink, B.; Brune, A. Electron shuttling via humic acids in microbial iron(III) reduction in a freshwater sediment. *FEMS Microbiol. Ecol.* **2004**, *47*, 85-92.
- Kappler, A.; Haderlein, S.B. Natural organic matter as reductant for chlorinated aliphatic pollutants. *Environ. Sci. Technol.* **2003**, *37*, 2714-2719.
- Karn, B.; Kuiken, T.; Otto, M. Nanotechnology and in situ remediation: a review of the benefits and potential risks. *Environ Health Persp* **2009**, 1823-1831.
- Khairou, K.S.; El-Sayed, A. Inhibition effect of some polymers on the corrosion of cadmium in a hydrochloric acid solution. *J Appl Polym Sci* **2003**, *88*, 866-871.
- Kile, D.E.; Chiou, C.T. Water solubility enhancements of DDT and trichlorobenzene by some surfactants below and above the critical micelle concentration. *Environ. Sci. Technol.* **1989**, *23*, 832-838.

- Kim, D.; Duckworth, O.W.; Strathmann, T.J. Hydroxamate siderophore-promoted reactions between iron(II) and nitroaromatic groundwater contaminants. *Geochim. Cosmochim. Acta* **2009**, *73*, 1297-1311.
- Kim, D.; Strathmann, T.J. Role of organically complexed iron(II) species in the reductive transformation of RDX in anoxic environments. *Environ. Sci. Technol.* **2007**, *41*, 1257-1264.
- Kim, H.; Hong, H.-J.; Jung, J.; Kim, S.-H.; Yang, J.-W. Degradation of trichloroethylene (TCE) by nanoscale zero-valent iron (nZVI) immobilized in alginate bead. *J Hazard Mater* **2010**, *176*, 1038-1043.
- Kim, H.J.; Phenrat, T.; Tilton, R.D.; Lowry, G.V. Fe⁰ nanoparticles remain mobile in porous media after aging due to slow desorption of polymeric surface modifiers. *Environ. Sci. Technol.* **2009**, *43*, 3824-3830.
- Kim, H.J.; Phenrat, T.; Tilton, R.D.; Lowry, G.V. Fe⁰ nanoparticles remain mobile in porous media after aging due to slow desorption of polymeric surface modifiers. *Environ. Sci. Technol.* **2009**, *43*, 3824-3830.
- Kim, H.J.; Phenrat, T.; Tilton, R.D.; Lowry, G.V. Fe-0 Nanoparticles Remain Mobile in Porous Media after Aging Due to Slow Desorption of Polymeric Surface Modifiers. *Environ. Sci. Technol.* **2009**, *43*, 3824-3830.
- Kim, Y.-H.; Carraway, E.R. Dechlorination of pentachlorophenol by zero valent iron and modified zero valent irons. *Environ. Sci. Technol.* **2000**, *34*, 2014-2017.
- Kim, Y.H.; Carraway, E.R. Dechlorination of chlorinated ethenes and acetylenes by palladized iron. *Environ. Technol.* **2003**, *24*, 809-819.
- Kirk, G. **2004**. The biogeochemistry of submerged soils. John Wiley & Sons.
- Kirwan, L.J.; Fawell, P.D.; van Bronswijk, W. In Situ FTIR-ATR examination of poly(acrylic acid) adsorbed onto hematite at low pH. *Langmuir* **2003**, *19*, 5802-5807.
- Kober, R.; Schlicker, O.; Ebert, M.; Dahmke, A. Degradation of chlorinated ethylenes by Fe-0: inhibition processes and mineral precipitation. *Environ Geol* **2002**, *41*, 644-652.
- Kocur, C.M.; Chowdhury, A.I.; Sakulchaicharoen, N.; Boparai, H.K.; Weber, K.P.; Sharma, P. et al. Characterization of nZVI Mobility in a Field Scale Test. *Environ. Sci. Technol.* **2014**, *48*, 2862-2869.
- Koene, L.; Hamer, W.J.; Wit, J.H.W. Electrochemical behaviour of poly(pyrrole) coatings on steel. *J. Appl. Electrochem.* **2006**, *36*, 545-556.
- Kojima, Y.; Suzuki, K.-i.; Fukumoto, K.; Sasaki, M.; Yamamoto, T.; Kawai, Y.; Hayashi, H. Hydrogen generation using sodium borohydride solution and metal catalyst coated on metal oxide. *Int. J. Hydrogen Energy* **2002**, *27*, 1029-1034.
- Koningsberger, D.; Prins, R. **1988**. X-ray absorption: principles, applications, techniques of EXAFS, SEXAFS, and XANES. John Wiley and Sons, New York, NY.
- Kretschmar, R.; Sticher, H. Transport of humic-coated iron oxide colloids in a sandy soil: influence of Ca²⁺ and trace metals. *Environ. Sci. Technol.* **1997**, *31*, 3497-3504.
- Kulkarni, S.V.; Blackwell, C.D.; Blackard, A.L.; Stackhouse, C.W.; Alexander, M.W. Textile dyes and dyeing equipment: classification, properties, and environmental aspects *Triangle Park. Agency EP, ed. , North Carolina.* **1985**,

- Kunisue, T.; Takayanagi, N.; Isobe, T.; Takahashi, S.; Nose, M.; Yamada, T. et al. Polybrominated diphenyl ethers and persistent organochlorines in Japanese human adipose tissues. *Environ Int* **2007**, *33*, 1048-1056.
- Kusic, H.; Koprivanac, N.; Srsan, L. Azo dye degradation using Fenton type processes assisted by UV irradiation: a kinetic study. *J Photoch Photobio A* **2006**, *181*, 195-202.
- Kustov, L.M.; Finashina, E.D.; Shuvalova, E.V.; Tkachenko, O.P.; Kirichenko, O.A. Pd-Fe nanoparticles stabilized by chitosan derivatives for perchloroethene dechlorination. *Environ Int* **2011**, *37*, 1044-1052.
- Lai, B.; Chen, Z.; Zhou, Y.; Yang, P.; Wang, J.; Chen, Z. Removal of high concentration p-nitrophenol in aqueous solution by zero valent iron with ultrasonic irradiation (US-ZVI). *J Hazard Mater* **2013**, *250-251*, 220-228.
- Larese-Casanova, P.; Scherer, M.M. Abiotic transformation of hexahydro-1,3,5-trinitro-1,3,5-triazine (RDX) by green rusts. *Environ. Sci. Technol.* **2008**, *42*, 3975-3981.
- Larkin, P. **2011**. Infrared and raman spectroscopy: principles and spectral interpretation. Elsevier.
- Law, R.J.; Bersuder, P.; Allchin, C.R.; Barry, J. Levels of the flame retardants hexabromocyclododecane and tetrabromobisphenol A in the blubber of harbor porpoises (*Phocoena phocoena*) stranded or bycaught in the UK, with evidence for an increase in HBCD concentrations in recent years. *Environ. Sci. Technol.* **2006**, *40*, 2177-2183.
- LeBel, C.P.; Ischiropoulos, H.; Bondy, S.C. Evaluation of the probe 2',7'-dichlorofluorescein as an indicator of reactive oxygen species formation and oxidative stress. *Chemical Research in Toxicology* **1992**, *5*, 227-231.
- Ledin, A.; Karlsson, S.; Düker, A.; Allard, B. Measurements in situ of concentration and size distribution of colloidal matter in deep groundwaters by photon correlation spectroscopy. *Water Res.* **1994**, *28*, 1539-1545.
- Lemine, O.M. Microstructural characterisation of nanoparticles using, XRD line profiles analysis, FE-SEM and FT-IR. *Superlattices Microstruct.* **2009**, *45*, 576-582.
- Lens, P.N.L.; Virkutyte, J.; Jegatheesan, V.; Kim, S.-H.; Al-Abed, S. Nanotechnology for water and wastewater treatment. *Water Intelligence Online* **2013**, *12*,
- Li, H.; Li, W.; Zhang, Y.; Wang, T.; Wang, B.; Xu, W. et al. Chrysanthemum-like α -FeOOH microspheres produced by a simple green method and their outstanding ability in heavy metal ion removal. *J. Mater. Chem.* **2011**, *21*, 7878-7881.
- Liang, F.; Fan, J.; Guo, Y.; Fan, M.; Wang, J.; Yang, H. Reduction of nitrite by ultrasound-dispersed nanoscale zero-valent iron particles. *Ind Eng Chem Res* **2008**, *47*, 8550-8554.
- Liang, L.; Korte, N.; Gu, B.; Puls, R.; Reeter, C. Geochemical and microbial reactions affecting the long-term performance of in situ 'iron barriers'. *Adv. Environ. Res.* **2000**, *4*, 273-286.
- Liang, P.; Li, Y.-C.; Zhang, C.; Wu, S.-C.; Cui, H.-J.; Yu, S.; Wong, M.H. Effects of salinity and humic acid on the sorption of Hg on Fe and Mn hydroxides. *J Hazard Mater* **2013**, *244-245*, 322-328.
- Libra, J.A.; Borchert, M.; Vigelahn, L.; Storm, T. Two stage biological treatment of a diazo reactive textile dye and the fate of the dye metabolites. *Chemosphere* **2004**, *56*, 167-180.

- Lin, C.-H. **2012**. Degradation of pentachlorophenol by surfactant modified Ni/Fe bimetallic nanoparticles. National Taiwan University, Taiwan.
- Lin, C.; Tseng, S. Electrochemically reductive dechlorination of pentachlorophenol using a high overpotential zinc cathode. *Chemosphere* **1999**, *39*, 2375-2389.
- Lin, Y.-H.; Tseng, H.-H.; Wey, M.-Y.; Lin, M.-D. Characteristics, morphology, and stabilization mechanism of PAA250K-stabilized bimetal nanoparticles. *Colloids and Surfaces A: Physicochemical and Engineering Aspects* **2009**, *349*, 137-144.
- Lin, Y.H.; Tseng, H.H.; Wey, M.Y.; Lin, M.D. Characteristics, morphology, and stabilization mechanism of PAA250K-stabilized bimetal nanoparticles. *Colloid Surface A* **2009**, *349*, 137-144.
- Lin, Y.H.; Tseng, H.H.; Wey, M.Y.; Lin, M.D. Characteristics of two types of stabilized nano zero-valent iron and transport in porous media. *Sci. Total Environ.* **2010**, *408*, 2260-2267.
- Lindsey, M.E.; Tarr, M.A. Inhibition of hydroxyl radical reaction with aromatics by dissolved natural organic matter. *Environ. Sci. Technol.* **2000**, *34*, 444-449.
- Litvin, V.A.; Galagan, R.L.; Minaev, B.F. Kinetic and mechanism formation of silver nanoparticles coated by synthetic humic substances. *Colloids and Surfaces A: Physicochemical and Engineering Aspects* **2012**, *414*, 234-243.
- Litvin, V.A.; Minaev, B.F. Spectroscopy study of silver nanoparticles fabrication using synthetic humic substances and their antimicrobial activity. *Spectrochim. Acta, Part A* **2013**, *108*, 115-122.
- Litvin, V.A.; Minaev, B.F. The size-controllable, one-step synthesis and characterization of gold nanoparticles protected by synthetic humic substances. *Mater. Chem. Phys.* **2014**, *144*, 168-178.
- Liu, J.; Zhao, Z.; Jiang, G. Coating Fe₃O₄ Magnetic Nanoparticles with Humic Acid for High Efficient Removal of Heavy Metals in Water. *Environ. Sci. Technol.* **2008**, *42*, 6949-6954.
- Liu, X.; Peng, P.a.; Fu, J.; Huang, W. Effects of FeS on the Transformation Kinetics of γ -Hexachlorocyclohexane. *Environ. Sci. Technol.* **2003**, *37*, 1822-1828.
- Liu, Y.; Lowry, G.V. Effect of particle age (Fe0 content) and solution pH on NZVI reactivity: H₂ evolution and TCE dechlorination. *Environ. Sci. Technol.* **2006**, *40*, 6085-6090.
- Lowry, G.V.; Johnson, K.M. Congener-specific dechlorination of dissolved PCBs by microscale and nanoscale zerovalent iron in a water/methanol solution. *Environ. Sci. Technol.* **2004**, *38*, 5208-5216.
- Lu, Y.; Allen, H.E. Characterization of copper complexation with natural dissolved organic matter (DOM)—link to acidic moieties of DOM and competition by Ca and Mg. *Water Res.* **2002**, *36*, 5083-5101.
- Lucas, M.S.; Peres, J.A. Decolorization of the azo dye Reactive Black 5 by Fenton and photo-Fenton oxidation. *Dyes Pigments* **2006**, *71*, 236-244.
- Luque, R.; Varma, R.S.; Clark, J.H.; Kraus, G.A. **2012**. Sustainable preparation of metal nanoparticles: methods and applications. Royal Society of Chemistry.
- Machado, S.; Pinto, S.L.; Grosso, J.P.; Nouws, H.P.A.; Albergaria, J.T.; Delerue-Matos, C. Green production of zero-valent iron nanoparticles using tree leaf extracts. *Sci. Total Environ.* **2013**, *445*, 1-8.

- Mackay, D.M.; Cherry, J.A. Groundwater contamination: pump-and-treat remediation. *Environ. Sci. Technol.* **1989**, *23*, 630-636.
- Mandzy, N.; Grulke, E.; Druffel, T. Breakage of TiO₂ agglomerates in electrostatically stabilized aqueous dispersions. *Powder Technol.* **2005**, *160*, 121-126.
- Mannisto, M.K.; Salkinoja-Salonen, M.S.; Puhakka, J.A. In situ polychlorophenol bioremediation potential of the indigenous bacterial community of boreal groundwater. *Water Res.* **2001**, *35*, 2496-2504.
- Martell, A.E.; Smith, R.M. **1974**. Critical stability constants. Springer.
- Martínez-Villegas, N.; Martínez, C.E. Importance of dynamic soil properties in metal retention: an example from long-term Cu partitioning and redistribution studies using model systems. *Environ. Sci. Technol.* **2012**, *46*, 8069-8074.
- Maurer, F.; Christl, I.; Fulda, B.; Voegelin, A.; Kretzschmar, R. Copper redox transformation and complexation by reduced and oxidized soil humic acid. 2. potentiometric titrations and dialysis cell experiments. *Environ. Sci. Technol.* **2013**, *47*, 10912-10921.
- Maurer, F.; Christl, I.; Hoffmann, M.; Kretzschmar, R. Reduction and reoxidation of humic acid: influence on speciation of cadmium and silver. *Environ. Sci. Technol.* **2012**, *46*, 8808-8816.
- Maurer, F.; Christl, I.; Kretzschmar, R. Reduction and reoxidation of humic acid: influence on spectroscopic properties and proton binding. *Environ. Sci. Technol.* **2010**, *44*, 5787-5792.
- Mavrocordatos, D.; Perret, D.; Leppard, G.G. Strategies and advances in the characterisation of environmental colloids by electron microscopy. *UPAC Series on Analytical and Physical Chemistry of Environmental Systems* **2007**, *10*, 345-404.
- Mavrocordatos, D.; Pronk, W.; Boller, M. Analysis of environmental particles by atomic force microscopy, scanning and transmission electron microscopy. *Water Sci Technol* **2004**, *50*, 9-18.
- Max, J.-J.; Chapados, C. Infrared spectroscopy of aqueous carboxylic acids: comparison between different acids and their salts. *The Journal of Physical Chemistry A* **2004**, *108*, 3324-3337.
- Maynard, C. **1983**. Handbook of industrial chemistry. Van Nostrand Reinhold, New York.
- Mezohegyi, G.; Fabregat, A.; Font, J.; Bengoa, C.; Stuber, F.; Fortuny, A. Advanced bioreduction of commercially important azo dyes: modeling and correlation with electrochemical characteristics. *Ind Eng Chem Res* **2009**, *48*, 7054-7059.
- Molinari, R.; Pirillo, F.; Falco, M.; Loddo, V.; Palmisano, L. Photocatalytic degradation of dyes by using a membrane reactor. *Chem Eng Process* **2004**, *43*, 1103-1114.
- Mondragon, R.; Julia, J.E.; Barba, A.; Jarque, J.C. Characterization of silica-water nanofluids dispersed with an ultrasound probe: a study of their physical properties and stability. *Powder Technol.* **2012**, *224*, 138-146.
- Morris, S.; Allchin, C.R.; Zegers, B.N.; Haftka, J.J.H.; Boon, J.P.; Belpaire, C.; Leonards, P.E.G.; Van Leeuwen, S.P.J.; De Boer, J. Distribution and fate of HBCD and TBBPA brominated flame retardants in north sea estuaries and aquatic food webs. *Environ. Sci. Technol.* **2004**, *38*, 5497-5504.
- Mylon, S.E.; Chen, K.L.; Elimelech, M. Influence of natural organic matter and ionic composition on the kinetics and structure of hematite colloid aggregation: Implications to iron depletion in estuaries. *Langmuir* **2004**, *20*, 9000-9006.

- Nadagouda, M.N.; Castle, A.B.; Murdock, R.C.; Hussain, S.M.; Varma, R.S. In vitro biocompatibility of nanoscale zerovalent iron particles (NZVI) synthesized using tea polyphenols. *Green Chemistry* **2010**, *12*, 114-122.
- Nadagouda, M.N.; Varma, R.S. Green synthesis of silver and palladium nanoparticles at room temperature using coffee and tea extract. *Green Chemistry* **2008**, *10*, 859-862.
- Naka, D.; Kim, D.; Carbonaro, R.F.; Strathmann, T.J. Abiotic reduction of nitroaromatic contaminants by iron(II) complexes with organothiols ligands. *Environ. Toxicol. Chem.* **2008**, *27*, 1257-1266.
- Naka, D.; Kim, D.; Strathmann, T.J. Abiotic reduction of nitroaromatic compounds by aqueous iron(II)-catechol complexes. *Environ. Sci. Technol.* **2006**, *40*, 3006-3012.
- Nanotechnologies, T.P.o.E. 2009. Nanoremediation Map. The Project on Emerging Nanotechnologies. p. This map shows the location of contaminated sites utilizing some form of nanomediation.
- Naumov, P. **2012**. Chemical X-Ray photodiffraction: principles, examples, and perspectives. In: K. Rissanen, editor Advanced X-Ray Crystallography. Springer Berlin Heidelberg, Berlin, Heidelberg. p. 111-131.
- Nilsson, L.; Löf, D.; Bergenstahl, B. Phenolic acid nanoparticle formation in iron-containing aqueous solutions. *J. Agric. Food. Chem.* **2008**, *56*, 11453-11457.
- Noubactep, C. A critical review on the process of contaminant removal in Fe⁰-H₂O systems. *Environ. Technol.* **2008**, *29*, 909-920.
- Oliveira, D.P.; Carneiro, P.A.; Rech, C.M.; Zanoni, M.V.; Claxton, L.D.; Umbuzeiro, G.A. Mutagenic compounds generated from the chlorination of disperse azo-dyes and their presence in drinking water. *Environ Sci Technol* **2006**, *40*, 6682-6689.
- Otto, M.; Floyd, M.; Bajpai, S. Nanotechnology for site remediation. *Remediation Journal* **2008**, *19*, 99-108.
- Ou, Y.-h. **2012**. Effect of short-chain organic acids on the removal of pentachlorophenol with zerovalent iron in soil. National Taiwan University, Taiwan.
- Park, B.S.; Smith, D.M.; Thoma, S.G. Determination of agglomerate strength distributions, Part 4. Analysis of multimodal particle size distributions. *Powder Technol.* **1993**, *76*, 125-133.
- Parshetti, G.K.; Doong, R.A. Dechlorination of trichloroethylene by Ni/Fe nanoparticles immobilized in PEG/PVDF and PEG/nylon 66 membranes. *Water Res.* **2009**, *43*, 3086-3094.
- Pawlett, M.; Ritz, K.; Dorey, R.A.; Rocks, S.; Ramsden, J.; Harris, J.A. The impact of zero-valent iron nanoparticles upon soil microbial communities is context dependent. *Environ Sci Pollut R* **2013**, *20*, 1041-1049.
- Pecora, R. **2013**. Dynamic light scattering: applications of photon correlation spectroscopy. Springer Science & Business Media.
- Pédrot, M.; Boudec, A.L.; Davranche, M.; Dia, A.; Henin, O. How does organic matter constrain the nature, size and availability of Fe nanoparticles for biological reduction? *J Colloid Interf Sci* **2011**, *359*, 75-85.
- Peng, Y.H.; Tso, C.P.; Tsai, Y.C.; Zhuang, C.M.; Shih, Y.H. The effect of electrolytes on the aggregation kinetics of three different ZnO nanoparticles in water. *Sci. Total Environ.* **2015**, *530-531*, 183-190.
- Peretyazhko, T.; Sposito, G. Reducing capacity of terrestrial humic acids. *Geoderma* **2006**, *137*, 140-146.

- Perey, J.R.; Chiu, P.C.; Huang, C.P.; Cha, D.K. Zero-valent iron pretreatment for enhancing the biodegradability of Azo dyes. *Water Environ Res* **2002**, *74*, 221-225.
- Pham, A.N.; Rose, A.L.; Waite, T.D. Kinetics of Cu(II) reduction by natural organic matter. *J. Phys. Chem. A* **2012**, *116*, 6590-6599.
- Phenrat, T.; Liu, Y.; Tilton, R.D.; Lowry, G.V. Adsorbed polyelectrolyte coatings decrease Fe⁰ nanoparticle reactivity with TCE in water: conceptual model and mechanisms. *Environ. Sci. Technol.* **2009**, *43*, 1507-1514.
- Phenrat, T.; Saleh, N.; Sirk, K.; Kim, H.J.; Tilton, R.D.; Lowry, G.V. Stabilization of aqueous nanoscale zerovalent iron dispersions by anionic polyelectrolytes: adsorbed anionic polyelectrolyte layer properties and their effect on aggregation and sedimentation. *J. Nanopart. Res.* **2008**, *10*, 795-814.
- Phenrat, T.; Saleh, N.; Sirk, K.; Tilton, R.D.; Lowry, G.V. Aggregation and sedimentation of aqueous nanoscale zerovalent iron dispersions. *Environ. Sci. Technol.* **2007**, *41*, 284-290.
- Piccolo, A. **2002**. The supramolecular structure of humic substances: a novel understanding of humus chemistry and implications in soil science. *Advances in Agronomy*. Academic Press. p. 57-134.
- Powell, R.M.; Puls, R.W.; Hightower, S.K.; Sabatini, D.A. Coupled iron corrosion and chromate reduction: mechanisms for subsurface remediation. *Environ. Sci. Technol.* **1995**, *29*, 1913-1922.
- Prado, A.G.S.; Torres, J.D.; Martins, P.C.; Pertusatti, J.; Bolzon, L.B.; Faria, E.A. Studies on copper(II)- and zinc(II)-mixed ligand complexes of humic acid. *J Hazard Mater* **2006**, *136*, 585-588.
- Pullin, M.J.; Cabaniss, S.E. The effects of pH, ionic strength, and iron-fulvic acid interactions on the kinetics of non-photochemical iron transformations. I. iron(II) oxidation and iron(III) colloid formation. *Geochim. Cosmochim. Acta* **2003**, *67*, 4067-4077.
- Qiu, X.; Fang, Z.; Liang, B.; Gu, F.; Xu, Z. Degradation of decabromodiphenyl ether by nano zero-valent iron immobilized in mesoporous silica microspheres. *J Hazard Mater* **2011**, *193*, 70-81.
- Ràfols, C.; Barceló, D. Determination of mono- and disulphonated azo dyes by liquid chromatography-atmospheric pressure ionization mass spectrometry *J. Chromatogr. A* **1997**, *77*, 177-192
- Rasheed, Q.J.; Pandian, K.; Muthukumar, K. Treatment of petroleum refinery wastewater by ultrasound-dispersed nanoscale zero-valent iron particles. *Ultrason Sonochem* **2011**, *18*, 1138-1142.
- Ratasuk, N.; Nanny, M.A. Characterization and quantification of reversible redox sites in humic substances. *Environ. Sci. Technol.* **2007**, *41*, 7844-7850.
- Raychoudhury, T.; Naja, G.; Ghoshal, S. Assessment of transport of two polyelectrolyte-stabilized zero-valent iron nanoparticles in porous media. *J. Contam. Hydrol.* **2010**, *118*, 143-151.
- Reichard, P.U.; Kretzschmar, R.; Kraemer, S.M. Dissolution mechanisms of goethite in the presence of siderophores and organic acids. *Geochim. Cosmochim. Acta* **2007**, *71*, 5635-5650.

- Reig, F.B.; Adelantado, J.G.; Moreno, M.M. FTIR quantitative analysis of calcium carbonate (calcite) and silica (quartz) mixtures using the constant ratio method. Application to geological samples. *Talanta* **2002**, *58*, 811-821.
- Reimer, L. **2013**. Transmission electron microscopy: physics of image formation and microanalysis. Springer.
- Reinsch, B.C.; Forsberg, B.; Penn, R.L.; Kim, C.S.; Lowry, G.V. Chemical transformations during aging of zerovalent iron nanoparticles in the presence of common groundwater dissolved constituents. *Environ. Sci. Technol.* **2010**, *44*, 3455-3461.
- Ricca, G.; Federico, L.; Astori, C.; Gallo, R. Structural investigations of humic acid from leonardite by spectroscopic methods and thermal analysis. *Geoderma* **1993**, *57*, 263-274.
- Ristić, M.; Musić, S.; Godec, M. Properties of γ -FeOOH, α -FeOOH and α -Fe₂O₃ particles precipitated by hydrolysis of Fe³⁺ ions in perchlorate containing aqueous solutions. *J. Alloys Compd.* **2006**, *417*, 292-299.
- Robrock, K.R.; Korytár, P.; Alvarez-Cohen, L. Pathways for the anaerobic microbial debromination of polybrominated diphenyl ethers. *Environ. Sci. Technol.* **2008**, *42*, 2845-2852.
- Rónavári, A.; Balázs, M.; Tolmácsóv, P.; Molnár, C.; Kiss, I.; Kukovecz, Á.; Kónya, Z. Impact of the morphology and reactivity of nanoscale zero-valent iron (NZVI) on dechlorinating bacteria. *Water Res.* **2016**, *95*, 165-173.
- Ross, N.C.; Spackman, R.A.; Hitchman, M.L.; White, P.C. An investigation of the electrochemical reduction of pentachlorophenol with analysis by HPLC. *Journal of Applied Electrochemistry* **1997**, *27*, 51-57.
- Ruan, T.; Wang, Y.W.; Wang, C.; Wang, P.; Fu, J.J.; Yin, Y.G.; Qu, G.B.; Wang, T.; Jiang, G.B. Identification and evaluation of a novel heterocyclic brominated flame retardant tris(2,3-dibromopropyl) isocyanurate in environmental matrices near a manufacturing plant in southern China. *Environ. Sci. Technol.* **2009**, *43*, 3080-3086.
- Sakulchaicharoen, N.; O'Carroll, D.M.; Herrera, J.E. Enhanced stability and dechlorination activity of pre-synthesis stabilized nanoscale FePd particles. *J Contam Hydrol* **2010**, *118*, 117-127.
- Saleh, N.; Sirk, K.; Liu, Y.Q.; Phenrat, T.; Dufour, B.; Matyjaszewski, K.; Tilton, R.D.; Lowry, G.V. Surface modifications enhance nanoiron transport and NAPL targeting in saturated porous media. *Environ Eng Sci* **2007**, *24*, 45-57.
- Saleh, N.B.; Pfefferle, L.D.; Elimelech, M. Aggregation kinetics of multiwalled carbon nanotubes in aquatic systems: Measurements and environmental implications. *Environ. Sci. Technol.* **2008**, *42*, 7963-7969.
- Schlesinger, H.I.; Brown, H.C.; Finholt, A.E.; Gilbreath, J.R.; Hoekstra, H.R.; Hyde, E.K. Sodium borohydride, its hydrolysis and its use as a reducing agent and in the generation of hydrogen. *J. Am. Chem. Soc.* **1953**, *75*, 215-219.
- Schlicker, O.; Ebert, M.; Fruth, M.; Weidner, M.; Wüst, W.; Dahmke, A. Degradation of TCE with iron: the role of competing chromate and nitrate reduction. *Ground Water* **2000**, *38*, 403-409.
- Schmidt, M.A.; Gonzalez, J.M.; Halvorson, J.J.; Hagerman, A.E. Metal mobilization in soil by two structurally defined polyphenols. *Chemosphere* **2013**, *90*, 1870-1877.
- Schrack, B.; Hydutsky, B.W.; Blough, J.L.; Mallouk, T.E. Delivery Vehicles for Zerovalent Metal Nanoparticles in Soil and Groundwater. *Chem Mater* **2004**, *16*, 2187-2193.

- Scott, T.B.; Dickinson, M.; Crane, R.A.; Riba, O.; Hughes, G.M.; Allen, G.C. The effects of vacuum annealing on the structure and surface chemistry of iron nanoparticles. *J. Nanopart. Res.* **2010**, *12*, 1765-1775.
- Sellstrom, U.; Kierkegaard, A.; de Wit, C.; Jansson, B. Polybrominated diphenyl ethers and hexabromocyclododecane in sediment and fish from a Swedish river. *Environ. Toxicol. Chem.* **1998**, *17*, 1065-1072.
- Shankar, S.S.; Ahmad, A.; Sastry, M. Geranium leaf assisted biosynthesis of silver nanoparticles. *Biotechnol. Progr.* **2003**, *19*, 1627-1631.
- Sharpless, C.M. Lifetimes of triplet dissolved natural organic matter (DOM) and the effect of NaBH₄ reduction on singlet oxygen quantum yields: implications for DOM photophysics. *Environ. Sci. Technol.* **2012**, *46*, 4466-4473.
- Shih, Y.H.; Chen, M.Y.; Su, Y.F. Pentachlorophenol reduction by Pd/Fe bimetallic nanoparticles: effects of copper, nickel, and ferric cations. *Appl Catal B-Environ* **2011**, *105*, 24-29.
- Shih, Y.H.; Chen, Y.C.; Chen, M.Y.; Tai, Y.T.; Tso, C.P. Dechlorination of hexachlorobenzene by using nanoscale Fe and nanoscale Pd/Fe bimetallic particles. *Colloids and Surfaces A: Physicochemical and Engineering Aspects* **2009**, *332*, 84-89.
- Shih, Y.H.; Hsu, C.Y.; Su, Y.F. Reduction of hexachlorobenzene by nanoscale zero-valent iron: Kinetics, pH effect, and degradation mechanism. *Sep. Purif. Technol.* **2011**, *76*, 268-274.
- Shih, Y.H.; Tai, Y.T. Reaction of decabrominated diphenyl ether by zerovalent iron nanoparticles. *Chemosphere* **2010**, *78*, 1200-1206.
- Shih, Y.H.; Tso, C.P.; Tung, L.Y. Rapid degradation of methyl orange with nanoscale zerovalent iron particles. *Journal of Environmental Engineering and Management* **2010**, *20*, 137-143.
- Shih, Y.H.; Zhuang, C.M.; Tso, C.P.; Lin, C.H. The effect of electrolytes on the aggregation kinetics of titanium dioxide nanoparticle aggregates. *J. Nanopart. Res.* **2012**, *14*, 1-11.
- Shu, H.-Y.; Chang, M.-C.; Yu, H.-H.; Chen, W.-H. Reduction of an azo dye Acid Black 24 solution using synthesized nanoscale zerovalent iron particles. *J Colloid Interf Sci* **2007**, *314*, 89-97.
- Si, Y.B.; Fang, G.D.; Zhou, J.; Zhou, D.M. Reductive transformation of 2,4-dichlorophenoxyacetic acid by nanoscale and microscale Fe₃O₄ particles. *J Environ Sci Heal B* **2010**, *45*, 233-241.
- Silva, B.F.d.; Pérez, S.; Gardinalli, P.; Singhal, R.K.; Mozeto, A.A.; Barceló, D. Analytical chemistry of metallic nanoparticles in natural environments. *TrAC, Trends Anal. Chem.* **2011**, *30*, 528-540.
- Singer, P.C.; Stumm, W. The solubility of ferrous iron in carbonate-bearing waters. *Journal (American Water Works Association)* **1970**, *62*, 198-202.
- Singh, R.; Misra, V.; Mudiam, M.K.R.; Chauhan, L.K.S.; Singh, R.P. Degradation of γ -HCH spiked soil using stabilized Pd/Fe₀ bimetallic nanoparticles: Pathways, kinetics and effect of reaction conditions. *J Hazard Mater* **2012**, *237-238*, 355-364.
- Sivaraman, S.; Kumar, S.; Santhanam, V. Room-temperature synthesis of gold nanoparticles - Size-control by slow addition. *Gold Bull* **2010**, *43*, 275-286.

- Smuleac, V.; Varma, R.; Sikdar, S.; Bhattacharyya, D. Green Synthesis of Fe and Fe/Pd Bimetallic Nanoparticles in Membranes for Reductive Degradation of Chlorinated Organics. *Journal of membrane science* **2011**, *379*, 131-137.
- Soderstrom, G.; Sellstrom, U.; De Wit, C.A.; Tysklind, M. Photolytic debromination of decabromodiphenyl ether (BDE 209). *Environ. Sci. Technol.* **2004**, *38*, 127-132.
- Song, H.; Carraway, E.R. Reduction of chlorinated ethanes by nanosized zero-valent iron: Kinetics, pathways, and effects of reaction conditions. *Environ. Sci. Technol.* **2005**, *39*, 6237-6245.
- Soukupova, J.; Zboril, R.; Medrik, I.; Filip, J.; Safarova, K.; Ledl, R.; Mashlan, M.; Nosek, J.; Cernik, M. Highly concentrated, reactive and stable dispersion of zero-valent iron nanoparticles: direct surface modification and site application. *Chemical Engineering Journal* **2015**, *262*, 813-822.
- Štajdohar, J.; Ristić, M.; Musić, S. The effect of experimental conditions on the microstructure of hematite particles precipitated by the forced hydrolysis of FeCl₃ solutions. *J. Mol. Struct.* **2013**, *1044*, 290-298.
- Stapleton, H.M.; Alae, M.; Letcher, R.J.; Baker, J.E. Debromination of the flame retardant decabromodiphenyl ether by juvenile carp (*Cyprinus carpio*) following dietary exposure. *Environ. Sci. Technol.* **2004**, *38*, 112-119.
- Stevenson, F.J. **1994**. Humus chemistry: genesis, composition, reactions. John Wiley & Sons.
- Strathmann, T.J.; Stone, A.T. Reduction of oxamyl and related pesticides by FeII: Influence of organic ligands and natural organic matter. *Environ. Sci. Technol.* **2002**, *36*, 5172-5183.
- Straub, K.L.; Benz, M.; Schink, B. Iron metabolism in anoxic environments at near neutral pH. *FEMS Microbiol. Ecol.* **2001**, *34*, 181-186.
- Su, C.M.; Puls, R.W. Nitrate reduction by zerovalent iron: Effects of formate, oxalate, citrate, chloride, sulfate, borate, and phosphate. *Environ. Sci. Technol.* **2004**, *38*, 2715-2720.
- Sugano, Y.; Matsushima, Y.; Tsuchiya, K.; Aoki, H.; Hirai, M.; Shoda, M. Degradation pathway of an anthraquinone dye catalyzed by a unique peroxidase DyP from *Thanatephorus cucumeris* Dec 1. *Biodegradation* **2009**, *20*, 433-440.
- Sun, F.; Osseo-Asare, K.A.; Chen, Y.; Dempsey, B.A. Reduction of As(V) to As(III) by commercial ZVI or As(0) with acid-treated ZVI. *J Hazard Mater* **2011**, *196*, 311-317.
- Sun, W.; Nešić, S.; Woollam, R.C. The effect of temperature and ionic strength on iron carbonate (FeCO₃) solubility limit. *Corros. Sci.* **2009**, *51*, 1273-1276.
- Sun, Y.; Li, X.; Zhang, W.; Wang, H. A method for the preparation of stable dispersion of zero-valent iron nanoparticles. *Colloids and Surfaces A: Physicochemical and Engineering Aspects* **2007**, *308*, 60-66.
- Sun, Y.P.; Li, X.Q.; Zhang, W.X.; Wang, H.P. A method for the preparation of stable dispersion of zero-valent iron nanoparticles. *Colloid Surface A* **2007**, *308*, 60-66.
- Takamatsu, T.; Yoshida, Y. Determination of stability constants of metal-humic acid complexes by potentiometric titration and ion-selective electrodes *Soil Science* **1978**, *125*, 377-386.
- Talsness, C.E.; Shakibaei, M.; Kuriyama, S.N.; Grande, S.W.; Sterner-Kock, A.; Schnitker, P.; de Souza, C.; Grote, K.; Chahoud, I. Ultrastructural changes observed in rat

- ovaries following in utero and lactational exposure to low doses of a polybrominated flame retardant. *Toxicol. Lett.* **2005**, *157*, 189-202.
- Thamdrup, B. **2000**. Bacterial manganese and iron reduction in aquatic sediments. *Advances in microbial ecology*. Springer. p. 41-84.
- Thi Thuy, N.; Sy Uan, N.; Dinh Tam, P.; Duc Chien, N.; Anh Tuan, M. Dispersion of denatured carbon nanotubes by using a dimethylformamide solution. *Advances in Natural Sciences: Nanoscience and Nanotechnology* **2011**, *2*, 035015.
- Thuan, N.T.; Chang, M.B. Investigation of the degradation of pentachlorophenol in sandy soil via low-temperature pyrolysis. *J Hazard Mater* **2012**, *229-230*, 411-418.
- Tiede, K.; Boxall, A.B.A.; Tear, S.P.; Lewis, J.; David, H.; Hassellöv, M. Detection and characterization of engineered nanoparticles in food and the environment. *Food Addit. Contam.* **2008**, *25*, 795-821.
- Tinnacher, R.M.; Honeyman, B.D. A New method to radiolabel natural organic matter by chemical reduction with tritiated sodium borohydride. *Environ. Sci. Technol.* **2007**, *41*, 6776-6782.
- Tiraferrri, A.; Chen, K.L.; Sethi, R.; Elimelech, M. Reduced aggregation and sedimentation of zero-valent iron nanoparticles in the presence of guar gum. *J Colloid Interf Sci* **2008**, *324*, 71-79.
- Tse, K.K.C.; Lo, S.L. Desorption kinetics of PCP-contaminated soil: Effect of temperature. *Water Res.* **2002**, *36*, 284-290.
- Tso, C.P.; Shih, Y.H. The reactivity of well-dispersed zerovalent iron nanoparticles toward pentachlorophenol in water. *Water Res.* **2015**,
- Tso, C.P.; Zhung, C.M.; Shih, Y.H.; Tseng, Y.M.; Wu, S.C.; Doong, R.A. Stability of metal oxide nanoparticles in aqueous solutions. *Water Sci Technol* **2010**, *61*, 127-133.
- Umoren, S.A.; Solomon, M.M.; Udosoro, I.I.; Udoh, A.P. Synergistic and antagonistic effects between halide ions and carboxymethyl cellulose for the corrosion inhibition of mild steel in sulphuric acid solution. *Cellulose* **2010**, *17*, 635-648.
- Urban, N.R.; Ernst, K.; Bernasconi, S. Addition of sulfur to organic matter during early diagenesis of lake sediments. *Geochim. Cosmochim. Acta* **1999**, *63*, 837-853.
- Valo, R.; Kitunen, V.; Salkinojasalonen, M.; Raisanen, S. Chlorinated phenols as contaminants of soil and water in the vicinity of 2 finnish sawmills. *Chemosphere* **1984**, *13*, 835-844.
- van der Zee, C.; Roberts, D.R.; Rancourt, D.G.; Slomp, C.P. Nanogoethite is the dominant reactive oxyhydroxide phase in lake and marine sediments. *Geology* **2003**, *31*, 993-996.
- Viollier, E.; Inglett, P.W.; Hunter, K.; Roychoudhury, A.N.; Van Cappellen, P. The ferrozine method revisited: Fe(II)/Fe(III) determination in natural waters. *Appl. Geochem.* **2000**, *15*, 785-790.
- Wang, A.Q.; Wang, W.B. Nanocomposite of carboxymethyl cellulose and attapulgite as a novel pH-sensitive superabsorbent: Synthesis, characterization and properties. *Carbohydr Polym* **2010**, *82*, 83-91.
- Wang, C.B.; Zhang, W.X. Synthesizing nanoscale iron particles for rapid and complete dechlorination of TCE and PCBs. *Environ. Sci. Technol.* **1997**, *31*, 2154-2156.
- Wang, H.; Kou, X.; Pei, Z.; Xiao, J.Q.; Shan, X.; Xing, B. Physiological effects of magnetite (Fe₃O₄) nanoparticles on perennial ryegrass (*Lolium perenne* L.) and pumpkin (*Cucurbita mixta*) plants. *Nanotoxicology* **2011**, *5*, 30-42.

- Wang, S.; Mulligan, C.N. An evaluation of surfactant foam technology in remediation of contaminated soil. *Chemosphere* **2004**, *57*, 1079-1089.
- Wang, T.; Su, J.; Jin, X.; Chen, Z.; Megharaj, M.; Naidu, R. Functional clay supported bimetallic nZVI/Pd nanoparticles used for removal of methyl orange from aqueous solution. *J Hazard Mater* **2013**, *262*, 819-825.
- Wang, W.; Jin, Z.; Li, T.; Zhang, H.; Gao, S. Preparation of spherical iron nanoclusters in ethanol–water solution for nitrate removal. *Chemosphere* **2006**, *65*, 1396-1404.
- Wang, W.; Zhou, M.H. Degradation of trichloroethylene using solvent-responsive polymer coated Fe nanoparticles. *Colloid Surface A* **2010**, *369*, 232-239.
- Wang, X.; Cheng, X.; Sun, D. Autocatalysis in Reactive Black 5 biodecolorization by *Rhodospseudomonas palustris* W1. *Appl Microbiol Biotechnol* **2008**, *80*, 907-915.
- Wang, X.; Wang, P.; Ma, J.; Liu, H.; Ning, P. Synthesis, characterization, and reactivity of cellulose modified nano zero-valent iron for dye discoloration. *Appl. Surf. Sci.* **2015**, *345*, 57-66.
- Wang, X.; Zhu, M.; Liu, H.; Ma, J.; Li, F. Modification of Pd–Fe nanoparticles for catalytic dechlorination of 2,4-dichlorophenol. *Sci. Total Environ.* **2013**, *449*, 157-167.
- Wang, Y.; Stone, A.T. Phosphonate- and carboxylate-based chelating agents that solubilize (hydr)oxide-bound Mn(III). *Environ. Sci. Technol.* **2008**, *42*, 4397-4403.
- Watlington, K. **2005**. Emerging nanotechnologies for site remediation and wastewater treatment. Environmental Protection Agency.
- Weber, E.J.; Adams, R.L. Chemical-mediated and sediment-mediated reduction of the azo-dye Disperse-Blue-79. *Environ. Sci. Technol.* **1995**, *29*, 1163-1170.
- Weber, F.-A.; Hofacker, A.F.; Voegelin, A.; Kretzschmar, R. Temperature dependence and coupling of iron and arsenic reduction and release during flooding of a contaminated soil. *Environ. Sci. Technol.* **2009**, *44*, 116-122.
- Weber, F.-A.; Voegelin, A.; Kaegi, R.; Kretzschmar, R. Contaminant mobilization by metallic copper and metal sulphide colloids in flooded soil. *Nat. Geosci.* **2009**, *2*, 267-271.
- Weber, F.-A.; Voegelin, A.; Kretzschmar, R. Multi-metal contaminant dynamics in temporarily flooded soil under sulfate limitation. *Geochim. Cosmochim. Acta* **2009**, *73*, 5513-5527.
- Wei, J.; Xu, X.; Liu, Y.; Wang, D. Catalytic hydrodechlorination of 2,4-dichlorophenol over nanoscale Pd/Fe: reaction pathway and some experimental parameters. *Water Res.* **2006**, *40*, 348-354.
- Winter, W.T. Measurement of suspended particles by quasi-elastic light scattering. *Journal of Polymer Science: Polymer Letters Edition* **1983**, *21*, 570.
- Wolfe, A.K.; Bjornstad, D.J.; Kerchner, N.D. Making decisions about hazardous waste remediation when even considering a remediation technology is controversial. *Environ. Sci. Technol.* **2003**, *37*, 1485-1492.
- Wu, L.F.; Ritchie, S.M.C. Removal of trichloroethylene from water by cellulose acetate supported bimetallic Ni/Fe nanoparticles. *Chemosphere* **2006**, *63*, 285-292.
- Wu, N.; Fu, L.; Su, M.; Aslam, M.; Wong, K.C.; Dravid, V.P. Interaction of fatty acid monolayers with cobalt nanoparticles. *Nano Lett.* **2004**, *4*, 383-386.
- Xie, B.; Xu, Z.; Guo, W.; Li, Q. Impact of natural organic matter on the physicochemical properties of aqueous C60 nanoparticles. *Environ. Sci. Technol.* **2008**, *42*, 2853-2859.

- Xie, Y.; Fang, Z.; Cheng, W.; Tsang, P.E.; Zhao, D. Remediation of polybrominated diphenyl ethers in soil using Ni/Fe bimetallic nanoparticles: Influencing factors, kinetics and mechanism. *Sci. Total Environ.* **2014**, *485–486*, 363-370.
- Xing, Y. Synthesis and electrochemical characterization of uniformly-dispersed high Loading Pt nanoparticles on sonochemically-treated carbon nanotubes. *The Journal of Physical Chemistry B* **2004**, *108*, 19255-19259.
- Xiong, Z.; Zhao, D.; Pan, G. Rapid and complete destruction of perchlorate in water and ion-exchange brine using stabilized zero-valent iron nanoparticles. *Water Res.* **2007**, *41*, 3497-3505.
- Xu, F.; Deng, S.; Xu, J.; Zhang, W.; Wu, M.; Wang, B.; Huang, J.; Yu, G. Highly active and stable Ni–Fe bimetal prepared by ball milling for catalytic hydrodechlorination of 4-chlorophenol. *Environ. Sci. Technol.* **2012**, *46*, 4576-4582.
- Xu, J.; Hao, Z.W.; Xie, C.S.; Lv, X.S.; Yang, Y.P.; Xu, X.H. Promotion effect of Fe²⁺ and Fe₃O₄ on nitrate reduction using zero-valent iron. *Desalination* **2012**, *284*, 9-13.
- Xu, R. **2001**. Particle characterization: light scattering methods. Springer Science & Business Media.
- Xu, X.H.; Zhang, Z.; Cissoko, N.; Wo, J.J. Factors influencing the dechlorination of 2,4-dichlorophenol by Ni-Fe nanoparticles in the presence of humic acid. *J Hazard Mater* **2009**, *165*, 78-86.
- Xu, Y.; Zhao, D. Reductive immobilization of chromate in water and soil using stabilized iron nanoparticles. *Water Res.* **2007**, *41*, 2101-2108.
- Yamamoto, M.; Nishida, A.; Otsuka, K.; Komai, T.; Fukushima, M. Evaluation of the binding of iron(II) to humic substances derived from a compost sample by a colorimetric method using ferrozine. *Bioresource Technol* **2010**, *101*, 4456-4460.
- Yan, H.; Zhang, W.; Kan, X.; Dong, L.; Jiang, Z.; Li, H.; Yang, H.; Cheng, R. Sorption of methylene blue by carboxymethyl cellulose and reuse process in a secondary sorption. *Colloids and Surfaces A: Physicochemical and Engineering Aspects* **2011**, *380*, 143-151.
- Yan, W.; Herzing, A.A.; Li, X.; Kiely, C.J.; Zhang, W. Structural evolution of Pd-doped nanoscale zero-valent iron (nZVI) in aqueous media and implications for particle aging and reactivity. *Environ. Sci. Technol.* **2010**, *44*, 4288-4294.
- Yang, G.C.C.; Tu, H.C.; Hung, C.H. Stability of nanoiron slurries and their transport in the subsurface environment. *Sep. Purif. Technol.* **2007**, *58*, 166-172.
- Zhang, M.; He, F.; Zhao, D.Y.; Hao, X.D. Degradation of soil-sorbed trichloroethylene by stabilized zero valent iron nanoparticles: Effects of sorption, surfactants, and natural organic matter. *Water Res.* **2011**, *45*, 2401-2414.
- Zhang, W.-x. Nanoscale Iron Particles for Environmental Remediation: An Overview. *Journal of Nanoparticle Research* **2003**, *5*, 323-332.
- Zhang, W.X. Nanoscale iron particles for environmental remediation: An overview. *J. Nanopart. Res.* **2003**, *5*, 323-332.
- Zhang, X.; Zhang, P.; Wu, Z.; Zhang, L.; Zeng, G.; Zhou, C. Adsorption of methylene blue onto humic acid-coated Fe₃O₄ nanoparticles. *Colloids and Surfaces A: Physicochemical and Engineering Aspects* **2013**, *435*, 85-90.
- Zhang, X.L.; Deng, B.L.; Guo, J.; Wang, Y.; Lan, Y.Q. Ligand-assisted degradation of carbon tetrachloride by microscale zero-valent iron. *J Environ Manage* **2011**, *92*, 1328-1333.

- Zhang, Y.; Chen, Y.; Westerhoff, P.; Crittenden, J. Impact of natural organic matter and divalent cations on the stability of aqueous nanoparticles. *Water Res.* **2009**, *43*, 4249-4257.
- Zhang, Y.; Liu, S.; Wang, L.; Qin, X.; Tian, J.; Lu, W.; Chang, G.; Sun, X. One-pot green synthesis of Ag nanoparticles-graphene nanocomposites and their applications in SERS, H₂O₂, and glucose sensing. *RSC Advances* **2012**,
- Zhang, Y.; Yang, M.; Portney, N.G.; Cui, D.; Budak, G.; Ozbay, E.; Ozkan, M.; Ozkan, C.S. Zeta potential: a surface electrical characteristic to probe the interaction of nanoparticles with normal and cancer human breast epithelial cells. *Biomed. Microdevices* **2008**, *10*, 321-328.
- Zhao, D.; Zheng, Y.; Li, M.; Baig, S.A.; Wu, D.; Xu, X. Catalytic dechlorination of 2,4-dichlorophenol by Ni/Fe nanoparticles prepared in the presence of ultrasonic irradiation. *Ultrason Sonochem* **2014**, *21*, 1714-1721.
- Zhong, L.S.; Hu, J.S.; Liang, H.P.; Cao, A.M.; Song, W.G.; Wan, L.J. Self-Assembled 3D Flowerlike Iron Oxide Nanostructures and Their Application in Water Treatment. *Adv. Mater.* **2006**, *18*, 2426-2431.
- Zhou, W.; Apkarian, R.; Wang, Z.L.; Joy, D. **2007**. Fundamentals of scanning electron microscopy (SEM). In: W. Zhou and Z. L. Wang, editors, *Scanning Microscopy for Nanotechnology: Techniques and Applications*. Springer, New York, NY. p. 1-40.
- Zhu, M.; Wang, H.; Keller, A.A.; Wang, T.; Li, F. The effect of humic acid on the aggregation of titanium dioxide nanoparticles under different pH and ionic strengths. *Sci. Total Environ.* **2014**, *487*, 375-380.
- Zille, A.; Ramalho, P.; Tzanov, T.; Millward, R.; Aires, V.; Cardoso, M.H.; Ramalho, M.T.; Gübitz, G.M.; Cavaco-Paulo, A. Predicting dye biodegradation from redox potentials. *Biotechnol. Progr.* **2004**, *20*, 1588-1592.
- Zollinger, H. **2003**. *Color chemistry: syntheses, properties, and applications of organic dyes and pigments*. 3rd, Revised Edition ed. Wiley-VCH Verlag GmbH, New York.

Supporting information



Table S1. The chemical properties of Leonardite HA (1S104H) (data offered by IHSS website:

<http://www.humicsubstances.org/index.html>)

Elemental compositions and stable isotopic ratios

H ₂ O	Ash	C	H	O	N	S	P	$\delta^{13}\text{C}$	$\delta^{15}\text{N}$
7.2	2.58	63.81	3.7	31.27	1.23	0.76	<0.01	-23.8	2.13

C, H, O, N, S, and P are the elemental composition in %(w/w) of a dry, ash-free sample. $\delta^{13}\text{C}$ and $\delta^{15}\text{N}$ are the abundances of the respective stable isotopes in units of per mil, or o/oo.

Acidic Functional Groups

Carboxyl	Phenolic
7.46	2.31

Carboxyl is the charge density (meq/g C) at pH 8.0; Phenolic is two times the change in charge density (meq/g C) between pH 8.0 and pH 10.0.

¹³C NMR estimates of carbon distribution

Carbonyl	Carboxyl	Aromatic	Acetal	Heteroaliphatic	Aliphatic
	190-165	165-110	110-90		
220-190 ppm	ppm	ppm	ppm	90-60 ppm	60-0 ppm
8	15	58	4	1	14

This table contains the electronically integrated peak area percentages for selected ranges of chemical shift.

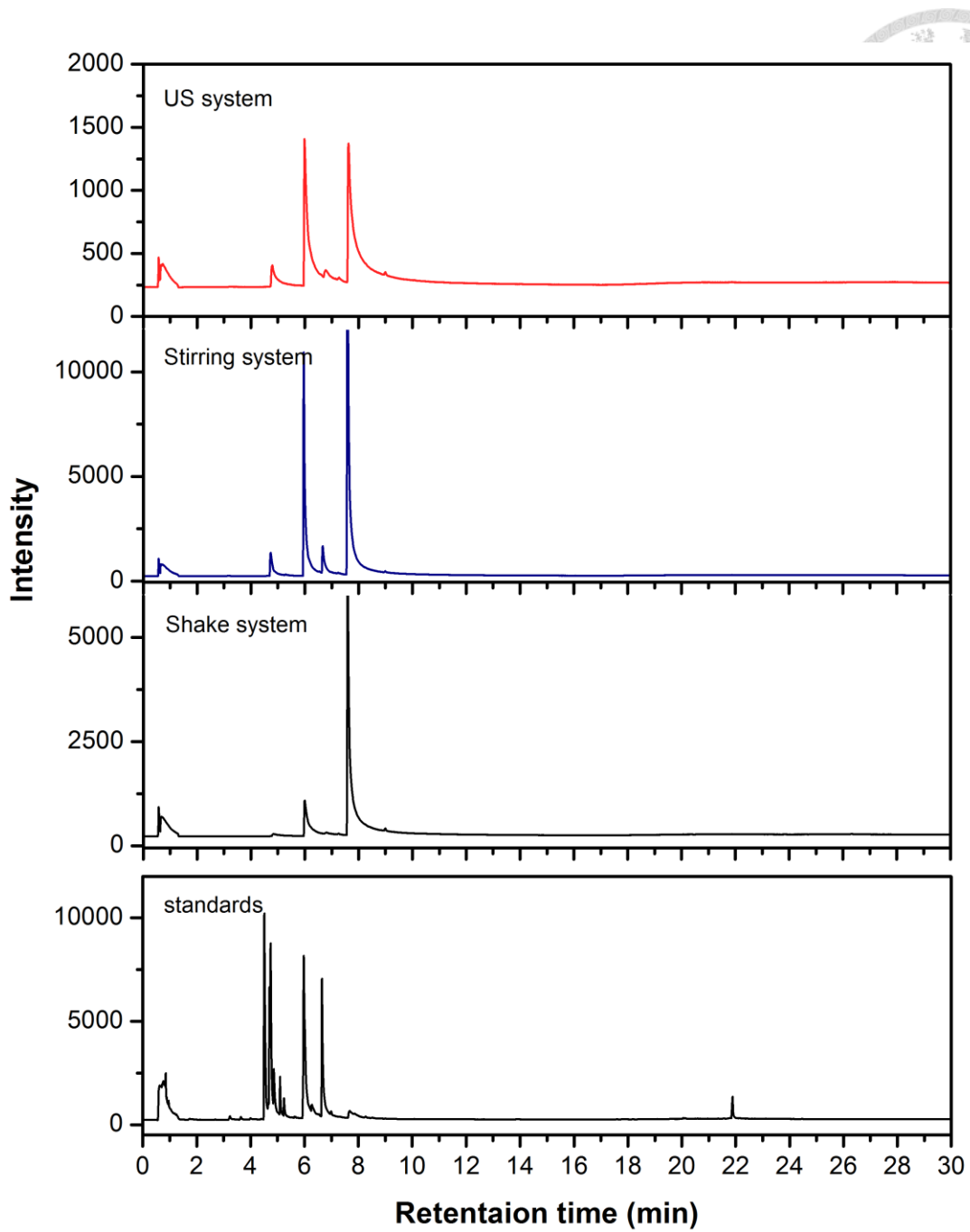


Figure S1. The PCP byproduct analysis.

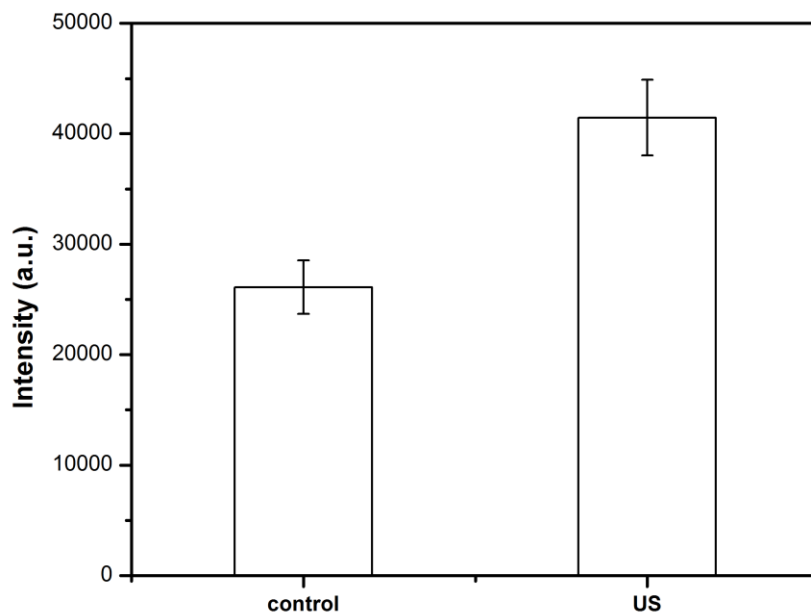


Figure S2. The ROS intensity in the US system after US irradiation for 40 minutes.

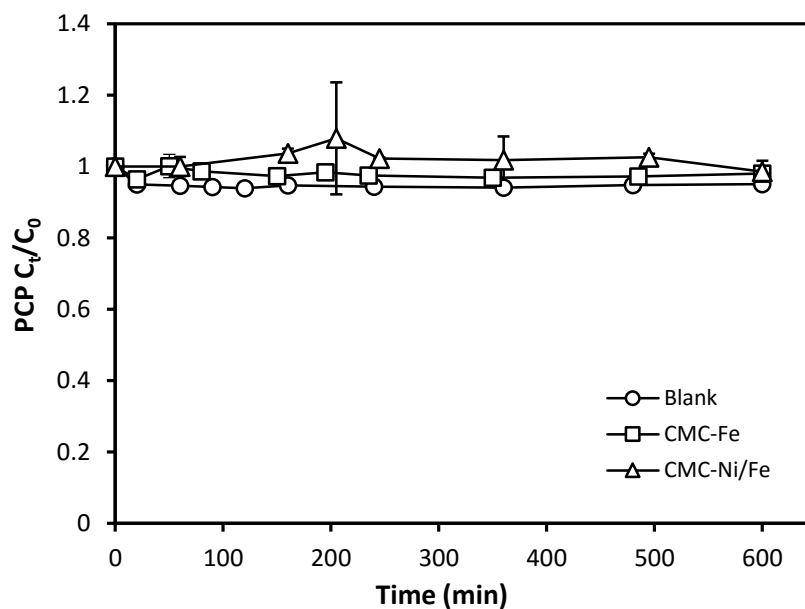


Figure S3. The removal of PCP with CMC-Fe and CMC-Ni/Fe. CMC concentration was 0.067 mM, Fe dosage was 12 g/L, Ni loading was 0.5 wt%, and PCP initial concentration was 5 mg/L (Lin, 2012).

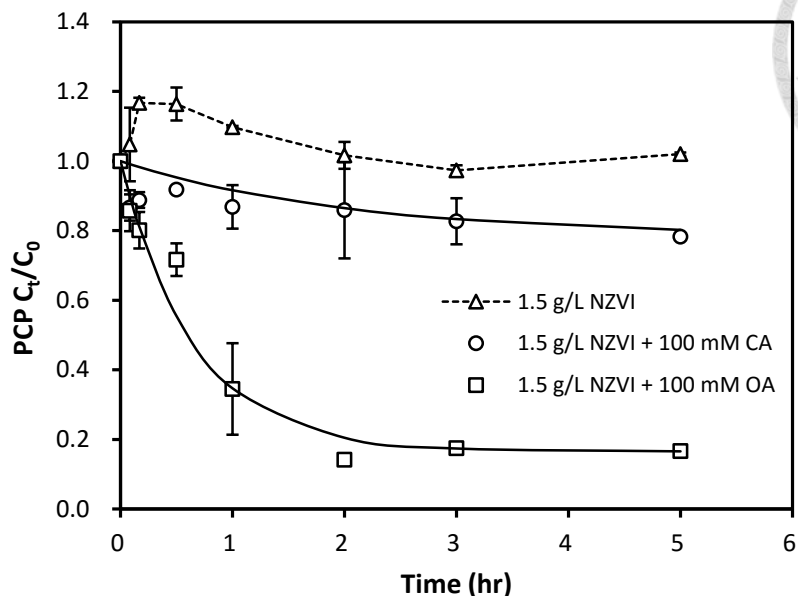
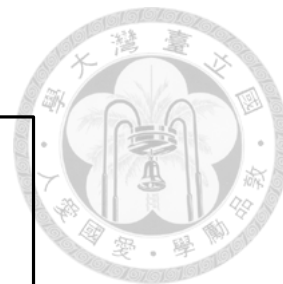


Figure S4. The removal of PCP by NZVI in the presence of organic ligands. Initial concentration of ligand was 100 mM. PCP concentration was 5 mg/L, Fe dosage was 1.5 g/L and initial pH was pH 3.0 (Ou, 2012).

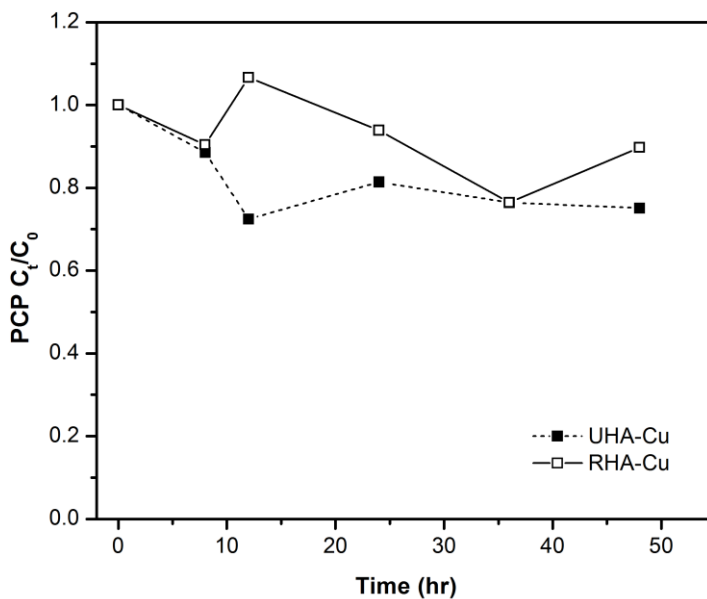


Figure S5. The removal of PCP with HA-Cu NPs. The initial concentration of PCP was 1 mg/L, HA and CuSO₄ concentrations were 1.0 g/L and 1.6 g/L, respectively.